



Universitat Autònoma de Barcelona

**ADVERTIMENT.** L'accés als continguts d'aquesta tesi doctoral i la seva utilització ha de respectar els drets de la persona autora. Pot ser utilitzada per a consulta o estudi personal, així com en activitats o materials d'investigació i docència en els termes establerts a l'art. 32 del Text Refós de la Llei de Propietat Intel·lectual (RDL 1/1996). Per altres utilitzacions es requereix l'autorització prèvia i expressa de la persona autora. En qualsevol cas, en la utilització dels seus continguts caldrà indicar de forma clara el nom i cognoms de la persona autora i el títol de la tesi doctoral. No s'autoritza la seva reproducció o altres formes d'explotació efectuades amb finalitats de lucre ni la seva comunicació pública des d'un lloc aliè al servei TDX. Tampoc s'autoritza la presentació del seu contingut en una finestra o marc aliè a TDX (framing). Aquesta reserva de drets afecta tant als continguts de la tesi com als seus resums i índexs.

**ADVERTENCIA.** El acceso a los contenidos de esta tesis doctoral y su utilización debe respetar los derechos de la persona autora. Puede ser utilizada para consulta o estudio personal, así como en actividades o materiales de investigación y docencia en los términos establecidos en el art. 32 del Texto Refundido de la Ley de Propiedad Intelectual (RDL 1/1996). Para otros usos se requiere la autorización previa y expresa de la persona autora. En cualquier caso, en la utilización de sus contenidos se deberá indicar de forma clara el nombre y apellidos de la persona autora y el título de la tesis doctoral. No se autoriza su reproducción u otras formas de explotación efectuadas con fines lucrativos ni su comunicación pública desde un sitio ajeno al servicio TDR. Tampoco se autoriza la presentación de su contenido en una ventana o marco ajeno a TDR (framing). Esta reserva de derechos afecta tanto al contenido de la tesis como a sus resúmenes e índices.

**WARNING.** The access to the contents of this doctoral thesis and its use must respect the rights of the author. It can be used for reference or private study, as well as research and learning activities or materials in the terms established by the 32nd article of the Spanish Consolidated Copyright Act (RDL 1/1996). Express and previous authorization of the author is required for any other uses. In any case, when using its content, full name of the author and title of the thesis must be clearly indicated. Reproduction or other forms of for profit use or public communication from outside TDX service is not allowed. Presentation of its content in a window or frame external to TDX (framing) is not authorized either. These rights affect both the content of the thesis and its abstracts and indexes.



**Universitat Autònoma de Barcelona**

**Layered materials for thermal management and sensing applications**

**Peng Xiao**

DOCTORAL THESIS

---

# Layered materials for thermal management and sensing applications

---

Peng Xiao

A THESIS SUBMITTED IN FULFILMENT OF THE REQUIREMENTS  
OF THE DEGREE OF

DOCTOR OF PHILOSOPHY IN PHYSICS  
AT THE  
UNIVERSITAT AUTONOMA DE BARCELONA

2022

Supervisor: Dr. Marianna Sledzinska

Supervisor: Prof. Dr. Clivia Marfa Sotomayor Torres

Tutor: Prof. Dr. Carles Navau Ros

Tutor: Prof. Dr. Jordi Mompert



# Abstract

2D van der Waals layered materials have been recently widely explored for electronics, opto-electronics, and sensing applications. Especially as layered materials-based field-effect transistors could be a possibility for replacing silicon-based transistor in chips. However, in order to overcome the device failure caused by overheating and apply layered materials more efficiently to electronic devices, a better understanding of thermal properties and thermal management methods are required. In this thesis, various layered materials, such as transition metal dichalcogenides MoS<sub>2</sub> and WS<sub>2</sub>; PtSe<sub>2</sub> and SnSe<sub>2</sub> were prepared by different techniques for the study of thermal management. Two main techniques have been extensively applied to measure the in-plane and cross-plane thermal conductivity of these materials using Two-laser Raman thermometry and Frequency domain thermoreflectance, respectively.

SnSe<sub>2</sub> and MoS<sub>2</sub> free-standing membranes of varying thickness (16 – 190 nm) were fabricated by a combination of mechanical exfoliation and dry-transfer methods. The results obtained show that the in-plane and cross-plane thermal conductivity of the layered materials increase with increasing thickness and that in-plane thermal conductivity of layered materials decreases with increasing temperature. In SnSe<sub>2</sub>, the thickness-independent thermal conductivity anisotropy ratio was found to be about ~8.4 and the temperature-dependence thermal conductivity became gradually weaker with decreasing thickness.

PtSe<sub>2</sub> crystalline (1 – 40 layers) and polycrystalline thin films were synthesized using the molecular beam epitaxy technique. Furthermore, the ballistic cross-plane heat transport was up to ~30 layers in PtSe<sub>2</sub>, and the cross-plane thermal conductivity of polycrystalline films was about 35% lower than that of a 20-layers-thick crystalline PtSe<sub>2</sub> film of the same thickness. PtSe<sub>2</sub> had the short acoustic phonon lifetimes in the range of picoseconds and an out-of-plane elastic constant of 31.8 GPa with a layer-dependent group velocity ranging from 1340 ms<sup>-1</sup> in bilayer to 1873 ms<sup>-1</sup> in eight layers.

The next, to control the thermal conductivity of MoS<sub>2</sub>, annealing and nanopatterning were applied to increase and decrease the thermal conductivity of MoS<sub>2</sub> materials, respectively. MoS<sub>2</sub> nanosheets were synthesized using the solution-exfoliation

method and fabricated for free-standing membranes. It was found that the thermal conductivity of MoS<sub>2</sub> nanosheets-based film improved by about 140% after annealing. Additionally, MoS<sub>2</sub> free-standing membranes of varying thickness (4.5 – 40 nm) were fabricated in the same way as layered SnSe<sub>2</sub> membrane, we studied of the in-plane thermal conductivity as a function of thickness, porosity, and temperature in both pristine and nanopatterned suspended MoS<sub>2</sub> membranes. After nanopatterning with a focused ion beam, we obtained a more than a 10-fold reduction of the thermal conductivities for the holey period of 500 nm and a value below 1 W/mK for the period of 300 nm, which shows the layered MoS<sub>2</sub> is much more sensitive to the holey array made by nanopatterning than silicon and silicon carbide. The results were supported by equilibrium molecular dynamic simulations for both pristine and nanopatterned MoS<sub>2</sub>. We also applied the nanopatterned MoS<sub>2</sub> for heat routing applications for blocking and guiding heat away from the hotspot through a pre-defined path in the in-plane direction. Accordingly, the patterned regions act as a high thermal resistance, and only four patterned lattice periods of 300 nm yielded a thermal resistance of  $4 \cdot 10^{-6} \text{ m}^2\text{K/W}$  with, highlighting the great potential of MoS<sub>2</sub> in thermal management applications.

Finally, the samples included MoS<sub>2</sub> and WS<sub>2</sub> nanosheets were synthesized using the solution-exfoliation method. MoS<sub>2</sub> and WS<sub>2</sub> nanosheets were applied for high-performance humidity sensors with fast responsivity and long working time, and another interesting finding is that the metal salts coated sensors showed reversed sensing behaviors owing to changes in their morphology during measurement.

# Preface

This PhD Thesis summarizes my work at the Phononic and Photonic Nanostructures Group of the Catalan Institute of Nanoscience and Nanotechnology (ICN2) during the period from January 2019 to July 2022. In accordance with decision of the commission of the PhD Programme of Physics at Universitat Autònoma de Barcelona, Spain, this thesis is presented as a collection of articles.

The articles are listed below in order of appearance in the thesis:

Article 1. Peng Xiao, Emigdio Chavez-Angel, Stefanos Chaitoglou, Marianna Sledzinska, Athanasios Dimoulas, Clivia M Sotomayor Torres, Alexandros El Sachat. *Anisotropic Thermal Conductivity of Crystalline Layered SnSe<sub>2</sub>*. Nano Letters, 21, 21, 9172-9179 (2021).

Article 2. Alexandros El Sachat, Peng Xiao, Davide Donadio, Frédéric Bonell, Marianna Sledzinska, Alain Marty, Céline Vergnaud, Hervé Boukari, Matthieu Jamet, Guillermo Arregui, Zekun Chen, Francesc Alzina, Clivia M. Sotomayor Torres, Emigdio Chavez-Angel. *Effect of crystallinity and thickness on thermal transport in layered PtSe<sub>2</sub>*. Npj 2D Mater Appl, 6, 32 (2022).

Article 3. Peng Xiao, Alexandros El Sachat, Emigdio Chávez Angel, Ryan C. Ng, Giorgos Nikoulis, Joseph Kioseoglou, Konstantinos Termentzidis, Clivia M. Sotomayor Torres, and Marianna Sledzinska. *Heat Routing in Nanopatterned MoS<sub>2</sub>*. Manuscript submitted to ACS nano (2022).

Article 4. Peng Xiao, Davide Mencarelli, Emigdio Chavez-Angel, Christopher Hardly Joseph, Antonino Cataldo, Luca Pierantoni, Clivia M Sotomayor Torres, Marianna Sledzinska. *Reversing the Humidity Response of MoS<sub>2</sub>-and WS<sub>2</sub>-Based Sensors Using Transition-Metal Salts*. ACS Appl. Mater. Interfaces, 13,19, 23201-23209 (2021).

Each article is preceded by a section that contains an introduction to the topic and summary of the results.

# Acknowledgements

Recalling when I had just decided to enrol on the PhD program four years ago because of some terrible experiences in some labs in Asia, I was still doubting if it was a good decision to go to Europe to start new research in a new lab. Now, looking back on the wonderful experience of research and life during the past four years, I am glad of my decision and very grateful for the opportunity to join the Phononic and Photonic Nanostructures Group (P2N) at the Catalan Institute of Nanoscience and Nanotechnology (ICN2), Barcelona, Spain. For this, I would like to thank my supervisors, colleagues and, friends I have made over the past four years for their care, help, and support.

First of all, I would like to thank my supervisor Dr. Marianna Sledzinska, who has spent a lot of time with me discussing my scientific work. She is very enlightened and has been supportive of me and my ideas for research in my chosen fields including material synthesis, thermal conductivity, Seebeck coefficient and gas/ humidity sensors. I hope that we will be able to continue to work together in the future. I also want to thank Prof. Dr. Clivia Marfa Sotomayor Torres because she gave me the opportunity to join her group. I have been impressed by her rigorous spirit and her attitude towards students. As the leader of a big research group, she has always taken the time out her busy schedule to review my reports, slides, and send me her advice. I also thank you for giving me chances to meet many researchers, work in different labs, and explore new research fields.

I would also like to thank Dr. Emigdio Chavez-Angel for the support with MATLAB and COMSOL simulation. He is an amazing teacher and always wanted to give me more knowledge and teach me techniques, such as the MATLAB programming and COMSOL simulation, 3-omega method, Frequency-domain thermorefectance, etc. A lot of new ideas were generated during our discussions. A special thanks goes to Dr. Alexandros El Sachat, who essentially supported my experiments and contributed to the main results of this thesis related to SnSe<sub>2</sub> and PtSe<sub>2</sub>. We are very good partners and will continue work together in the future.



Many thanks also to Dr. Francesc Alzina for teaching me the knowledge and simulation skills of Brillouin scattering. I would like also to thank Prof. Dr. Daniel Navarro-Urrios for his encouragement and support particularly in our attempt to put a single nanosphere on a nanobridge together for the optomechanical crystals. I thank Dr. Alois Arrighi for his advice at the beginning of my PhD programme and I am also grateful to Dr. Jeremie Maire for many scientific discussions. Thanks also to the project managers of the group Mrs. Cristina Morales and Mrs. Ariadna Peral for their help during my stay in this group. I want to thank all the people I have overlapped with in the group of Clivia: Dr. Guillermo Arregui Bravo, Dr. Martin F Colombano, Francisco Cespedes Urqueta, Omar Florez, Gil Jumbert, Eulalia Puig Vilardell, Dr. Philippe Djorwe, Dr. Juliana Jaramillo Fernandez, Dr. Ryan Cecil Ng, Dr. Martin Poblet, Dr. Guy L. Whitworth, Dr. Guilhem Madiot, and Dr. Lisa Maria Mitterhuber-Gressl.

I am immensely thankful to have had the opportunity to work with Dr. Maria Jose Esplandiu Egido on the chemical vapor deposition synthesis of monolayer materials, especially for her help on synthesis and transfer of graphene. I would like to thank her group members Cubakhanim Shahnazarova and Nour al Hoda Bast for their help. I'd also like to thank Dr. Raul Perez Rodriguez, Dr. Xavier Borrise Nogue, Dr. Belen Ballesteros Perez, Dr. Marcos Rosado Iglesias, and Dr. Francisco Javier Belarre Trivino for their help with nanofabrication. I would like to thank my Chinese partners I met in the campus of UAB: Dr. Haibing Xie, Dr. Ying Liu, Dr. Pengyi Tang, Dr. Dr. Zhi Li, Dr. Yue Zhang, Dr. Ting Zhang, Dr. Zhifu Liang, Dr. Yang Liu, Junjie Zhu, Junda Zhang, Xu Han, Yunhui Yang, Lei Zhao, Liming Hu, Qiuyue Yang, Minghua Kong, Tingfeng Song.

I am very thankful to have been able to visit MIT twice to work with the group of Prof. Dr. Keith Nelson for more than one month through support provided by the MIT-Spain "La Caixa" Programme. I would like to thank Dr. Alexei Maznev for supervising my work in MIT, as well as for the guidance and advice he gave me to consider my work from a fundamental physics perspective. I am particularly grateful to Dr. Ryan Andrew Duncan for his help during the twice research visit in Nelson Group, and the equipment training of the Transient Grating Spectroscopy he supplied.

The work studying the humidity sensing properties of the MoS<sub>2</sub> and WS<sub>2</sub> nanosheets presented in Chapter 6 was done in close collaboration with the research group of Prof.

Dr. Luca Pierantoni. I would like to specifically thank Dr. Hardly Joseph Christopher and Dr. Davide Mencarelli for their discussion and contribution on the simulator model of humidity sensing in Chapter 6. This work was funded by the European Horizon 2020 NanoSmart project. I benefited from the project during the discussion on its progress meetings. In particular, I want to thank Prof. Dr. Deligeorgis George for the opportunity to visit his group at the Institute of Electronic Structure and Laser of FORTH, Heraklion, Greece. George gave me many valuable suggestions on the development of the humidity sensor. I also want to thank his group members Dr. Iacovella Fabrice and Dr. Loulouakis Dimitris for their help in Heraklion. I am very thankful to have collaborated with many researchers from different fields in the NanoSmart project: Dr. Afshin Ziaei, Dr. Mircea Dragoman, Dr. Johan Liu, Dr. Yifeng Fu, Dr. Lilei Ye, Dr. Martino Aldrigo, and Dr. Stephane Xavier.

An incredible experience was a three-months research visit to the Institut Neel of CNRS in Grenoble, France through the funding of ICN2 Severo-Ochoa Outbound Mobility Programme and the P2N group. I am immensely thankful for being able to work with Prof. Olivier Bourgeois for three-months. Although the time was a bit short, I learned a lot and gained valuable knowledge on the Seebeck coefficient measurement at low temperatures. I have been impressed by his dedication in research, and his way of thinking has significantly influenced me. I hope that we will continue to work together in the future. I would like to specifically thank Dr. Sunanda Mitra, Dr. Jessy Paterson, Boris Brisuda, Pierre Gsaner, Jajar Ajiyel, Roderic Cravero, Judith Stein, Jean-Francois Motter, Gwenaelle Julie, Nolwenn Chessel, Dr. Jean-Luc Garden, Gael Moriroux, Charlotte Latargez, and Baptiste Pelerin, for their help at Institut Neel. Furthermore, Grenoble is a beautiful place surrounded by majestic mountains, I would like to thank my friends Yanfei Zhang, Dr. Chao Hou, Tingting Zhang, Minhan Li, Chao Zhang, and WuWen Yao, with whom went hiking in Grenoble every weekend.

None of the works I present in this thesis would have been possible without the generous support from many funding organisations. I would like to gratefully acknowledge the Marie-Sklodowska-Curie Cofund BIST Predoctoral fellowship (754558); the EU Project Nanosmart (H2020 ICT-07-2018); and the Spanish Mineco project SIP (PGC2018-1017430B-I00). I am also grateful for the previously mentioned MIT-Spain “La Caixa” Programme and the ICN2 Severo-Ochoa Outbound Mobility Programme that funded me to travel to MIT and Institut Neel (CNRS), respectively. I

would also like to give thanks for the support provided under the new H2020 project NFFA EUROPE Pilot, which is the first project I applied for and was awarded outside of the ICN2.

In addition, I am very grateful to the long-term encouragement and help from my former supervisors and friends: Prof. Dr. Shaoqing Xiao, Prof. Dr. Soonmin Seo, and Prof. Dr. Ju-Hyung Kim, Yange Luan, and Zhangfu Chen.

Last but not least, I would like to thank Tiantian and my parents for their love and support. I love them dearly and words can't express how deeply grateful I am to my family for everything they have done for me.

# List of Abbreviations

TMDs: Transition metal dichalcogenides  
2D: Two-dimensional  
vdWs: Van der Waals  
FET: Field-effect transistor  
MoS<sub>2</sub>: Molybdenum disulphide  
WS<sub>2</sub>: Tungsten disulphide  
PtSe<sub>2</sub>: Platinum diselenide  
ZnO: Zinc oxide  
MBE: Molecular beam epitaxy  
CVD: Chemical vapor deposition  
k<sub>r</sub>: In-plane/radial direction thermal conductivity  
k<sub>z</sub>: Cross-plan thermal conductivity  
R<sub>int</sub>: Interface thermal resistance  
MFP: Mean free path  
Λ<sub>z</sub>: Phonon mean free path in the cross-plane direction  
1LRT: One-laser Raman thermometry  
2LRT: Two-laser Raman thermometry  
FDTR: Frequency domain thermoreflectance  
TEM: Transmission electron microscopy  
SThM: Scanning thermal microscopy  
AFM: Atomic force microscopy  
FIB: Focused ion beam  
EBL: E-beam lithography  
ICP: Ion-coupled plasma  
LBM: Layer breathing modes  
BTE: Boltzmann transport equation  
DFT: Density functional theory  
RHEED: Reflection high energy electron diffraction

# Table of Contents

Abstract .....	IV
Preface .....	VI
Acknowledgements .....	VII
List of Abbreviations .....	XI
Table of Contents .....	XII
1. Motivation and Introduction .....	1
2. Experimental Methods.....	7
2.1 Preparation of layered materials .....	7
2.1.1 Synthesis of Graphene, MoS <sub>2</sub> , and WS <sub>2</sub> monolayer and few-layers by chemical vapour deposition (CVD) .....	8
2.1.2 Mechanical exfoliation of layered materials and the dry-transfer technique .....	11
2.1.3 Solution-exfoliation of MoS <sub>2</sub> and WS <sub>2</sub> nanosheets .....	13
2.2 Nanopatterning of free-standing holey membranes .....	14
2.2.1 Holey membrane fabricated by Focused ion beam (FIB).....	14
2.2.2 Holey membrane fabricated by E-beam lithography and plasma etching system .....	15
2.3 Raman Thermometry .....	18
2.3.1 One-laser Raman Thermometry (1LRT) .....	19
2.3.2 Two-laser Raman Thermometry (2LRT) .....	20
2.4 Frequency-domain thermorelectance (FDTR).....	22
3. Anisotropic thermal conductivity of layered SnSe <sub>2</sub> .....	24
3.1 Introduction .....	24
3.2 In-plane and cross-plane thermal conductivity of layered SnSe <sub>2</sub> .....	25
3.4 Conclusion .....	27
Article 1 .....	29
Article 1 Supporting information .....	38
4. Thermal transport in layered PtSe <sub>2</sub> .....	58
4.1 Introduction .....	58
4.2 Material growth, structural characterization, and phonon dynamics.....	59
4.3 Thermal conductivity and interfacial heat transport measurements .....	60
4.4 Conclusion .....	62
Article 2 .....	64

Article 2 Supporting Information .....	74
5. Manipulating thermal conductivity of layered MoS <sub>2</sub> .....	90
5.1 Introduction .....	90
5.2 Improving thermal conductivity of layered MoS <sub>2</sub> by annealing .....	92
5.3 Heat routing in nanopatterned MoS <sub>2</sub> .....	96
5.4 Conclusion .....	97
Article 3 .....	99
Article 3 Supporting Information .....	117
6. MoS <sub>2</sub> - and WS <sub>2</sub> -nanosheets based humidity sensors .....	130
6.1 Introduction .....	130
6.2 Fast-response humidity sensors based on TMDs-nanosheets and metal ion composites.....	132
6.3 Reversing the humidity response of MoS <sub>2</sub> - and WS <sub>2</sub> -based sensors with metal coatings.....	138
6.4 Conclusion .....	142
Article 4 .....	144
Article 4 Supporting information .....	154
7. Conclusions and perspectives.....	167
Bibliography .....	171
List of Publications .....	184

# 1. Motivation and Introduction

All organisms adapt to their living environment, especially to the ambient temperature, as almost all living things can feel temperature changes. After humans learned to think, they studied how to keep warm and found they could judge the ambient temperature of things through changes in shape, the colour of and the distance from fire, and that thermal insulation materials could maintain temperature. Temperature has been crucial for the development of humankind and has been systematically studied since temperature scales first appeared in the Renaissance. For examples, Carlo Rinaldini (1615-1698) defined twelve steps between the melting point of ice and the boiling point of water.<sup>1</sup> During the first Industrial Revolution, Benjamin Franklin (1706-1790) and Jean Ingen-Housz (1730-1799) were the first to study thermal transport properties. Ingen-Housz used hot oil as a stable heating source to heat up seven kinds of metal rods (gold, silver, copper, tin, steel, iron, and lead) with the same length and diameter, to observe the speed of propagation of the fusion of max along the metal rods. Afterwards, thermal research accelerated and made significant progress. Joseph Fourier (1768-1830) conducted experiments and devised the first mathematically method for estimating thermal conductivity of a material. James David Forbes (1809-1868) found that wrought iron has different thermal conductivities at different temperatures and Henri Hureau de Senarmont (1808-1862) observed the anisotropic thermal conductivities in various crystals.<sup>2</sup> At the same time, thermal knowledge of materials guided people to design and improve products, and a wide variety of materials were used in a variety of applications. For example, highly thermally conductive materials such as copper and aluminium were machined into a radiator for transferring heat flow. More recently, high-temperature-resistant materials with low thermal conductivities have been used for rockets and space shuttles to block heat flow, and low thermal conductivity materials with good electrical performance have been used in the thermoelectric devices to convert temperature gradients to electrical energy.

Over the past two hundred years, a better understanding of thermal properties and the rapid development of technologies has helped to improve society and living conditions, but these developments have also created many global problems. Advances in

industrial productivity has accelerated the consumption of fossil fuels (such as coal, crude oil, and natural gas) and generated tons of carbon dioxide. In 1824, Joseph Fourier proposed the greenhouse effect, i.e., the accumulation of CO<sub>2</sub> and other gases that absorb solar energy and warm up our planet. The newly generated carbon dioxide, one of the main greenhouse gases, has started to destroy the earth's heat balance and ecosystem and there is urgent need to control the greenhouse effect to stop the increase in global temperatures.<sup>3</sup> One solution is to cut down the use of fossil fuels and replace them with green energy such as electrical energy generated by solar cells, wind turbines, and water turbines. Additionally, temperature gradients formed between heat sources from mechanical movement, chemical reactions, and even solar irradiation have been utilized to generate electrical energy using thermoelectric devices. Since the 1960s, Moore's law based on silicon technology has powered the information technology revolution but 1960s this will be difficult to continue.<sup>4</sup> One of the main reasons is that electrons move increasingly faster through increasingly smaller silicon circuits, the chips overheat. The chip is the brain of modern technology. New good performance materials were desired to solve the heating problem to enrich the capacity and speed of chips.

In particular, layered materials, including graphene, transition metal dichalcogenides, and the post-transition metal dichalcogenides have been proposed as replacements for silicon for next-generation electronics. The main advantage of these materials is that the thickness of individual layers can be at the sub-nanometer level with a van der Waals gap between the layers without bonding. This means, that carrier mobility can be maintained at the sub-nanometer range to overcome the short-channel effect.<sup>5</sup> Many kinds of layered materials, especially molybdenum disulphide (MoS<sub>2</sub>), have been applied in electronic applications. However, the lack of thermal management of layered materials is slowing down their adoption in electronic applications. For instance, hotspots created by current flow in field-effect transistors (FETs) can damage the layered materials,<sup>6</sup> and the electron flow affected by temperature is also problematic. In order to address these challenges, better thermal management is required for various kinds of layered materials.

The intrinsic thermal conductivity of layered materials has been reported in various publications. Layered MoS<sub>2</sub> has shown a thickness-dependent in-plane ( $k_r$ ) thermal conductivity from  $34.5 \pm 4$  W/mK for a monolayer to 85 - 112 W/mK for bulk.<sup>7</sup>



Subsequently, the  $k_z$  of layered MoS<sub>2</sub> was studied by A. Sood et al, which increased from  $0.8 \pm 0.5$  W/mK at 20 nm to  $2 \pm 0.8$  W/mK at 100 nm.<sup>8</sup> The anisotropic ratio between the  $k_r$  and  $k_z$  of layered MoS<sub>2</sub> has been found to be about 50, which has been used to estimate the difference in thermal transport properties in different directions in layered MoS<sub>2</sub>. The large anisotropic thermal properties of the layered materials are due to their layer system structure, which makes phonon scattering difficult at the van der Waals gap without bonding. Work on MoS<sub>2</sub> has only started in the last ten years, but thermal properties of many other layered materials have not yet been studied yet. It will make sense to study the  $k_r$  and  $k_z$  of some other high-potential layered materials at the same time.

An emerging issue is that the reported  $k_r$  values have not always been consistent,<sup>7</sup> because there are many factors that can affect the thermal measurement results of layered materials. For example, when the layered materials were placed and measured on some substrates, the interface thermal conductivity was not considered or well estimated because of a lack of good measurement techniques or references. Moreover, the measured thermal values had a big error bar when measuring the free-standing membrane due to the small free-standing area. Additionally, assist polymer residues attached to the surface of layered materials have shown big effects on the thermal property measurement of ultrathin layered materials, especially monolayers, due to the fact that polymer was used to support and transfer the ultrathin layered materials because of their ultra-fragile nature. In addition, the layered materials cannot always be kept for a long period in an ambient environment, as humidity and oxygen can damage the surface of ultrathin layered materials very quickly. Herein, it has been considered important to systematically study the effect of humidity and oxygen on the layered materials. To do synthesis and measurement of materials in the same lab to avoid the affection of oxygen and humidity from the transportation also should be considered.

Layered materials have also been considered as potential materials for high-performance thermoelectric devices, because of their excellent electronic mobility, ultrathin nature, and high Seebeck efficiency, especially the layered SnSe that has a good Seebeck coefficient of  $\sim 500$   $\mu\text{V}/\text{K}$ .<sup>9</sup> But thermoelectric performance of layered materials were estimated small because of their relatively high thermal conductivity.<sup>10</sup> The main strategies for reducing the thermal conductivities of layered materials for

improving their thermoelectric performance was considered is to increase the boundary scattering of phonons by doping, amorphization, nanopatterning, etc.<sup>11,12</sup> But the methods for reducing the thermal conductivity of layered materials have been rarely reported in the literature.

In recent decades, based on Fourier's Law of thermal conduction, many technologies have been developed to study the thermal properties of materials. For instance, the steady-state methods including the absolute method,<sup>13</sup> the steady-state infrared method,<sup>14</sup> etc. were applied for thermal conductivity measurements of macro-size objects in a simple way.<sup>15</sup> These new technologies tend to be miniaturized and simplified for the thermal measurement of smaller and smaller materials which are placed in a small vacuum chamber and are good for the measurement of thermal properties at low temperature, whereas a high vacuum is good for improving thermal measurement accuracy by avoiding the effects of humidity, oxygen, etc. Therefore, some technologies such as 3- $\omega$  method,<sup>16,17</sup> laser thermometry,<sup>18-20</sup> time-domain thermoreflectance method,<sup>8,18</sup> frequency-domain thermoreflectance method,<sup>18,21</sup> micro-bridge method,<sup>22</sup> and Volklein method,<sup>23</sup> etc. have been developed for the thermal measurement of low-dimensional materials. 3- $\omega$  method and frequency domain thermoreflectance have a similar mechanism, both can heat up a sample surface periodically and measure the temperature oscillations for calculating the  $k_z$ . Laser thermometry and the micro-bridge method can make the temperature gradient on the sample suitable for direct thermal conductivity measurement. Time-domain thermoreflectance can measure the reflectivity of a reflected pulsed laser with respect to time, which can be matched to a model for calculating thermal properties. In the Volkein method, a film bolometer is first calibrated, and then another film is deposited on the bolometer for thermal properties measurement. The difference is that the 3- $\omega$ , micro-bridge, and Volkein methods need a current flow on an electrode to heat up the samples, and the fabrication process of an electrode deposited on the sample surface and the electrode itself always irreversible changes material properties.

In contrast, laser-based techniques including TDTR and FDTR, and laser thermometry, do not need to contact the materials during measurement. TDTR and FDTR are normally used to study the  $k_z$  of materials by applying a pulse laser. Laser infrared thermometry is the main type of laser thermometry and has been widely used in industrial and medical applications. In the past few decades, Doppler Broadening

Thermometry has been developed for measuring gas temperature,<sup>24</sup> but has not been used for other thermal property measurement.

The main laser thermometry used for thermal conductivity measurement is Raman thermometry which is based on the Raman effect. In 1928, C.V. Raman revealed the Raman effect, in which a different frequency light compared to the incident light (called as Raman shift) is generated when the electromagnetic waves of the incident light interact with molecules.<sup>25</sup> This happens because according to the laws of quantum theory, the molecules gain or lose amounts of energy during the collision between photons and molecules i.e., the collision is inelastic. Raman spectroscopy was quickly developed after the power laser replaced sunlight as the excitation light because the Raman effect is very weak at on part in a million of the incident light. Nowadays, Raman spectroscopy is widely used to identify molecules by providing their structural fingerprint. Since Raman spectroscopy is sensitive to the vibrational frequency of the chemical bonds, which depends on temperature, the temperature changes in materials can be expressed by the Raman shift. In general, infrared spectroscopy and Raman spectroscopy are complementary techniques but the selection rule is different. Herein, Raman spectroscopy has been used to measure the thermal conductivity of materials when its laser is also used for heating up the materials. These techniques are named one-laser Raman thermometry (1LRT) or two-laser Raman thermometry (2LRT) according to the number of lasers used. Raman thermometry has become widely used for the study of  $k_r$  of layered materials.<sup>18–20</sup>

Additionally, this thesis focuses on techniques and methods to improve the thermal management of layered materials. To make sure that the measurements were high-quality and fresh, most of the samples were synthesized and prepared in our lab. We studied study the thermal conductivity of the new layered materials, such as SnSe<sub>2</sub> and PtSe<sub>2</sub>, and also tried the nanopatterning and annealing method to actively control the thermal conductivity of layered MoS<sub>2</sub>.  $k_r$  of all samples was measured using the 1LRT or 2LRT.  $k_z$  of all samples was measured using the frequency domain thermoreflectance. We also studied the humidity effects on the properties of layered materials. The contents of the individual chapters are given below.

**Chapter 2** presents the main techniques used for sample preparations, including the Chemical Vapor Deposition (CVD) synthesis method for MoS<sub>2</sub> and WS<sub>2</sub> monolayer

and few-layers, and the mechanical exfoliation and the dry-transfer method for various layered MoS<sub>2</sub>, SnSe<sub>2</sub>, and WS<sub>2</sub>, and the solution-exfoliation method for MoS<sub>2</sub> and WS<sub>2</sub> nanosheets. In particular, two kinds of techniques used to fabricate the holey layered membrane are discussed together with Raman thermometry and Frequency-domain thermoreflectance techniques used for the thermal conductivity measurements.

**Chapter 3** describes a study of the  $k_r$  and  $k_z$  of the layered SnSe<sub>2</sub> using two-laser Raman thermometry and Frequency domain thermoreflectance, respectively. Also explored are the influence of film thickness on the thermal conductivity of SnSe<sub>2</sub> and the temperature-dependent  $k_r$  of SnSe<sub>2</sub>. In this study, the  $k_r$  and cross-plane phonon mean free path (MFP) distribution of SnSe<sub>2</sub> was extracted using the mean free path reconstruction method.

In **Chapter 4**, the phonon dynamics and thermal properties of crystalline and polycrystalline PtSe<sub>2</sub> thin films of varying thickness (1 to 40 layers) are explored. The low-frequency Raman spectra and pump-probe coherent phonon spectra of these samples are presented as part of a discussion on their layer-breathing modes, out-of-plane elastic constant, layer-dependent sound velocity, and acoustic phonon lifetimes. The  $k_z$  of the PtSe<sub>2</sub> films affected by the crystallinity and size is also explored, and the thermal results are verified using the first-principles Boltzmann transport equation.

**Chapter 5** contains a study of the thickness-dependent  $k_r$  of layered MoS<sub>2</sub> free-standing membrane before and after nanopatterning characterized using a two-laser Raman thermometry. Also presented is the temperature-dependent thermal conductivity of the nanopatterned MoS<sub>2</sub> membrane with results verified by the equilibrium molecular dynamics (EMD) simulation. In addition, a thermal insulator and heating guidance based on the nanopatterned MoS<sub>2</sub> is discussed.

In **Chapter 6**, study on the humidity sensing properties of solution exfoliated MoS<sub>2</sub> and WS<sub>2</sub> nanosheets is presented. In particular, we found that humidity sensing behaviour of MoS<sub>2</sub> and WS<sub>2</sub> nanosheets with the metal coating was reversed after a certain working time. The mechanism is explained through an electric model simulation.

## 2. Experimental Methods

### 2.1 Preparation of layered materials

The discovery of graphene has motivated the scientific community to extensively explore potential applications of this material due to its remarkable physical-chemical properties.<sup>26,27</sup> Graphene is commonly referred as a two-dimensional atom thick membrane with  $sp^2$  hybridized carbon atoms configured in a hexagonal or honeycomb-like structure.<sup>28</sup> The basic physical studies in the research community require the high quality of layered materials, especially the monolayer graphene, and layered TMDs materials.

Layered materials are mainly synthesized by two techniques: bottom-up growth and top-down exfoliation. Bottom-up growth means that the layered materials are formed by small molecules, atoms, and metal ions, which are decomposed from the related precursors under some extreme force such as high-temperature, electron field, magnetic field, and chemical forces. The bottom-up growth of layered materials can be realized by CVD, Metal-organic CVD, Physical vapour deposition (PVD), Molecular beam epitaxy (MBE), Sputtering, a simple oven for the sulfurization of metal layers, and even chemical reaction or decomposition in solution. Like most materials, the layered materials were first found in nature. Top-down exfoliation methods such as the mechanical exfoliation and solution-exfoliation, are applied to synthesize nano-size layered materials from the natural crystals. It is worth mentioning that the exfoliated graphene by Andre Geim and Kostya Novoselov opened the horizon of the two-dimensional world. For the wide range of applications of layered materials, nanosheets exfoliated from natural crystals in solution by sonication are an ideal material, because the fabrication method is simple, cheap, highly efficient, and environmentally friendly. In this thesis, we focus on three techniques: CVD, Mechanical-exfoliation, and solution-exfoliation because they are cost-effective, and the most common techniques applied in the research field of layered materials. Additionally, the three techniques have several advantages. The CVD system can deposit the materials on a substrate using chemical vapour by a chemical reaction occurring in a certain part of the CVD

system's furnace. This enables the synthesis of high-quality and large area-monolayer and few-layers TMDs which can be applied in the application of monolayer TMD-based applications. However, many factors such as pollutants from the reaction chamber and air, the unstable ratio of different precursors, temperature, pressure, humidity, temperature gradient of reaction chamber can affect the quality of the synthesized layered materials, by changing their lattice structures, creating dopants, defects, and pendulums. Herein, the CVD-synthesized layered materials show a bit lower performance in optical, thermal, and electric performance than the mechanical-exfoliated layered materials. Mechanical exfoliated layered materials were used in the intrinsic thermal conductivity value measurement, but efficiency of this method for getting monolayer materials is quite low. Large amounts of solution exfoliated MoS<sub>2</sub> and WS<sub>2</sub> nanosheets allowed us to study their humidity sensing performance. In order to study the thermal properties of the layered materials and their related devices. We have investigated the techniques to synthesize layered materials using CVD, mechanical exfoliation method, and solution-exfoliation method, the details of which are introduced as below.

### 2.1.1 Synthesis of Graphene, MoS<sub>2</sub>, and WS<sub>2</sub> monolayer and few-layers by chemical vapour deposition (CVD)

Temperature and pressure are the two key indicators for CVD systems. Some CVD systems can reach a high temperature for sublimating or evaporating precursors, while others can only work in ambient pressure and are classified as Atmospheric Pressure CVDs (APCVD). Other CVD systems can control pressure lower than ambient pressure for reaction and are classified as Low-pressure CVDs (LPCVD). The LPCVD can synthesize relatively cleaner layered materials, because the sublimation and melting points of precursors, and the pollutants in chamber decrease with the decrease in pressure. In some cases, multi-heating zones are required for the synthesis of some complex layered materials because of precursors with different melting points or special synthesis processes, so CVD systems can also be evaluated according to their heating zones. Here, we used a one-heating zone APCVD to synthesize, graphene, monolayer and few-layers MoS<sub>2</sub> and WS<sub>2</sub>.

A one-heating zone Atmospheric Pressure Chemical Vapour Deposition (APCVD) system was used to grow graphene. The first step was to wet cleanse the quartz tube and anneal it at the growth temperature (1000 °C) in ambient pressure, without any gases or closing the end of the tube. The quartz tube always cleaned after using it 5 times. The system's gas pipes were cleaned every time with a flow of Ar ~500sccm, H<sub>2</sub> ~200sccm, CH<sub>4</sub> ~50sccm for 5 minutes. A high quality of copper foil (99.999%) was used as the substrate for the growth of graphene, which was cleaned using a sonication bath in acetone, 2-propanol, and deionized water for 5 minutes successively. Then the copper foil was treated using the electro-polishing method. To do the electropolishing, the positive electrode was connected to the high-quality copper foil using an alligator clip, which was oxidized in a controlled way to flatten the surface. The new formed Cu<sup>+2</sup> ions were transferred into the solution which turned to a blue colour. The negative electrode was connected to a normal copper foil and the electrode surface was reduced and appeared the hydrogen bubbles. The reaction was maintained about 90 seconds as the voltage was increased to around 3 V with the current at 0.34 A. The polished copper foil was cleaned by deionized water again and dried with a nitrogen blow. The well-prepared foil was then placed on the quartz holder and moved into the tube centre of the furnace. Before the growth, the copper foil was annealed at 1000 °C with the gas flow of Ar ~500 sccm, and H<sub>2</sub> ~200 sccm for 1 hour. The growth started when the gas flow increased to Ar ~450 sccm, H<sub>2</sub> ~50 sccm, CH<sub>4</sub> ~1.5 sccm for 15 minutes, and the CH<sub>4</sub> gas flow was increased to 5 sccm for the last 5 minutes. Then graphene was full coverage on the surface of copper foil which surface touched the quartz holder. After that, the CH<sub>4</sub> gas flow was set to 0 sccm, the furnace was turned off and the tube was taken out for fast cooling. After removing from vacuum and taking out the graphene/copper foil, the sample was heated up to 150 °C on a hot plate with a clean glass slide to wait for the colour changes until the graphene covered area was bright, and the uncovered area was red.

The same APCVD system was used to synthesize MoS<sub>2</sub> and WS<sub>2</sub>. To avoid the pollution of other elements, each new quartz tube was only used for synthesizing the same material. MoS<sub>2</sub> and WS<sub>2</sub> have a similar synthesis process, except for the higher melting point of WS<sub>2</sub>. Herein, we just discuss the synthesis process of MoS<sub>2</sub>. Only monolayer and few-layers MoS<sub>2</sub> needed to be synthesized and deposited on the surface of the substrate, as only as extremely small amount of precursor MoO<sub>3</sub> about

0.1 mg was placed under the polished SiO<sub>2</sub> wafer. The SiO<sub>2</sub> (400nm)/Si was used as the substrate for the MoS<sub>2</sub>, which was cleaned in a sonication bath in acetone and 2-propanol for 5 minutes. Then the wafer was etched using SF<sub>6</sub>/O<sub>2</sub> (5 / 50 sccm) for 4 minutes with an etching rate of 25 nm/min. The SiO<sub>2</sub> layer thickness reduced to 300nm and showed a better contact between MoS<sub>2</sub> monolayer and the 300nm-SiO<sub>2</sub> substrate under an optical microscope. The other precursor sulphide used a large amount of ~1 g to participate in the chemical reaction and create a sulphide environment to protect the new formed MoS<sub>2</sub> molecules. Sulphide and molybdenum trioxide (MoO<sub>3</sub>) have different temperature evaporation points of ~145. 2 °C and ~700 °C, respectively. Therefore, the boat with MoO<sub>3</sub> was placed in the centre of the furnace, and the boat with sulphide was placed at the boundary of the heating zone in the growth process. Excessive sulphide may affect the morphology of the monolayers but has no other side effects. In our study, the sulphide was cleaned at the end of the reaction in the high temperature environment because of its low vaporizing point. In the pre-growth process, the boat-shape holder with MoO<sub>3</sub> covered by a SiO<sub>2</sub>/Si wafer substrate was placed in the centre of the heating zone, see Figure 1 (a). The SiO<sub>2</sub> wafer was placed face down on the boat. The other boat with full sulphide was placed at the boundary of the heating zone near to the source of the Argon carrier gas, where the temperature was not too high for the sulphide to keep a slow evaporation speed in the reaction. After placing the samples in the equipment, the quartz tube was moved about 5 cm to the left to move the sulphide out of the tube, see Figure 1 (a). 200 sccm Argon gas was flowed in the tube for about 30 minutes to remove oxygen content. The growth process was started by increasing the temperature in steps to 800 °C in 40 minutes, as shown in Figure 1 (c). The tube was moved to the right position at 700 °C to start the evaporation of sulphide, see Figure 1 (b). After the temperature reached to 800 °C it was increased to 820 °C for 10 minutes. After that, the system was cooled rapidly by opening the furnace and flowing the fast argon gas at a speed of 200 sccm. After taking out the sample, upon visual inspection, we could recognize the blue layer MoS<sub>2</sub> covered on the substrate. Figure 1 (d), (e), and (f) show the optical images of MoS<sub>2</sub> monolayer, few-layers, and thin film respectively. Characterization of thin film was performed by Raman spectroscopy.



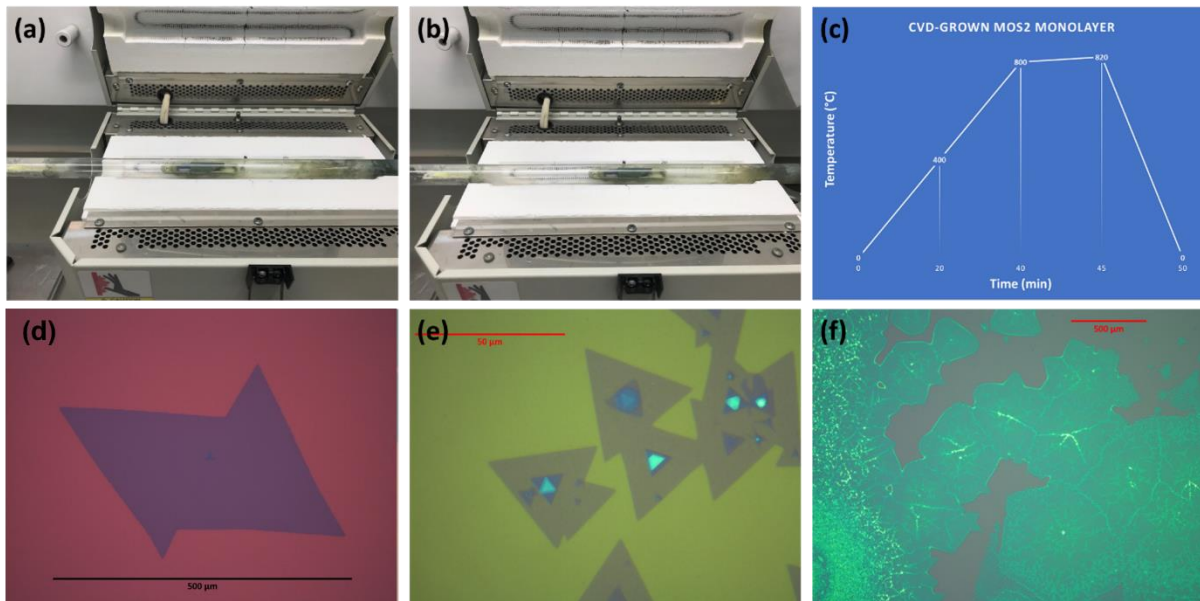


Fig. 1. Synthesis MoS<sub>2</sub> monolayer and few-layers using a one-heating zone LPCVD system. Optical images of the CVD system with the sample placed in the chamber with sulphide out of the heating zone (a) and the sample placed in the chamber with sulphide in the heating area (b). (c) the curve of the temperature distribution for the growth of MoS<sub>2</sub>. (d), (e), and (f) show the MoS<sub>2</sub> monolayer, few-layers with different stacking, and MoS<sub>2</sub> thin film, respectively.

## 2.1.2 Mechanical exfoliation of layered materials and the dry-transfer technique

Mechanical exfoliation was originally created for the exfoliation of graphene, then extended to the exfoliation of other layered materials. The early method was used scotch tapes to exfoliate layered materials from their nature crystals. But the adhesive polymer from the scotch tape could bring residue and pollute substrates. As a result, new mechanical exfoliation and dry-transfer technique have been developed to exfoliate layered materials using polydimethylsiloxane (PDMS) owing to its natural transparent and flexible properties. The exfoliated layered materials of MoS<sub>2</sub>, WS<sub>2</sub>, and SnSe<sub>2</sub> fabricated in this thesis were exfoliated using PDMS. The flexibility of PDMS can be controlled by controlling the ratio between its base and curing agent when synthesizing. The synthesis ratios for PDMS applied in this our study is ~ 10 to 1. In this process, PDMS attach onto the natural crystal and can be peeled off directly. Thin flakes can be found on the PDMS under optical microscope.

The selected flakes can be transferred onto other substrates by pressing the PMDS to contact the flakes and substrates directly. For making free-standing layered materials, we developed a simple and cheap dry-transfer stage which the most expensive part is the 20X objective lens, as shown in figure 2. By connecting the camera to a laptop, we could view the sample and substrate clearly and then handle the transfer process. To increase the success rate for making free-standing membranes, gold and titanium were deposited on holey substrates for enhancing the adhesion between the layered materials and substrates. A uniform flake without wrinkles is also good for this process.

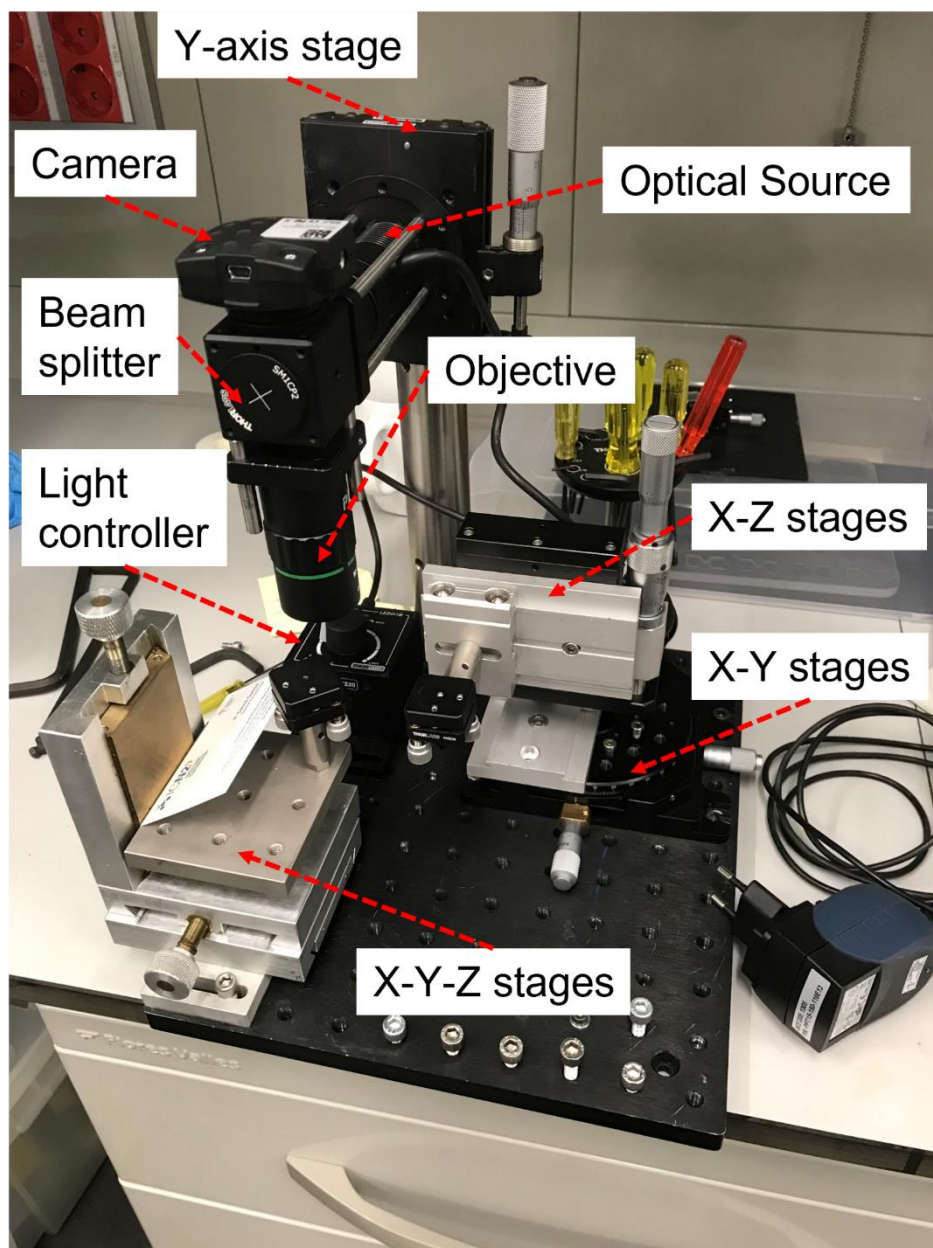


Fig. 2. An optical image of the dry-transfer setup.

### 2.1.3 Solution-exfoliation of MoS<sub>2</sub> and WS<sub>2</sub> nanosheets

MoS<sub>2</sub> and WS<sub>2</sub> nanosheets were sonicated and exfoliated in ethanol solution using a high-power sonicator probe system (400 W, Fisher brand FB505). Figure 3(a) shows a schematic diagram of the experimental steps for exfoliation and extraction of MoS<sub>2</sub> nanosheets in an alcohol solution. MoS<sub>2</sub> (WS<sub>2</sub>) microcrystals (500 mg) (99.5%, Sigma-Aldrich) were dissolved in 250 mL of 50% ethanol solution and then sonicated by the sonication probe with 80% amplitude and an 8 s/8 s ON/OFF pulse for 10 h. The upper solution without precipitate was centrifuged at a rotation speed of 7000 rpm for 10 min. The suspension consisting of MoS<sub>2</sub> (WS<sub>2</sub>) nanosheets was used for the subsequent experiments.

MoS<sub>2</sub> nanosheets in size ranges <200 nm, 200-450 nm, 450-800 nm, and >800 nm was separated and extracted using a vacuum filtration system and a centrifuge for the following experiments, as shown in figure 3(b). We also modified the MoS<sub>2</sub> and WS<sub>2</sub> Nanosheets by applying a coating of metal and metal salt layers. For example, Cu nanoparticles were coated on the surface of MoS<sub>2</sub> nanosheets using a CuCl<sub>2</sub> solution. Various volumes of 0.1 g/mL CuCl<sub>2</sub> (99.8%, Labbox) salt solution was mixed with 15 mL of MoS<sub>2</sub> nanosheet solutions in a dark environment for 24 h to synthesize the MoS<sub>2</sub>@Cu nanosheets. Then, the Cu-coated MoS<sub>2</sub> nanosheets were dropped into the solution and formed a precipitate at the bottom of the mixture. Finally, the precipitate consisting of Cu-coated MoS<sub>2</sub> nanosheets and was collected by the removal of the upper transparent solution. WS<sub>2</sub>@ Cu, MoS<sub>2</sub>@Ag, and WS<sub>2</sub>@Ag nanosheets were prepared by the same procedure using the same CuCl<sub>2</sub> and AgNO<sub>3</sub> (99.8%, Labbox), respectively. Figure 3(c) shows the optical image of MoS<sub>2</sub> nanosheets coated by AgNO<sub>3</sub> and formed precipitate at the bottom of the vial. Figure 3(d) show the optical images of the high-power sonicator and the vacuum filtration system used.

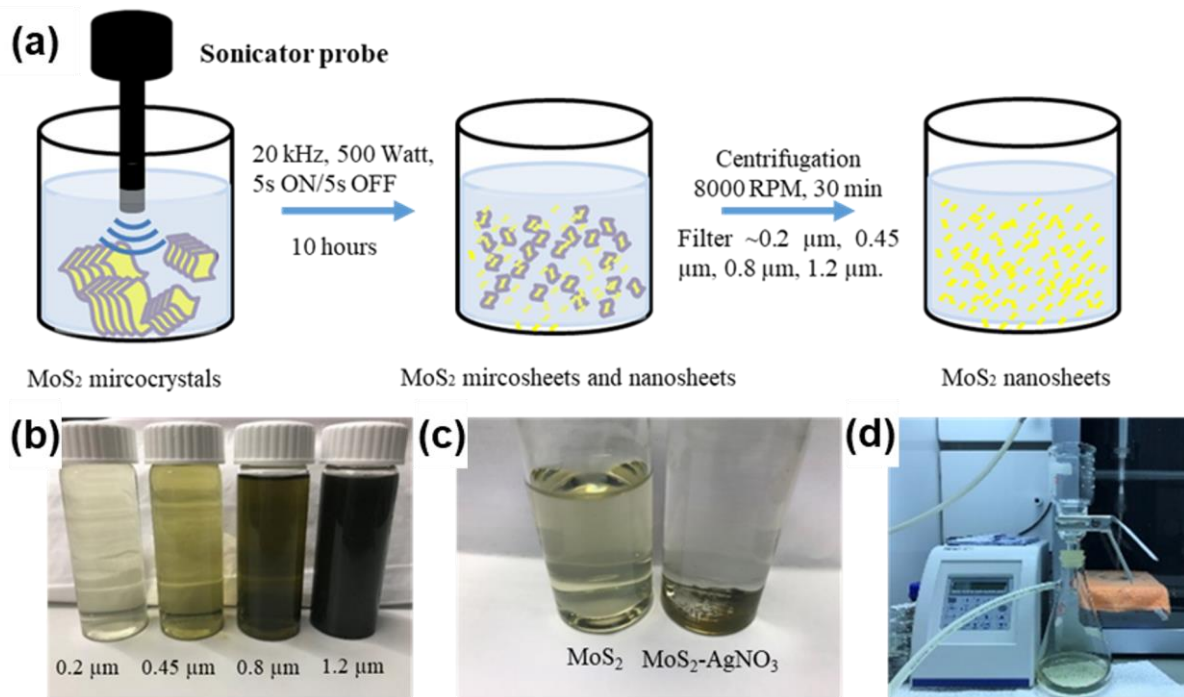


Fig 3. (a) Schematic diagram of synthesis and extraction of MoS<sub>2</sub> nanosheets. (B) MoS<sub>2</sub> nanosheets solution filtered using different pore size filter membranes (200 nm, 450 nm, 800 nm, 1200 nm). (c) the MoS<sub>2</sub>@Ag nanosheets precipitate synthesized after mixing MoS<sub>2</sub> nanosheets solution and AgNO<sub>3</sub> solution. (D) Optical images of a high-power sonicator system and a vacuum filtration system.

## 2.2 Nanopatterning of free-standing holey membranes

In order to manage the thermal conductivity of layered materials, an effective method is to make hole arrays on the materials by decreasing the phonon MFP. In this study, hole arrays were made on the CVD grown MoS<sub>2</sub> monolayer and few-layers, polycrystalline MoS<sub>2</sub> membrane, and mechanical exfoliated MoS<sub>2</sub> few-layers to study the effects of hole arrays on their thermal conductivity. The details for hole array fabrication were presented below.

### 2.2.1 Holey membrane fabricated by Focused ion beam (FIB)

A Gallium Focused Ion Beam (GA-FIB) (Zeiss 1560XB Cross Beam, Germany) was used to etch holes as phononic crystals on the MoS<sub>2</sub> membrane, with the parameter of holes etched being 2 pA, 30 kV, and 10 milliseconds. For the thermal conductivity measurement using optical thermometry, holes were fabricated on the free-standing membranes using FIB except for the center area, which was using as a heating island with a diameter of ~5 μm. The details of the Ga-FIB fabrication process effects on the free-standing MoS<sub>2</sub> membranes are presented in Chapter 5.

### 2.2.2 Holey membrane fabricated by E-beam lithography and plasma etching system

Because Ga-FIB can implant gallium elements into the targets and change their electronic and thermal properties, we created nanopatterns on the layered materials by combining Electron-beam lithography and the plasma etching system.

The schematic of fabrication process and the related fabrication parameters of phononic crystal on a polycrystalline MoS<sub>2</sub> membrane are shown in Figure. 4 and Table 1, respectively. Large-area MoS<sub>2</sub> polycrystalline membrane on glass substrates was transferred directly onto the surface of deionized water by slowly putting the materials into water. Because the MoS<sub>2</sub> is hydrophobic and was separated with the substrate, it floated on the surface once it touched water. The floating MoS<sub>2</sub> membrane was then lifted up using a free-standing SiN<sub>x</sub> holey membrane for a suspended MoS<sub>2</sub> membrane. The sample was then heated up to 70 °C for 10 minutes to remove the water between the MoS<sub>2</sub> and the free standing SiN<sub>x</sub> substrate. For the next plasma etching process, a nano-scale mask was synthesized on the MoS<sub>2</sub> membrane by a standard Electron-beam lithography (EBL) procedure using CASR 6200 E-beam resist. At first, 200nm the thick CSAR resist was spin-coated on the surface of the MoS<sub>2</sub> membrane using a spin coater at 4000 rpm for 1 minutes. The sample was then baked at 150 °C for 1 minute to cure the E-beam resist. The EBL system was used to expose the resist by following a designed pattern using an electron beam (area: 50 μm/cm<sup>2</sup>, dots: 0.2 pC). After the development process of the CSAR E-beam resist, an ion-coupled plasma system (PlasmaPro 100 Cobra, Oxford) producing C<sub>4</sub>F<sub>8</sub>/Ar plasma was applied to etch MoS<sub>2</sub> membranes for a designed holey array. The nanopatterned

MoS<sub>2</sub> membranes was shown in Figure 5. However, the remaining issue was that the remaining e-beam resist could not be removed using a standard remover or acetone. Furthermore, use of oxygen plasma to remove the e-beam resist can easily damage the MoS<sub>2</sub> layer. Consequently, we chose to use the Ga-FIB for nanopatterning of layered materials. This technology based on the E-beam lithography and plasma-etching was continued to be applied for nanopatterning other materials, such as silicon and silicon nitride.

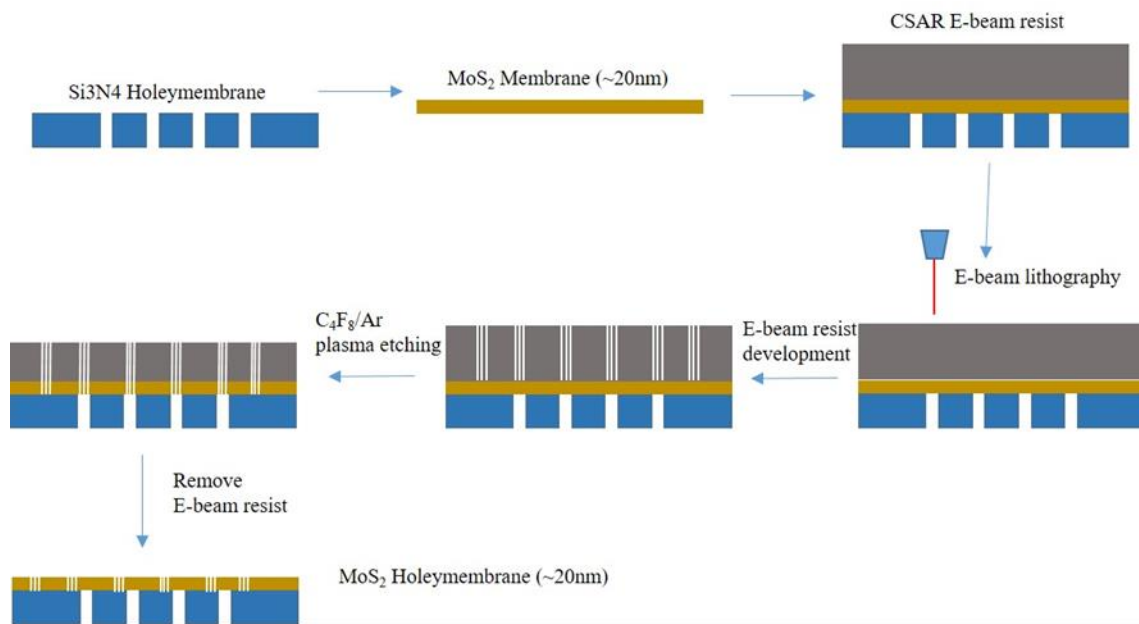


Fig. 4. Schematic of the fabrication process of MoS<sub>2</sub> phononic crystal.

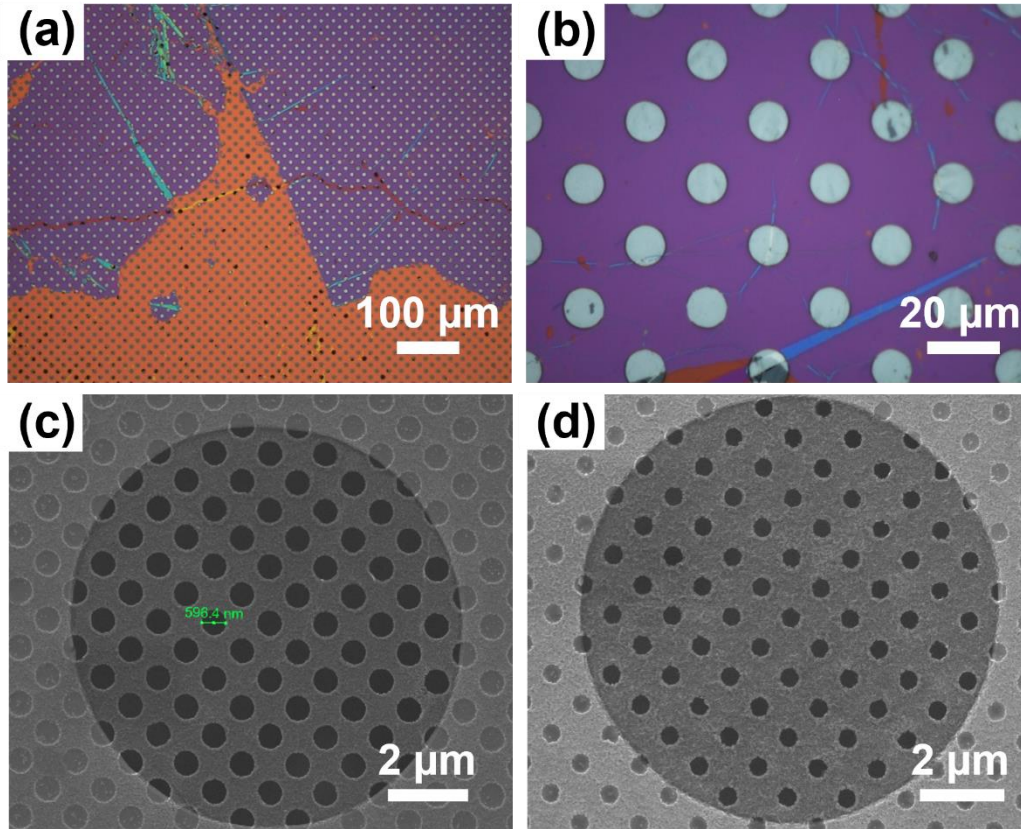


Fig. 5. (a-b) shows optical images of suspended MoS<sub>2</sub> polycrystalline on SiN<sub>x</sub> substrate. (c-d) shows the SEM images of nanopatterned suspended MoS<sub>2</sub> polycrystalline membranes.

	Period(nm)	Dose factor	Pore design size (nm)	Pore Real size (nm)
Pattern 1	2000	0.7-1.2	300	371-644
Pattern 2	1430	0.7-1.2	400	427-650
Spin coating speed: 4000rpm, 1 min. E-Beam lithography: 30kV, Spot 2, WF 200μm, Aperture 7, 100μC/cm <sup>2</sup> . Development: AR 600-546, 1 min. RIE etching: C <sub>4</sub> F <sub>8</sub> / Ar 10/40 sccm, HF/ICP 20/200W, 10pa, 1min. Removal: Acetone 1 night or AR 600-71 1 night in room environment.				

Table 1. Parameters for fabrication of MoS<sub>2</sub> phononic crystals.

## 2.3 Raman Thermometry

Light has always been explained as a classical electromagnetic wave or a stream of photons to introduce the Raman effect. Light scattering includes elastic scattering and also inelastic scattering, which happens when electromagnetic waves interact with obstacles. Elastic scattering is called Rayleigh or Mie Tyndall scattering and is the same frequency as incident light. Inelastic scattering is known as Raman or Brillouin scattering and has a different frequency compared to incident light. According to the laws of quantum theory, molecules will gain or lose energy during the collision between photons and molecules i.e. the collision is inelastic. The changed energy represents a change in the vibrational and/or rotational energy of the molecule. For the Raman effect, the photons transfer their energy to the matter in order to displace the electrons and produce an induced dipole moment. Due to the fact that a large mass of matter does not allow the transition of energy, most of the incident light (photons) is transmitted without change of frequency, and the scattering light is elastic scattering. But some new frequency lights have been generated in terms of energy transfer between the incident light and the scattering lights. The scattered photons which gain and lose energy are called anti-Stokes and Stokes scattering. The inelastic scattered wave with a frequency lower than the incident beam is referred to as a 'Stokes' scattering wave while that at a higher frequency is called as an 'anti-Stokes' scattering wave.

Raman spectroscopy is also applied to measure the local temperature of materials, and consequently, its thermal properties because the Raman peak linewidths and shifts have demonstrated to be a function of temperature.<sup>29,30</sup> The ratio of the intensities of Stokes and anti-Stokes is related to the phonon population, which also varies with temperature. Changes of temperature, volumetric expansion or contraction of the crystal lattice will cause changes in the anharmonicity of the bonds for the displacement of atoms from their equilibrium positions. This change in the interatomic force is reflected in the position and linewidth of Raman peaks. Hence, Raman scattering could work as a temperature probe where the probe laser power is kept low to obtain sufficient Raman signal without heating the sample.<sup>20</sup> Raman thermometry includes a source of a high intensity monochromatic light (532 nm laser), a double



monochromator (532 nm laser filter) to reject the excitation light, and a charge coupled device (CCD) detector.

In this work, Raman scattering intensity was evaluated by the frequency shift (also called as Raman shift) between the scattered light and the incident light with wavenumber used as the typical unit of the Raman shift. Because a Raman spectrum plotted on a wavelength scale is very narrow and hard to read, a wavenumber scale for Raman spectra was used for easy comparison of linearly with energy. The Raman Shift of Raman Scattering was calculated by the formula,

$$\Delta(cm^{-1}) = 10^{-7} \left( \frac{1}{\lambda_{excitation}} - \frac{1}{\lambda_{Raman}} \right).$$

In previous studies, for MoS<sub>2</sub>, the Raman shift was about 380 cm<sup>-1</sup> for E<sub>12g</sub> mode, and 406 cm<sup>-1</sup> for A<sub>1g</sub> mode. The position difference between the two Raman peaks decreased from ~ 25 to ~19 cm<sup>-1</sup> when the number of MoS<sub>2</sub> layers decreased from bulk to monolayer. The Raman shift of MoS<sub>2</sub> shifted with changes in its temperature, resulting in the possibility to measure its thermal conductivity using Raman spectroscopy. The technique also called Raman thermometry, include One-laser Raman Thermometry (1LRT) and Two-laser Raman Thermometry (2LRT). The main advantage over electrical techniques is that no contact and the pre-processing stage of samples is not required.<sup>31</sup>

### 2.3.1 One-laser Raman Thermometry (1LRT)

Raman spectra of materials depend on their temperature for the changing of the lattice constant. After determining the relationship between Raman spectra and temperature of materials by measuring the Raman spectra at different temperatures (this process is called as temperature coefficient process), the Raman can be applied as a thermal couple to read the temperature of materials. According to Fourier's law:  $q = -\kappa \cdot \Delta T$ , the thermal conductivity calculation is based on local heat flux density and temperature gradient. Thanks to the development of laser technology, the laser energy is high enough to heat up the materials, which allows us making a hot spot on the surface of

materials. Hence, the thermal conductivity of layered materials can be studied using 1LRT. The thermal conductivity of an isotropic material is given by<sup>18</sup>

$$k(T) = -\frac{P_{abs}}{4\sqrt{\pi}\Delta T\sigma}$$

where  $P_{abs}$  is the power absorbed by the materials,  $\Delta T$  is the temperature difference between the hotspot made by the laser and the semi-infinite point (normally is the ambient temperature), and  $\sigma$  is the laser spot size. The  $P_{abs}$  value was calculated by the difference between the measured incident power and lost laser power, and the power lost by the laser reflectance on materials. The transmitted power was also considered as a part of the lost power when a material is transparent. Temperature at the hot spot under laser can be calculated using the temperature coefficient. Spot size of laser also can be measured by a digital camera or a motorized nano-precision X-Y axis stage. This method is accurate to extract the thermal conductivity of suspended thin membranes. However, the formular is not suitable for thick suspended samples or supported samples, whose thermal conductivity was extracted using the finite elements method of COMSOL Multiphysics.

### 2.3.2 Two-laser Raman Thermometry (2LRT)

In this thesis, 2LRT has been used the key technique to measure the  $k_r$  of suspended layered materials in this thesis because 2LRT can extract the temperature distribution by a mapping or line scanning measurement on the suspended materials. The 1LRT was used but mainly for a one-point measurement for keeping the accurate of this measurement. The temperature distribution on the material during the 1LRT measurement is unknown, the temperature distribution on the material by doing the 2LRT measurement can be seen directly. Accordingly, that 1LRT and 2LRT can be seen as one-dimensional and two-dimensional temperature distribution measurement techniques, respectively.

The  $A_{1g}$  peak position of  $\text{MoS}_2$  Raman spectrum was used to probe the temperature of  $\text{MoS}_2$  membrane in this work, because its peak intensity was much stronger than the  $E_{2g}^1$  peak. The heating laser and the free-standing membrane were fixed on a

motorized stage (Marzhauser), then their relative position and the focus of the violet laser remained unchanged during the measurement to ensure a stable and uncontacted heating source. The probe laser was coupled to the Raman spectrometer (T64000) and scanned the sample collecting a Raman spectrum at various points. The probe laser spot size was 1.2  $\mu\text{m}$ .

All the samples were measured in a temperature-controlled, vacuum chamber at a pressure of  $\sim 3 \times 10^{-3}$  mTorr (Linkam). The gold layer also acted as a heat sink to ensure that the MoS<sub>2</sub> temperature in the supported area is the same as that of the environment. For calculating the thermal conductivity, a temperature distribution around the heating source on the free-standing membrane was required. Line scanning measurement is a simple way for getting a temperature distribution was normally carried out on the membrane using 2LRT. A probe laser (532 nm, Cobolt) and a heating laser (405 nm, Cobolt) were focused on the center of a free-standing membrane from the topside and bottom-side, respectively. The basic idea of this method is to measure the Raman shift along a line on the membrane using a low power probing laser will not heat up the sample and cause a shift of the Raman peaks. At the same time, the centre point of the suspended membrane was heated up using a high power, steady-state pump laser as shown schematically in Figure. 6.<sup>19</sup> Laser power absorbed by the membranes was measured *in-situ* using the configuration described elsewhere<sup>32,33</sup>.

When the heating laser of the contactless 2-laser Raman thermometry heats the centre of the membrane, the Raman spectrum at each point along a line through the centre point is recorded by the probe laser. After converting the Raman peak position into temperature, the diffusive heat flow and the zero-temperature gradient of the membrane can be understood by plotting out its radial heat by Fourier's law:  $P_0/(2\pi r t) = -k(T)dT/dr$ , where  $t$  is the membrane thickness,  $r$  is the relative position with respect the heating laser spot on the membrane. Then the thermal conductivity is stated as a function of temperature and determined by the expression:

$$k(T) = -\frac{P_{abs}}{2\pi t \xi(r)}$$

where  $P_{\text{abs}}$  is the absorbed power, and  $\xi(r) = dT/d(\ln r)$ . Therefore, the temperature of the devices was indicated by the shift of Raman peaks. More measurement details are discussed in Chapters 3 and 5.

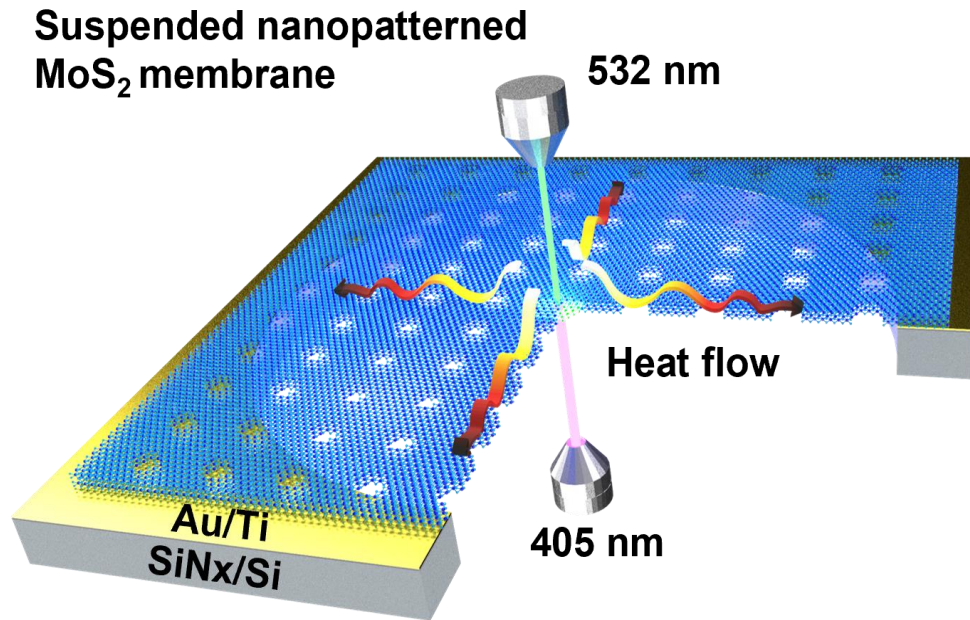


Fig. 6. Schematics of in-plane thermal conductivity measurement of a suspended  $\text{MoS}_2$  membrane using the two-laser Raman thermometry.

## 2.4 Frequency-domain thermoreflectance (FDTR)

As previously mentioned, layered materials show large anisotropic thermal conductivities. Here the  $k_r$  was studied using 1LRT and 2LRT while the  $k_z$  was measured using a FDTR setup, as shown in Figure 7.

The FDTR has two laser sources: a 532 nm green laser and a 488 nm pump laser.<sup>18</sup> The green laser was used as a probe laser and in order to get a high thermoreflectance signal from the gold transducer film, a 100nm untransparent gold film was deposited on the surface of the layered materials as the transducer film. The pump laser was modulated with a frequency from 10 kHz to 20 MHz for heating up the transducer. Both lasers were focused on the same point on the samples and reflected back through an objective and received by a detector. To avoid damaging the detector, the reflected pump laser was filtered using a 488nm Notch filter.

The phase and amplitude information from the thermoreflectance response signals measured by a lock-in amplifier, can be used in the thermal model to derive the thermal properties of samples. Because the phase change is more sensitive to the thermoreflectance than the amplitude response, in this study, the here phase signal was applied to analyse the thermal properties. However, as the phase signal was affected by the laser path lengths, and errors caused by laser modulation, detectors, cables, and instruments. A zero-thermoreflectance mirror was used as a sample for calibrating the system to correct these errors and obtain the correct phase signal.

The  $k_z$  was derived by analysing the phase signal using a model based on laser spot size, dimensions of the sample, and dimensions and thermal properties of the gold transducer film. Additionally, to ensure accurate measurement, the pump laser was controlled to avoid overheating of the surface, which can change the material thermal conductivity and thermoreflectance efficiency. More details about this measurement are discussed in the Chapters 3 and 4.

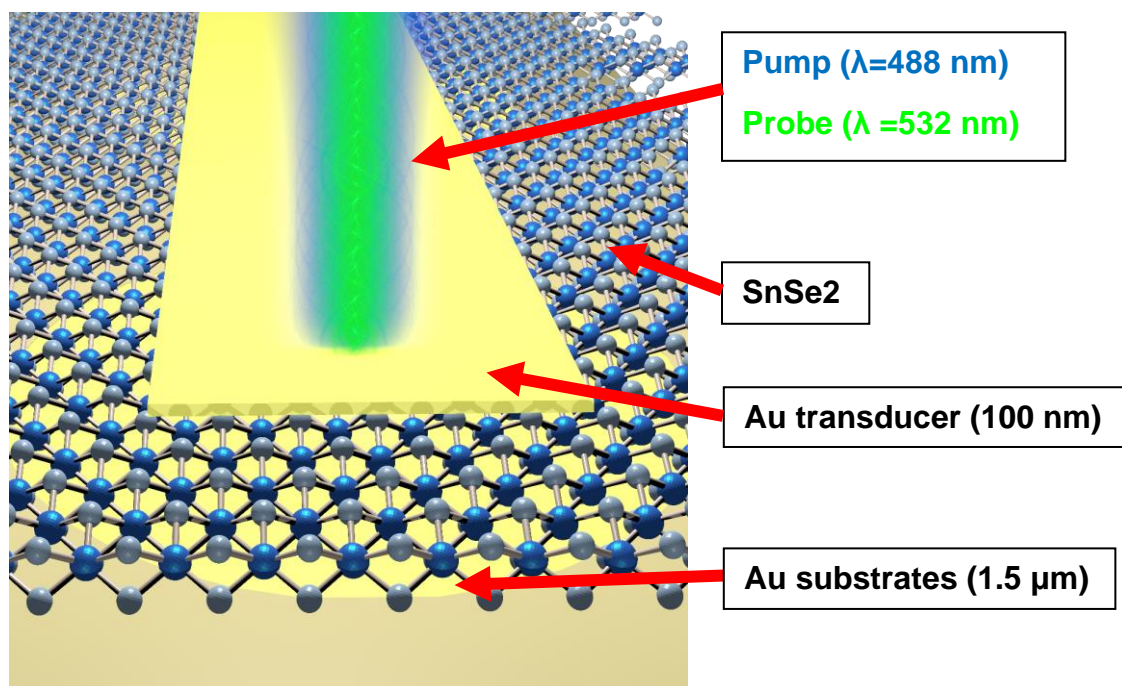


Fig. 7. Schematics of cross-plane thermal conductivity measurement of a suspended SnSe<sub>2</sub> membrane using the Frequency-domain thermoreflectance.

# 3. Anisotropic thermal conductivity of layered SnSe<sub>2</sub>

## 3.1 Introduction

Understanding cross-plane and in-plane heat propagation in thin films is critical for the thermal management of future 2D nanoelectronics devices. SnSe<sub>2</sub> is a promising two-dimensional material with desirable properties such as high electron mobility of 8.6 cm<sup>2</sup>V<sup>-1</sup>s<sup>-1</sup> at room temperature and low lattice thermal conductivity, according to recent first principle calculations.<sup>34–37</sup> It has already showed excellent performance in field-effect transistors (FETs),<sup>38–40</sup> phase-change memory<sup>41</sup> and optoelectronic devices,<sup>42</sup> and recently has been suggested as an ideal layered material for thermoelectric applications.<sup>34,35,43</sup> In particular, the latest calculations have shown that at high temperatures the thermoelectric figure of merit in a and c directions can reach values of 2.95 and 0.68, respectively.<sup>43</sup>

Despite extensive electrical and optical characterization of SnSe<sub>2</sub>,<sup>44–48</sup> experimental studies on the intrinsic thermal properties of SnSe<sub>2</sub> thin films are limited.<sup>49,50</sup> Until now, its thickness-dependence  $k_r$  has been investigated only in a few CVD samples of short thickness range using the traditional opto-thermal Raman technique.<sup>49</sup> Moreover, there are no reports on  $k_z$  measurements in SnSe<sub>2</sub>, thus its anisotropic thermal properties have not been experimentally investigated so far.

In this work, we have investigated the  $k_r$  and  $k_z$  of high crystalline quality exfoliated SnSe<sub>2</sub> films with thickness between 16 and 190 nm using 2LRT and FDTR. We focus on unravelling the influence of thickness on the  $k_r$  and  $k_z$  of SnSe<sub>2</sub> films and extract the anisotropic ratio of the thermal conductivity. In addition, using the mean free path reconstruction method<sup>51–53</sup>, we found that the phonons with mean free path larger than 45 nm and 61 nm in the c and a directions, respectively, contribute above 50% of the total bulk thermal conductivity.

## 3.2 In-plane and cross-plane thermal conductivity of layered SnSe<sub>2</sub>

The SnSe<sub>2</sub> films were mechanically exfoliated from single crystals (purchased from HQ Graphene) and dry-transferred onto gold-coated silicon nitride substrates with 20 and 30  $\mu\text{m}$  diameter holes. The crystal and morphological characterization of the samples was studied by high-resolution scanning transmission electron microscopy (TEM), atomic force microscopy (AFM), and Raman spectroscopy measurements. We extracted the  $k_r$  lattice constants  $a = b = 0.387$  nm from the simulations. The chemical structure of SnSe<sub>2</sub> was confirmed by Raman spectroscopy, which exhibits two Raman active vibrational modes at  $113\text{ cm}^{-1}$  ( $E_g$ ) and  $180\text{ cm}^{-1}$  ( $A_{1g}$ ).

The  $k_r$  of suspended SnSe<sub>2</sub> films at room temperature was measured by using our steady state 2LRT technique. In this approach, a hot spot is produced by a heating laser with wavelength  $\lambda_1 = 405$  nm fixed in the centre of a suspended film, while a second laser with  $\lambda_2 = 532$  nm measures the temperature distribution based on a calibration of its Raman spectra with temperature. We point out that for the  $k_r$  measurements it is important to ensure that the phonons with large MFP are not affected by the lateral dimensions. In our experiments, the lateral size effect should not have affected the measured thermal conductivity considering that SnSe<sub>2</sub> has MFP distribution (1–1000 nm) much smaller than the size of the suspended films and the heat sink was located 10 or 15  $\mu\text{m}$  away from the heating area. Then, to improve the efficiency of the heat sink at the boundaries, we deposited 100 nm Au layer on the SiN<sub>4</sub> substrates and later the films were deposited. All the measurements were conducted in vacuum at  $10^{-3}$  mbar to avoid heat conduction through the air.

To measure  $k_z$  of the SnSe<sub>2</sub> films, we performed pump- and probe experiments using the FDTR technique. The experimental setup is based on two lasers operating at 488 nm (pump) and 532 nm (probe). Prior to the FDTR measurements 100 nm and 1.5  $\mu\text{m}$  thick Au layers were deposited on the top and bottom of the suspended films, respectively. The top Au layers were used as transducers, while the thick bottom Au layers become the substrates. Therefore, our multilayer system consists of Au/SnSe<sub>2</sub>/Au stacks. First, we extracted  $k_z$  by fitting the experimental data in a low frequency range (20 kHz to 1 MHz), where the phase signal sensitivity to  $R_1$ ,  $R_2$ , and heat capacity of the films was negligible. Then, we fixed  $k_z$  and fit the experimental

data in a high frequency range (1–40 MHz) to estimate simultaneously  $R_1$  and  $R_2$ . For the first estimate to determine the value of the free parameters ( $k_z$ ,  $R_1$ , and  $R_2$ ), we used previous reported values of similar materials.

In this thesis, we presented the measured  $k_r$  and  $k_z$  values for all the  $\text{SnSe}_2$  films with thicknesses between 16 and 190 nm, and both  $k_r$  and  $k_z$  monotonically increased with increasing thickness and reach the calculated bulk  $k_r$  and  $k_z$  values. We noted that the linear  $k_z$  increase with increasing thickness might indicate quasi-ballistic phonon propagation. The origin of the  $k_r$  and  $k_z$  decreased with decreasing film thickness can be understood considering phonon diffuse (incoherent) boundary scattering at the surface of the films as the main scattering mechanism. In particular, at room temperature the only characteristic dimension that dominates phonon scattering is the thickness of the  $\text{SnSe}_2$  films. Thus,  $t$  is the dimension that sets a cut off to the phonon-MFP due to diffuse boundary scattering, i.e., phonons with  $\text{MFP} > t$  will not fully propagate, thus reducing their contribution to  $k_r$  and  $k_z$ . Moreover, the similar rate of increase of  $k_r$  and  $k_z$  with increasing film thickness observed in this thesis suggests that phonons with MFP commensurate with the sample thickness contribute to the thermal conductivity. To gain a further insight on how phonons contribute to the thermal conductivity, we use the MFP reconstruction model to extract the cross-plane and in-plane phonon MFP distribution. It is seen that the MFP distribution shifts to longer values for in-plane transport compared to the cross-plane. In particular, we found that phonons with MFP ranging from 1 to 53 nm and from 1 to 30 nm contribute to 50% of the  $k_r$  and  $k_z$ , respectively. From the experimental  $k_r$  and  $k_z$  values, we directly obtained the anisotropy ratio  $k_r / k_z$  for each film thickness. The average value of  $k_r / k_z$  was  $8.4 \pm 1$ .

The observed variation of  $R_{\text{int}}$  can be attributed to the sample processing (exfoliation and transfer conditions, storage before gold evaporation, etc.), which could result in different interfacial energy coupling. However, we cannot exclude the possibility that the increase in  $R_{\text{int}}$  was due to reduced mechanical coupling of the films to the underlying Au resulting from a potential increase in sample stiffness or changes in the vibrational spectra as the thickness is increasing.

To examine the dependence of  $k_r$  of suspended  $\text{SnSe}_2$  films on temperature, we conducted single-laser Raman thermometry measurements at different ambient conditions. The  $k_r$  of the  $\text{SnSe}_2$  films was extracted by measuring the absorbed power and the temperature rise of the films at the laser spot at different ambient temperatures



(298, 373, and 473 K) and solving the 2D heat equation. We observe a systematic decrease of the  $k_r$  with increasing temperature for all the SnSe<sub>2</sub> films and a maximum reduction of ~56% at 473 K for the thickest SnSe<sub>2</sub> film compared with the room temperature value. We observed that the dependence of  $k_r$  with temperature becomes weaker for thinner samples. In other words, as the temperature increases,  $k_r$  became less sensitive to the sample thickness since these phonons responsible for most of the heat transport had an MFP shorter than the film thickness. The weaker temperature dependence in thinner films seems to be reasonable given that phonon boundary scattering becomes dominant.

More details are discussed in the following paper Article 1.

### 3.4 Conclusion

In conclusion, we studied the thickness dependence of  $k_r$  and  $k_z$  of crystalline SnSe<sub>2</sub> films. Both show strong thickness dependence in the 16-190 nm range, with values reduced by a factor of 2.5 compared with bulk values. From this result, the thermal conductivity anisotropy ratio was directly obtained. This anisotropy ratio was about 8.4, independent of the film thickness. Importantly, we have shown that at high temperatures, the  $k_r$  of the suspended SnSe<sub>2</sub> membrane can drop by more than 50% relative to room temperature. The strong dependence of thermal conductivity on temperature gradually diminishes as the thickness decreases due to the dominant role of phonon boundary scattering. Finally, using the MFP reconstruction method, we have shown that the major heat transfer phonons that contribute to  $k_r$  with a mean free path of tens of nanometres at room temperature.

Our results provide valuable information for understanding the heat transport of layered materials and for realizing functional devices that require highly anisotropic properties, i.e., thermoelectric, transistors, optical sensors, or high temperature operation. Highly anisotropic 2D layered materials such as SnSe<sub>2</sub> can provide insulation primarily through in-plane thickness and heat flux propagation. This can be beneficial in heat-sensitive electronic components such as microchips that require directed heat flow to avoid hotspots, and in cooling circuits.<sup>54,55</sup> Finally, changes and quantitative knowledge of functional thermal phonon MFPs that manipulate heat

transfer by either dimensional limits or temperature provide important insights into the design of 2D thermoelectric devices with improved thermal management.

# Article 1

# Anisotropic Thermal Conductivity of Crystalline Layered SnSe<sub>2</sub>

Peng Xiao,<sup>†</sup> Emigdio Chavez-Angel,<sup>†</sup> Stefanos Chaitoglou, Marianna Sledzinska, Athanasios Dimoulas, Clivia M. Sotomayor Torres, and Alexandros El Sachat\*<sup>‡</sup>



Cite This: *Nano Lett.* 2021, 21, 9172–9179



Read Online

ACCESS |



Metrics & More



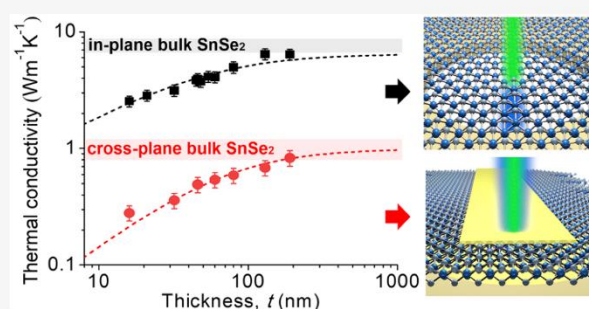
Article Recommendations



Supporting Information

**ABSTRACT:** The degree of thermal anisotropy affects critically key device-relevant properties of layered two-dimensional materials. Here, we systematically study the in-plane and cross-plane thermal conductivity of crystalline SnSe<sub>2</sub> films of varying thickness (16–190 nm) and uncover a thickness-independent thermal conductivity anisotropy ratio of about ~8.4. Experimental data obtained using Raman thermometry and frequency domain thermoreflectance showed that the in-plane and cross-plane thermal conductivities monotonically decrease by a factor of 2.5 with decreasing film thickness compared to the bulk values. Moreover, we find that the temperature-dependence of the in-plane component gradually decreases as the film becomes thinner, and in the range from 300 to 473 K it drops by more than a factor of 2. Using the mean free path reconstruction method, we found that phonons with MFP ranging from ~1 to 53 and from 1 to 30 nm contribute to 50% of the total in-plane and cross-plane thermal conductivity, respectively.

**KEYWORDS:** Phonon transport, mean free path, SnSe<sub>2</sub>, thermal conductivity anisotropy, frequency-domain thermoreflectance, Raman thermometry



Understanding the propagation of heat in two-dimensional (2D) materials is of paramount importance to establish its potential in, for example, energy harvesting in thermal management in future nanoelectronic devices. SnSe<sub>2</sub> is a promising 2D material with desirable properties such as relatively high electron mobility of ~85 cm<sup>2</sup> V<sup>-1</sup> s<sup>-1</sup> at room temperature,<sup>1</sup> high bulk electron affinity of 5.2 eV,<sup>2</sup> and low thermal conductivity according to recent first principle calculations.<sup>3–6</sup> It has already shown excellent performance in field-effect transistors (FETs),<sup>7–9</sup> phase-change memory,<sup>10</sup> and optoelectronic devices,<sup>11</sup> and recently it has been suggested that it is an ideal layered material for thermoelectric applications.<sup>3,5,12</sup> In particular, recent calculations have shown that at 800 K the thermoelectric figure of merit in *a* and *c* directions can reach values as high as 2.95 and 0.68, respectively.<sup>12</sup>

While extensive electrical and optical characterization of SnSe<sub>2</sub> is available,<sup>13–17</sup> experimental studies on the intrinsic thermal properties of SnSe<sub>2</sub> are few and far between.<sup>18,19</sup> To date, the thickness-dependence of the in-plane thermal conductivity (*k<sub>p</sub>*) has been investigated only in a few samples grown by chemical vapor deposition in a narrow range of thickness using the traditional optothermal Raman technique.<sup>18</sup> Moreover, there are no reports on measurements of the cross-plane thermal conductivity (*k<sub>c</sub>*) in SnSe<sub>2</sub>; thus its anisotropic thermal properties have so far not been experimentally investigated.

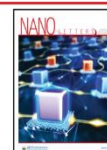
In this work, we study the in-plane and cross-plane thermal conductivity of crystalline SnSe<sub>2</sub> films with thickness between 16 and 190 nm using two different thermal characterization techniques, namely, Raman thermometry and frequency domain thermoreflectance (FDTR). We focus on unraveling the influence of film thickness on *k<sub>p</sub>* and *k<sub>c</sub>* in suspended and supported SnSe<sub>2</sub>, respectively, from which we obtain the thermal conductivity anisotropy ratio. In addition, we study the effect of film thickness on the temperature-dependent *k<sub>p</sub>* of suspended SnSe<sub>2</sub> films. Finally, using the mean free path reconstruction method,<sup>20–22</sup> we extract the in-plane and cross-plane phonon mean free path (MFP) distribution, showing that the main contribution to the thermal transport is made by phonons with MFPs of tens to hundreds of nanometers.

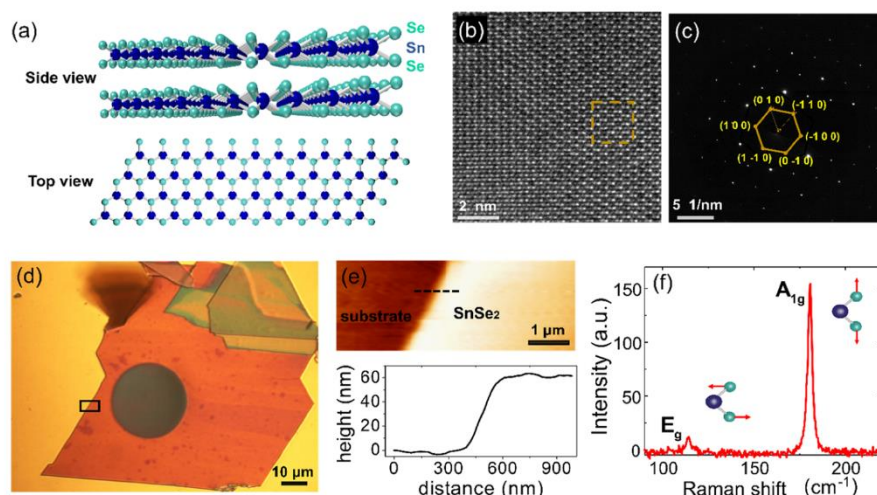
The SnSe<sub>2</sub> films were mechanically exfoliated from single crystals (purchased from HQ Graphene) by the assistance of a viscoelastic stamp (GelPak)<sup>23</sup> onto gold-coated silicon nitride substrates with 20 and 30 μm holes. Schematics of the SnSe<sub>2</sub> crystal structure are shown in Figure 1a. The crystal and

Received: August 5, 2021

Revised: October 12, 2021

Published: October 28, 2021





**Figure 1.** (a) Side and top views of the SnSe<sub>2</sub> crystal structure. Each SnSe<sub>2</sub> layer consists of three atomic sublayers, in which Sn atoms (blue spheres) are sandwiched between Se atoms (green spheres). (b) HR-STEM image of a 30 nm thick exfoliated suspended SnSe<sub>2</sub> film and (c) Fourier transform of the squared region depicted in (b), from which we extract the *a* and *b* lattice constants, *a* = *b* = 0.387 nm. (d) Representative optical image of a 60 nm thick SnSe<sub>2</sub> film. The diameter of the suspended circular area is 30 μm. (e) AFM image of the region outlined by the rectangle box in (d) and the corresponding measured height profile along the dashed black line in the topography image. (f) Raman spectrum of a 60 nm thick SnSe<sub>2</sub> film using an excitation wavelength of 532 nm and a 50× objective. In the inset to (f), red arrows indicate the direction of the movement of Sn and Se atoms.

morphological characterization of the samples was studied by high-resolution scanning transmission electron microscopy (HR-STEM), atomic force microscopy (AFM), and Raman spectroscopy measurements. Figure 1b and Figure 1c display the planar HR-STEM and the corresponding electron diffraction image, respectively, of a 30 nm thick SnSe<sub>2</sub> suspended film. The high-magnification HR-STEM image (Figure 1b) depicts a honeycomb arrangement of atoms, indicating the single-crystalline structure. The simulated FFT pattern (yellow spots in the inset of Figure 1c) displays hexagonal symmetrical patterns, indicating the hexagonal lattice structure of the SnSe<sub>2</sub>. From the simulations, we extracted the in-plane lattice constants *a* = *b* = 0.387 nm, in very good agreement with the literature.<sup>24,25</sup> Figure 1d displays a representative optical image of a 60 nm thick suspended exfoliated SnSe<sub>2</sub> film. The AFM topography image of the interface between the substrate and the exfoliated film together with the corresponding height profile is shown in Figure 1e. All the thicknesses of the SnSe<sub>2</sub> films were measured in tapping mode by AFM (see Supporting Information). The chemical structure of SnSe<sub>2</sub> was confirmed by Raman spectroscopy as shown in Figure 1f. The crystalline SnSe<sub>2</sub> exhibits two Raman active vibrational modes at 113 cm<sup>-1</sup> (E<sub>g</sub>) and 180 cm<sup>-1</sup> (A<sub>1g</sub>), in agreement with previous reports.<sup>19,26</sup>

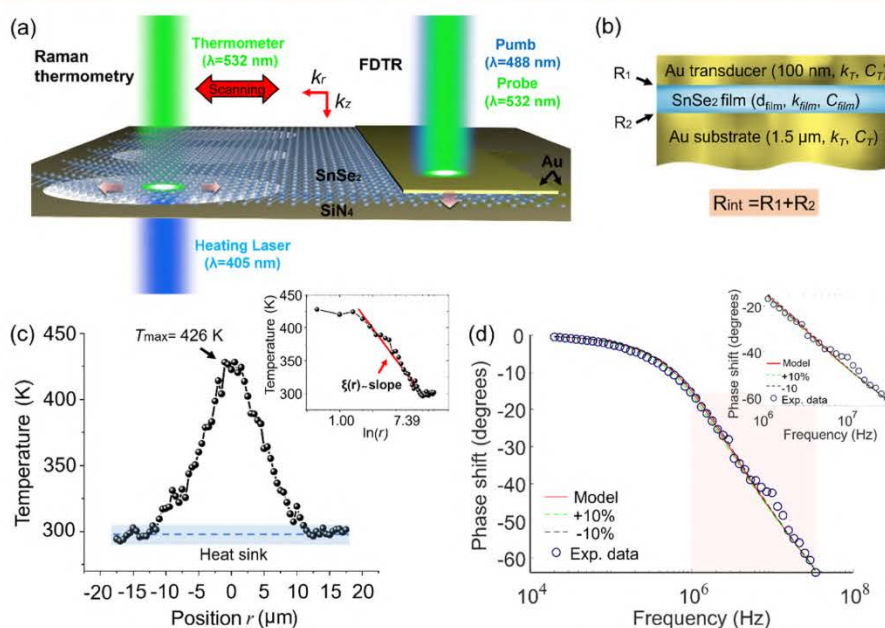
The *k<sub>r</sub>* of suspended SnSe<sub>2</sub> films at room temperature was measured by using our steady-state two-laser Raman thermometry technique.<sup>27–29</sup> In this approach, a hot spot is produced by a heating laser with wavelength λ<sub>1</sub> = 405 nm fixed in the center of a suspended film, while a second laser with λ<sub>2</sub> = 532 nm measures the temperature distribution based on a calibration of its Raman spectra with temperature (see Figure 2a). In these measurements, we monitored the temperature through the frequency of the longitudinal (LO) optical phonons of SnSe<sub>2</sub> at ~180 cm<sup>-1</sup>. Both lasers were focused using a 50× NA = 0.55 objective. The main advantage of this approach, with respect to the conventional optothermal Raman technique, is that no assumption has to be made to obtain the

thermal conductivity since it yields directly maps of the thermal field, both connected through the Fourier's law,  $Q/A = -k_r T$ , where *Q* is the heat flux, *A* is the area of the heat flux, and *T* is the temperature.

We point out that for the in-plane thermal conductivity measurements it is important to ensure that the phonons with large MFP are not affected by the lateral dimensions. For the case of graphene, the in-plane MFP distribution is very broad (200 nm to 10 μm)<sup>30</sup> and the impact of the lateral dimensions on the in-plane thermal conductivity has been detected experimentally.<sup>31</sup> However, in our experiments the lateral size effect should not affect the measured thermal conductivity considering that SnSe<sub>2</sub> has MFP distribution (1–1000 nm)<sup>6,12</sup> much smaller than the size of the suspended films and the heat sink is located 10 or 15 μm away from the heating area. In the two-dimensional case, where no temperature gradients are present in the third dimension and for temperature ranges that exhibit a purely diffusive heat transport regime, the radial symmetry of the temperature distribution upon a Gaussian thermal excitation allows reduction of Fourier's law to its one-dimensional form depending only on the radial coordinate *r* and the area  $A = 2\pi r t$ , where *t* is the thickness of the suspended film. Thus, the Fourier law gives a simple expression for the thermal conductivity as follows:

$$k_r(T) = \frac{-P_0}{2\pi t \xi(r)} \quad (1)$$

where *P*<sub>0</sub> is the absorbed power by the film and ξ(*r*) = *dT*/(*d ln r*). In the case of a temperature-independent thermal conductivity in the temperature range under study, the thermal field decays as  $T(r) \propto \ln r$  in the diffusive limit and *k<sub>r</sub>* is directly obtained from eq 1 after extracting ξ(*r*) from the slope of a linear fit to the logarithmic temperature profile and by measuring *P*<sub>0</sub> and *t*. We note that this procedure is valid for a data range starting at a distance of a few micrometers from the central point *r* = 0, where diffusive transport dominates.



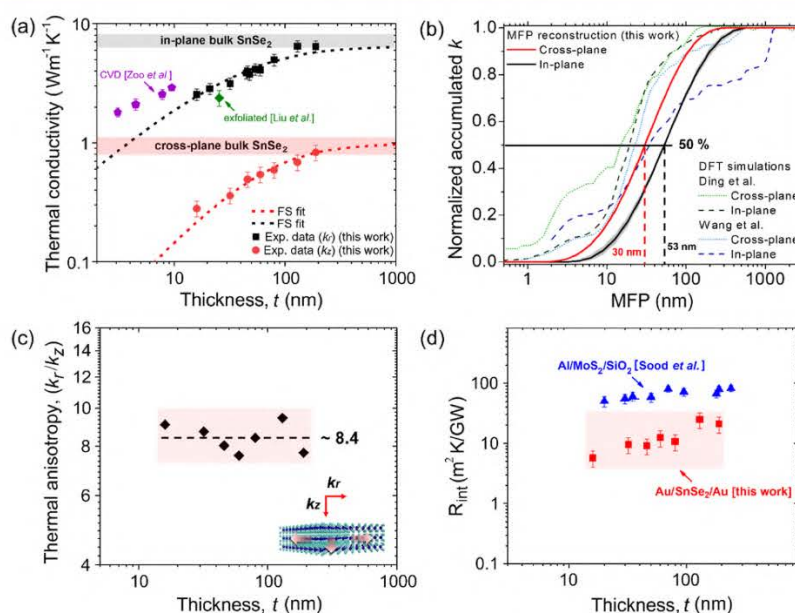
**Figure 2.** Schematics of (a) the two-laser Raman thermometry and FDTR experimental configurations and (b) the multilayer structure (Au/SnSe<sub>2</sub>/Au) with the two interface thermal resistances  $R_1$  and  $R_2$ . (c) Representative temperature profile of a 16 nm thick suspended SnSe<sub>2</sub> film with a maximum temperature rise at the heating spot at the center of the membrane of  $T_{\max} = 426$  K. The inset shows the linear fit of the temperature profile in logarithmic scale from which we extract the logarithmic derivative  $\xi(r) \sim dT/(d \ln r)$ . (d) Typical FDTR data measured in a 130 nm thick supported SnSe<sub>2</sub> film (blue circles) and the corresponding best model fit (red curve) in the whole frequency range. The light red area indicates the fitting frequency range used to extract  $R_1$  and  $R_2$ , and the inset to (d) shows the fitting of the experimental data in this range.

A representative temperature profile of the 16 nm thick suspended SnSe<sub>2</sub> film is shown in Figure 2c. The temperature accuracy was  $\pm 2$  K with a spatial resolution better than 600 nm (given by  $\lambda_2$ ). The inset to Figure 2c shows the linear fit of the measured temperature profile in logarithmic scale. For each sample we measured a line scan  $T(r)$  fulfilling the condition that the maximum temperature is that at the heating laser spot at  $r = 0$ . The range  $r$  was chosen to observe as full relaxation as possible of the temperature field to the heat sink temperature,  $T_{\text{sink}} = 300$  K. However, preliminary measurements indicated that this depends on the thermal conductivity of each sample. Then, to improve the efficiency of the heat sink at the boundaries, we deposited 100 nm Au layer on the SiN<sub>4</sub> substrates and later the films were deposited. The measured  $k_r$  values are plotted in Figure 3a. All the measurements were conducted in vacuum at  $10^{-3}$  mbar to avoid heat conduction through the air.<sup>29</sup> The experimental data of the thickness-dependent absorbance at room temperature are shown in Figure S12 in the Supporting Information.

To measure  $k_z$  of the SnSe<sub>2</sub> films, we performed pump-and-probe experiments using the FDTR technique.<sup>32,33</sup> The experimental setup is based on two lasers operating at 488 nm (pump) and 532 nm (probe). The modulated pump beam is focused on the SnSe<sub>2</sub> samples using a 50 $\times$  objective, creating a periodic heat flux with a Gaussian spatial distribution on the sample surface (see Figure 2a). The reflected low power probe beam is aligned with the pump beam and focused with the pump spot to monitor temperature variation through changes in optical reflectivity of the surface. We used a lock-in amplifier (Zurich Instruments HF2LI) to record the amplitude and phase response of the reflected probe beam to the thermal wave. The pump signal was used as reference while the phase

lag between the pump and probe beam as the observable quantity.

Prior to the FDTR measurements 100 nm and 1.5  $\mu\text{m}$  thick Au layers are deposited on the top and bottom of the suspended films, respectively. The top Au layers were used as transducers, while the thick bottom Au layers become the substrates. Therefore, our multilayer system consists of Au/SnSe<sub>2</sub>/Au stacks (see Figure 2b). For each SnSe<sub>2</sub> film we obtained frequency-domain measurements and extracted the  $k_z$  following a multilayer three-dimensional heat diffusion model.<sup>34</sup> This model requires material parameters such as the volumetric heat capacity ( $C$ ), thickness, interface thermal resistance, and  $k_z$ . The thermal conductivity and volumetric heat capacity of Au as well as the volumetric specific heat of SnSe<sub>2</sub> were taken from the literature.<sup>32,35</sup> The thickness of the Au transducer layer was measured by AFM (see Figure S14, e of the Supporting Information). Thus, the remaining parameters are the  $k_z$  of SnSe<sub>2</sub>, the thermal resistance of the top layer Au/SnSe<sub>2</sub> interface ( $R_1$ ), and the thermal resistance of the SnSe<sub>2</sub>/Au (substrate) interface ( $R_2$ ). To quantify the sensitivity of the measured phase signal to different parameters in the case of Au/SnSe<sub>2</sub>/Au stacks, a sensitivity analysis is carried out in a similar manner to that of Schmidt et al.<sup>34</sup> In Figure S2 of the Supporting Information we show the calculated phase sensitivity ( $-V_{\text{in}}/V_{\text{out}}$ ) to multiple parameters ( $k_z$ ,  $C$ , anisotropy,  $R_1$ , and  $R_2$ ) as a function of thickness and modulation frequency. From this analysis we found that the sensitivity of the recorded phase signal strongly depends on the modulation frequency; thus it is possible to extract different thermal properties directly from the model fit of the experimental data in a specific frequency range. In Figure S3 we also show the phase sensitivity as a function of the modulation frequency for the case of a 16 nm thick SnSe<sub>2</sub> film.



**Figure 3.** (a) In-plane (black squares) and cross-plane (red circles) thermal conductivities of exfoliated SnSe<sub>2</sub> films with thickness between 16 and 190 nm measured with 2LRT and FDTR. The in-plane<sup>32,33</sup> and cross-plane<sup>19,34</sup> Fuchs–Sondheimer (FS) fits to the experimental data are indicated with black and red dashed lines, respectively. The light gray and red areas display the calculated in-plane and cross-plane bulk thermal conductivities taken from the literature.<sup>6,12</sup> The errors in  $k_x$  were estimated by the standard deviation of several measurements, including the numerical errors from the fits. The errors in  $k_z$  were obtained from the error propagation of each parameter of eq 1. (b) Normalized accumulated thermal conductivity as a function of the phonon MFP (red and black solid curves). In dashed curves we plot the phonon MFP distribution in bulk SnSe<sub>2</sub> calculated by Wang et al.<sup>6</sup> and Ding et al.<sup>12</sup> (c) Thermal conductivity anisotropy ( $k_x/k_z$ ) as a function of SnSe<sub>2</sub> film thickness. (d) Total interface thermal resistance,  $R_{\text{int}} = R_1 + R_2$  (red squares), plotted versus film thickness extracted from the FDTR measurements. Previous total interface thermal resistance calculations on Al/MoS<sub>2</sub>/SiO<sub>2</sub> (blue triangles) where similar interfacial contributions from bottom (2D material/substrate) and top (metal/2D material) interfaces were taken into account.

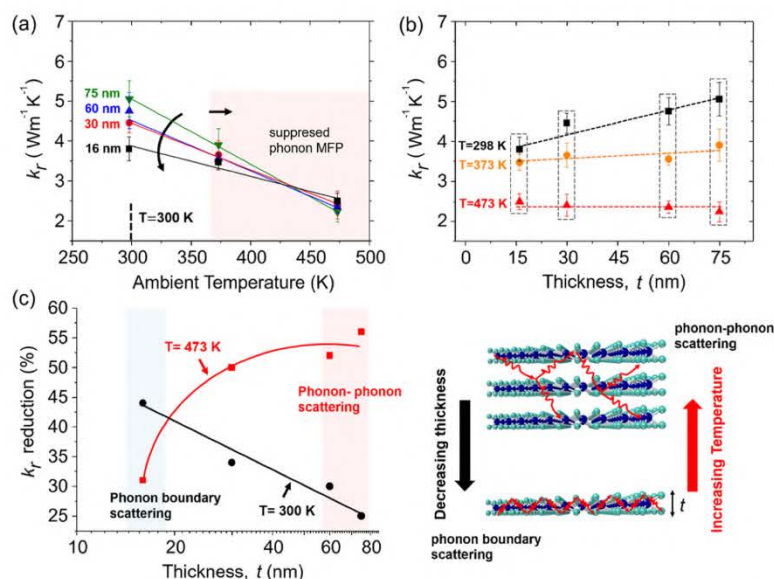
In particular, to extract the  $k_z$  of each film from a single FDTR measurement, we followed a fitting approach similar to that used in previous works<sup>34,36</sup> and supported by our sensitivity analysis. First, we extract  $k_z$  by fitting the experimental data in a low frequency range (20 kHz to 1 MHz), where the phase signal sensitivity to  $R_1$ ,  $R_2$ , and heat capacity of the films is negligible. Then, we fix  $k_z$  and fit the experimental data in a high frequency range (1–40 MHz) to estimate simultaneously  $R_1$  and  $R_2$ . For the first estimate to determine the value of the free parameters ( $k_x$ ,  $R_1$ , and  $R_2$ ), we used previous reported values of similar materials.<sup>37–39</sup> A typical example of the recorded phase signal and corresponding best model fit for a 130 nm thick SnSe<sub>2</sub> film is shown in Figure 2d. The inset in Figure 2d shows the fitting of our experimental data in the high frequency range.

Figure 3a displays the measured  $k_x$  and  $k_z$  values for all the SnSe<sub>2</sub> films with thicknesses between 16 and 190 nm. We observe that both  $k_x$  and  $k_z$  monotonically increase with increasing thickness and reach the calculated bulk in-plane and cross-plane thermal conductivity values, respectively.<sup>6,12</sup> In particular, the  $k_x$  values range from  $6.45 \pm 0.71 \text{ W m}^{-1} \text{ K}^{-1}$  for the thickest film ( $t = 190 \text{ nm}$ ) down to  $2.54 \pm 0.31 \text{ W m}^{-1} \text{ K}^{-1}$  for the thinnest film ( $t = 16 \text{ nm}$ ), which corresponds to about a 2.5-fold reduction. A similar decrease was observed in the  $k_z$ , with the values dropping from  $0.83 \pm 0.12 \text{ W m}^{-1} \text{ K}^{-1}$  in the thickest SnSe<sub>2</sub> film down to  $0.28 \pm 0.05$  in the thinnest film. We note that the linear  $k_z$  increase with increasing thickness might indicate quasi-ballistic phonon propagation, similar to previous experiments in MoS<sub>2</sub>,<sup>40</sup> however, more calculations are necessary to conclude. In the same graph we plot

previously reported in-plane thermal conductivity data in CVD and exfoliated SnSe<sub>2</sub> by Zou et al.<sup>18</sup> and Liu et al.,<sup>19</sup> respectively, which are in good agreement with our measurements.

The origin of the  $k_x$  and  $k_z$  decreasing with decreasing film thickness can be understood considering phonon diffuse (incoherent) boundary scattering at the surface of the films as the main scattering mechanism. In particular, at room temperature the only characteristic dimension that dominates phonon scattering is the thickness of the SnSe<sub>2</sub> films. Thus,  $t$  is the dimension that sets a cutoff to the phonon-MFP due to diffuse boundary scattering, i.e., phonons with  $\text{MFP} > t$  will not fully propagate, thus reducing their contribution to  $k_x$  and  $k_z$ . Moreover, the similar rate of increase of  $k_x$  and  $k_z$  with increasing film thickness observed in Figure 3a suggests that phonons with MFP commensurate with the sample thickness contribute to the thermal conductivity.

To gain a further insight on how phonons contribute to the thermal conductivity, we use the MFP reconstruction model to extract the cross-plane and in-plane phonon MFP distribution (see details in Supporting Information). A detailed description of this model can be found elsewhere.<sup>20–22,41–43</sup> Figure 3b displays the normalized accumulated thermal conductivity as a function of the phonon MFP. It is seen that the MFP distribution shifts to longer values for in-plane transport compared to the cross-plane. In particular, we found that phonons with MFP ranging from 1 to 53 nm and from 1 to 30 nm contribute to 50% of the  $k_x$  and  $k_z$ , respectively. Similar observations were also predicted by Wang et al.<sup>6</sup> and Ding et al.<sup>12</sup> in SnSe<sub>2</sub> bulk using DFT calculations, while the same



**Figure 4.** Influence of ambient temperature and thickness on the in-plane thermal conductivity of SnSe<sub>2</sub> films. (a) Temperature and (b) thickness dependence of  $k_r$  for a series of suspended crystalline SnSe<sub>2</sub> films with thickness between 16 and 75 nm, from 300 to 473 K. The y-axis in (a) and (b) shows the extracted thermal conductivities using single laser Raman thermometry measurements and FEM simulations (see details in Supporting Information). The x-axis in (a) and the temperatures indicated in (b) correspond to the ambient temperatures inside the cryostat. The rectangular dashed regions depicted in (b) show the gradual weaker temperature dependence of  $k_r$  with decreasing thickness (c) The percentage of the  $k_r$  decrease at 300 K with respect to the bulk SnSe<sub>2</sub> value (black full circles) and the percentage of decrease of  $k_r$  at 473 K with respect to the  $k_r$  at 300 K (red full squares). The black line and red curve are a guide for the eye. The right image in (c) depicts the dominant scattering mechanisms with decreasing thickness and increasing temperature.

methodology was used by Zhang et al.<sup>21</sup> to estimate the MFP distribution in graphite. From the experimental  $k_r$  and  $k_z$  values, we directly obtain the anisotropy ratio  $k_r/k_z$  for each film thickness, as is shown in Figure 3c. The average value of  $k_r/k_z$  is  $8.4 \pm 1$ , which is in close agreement with theoretical calculations that showed a thermal anisotropy ratio of 7.1 in the SnSe<sub>2</sub> bulk sample.<sup>6</sup>

Our result is also in agreement with a recent experimental study that showed a similar thickness-independent thermal anisotropy ratio ( $\sim 10$ ) in InSe thin films using time-domain thermoreflectance measurements.<sup>44</sup> Moreover, in Figure 3d we plot the calculated total interface thermal resistance,  $R_{\text{tot}} = R_1 + R_2$ , as a function of film thickness and compare our values with those of supported MoS<sub>2</sub> films also extracted using time-domain thermoreflectance measurements.<sup>40</sup> The observed variation of  $R_{\text{int}}$  can be attributed to the sample processing (exfoliation and transfer conditions, storage before gold evaporation, etc.), which could result in different interfacial energy coupling. However, we cannot exclude the possibility that  $R_{\text{int}}$  is increased due to reduced mechanical coupling of the films to the underlying Au resulting from a potential increase in sample stiffness or changes in the vibrational spectra as the thickness is increasing. Similar thickness-dependent  $R_{\text{int}}$  has been found in MoS<sub>2</sub>, InSe, and graphene stacks.<sup>40,44,45</sup>

To examine the dependence of  $k_r$  of suspended SnSe<sub>2</sub> films on temperature, we conducted single-laser Raman thermometry measurements at different ambient conditions. The  $k_r$  of the SnSe<sub>2</sub> films was extracted by measuring the absorbed power and the temperature rise of the films at the laser spot at different ambient temperatures (298, 373, and 473 K) and solving the 2D heat equation, as described in detail in our previous work.<sup>46</sup> The temperature of each suspended membrane at the laser spot as a function of the absorbed

power at different ambient temperatures is shown in Figure S7 in the Supporting Information. The temperature coefficient ( $-0.0107 \pm 0.0015$  K/(cm<sup>-1</sup>)) was determined in advance through a calibration procedure (see Figure S6 in Supporting Information). A deeper analysis of the power measurements and the FEM simulations is given in the Supporting Information (see Figures S9 and S10).

Figure 4a shows the measured  $k_r$  of four suspended SnSe<sub>2</sub> films with  $t = 16, 25, 60,$  and  $75$  nm as a function of ambient temperature. We observe a systematic decrease of the  $k_r$  with increasing temperature for all the SnSe<sub>2</sub> films and a maximum reduction of  $\sim 56\%$  at 473 K for the thickest SnSe<sub>2</sub> film compared to the room temperature value. This trend originates in the temperature dependence of the phonon MFP, since with increasing temperature the thermal phonon MFP becomes shorter as higher energy phonon states are populated.<sup>47</sup> Therefore, the decrease of  $k_r$  with increasing temperature can be attributed to the phonon MFP suppression due to phonon-phonon scattering processes, as has previously been reported in thin film semiconductors at high temperatures.<sup>29,48,49</sup> Furthermore, by plotting  $k_r$  as a function of thickness at different ambient temperatures (Figure 4b), we observe that the dependence of  $k_r$  with temperature becomes weaker for thinner samples. In other words, as the temperature increases,  $k_r$  becomes less sensitive to the sample thickness since these phonons responsible for most of the heat transport have a MFP shorter than the film thickness. The weaker temperature dependence in thinner films seems to be reasonable given that phonon boundary scattering becomes dominant.

In Figure 4c we show the importance of different scattering mechanism by plotting the percentage of the  $k_r$  decrease at 300 K with respect to the bulk SnSe<sub>2</sub> value (black points) and the percentage of the  $k_r$  decrease at 473 K with respect to the  $k_r$  at



300 K (red points). The nearly linear behavior of the black data points is analogous to the observed linear thickness-dependent behavior of  $k_r$  (see Figure 3a) and suggests that at room-temperature phonon boundary scattering becomes dominant with decreasing thickness. On the other hand, from the red data points we observe the dominant role of phonon–phonon scattering processes at high temperatures as the film thickness increases. The competing role of the two different scattering mechanisms is illustrated in Figure 4c (right image).

We point out that phonons with MFP longer than the film thickness still contribute to the thermal conductivity provided that phonons wavevector directions are close to the direction of the temperature gradient. However, at high temperatures, the wavelength of phonons dominating the heat transport becomes shorter; thus boundary scattering becomes less probable unless the thickness of the film is close to the MFP of the phonons responsible for most of the heat transport. For instance, in the case of the 16 nm thick film, the  $k_r$  at room temperature decreased by 45% compared to the bulk value, whereas the influence of thickness on its temperature dependence is relatively small. Thus, phonons with MFP > 16 nm contribute substantially to the thermal conductivity with a rather small influence on its temperature dependence.

In conclusion, we investigated the thickness-dependence of the in-plane and cross-plane thermal conductivity of crystalline SnSe<sub>2</sub> films. Both show a strong thickness dependence in the range of 16–190 nm, with a 2.5-fold reduction in their values with respect to the bulk values. From this result we directly obtained the thermal conductivity anisotropy ratio, which was found to be independent of the film thickness and approximately 8.4. Importantly, we showed that at high temperatures the in-plane thermal conductivity of suspended SnSe<sub>2</sub> films can be reduced by more than ~50% with respect to the room temperature value. The strong dependence of the thermal conductivity on temperature becomes gradually weaker with decreasing thickness due to the dominant role of phonon boundary scattering. Finally, by using the MFP reconstruction method, we showed that at room temperature the main heat-carrying phonons that contribute to in-plane and cross-plane thermal conductivity have mean free paths of several tens of nanometers.

Our results provide valuable information to understand thermal transport in two-dimensional materials and realize functional devices that require highly anisotropic properties, i.e., thermoelectrics, transistors, and optical sensors or operating at high temperatures. Highly anisotropic 2D layered materials like SnSe<sub>2</sub> can provide a through-thickness thermal insulation and heat flow propagation mainly in the in-plane direction. This can be advantageous, for example, in heat-sensitive electronic components, such as microchips, where directional heat flow is necessary to prevent hot spots or for cooling circuits.<sup>50,51</sup> Finally, the ability to manipulate heat propagation through either dimensionality confinement or temperature modifications and the quantitative knowledge of the thermal phonon MFPs give important insights for the design of 2D thermoelectric devices with improved heat management.

## ■ ASSOCIATED CONTENT

### SI Supporting Information

The Supporting Information is available free of charge at <https://pubs.acs.org/doi/10.1021/acs.nanolett.1c03018>.

Optical images and atomic force microscopy measurements of the exfoliated SnSe<sub>2</sub> films; mean free path reconstruction method; FDTR sensitivity analysis; spot size measurements; single-laser Raman thermometry measurements and FEM calculations; power absorption measurements; Raman thermometry calibration; effect of strain, defects, and nonuniform Raman signal on suspended samples (PDF)

## ■ AUTHOR INFORMATION

### Corresponding Author

Alexandros El Sachat – *Catalan Institute of Nanoscience and Nanotechnology (ICN2), CSIC and BIST, Bellaterra 08193 Barcelona, Spain*; [orcid.org/0000-0003-3798-9724](https://orcid.org/0000-0003-3798-9724); Email: [alexandros.elsachat@icn2.cat](mailto:alexandros.elsachat@icn2.cat)

### Authors

Peng Xiao – *Catalan Institute of Nanoscience and Nanotechnology (ICN2), CSIC and BIST, Bellaterra 08193 Barcelona, Spain; Departamento de Física, Universidad Autónoma de Barcelona, Bellaterra 08193 Barcelona, Spain*; [orcid.org/0000-0002-4711-2566](https://orcid.org/0000-0002-4711-2566)

Emigdio Chavez-Angel – *Catalan Institute of Nanoscience and Nanotechnology (ICN2), CSIC and BIST, Bellaterra 08193 Barcelona, Spain*; [orcid.org/0000-0002-9783-0806](https://orcid.org/0000-0002-9783-0806)

Stefanos Chaitoglou – *National Center for Scientific Research "Demokritos", 15310 Athens, Greece*

Marianna Sledzinska – *Catalan Institute of Nanoscience and Nanotechnology (ICN2), CSIC and BIST, Bellaterra 08193 Barcelona, Spain*; [orcid.org/0000-0001-8592-1121](https://orcid.org/0000-0001-8592-1121)

Athanasios Dimoulas – *National Center for Scientific Research "Demokritos", 15310 Athens, Greece*; [orcid.org/0000-0003-3199-1356](https://orcid.org/0000-0003-3199-1356)

Clivia M. Sotomayor Torres – *Catalan Institute of Nanoscience and Nanotechnology (ICN2), CSIC and BIST, Bellaterra 08193 Barcelona, Spain; ICREA, 08010 Barcelona, Spain*; [orcid.org/0000-0001-9986-2716](https://orcid.org/0000-0001-9986-2716)

Complete contact information is available at: <https://pubs.acs.org/10.1021/acs.nanolett.1c03018>

### Author Contributions

<sup>†</sup>P.X. and E.C.-A. contributed equally. The work was conceived by A.E.S. and E.C.-A. The sample fabrication was done by P.X. and S.C., and the Raman characterization was performed by P.X. and A.E.S. The AFM and FDTR characterization was carried out by A.E.S. The MFP reconstruction algorithm and TEM analysis were performed by E.C.-A. P.X., E.C.-A., S.C., M.S., A.D., C.M.S.T., and A.E.S. reviewed and edited the manuscript. C.M.S.T. and A.E.S. supervised the work. All authors have read and agreed to the published version of the manuscript. All authors have given approval to the final version of the manuscript. The manuscript was written by A.E.S. and E.C.-A.

### Notes

The authors declare no competing financial interest.

## ■ ACKNOWLEDGMENTS

This work has been supported by the Severo Ochoa program, the Spanish Research Agency (AEI, Grant SEV-2017-0706), and the CERCA Programme/Generalitat de Catalunya. The authors acknowledge support from Spanish MICINN Project

SIP (Grant PGC2018-101743-B-I00) and the EU Project NANOPOLY (Grant GA 289061). S.C. and A.D. acknowledge financial support from the Flag-Era JTC 2017 Project MELODICA. P.X. acknowledges support by a Ph.D. fellowship from the EU Marie Skłodowska-Curie COFUND PREBIST (Grant Agreement 754558).

## ABBREVIATIONS

AFM, atomic force microscopy; TEM, transmission electron microscopy; FDTR, frequency domain thermoreflectance; MFP, mean free path; 2LRT, two-laser Raman thermometry

## REFERENCES

- (1) Guo, C.; Tian, Z.; Xiao, Y.; Mi, Q.; Xue, J. Field-Effect Transistors of High-Mobility Few-Layer SnSe 2. *Appl. Phys. Lett.* **2016**, *109* (20), 203104.
- (2) Schlaf, R.; Lang, O.; Pettenkofer, C.; Jaegermann, W. Band Lineup of Layered Semiconductor Heterointerfaces Prepared by van Der Waals Epitaxy: Charge Transfer Correction Term for the Electron Affinity Rule. *J. Appl. Phys.* **1999**, *85* (5), 2732–2753.
- (3) Li, G.; Ding, G.; Gao, G. Thermoelectric Properties of SnSe<sub>2</sub> monolayer. *J. Phys.: Condens. Matter* **2017**, *29* (1), 015001.
- (4) Xu, P.; Fu, T.; Xin, J.; Liu, Y.; Ying, P.; Zhao, X.; Pan, H.; Zhu, T. Anisotropic Thermoelectric Properties of Layered Compound SnSe<sub>2</sub>. *Sci. Bull.* **2017**, *62* (24), 1663–1668.
- (5) Sun, B.-Z.; Ma, Z.; He, C.; Wu, K. Anisotropic Thermoelectric Properties of Layered Compounds in SnX<sub>2</sub> (X = S, Se): A Promising Thermoelectric Material. *Phys. Chem. Chem. Phys.* **2015**, *17* (44), 29844–29853.
- (6) Wang, H.; Gao, Y.; Liu, G. Anisotropic Phonon Transport and Lattice Thermal Conductivities in Tin Dichalcogenides SnS<sub>2</sub> and SnSe<sub>2</sub>. *RSC Adv.* **2017**, *7* (14), 8098–8105.
- (7) Roy, T.; Tosun, M.; Hettick, M.; Ahn, G. H.; Hu, C.; Javey, A. 2D-2D Tunneling Field-Effect Transistors Using WSe<sub>2</sub>/SnSe<sub>2</sub> Heterostructures. *Appl. Phys. Lett.* **2016**, *108* (8), 083111.
- (8) Su, Y.; Ebrish, M. A.; Olson, E. J.; Koester, S. J. SnSe<sub>2</sub> Field-Effect Transistors with High Drive Current. *Appl. Phys. Lett.* **2013**, *103* (26), 263104.
- (9) Li, M. O.; Esseni, D.; Nahas, J. J.; Jena, D.; Xing, H. G. Two-Dimensional Heterojunction Interlayer Tunneling Field Effect Transistors (Thin-TFETs). *IEEE J. Electron Devices Soc.* **2015**, *3* (3), 200–207.
- (10) Chung, K.-M.; Wamwangi, D.; Woda, M.; Wuttig, M.; Bensch, W. Investigation of SnSe, SnSe<sub>2</sub>, and Sn<sub>2</sub>Se<sub>3</sub> Alloys for Phase Change Memory Applications. *J. Appl. Phys.* **2008**, *103* (8), 083523.
- (11) Rai, R. K.; Islam, S.; Roy, A.; Agrawal, G.; Singh, A. K.; Ghosh, A.; N., R. Morphology Controlled Synthesis of Low Bandgap SnSe<sub>2</sub> with High Photodetectivity. *Nanoscale* **2019**, *11* (3), 870–877.
- (12) Ding, Y.; Xiao, B.; Tang, G.; Hong, J. Transport Properties and High Thermopower of SnSe<sub>2</sub>: A Full Ab-Initio Investigation. *J. Phys. Chem. C* **2017**, *121* (1), 225–236.
- (13) Huang, Y.; Chen, X.; Zhou, D.; Liu, H.; Wang, C.; Du, J.; Ning, L.; Wang, S. Stabilities, Electronic and Optical Properties of SnSe<sub>2</sub>(1-x)S<sub>2x</sub> Alloys: A First-Principles Study. *J. Phys. Chem. C* **2016**, *120* (10), 5839–5847.
- (14) Saritha, K.; Suryanarayana Reddy, A.; Ramakrishna Reddy, K. T. Investigation on Optical Properties of SnSe<sub>2</sub> Thin Films Synthesized by Two – Stage Process. *Mater. Today Proc.* **2017**, *4* (14), 12512–12517.
- (15) Martínez-Escobar, D.; Ramachandran, M.; Sánchez-Juárez, A.; Narro Rios, J. S. Optical and Electrical Properties of SnSe<sub>2</sub> and SnSe Thin Films Prepared by Spray Pyrolysis. *Thin Solid Films* **2013**, *535*, 390–393.
- (16) Evans, B. L.; Hazelwood, R. A. Optical and Electrical Properties of SnSe<sub>2</sub>. *J. Phys. D: Appl. Phys.* **1969**, *2* (11), 1507–1516.

(17) Bertrand, Y.; Leveque, G.; Raisin, C.; Levy, F. Optical Properties of SnSe<sub>2</sub> and SnS<sub>2</sub>. *J. Phys. C: Solid State Phys.* **1979**, *12* (14), 2907–2916.

(18) Zou, B.; Zhou, Y.; Zhang, X.; Zhang, M.; Liu, K.; Gong, M.; Sun, H. Thickness-Dependent Ultralow In-Plane Thermal Conductivity of Chemical Vapor-Deposited SnSe<sub>2</sub> Nanofilms: Implications for Thermoelectrics. *ACS Appl. Nano Mater.* **2020**, *3* (10), 10543–10550.

(19) Liu, X.; Li, Z.; Min, L.; Peng, Y.; Xiong, X.; Lu, Y.; Ao, J.-P.; Fang, J.; He, W.; Li, K.; Wu, J.; Mao, W.; Younis, U.; Divakar Botcha, V. Effect of Stress Layer on Thermal Properties of SnSe<sub>2</sub> Few Layers. *J. Alloys Compd.* **2019**, *783*, 226–231.

(20) Minnich, A. J. Determining Phonon Mean Free Paths from Observations of Quasiballistic Thermal Transport. *Phys. Rev. Lett.* **2012**, *109* (20), 205901.

(21) Zhang, H.; Chen, X.; Jho, Y.-D.; Minnich, A. J. Temperature-Dependent Mean Free Path Spectra of Thermal Phonons Along the c-Axis of Graphite. *Nano Lett.* **2016**, *16* (3), 1643–1649.

(22) Sanchez-Martinez, M.-Á.; Alzina, F.; Oyarzo, J.; Sotomayor Torres, C.; Chavez-Angel, E. Impact of the Regularization Parameter in the Mean Free Path Reconstruction Method: Nanoscale Heat Transport and Beyond. *Nanomaterials* **2019**, *9* (3), 414.

(23) Castellanos-Gomez, A.; Buscema, M.; Molenaar, R.; Singh, V.; Janssen, L.; van der Zant, H. S. J.; Steele, G. A. Deterministic Transfer of Two-Dimensional Materials by All-Dry Viscoelastic Stamping. *2D Mater.* **2014**, *1* (1), 011002.

(24) Liu, K.; Liu, H.; Wang, J.; Feng, L. Synthesis and Characterization of SnSe<sub>2</sub> Hexagonal Nanoflakes. *Mater. Lett.* **2009**, *63* (5), 512–514.

(25) Gonzalez, J. M.; Oleynik, I. I. Layer-Dependent Properties of SnS<sub>2</sub> and SnSe<sub>2</sub> Two-Dimensional Materials. *Phys. Rev. B: Condens. Matter Mater. Phys.* **2016**, *94* (12), 125443.

(26) Smith, A. J.; Meek, P. E.; Liang, W. Y. Raman Scattering Studies of SnS<sub>2</sub> and SnSe<sub>2</sub>. *J. Phys. C: Solid State Phys.* **1977**, *10* (8), 1321–1323.

(27) Reparaz, J. S.; Chavez-Angel, E.; Wagner, M. R.; Graczykowski, B.; Gomis-Bresco, J.; Alzina, F.; Sotomayor Torres, C. M. A Novel Contactless Technique for Thermal Field Mapping and Thermal Conductivity Determination: Two-Laser Raman Thermometry. *Rev. Sci. Instrum.* **2014**, *85* (3), 034901.

(28) El Sachat, A.; Alzina, F.; Sotomayor Torres, C. M.; Chavez-Angel, E. Heat Transport Control and Thermal Characterization of Low-Dimensional Materials: A Review. *Nanomaterials* **2021**, *11* (1), 175.

(29) Graczykowski, B.; El Sachat, A.; Reparaz, J. S.; Sledzinska, M.; Wagner, M. R.; Chavez-Angel, E.; Wu, Y.; Volz, S.; Wu, Y.; Alzina, F.; Sotomayor Torres, C. M. Thermal Conductivity and Air-Mediated Losses in Periodic Porous Silicon Membranes at High Temperatures. *Nat. Commun.* **2017**, *8* (1), 415.

(30) Qin, G.; Qin, Z.; Wang, H.; Hu, M. On the Diversity in the Thermal Transport Properties of Graphene: A First-Principles-Benchmark Study Testing Different Exchange-Correlation Functionals. *Comput. Mater. Sci.* **2018**, *151*, 153–159.

(31) Gu, X.; Wei, Y.; Yin, X.; Li, B.; Yang, R. Colloquium: Phononic Thermal Properties of Two-Dimensional Materials. *Rev. Mod. Phys.* **2018**, *90* (4), 041002.

(32) Sandell, S.; Maire, J.; Chávez-Ángel, E.; Sotomayor Torres, C. M.; Kristiansen, H.; Zhang, Z.; He, J. Enhancement of Thermal Boundary Conductance of Metal–Polymer System. *Nanomaterials* **2020**, *10* (4), 670.

(33) Sandell, S.; Chávez-Ángel, E.; El Sachat, A.; He, J.; Sotomayor Torres, C. M.; Maire, J. Thermoreflectance Techniques and Raman Thermometry for Thermal Property Characterization of Nanostructures. *J. Appl. Phys.* **2020**, *128* (13), 131101.

(34) Schmidt, A. J.; Cheaito, R.; Chiesa, M. A Frequency-Domain Thermoreflectance Method for the Characterization of Thermal Properties. *Rev. Sci. Instrum.* **2009**, *80* (9), 094901.

- (35) Wiedemeier, H.; Pultz, G.; Gaur, U.; Wunderlich, B. Heat Capacity Measurements of SnSe and SnSe<sub>2</sub>. *Thermochim. Acta* **1981**, *43* (3), 297–303.
- (36) Schmidt, A. J.; Chen, X.; Chen, G. Pulse Accumulation, Radial Heat Conduction, and Anisotropic Thermal Conductivity in Pump-Probe Transient Thermoreflectance. *Rev. Sci. Instrum.* **2008**, *79* (11), 114902.
- (37) Siemens, M. E.; Li, Q.; Yang, R.; Nelson, K. A.; Anderson, E. H.; Murnane, M. M.; Kapteyn, H. C. Quasi-Ballistic Thermal Transport from Nanoscale Interfaces Observed Using Ultrafast Coherent Soft X-Ray Beams. *Nat. Mater.* **2010**, *9* (1), 26–30.
- (38) Subramanyan, H.; Kim, K.; Lu, T.; Zhou, J.; Liu, J. On the Importance of Using Exact Full Phonon Dispersions for Predicting Interfacial Thermal Conductance of Layered Materials Using Diffuse Mismatch Model. *AIP Adv.* **2019**, *9* (11), 115116.
- (39) Liu, X.; Zhang, G.; Zhang, Y.-W. Thermal Conduction across the One-Dimensional Interface between a MoS<sub>2</sub> Monolayer and Metal Electrode. *Nano Res.* **2016**, *9* (8), 2372–2383.
- (40) Sood, A.; Xiong, F.; Chen, S.; Cheaito, R.; Lian, F.; Asheghi, M.; Cui, Y.; Donadio, D.; Goodson, K. E.; Pop, E. Quasi-Ballistic Thermal Transport Across MoS<sub>2</sub> Thin Films. *Nano Lett.* **2019**, *19* (4), 2434–2442.
- (41) Yang, F.; Dames, C. Mean Free Path Spectra as a Tool to Understand Thermal Conductivity in Bulk and Nanostructures. *Phys. Rev. B: Condens. Matter Mater. Phys.* **2013**, *87* (3), 035437.
- (42) Cuffe, J.; Eliason, J. K.; Maznev, A. A.; Collins, K. C.; Johnson, J. A.; Shchepetov, A.; Prunnila, M.; Ahopelto, J.; Sotomayor Torres, C. M.; Chen, G.; Nelson, K. A. Reconstructing Phonon Mean-Free-Path Contributions to Thermal Conductivity Using Nanoscale Membranes. *Phys. Rev. B: Condens. Matter Mater. Phys.* **2015**, *91* (24), 245423.
- (43) Chavez-Angel, E.; Zarate, R. A.; Fuentes, S.; Guo, E. J.; Kläui, M.; Jakob, G. Reconstruction of an Effective Magnon Mean Free Path Distribution from Spin Seebeck Measurements in Thin Films. *New J. Phys.* **2017**, *19* (1), 013011.
- (44) Rai, A.; Sangwan, V. K.; Gish, J. T.; Hersam, M. C.; Cahill, D. G. Anisotropic Thermal Conductivity of Layered Indium Selenide. *Appl. Phys. Lett.* **2021**, *118* (7), 073101.
- (45) Estrada, D.; Li, Z.; Choi, G.-M.; Dunham, S. N.; Serov, A.; Lee, J.; Meng, Y.; Lian, F.; Wang, N. C.; Perez, A.; Haasch, R. T.; Zuo, J.-M.; King, W. P.; Rogers, J. A.; Cahill, D. G.; Pop, E. Thermal Transport in Layer-by-Layer Assembled Polycrystalline Graphene Films. *npj 2D Mater. Appl.* **2019**, *3* (1), 10.
- (46) Chávez-Angel, E.; Reparaz, J. S.; Gomis-Bresco, J.; Wagner, M. R.; Cuffe, J.; Graczykowski, B.; Shchepetov, A.; Jiang, H.; Prunnila, M.; Ahopelto, J.; Alzina, F.; Sotomayor Torres, C. M. Reduction of the Thermal Conductivity in Free-Standing Silicon Nano-Membranes Investigated by Non-Invasive Raman Thermometry. *APL Mater.* **2014**, *2* (1), 012113.
- (47) Cho, J.; Goodson, K. E. Cool Electronics. *Nat. Mater.* **2015**, *14* (2), 136–137.
- (48) Liu, W.; Asheghi, M. Thermal Conduction in Ultrathin Pure and Doped Single-Crystal Silicon Layers at High Temperatures. *J. Appl. Phys.* **2005**, *98* (12), 123523.
- (49) Asheghi, M.; Leung, Y. K.; Wong, S. S.; Goodson, K. E. Phonon-Boundary Scattering in Thin Silicon Layers. *Appl. Phys. Lett.* **1997**, *71* (13), 1798.
- (50) Chung, D.; Takizawa, Y. Performance of Isotropic and Anisotropic Heat Spreaders. *J. Electron. Mater.* **2012**, *41* (9), 2580–2587.
- (51) Yamaguchi, S.; Tsunekawa, I.; Komatsu, N.; Gao, W.; Shiga, T.; Kodama, T.; Kono, J.; Shiomi, J. One-Directional Thermal Transport in Densely Aligned Single-Wall Carbon Nanotube Films. *Appl. Phys. Lett.* **2019**, *115* (22), 223104.

# Article 1 Supporting information

## Supporting Information:

# Anisotropic Thermal Conductivity of Crystalline Layered SnSe<sub>2</sub>

*Peng Xiao,<sup>1,2, †</sup> Emigdio Chavez-Angel,<sup>1, †</sup> Stefanos Chaitoglou,<sup>3</sup> Marianna Sledzinska<sup>1</sup>, Athanasios Dimoulas,<sup>3</sup> Clivia M. Sotomayor Torres<sup>1, 4</sup> and Alexandros El Sachat<sup>1,\*</sup>*

<sup>1</sup> Catalan Institute of Nanoscience and Nanotechnology (ICN2), CSIC and BIST, Campus UAB, Bellaterra, 08193 Barcelona, Spain

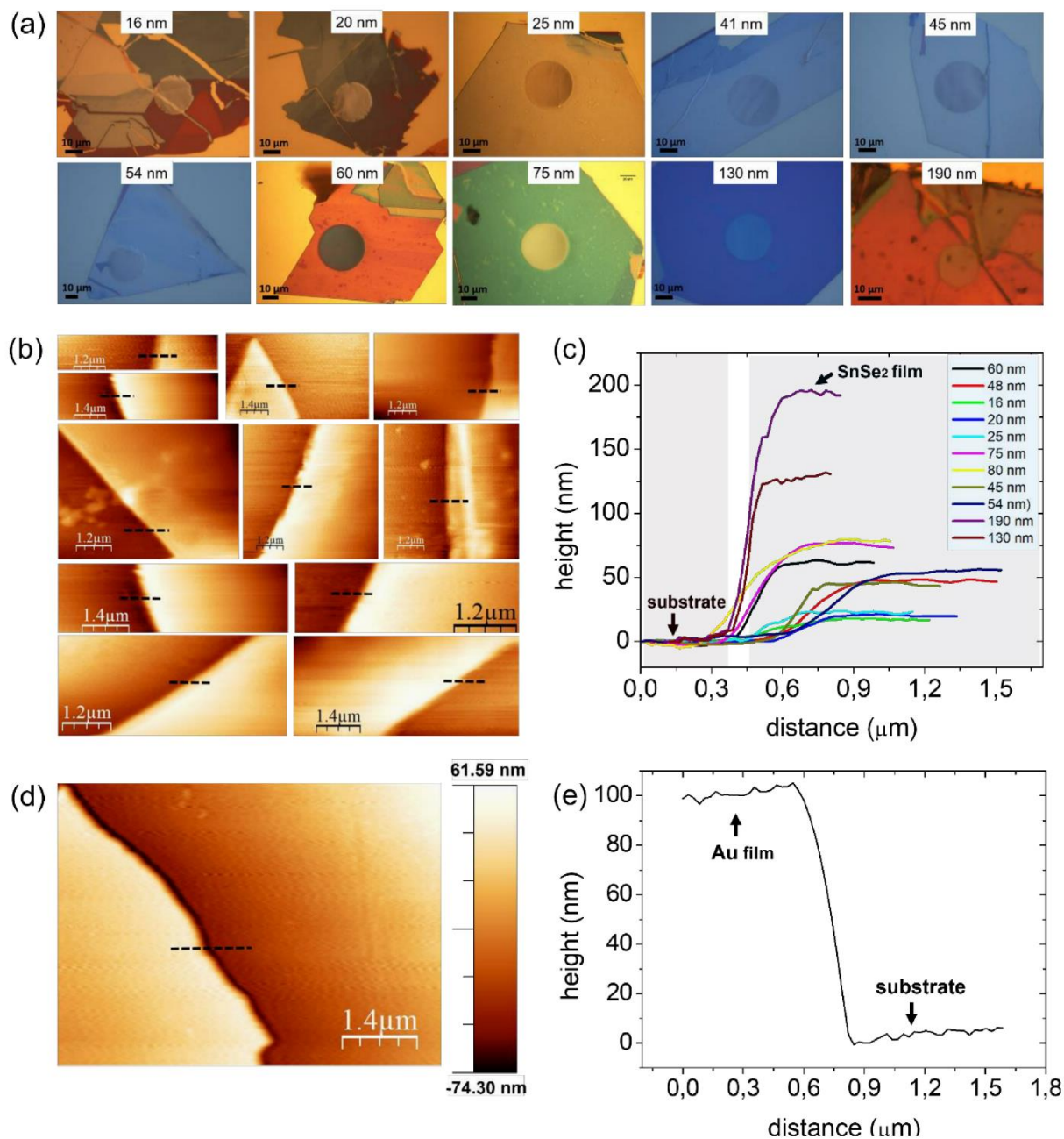
<sup>2</sup> Departamento de Física, Universidad Autónoma de Barcelona, Bellaterra, 08193 Barcelona, Spain

<sup>3</sup> National Center for Scientific Research “Demokritos”, 15310 Athens, Greece

<sup>4</sup> ICREA, Passeig Lluís Companys 23, 08010 Barcelona, Spain

\*Corresponding author: [alexandros.elsachat@icn2.cat](mailto:alexandros.elsachat@icn2.cat)

# 1. Optical images and atomic force microscopy measurements of the exfoliated SnSe<sub>2</sub> films



**Figure S1.** (a) Optical images of SnSe<sub>2</sub> films of different thickness. (b) Tapping mode atomic force microscopy images showing the edges of the SnSe<sub>2</sub> films with the substrate and (c) the corresponding topography profiles measured from the dashed lines depicted in (b). (d) AFM

image of the deposited Au transducer and (e) the corresponding topography profile from the black dashed line depicted in (d).

## 2. Mean Free path reconstruction method

In a bulk system, the thermal transport is mainly limited by different scattering events introduced by (quasi-)particles, impurities, defects and so on. However, reducing the size of the system, the surface scattering mechanism has also a strong influence on the thermal transport. For the case of electronic transport, Fuchs<sup>1</sup> showed that the boundary scattering is a surface phenomenon and its effect has to be included in the electron mean free path when the Boltzmann transport equation is used. The inclusion of the boundary scattering led to modification of the electronic distribution function, resulting in a modified formulation of the electronic conductivity. Years later, inspired by this work, Chambers extended this model to nanowires<sup>2</sup>, Sondheimer simplified it to thin film and nanowires<sup>3</sup> and Asheghi applied to the thermal transport<sup>4</sup>.

The Fuchs-Sondheimer (FS) model assumes that a fraction  $p$  of carriers is specularly reflected and  $(1 - p)$  carriers are diffusively reflected by the surface, respectively. The  $p$ -parameter was introduced to describe the way electrons interact with the wall. Now, if we considered pure diffusive scattering, i.e.,  $p = 0$ , the transport property of the thin-film,  $\alpha_{film}$ , can be related to the transport property of the bulk,  $\alpha_{bulk}$ , by:

$$\alpha_{film} = \alpha_{bulk} S(\chi) \quad (1)$$

where  $S(\chi)$  is the FS suppression function,  $\chi = \Lambda/t$  is the Knudsen number,  $\Lambda$  is the bulk-MFP and  $t$  the film thickness. For the in-plane transport configuration the FS suppression function is given by:

$$S(\chi) = 1 - \frac{3}{8}\chi + \frac{3}{2}\chi \int_1^{\infty} (y^{-3} - y^{-5}) \exp[-y/\chi] dy \quad (2)$$

and for the cross-plane transport this function is described by<sup>5</sup>:

$$S(\chi) = 1 - \chi(1 - \exp[-1/\chi]) \quad (3)$$

Taking into account this effect, Minnich<sup>6</sup> suggested an inverse method to extract the MFP accumulation function based on: (i) a characteristic suppression function, (ii) experimental data and (iii) a given geometry and the experimental configuration of the sample. Based on this approach, Cuffe et al.<sup>7</sup> showed that the measured thermal conductivity of a film ( $\alpha_{film}(t)$ ) and the FS suppression function are related through a cumulative MFP distribution given by: <sup>6,7</sup>

$$\alpha_{film}(t) = \int_0^{\infty} S(\chi)f(\Lambda)d\Lambda \quad (4)$$

$$\alpha = \frac{\alpha_{film}(t)}{\alpha_{bulk}} = \int_0^{\infty} K(\chi)F_{acc}(\Lambda)d\Lambda, \text{ with} \quad (5)$$

$$F_{acc}(\Lambda_C) = \frac{1}{\alpha_{bulk}} = \int_0^{\Lambda_C} f(\Lambda')d\Lambda', \text{ and } K(\chi) = -\frac{dS(\chi)}{d\chi} \frac{d\chi}{d\Lambda} \quad (6)$$

where  $F_{acc}(\Lambda_C)$  represents the fraction of transport property contribution from all the carriers (phonons in this case) with MFP less than  $\Lambda_C$  and  $K(\chi)$  represents the Kernel of the integral. The solution of Eq. (6) is technically an ill-posed problem and, in principle, with infinite solutions. However, Minnich<sup>6</sup> showed that it is possible to discretize the integral and impose certain constrains to the  $F_{acc}$  to obtain a unique solution. These constrains are mainly related to “the shape” of the reconstructed function, which have to be a smooth distribution without abrupt jumps and increasing monotonically from 0 to a maximum value given by the bulk transport property. These constrains and discretization of the integral can be expressed in terms of a minimization problem through the Tikhonov regularization method given by:

$$\min \left\{ \|A \cdot F - \alpha\|_2^2 + \mu^2 \|L \cdot F\|_2^2 \right\} \quad (7)$$

where  $\| \cdot \|_2$  is the second-norm operator,  $\alpha_i$  is the normalized electrical conductivity of the  $i^{\text{th}}$  measurement,  $A_{i,j} = K(\chi_{i,j}) \cdot \beta_j$  is a  $m \times n$  matrix with  $m$  the number of measurements and  $n$  the



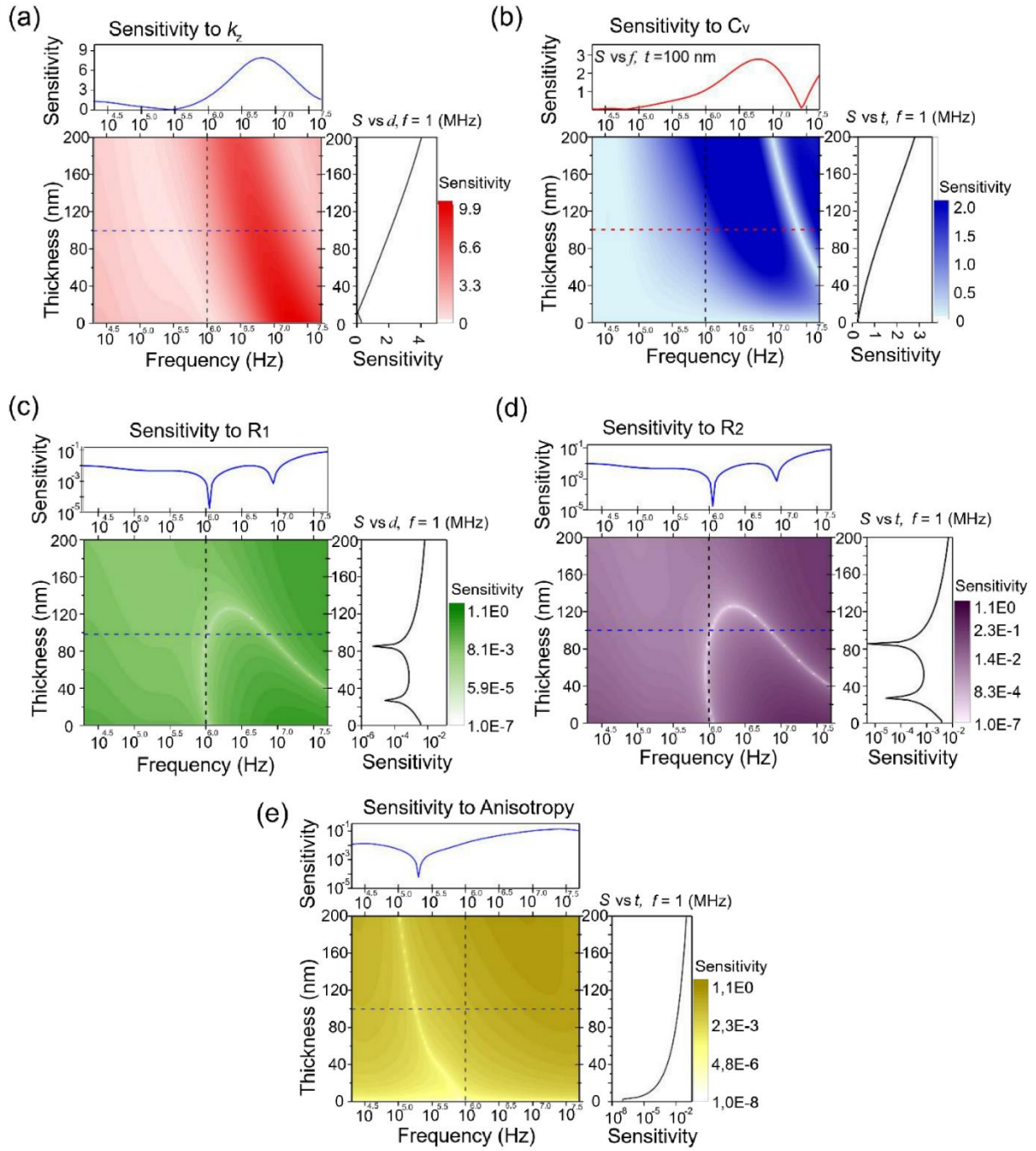
discretization points of the integral,  $\beta_j$  is the weight of the quadrature point at  $\chi_{i,j} = \Lambda_j/d_i$ ,  $F$  is a vector of the desired accumulation function ( $F_{acc}$ ),  $\mu$  is the regularization parameter to control the smoothness of  $F$  and  $L$  is a  $(n-2) \times n$  tridiagonal Toeplitz matrix which represents an approximation of a second derivative operator, i.e.,  $L \cdot F = F_{i+1} - 2F_i + F_{i-1}$ . Now, to recover  $F_{acc}(\Lambda)$  from the experimental data it is necessary to have a wide enough range of measurements at different film thicknesses.

The minimization of Eq. (7) was performed by using CVX, a package for specifying and solving convex programs<sup>8,9</sup>, and the experimental data measured by us. The regularization parameter was estimated through *L-curve criterion*.<sup>10,11</sup> An extended description of this method can be found in the work of Sanchez-Martinez et al.<sup>12</sup>

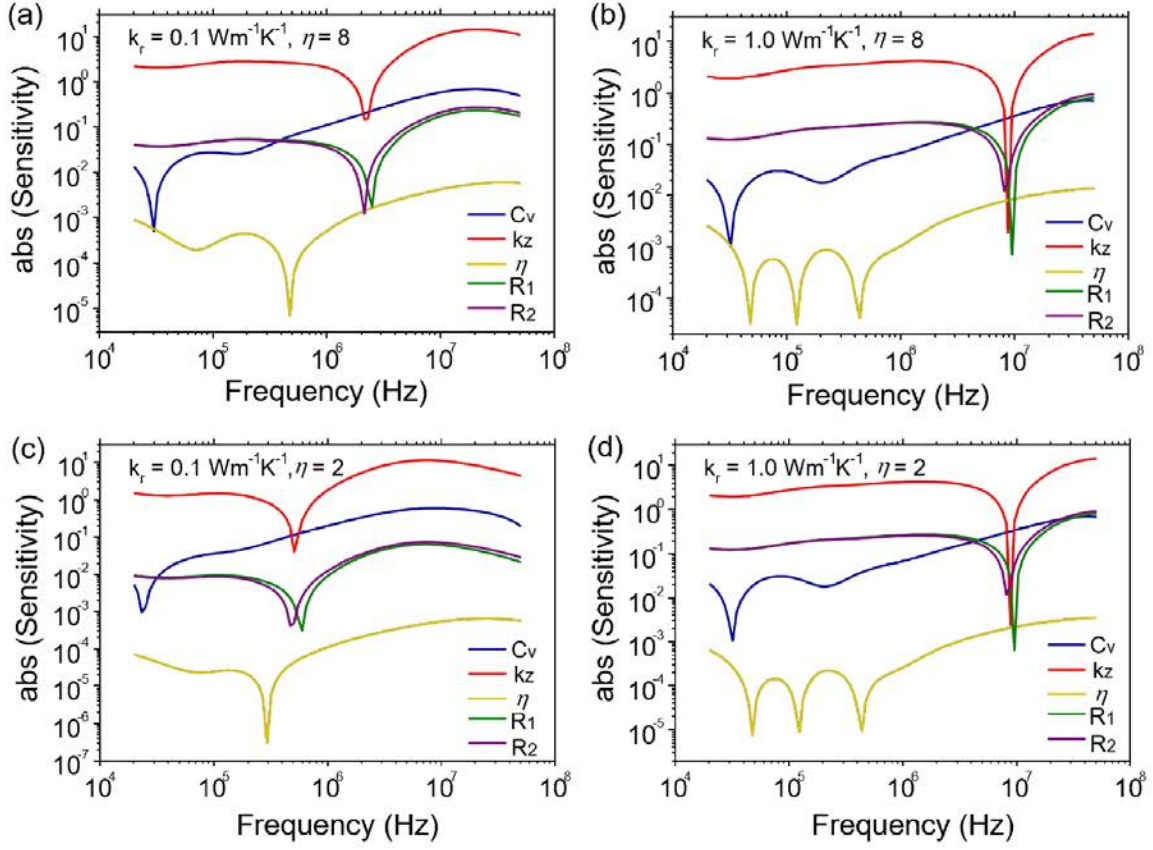
### 3. FDTR sensitivity analysis

To determine the phase sensitivity to multiple thermal properties we followed a similar methodology to that of Schmidt *et al.*<sup>13</sup> The calculated phase sensitivity to different parameters as a function of thickness and modulation frequency for the case of Au/SnSe<sub>2</sub>/Au stacks is shown in Figures S3(a-e). For the sensitive analysis, we fit the experimental thickness dependence of the cross-plane thermal conductivity ( $k_z$ ) using the Eq. (3) considering only cross-plane heat transport. This fit allows us to have a continuous function to plot the sensitivity as a function of excitation frequency (20 kHz–40 MHz) and sample thickness.

From Figures S2a,e we observe that the sensitivity of the recorded phase signal to in-plane heat transport is relatively low in comparison with the sensitivity to the cross-plane thermal conductivity. This is due to the much larger thermal diffusivity of the Au substrate compared to heat capacity of the SnSe<sub>2</sub> films and the relatively large pump and probe spot sizes. Moreover, from Figures S2c,d we find that the sensitivity of the phase signal to  $R_1$  and  $R_2$  is relatively low and only at high frequencies.

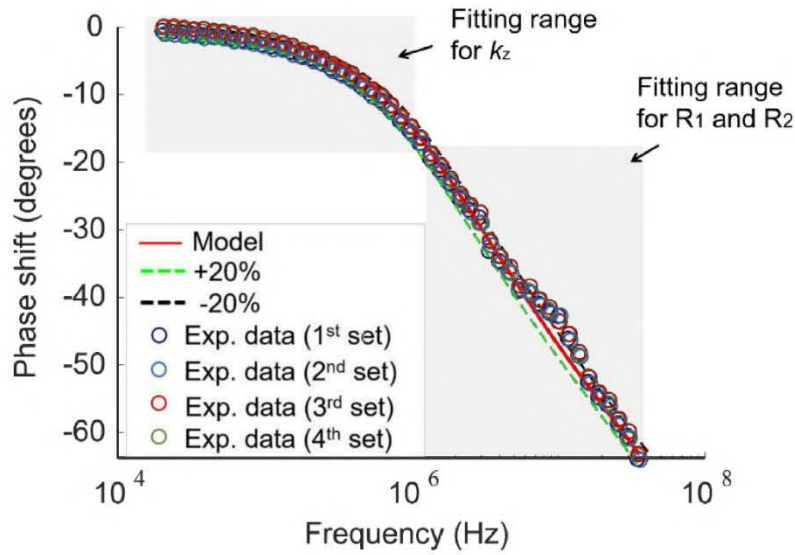


**Figure S2.** Calculated phase sensitivity to (a)  $k_z$ , (b)  $C_v$ , (c)  $R_1$  and (d)  $R_2$  and (e) anisotropy ( $\eta$ ) as a function of thickness and modulation frequency for the case of Au/SnSe<sub>2</sub>/Au stacks.



**Figure S3.** Phase sensitivity analysis for the case of a 16 nm thick SnSe<sub>2</sub> film covered with 100 nm (transducer) and 1.5 μm (substrate) of gold for different parameters of the film:  $k_z$ ,  $C_v$ ,  $\eta$ ,  $R_1$  and  $R_2$ . The FDTR signal is mainly sensitive to the  $k_z$  regardless of the anisotropy value. We attribute this behavior to the large thermal conductivity of the substrate which ensures that the heat flux will flow from the transducer top to the substrate, i.e. a pure one-dimensional heat flow across the film.

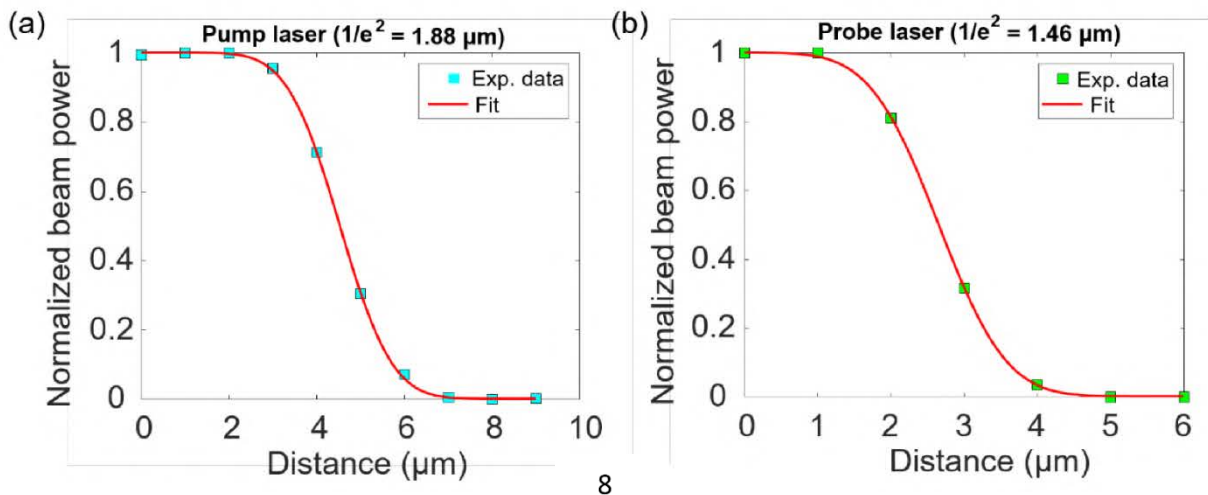
Furthermore, the uncertainty of Au-film-substrate configuration have been analyzed by Yang et al.<sup>14,15</sup> He found that for thermal conductivities below 5 W K<sup>-1</sup>m<sup>-1</sup> the uncertainty oscillates around 10%. In our measurements, the error bars of the  $k_z$ , were estimated by the standard deviation of several measurements, including the numerical errors from the fits (see Figure S4).



**Figure S4.** FDTR data sets measured in a 130 nm thick SnSe<sub>2</sub> film. The light blue and red areas in the graph indicate the different fitting ranges used to extract  $k_z$ ,  $R_1$  and  $R_2$ .

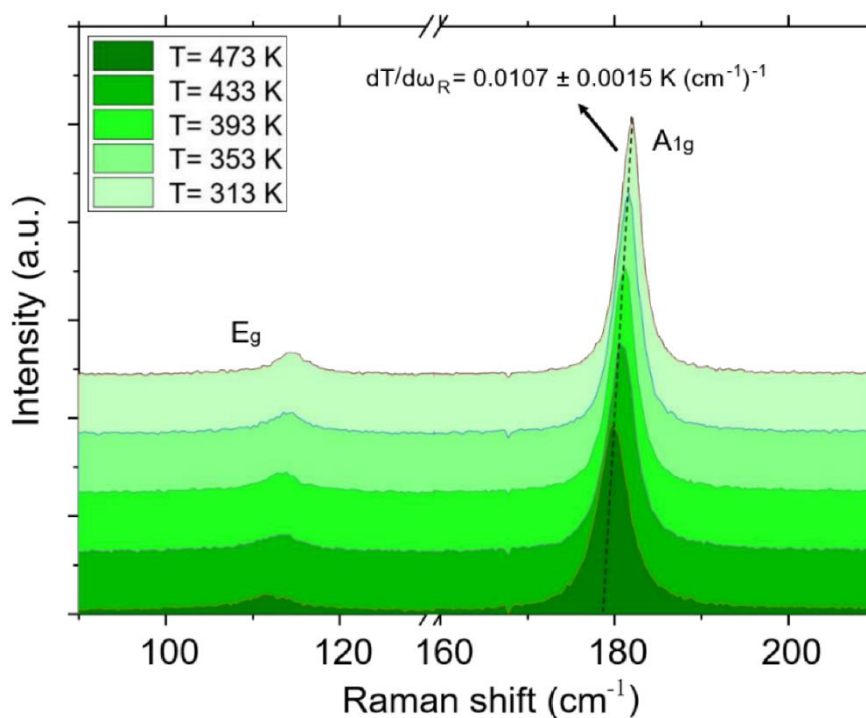
#### 4. Spot size measurements

The spot size of each measurement was measured by using the knife's edge method. The edge of the Au transducer layer was used as a sharp edge to measure the intensity of the reflected light as a function of stage position. The beam intensity as a function of translation distance was fitted to an error function curve<sup>16</sup> and the  $1/e^2$  radius of this curve was taken as the laser spot radius.

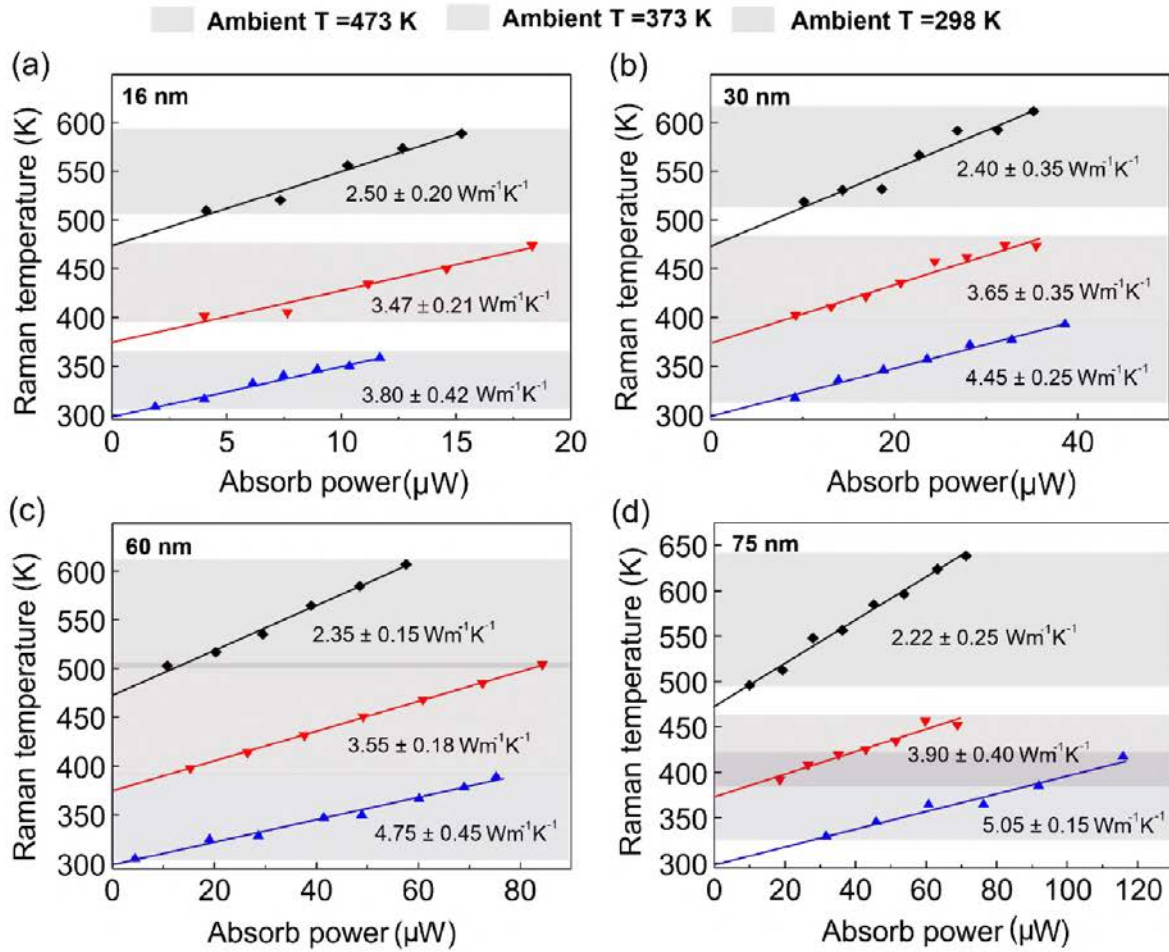


**Figure S5.** Typical examples of measured (a) pump and (b) probe spot sizes in 16 nm SnSe<sub>2</sub> film using the knife edge method.

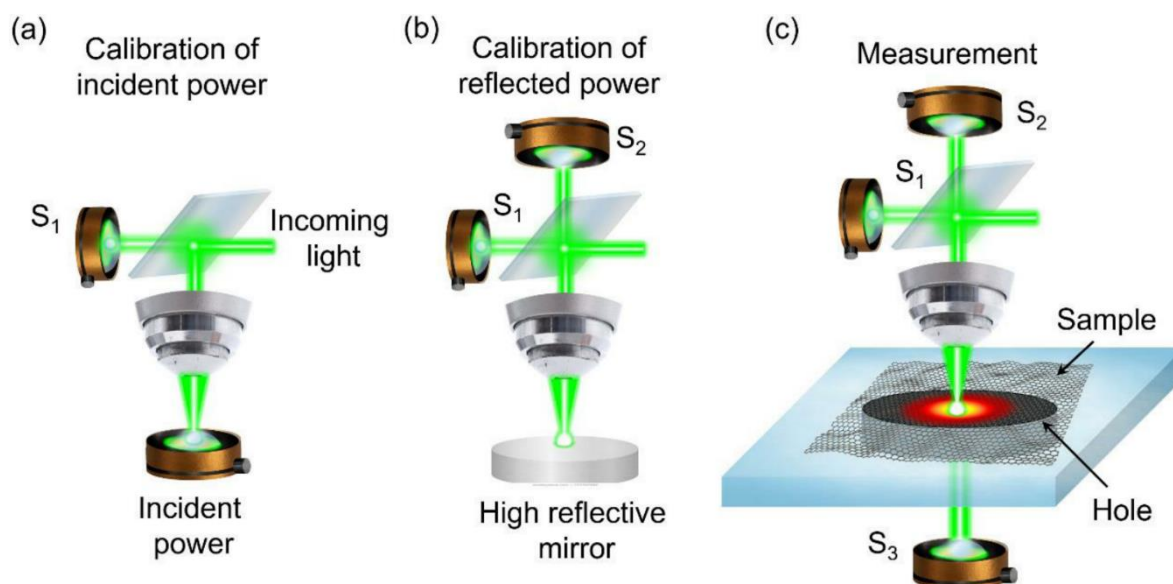
## 5. Single-laser Raman Thermometry measurements



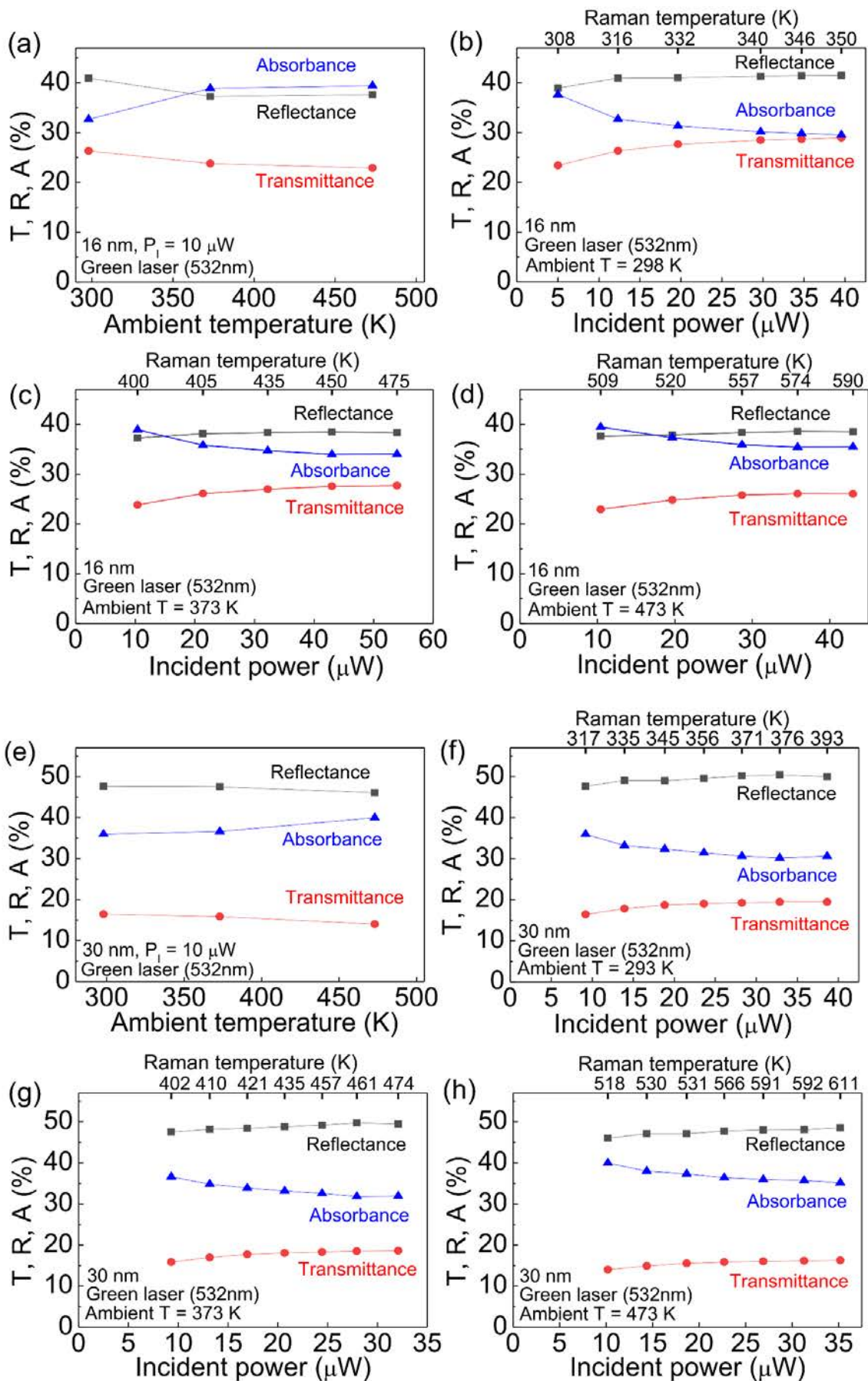
**Figure S6.** Raman thermometry calibration. Temperature as a function of SnSe<sub>2</sub> longitudinal optical phonon frequency. The temperature coefficient between 331 and 473 K was determined as  $dT/d\Delta\omega_R = -0.0107 \pm 0.0015 \text{ K (cm}^{-1}\text{)}^{-1}$ .



**Figure S7.** Measured Raman temperatures in (a) 16 nm, (b) 30 nm, (c) 60 nm and (d) 75 nm thick suspended SnSe<sub>2</sub> films at the laser spot as a function of the absorb power at different ambient temperatures. The measurements carried out using single laser Raman thermometry. The blue, red and grey regions inside the figures show the ambient temperatures of 298, 373 and 473 K, respectively. The solid lines are best fits to the experimental data points using FEM calculations, from which we extracted  $k_r$  following the methodology used in our previous work<sup>17</sup>. Examples of the FEM calculations are provided in Figure S10.

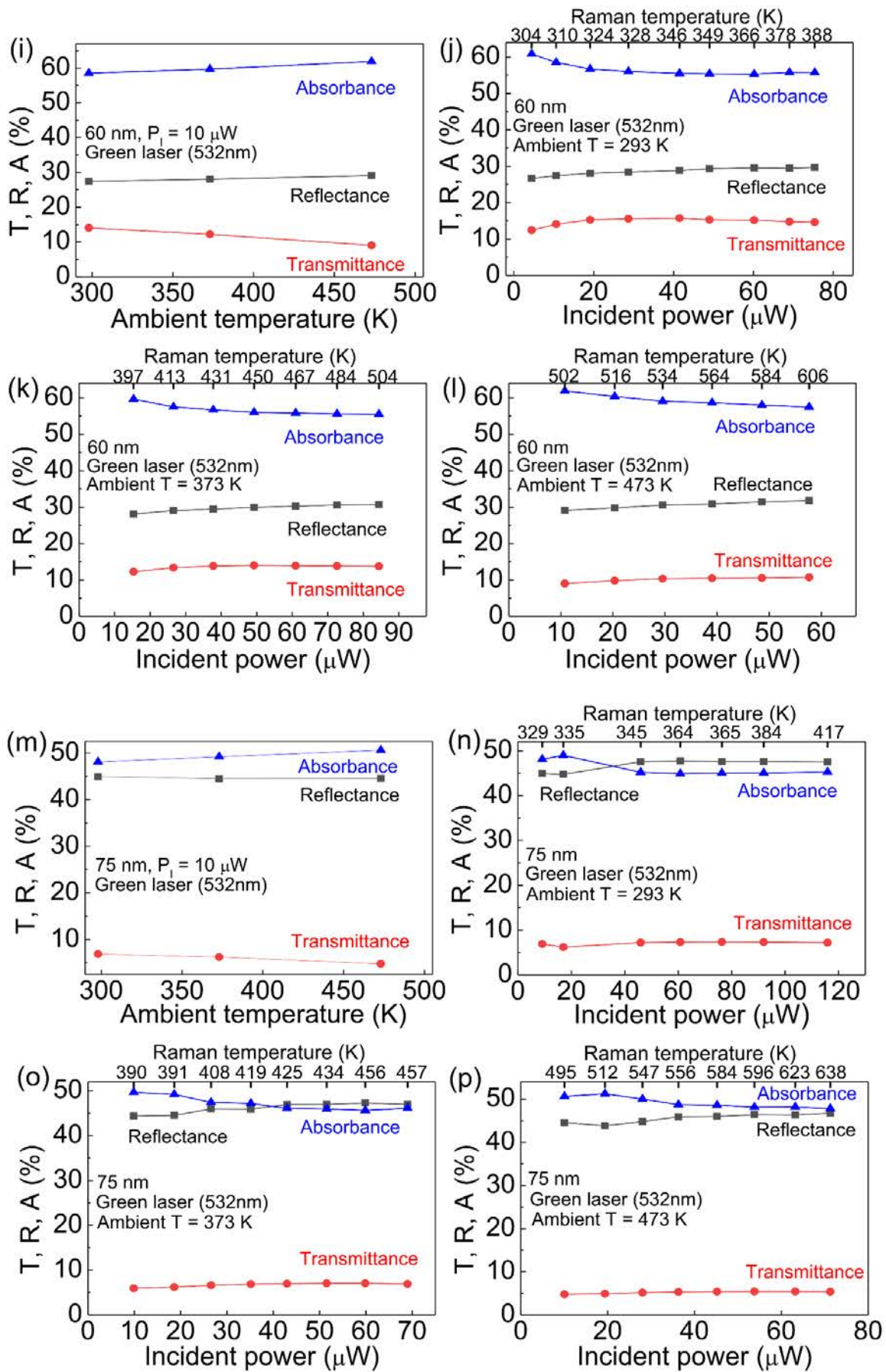


**Figure S8.** (a) Schematic representation of incident, reflected, and transmitted power measurements. Three steps are needed: (a) calibration of the incident power with respect to the incident power sensor, (b) calibration of the reflected power using a highly reflective mirror with incident power and (c) the measurement of the incident, transmitted, and reflected powers simultaneously using the sample. This calibration process accounts for the optical losses in the system, such as absorption/reflection from the microscope objective and the beam splitter. This custom built setup is attached to our Raman thermometry setup. The absorbed power  $P_0$  was measured on site for each  $\text{SnSe}_2$  film as the difference between incident and transmitted plus reflected light intensities probed by a calibrated system based on a cube non-polarizing beam splitter with an error of  $\Delta P_0 = 2\%$  and three fixed power meters. More details of the measurements of the absorbed power can be found in our previous publications.<sup>17–19</sup>

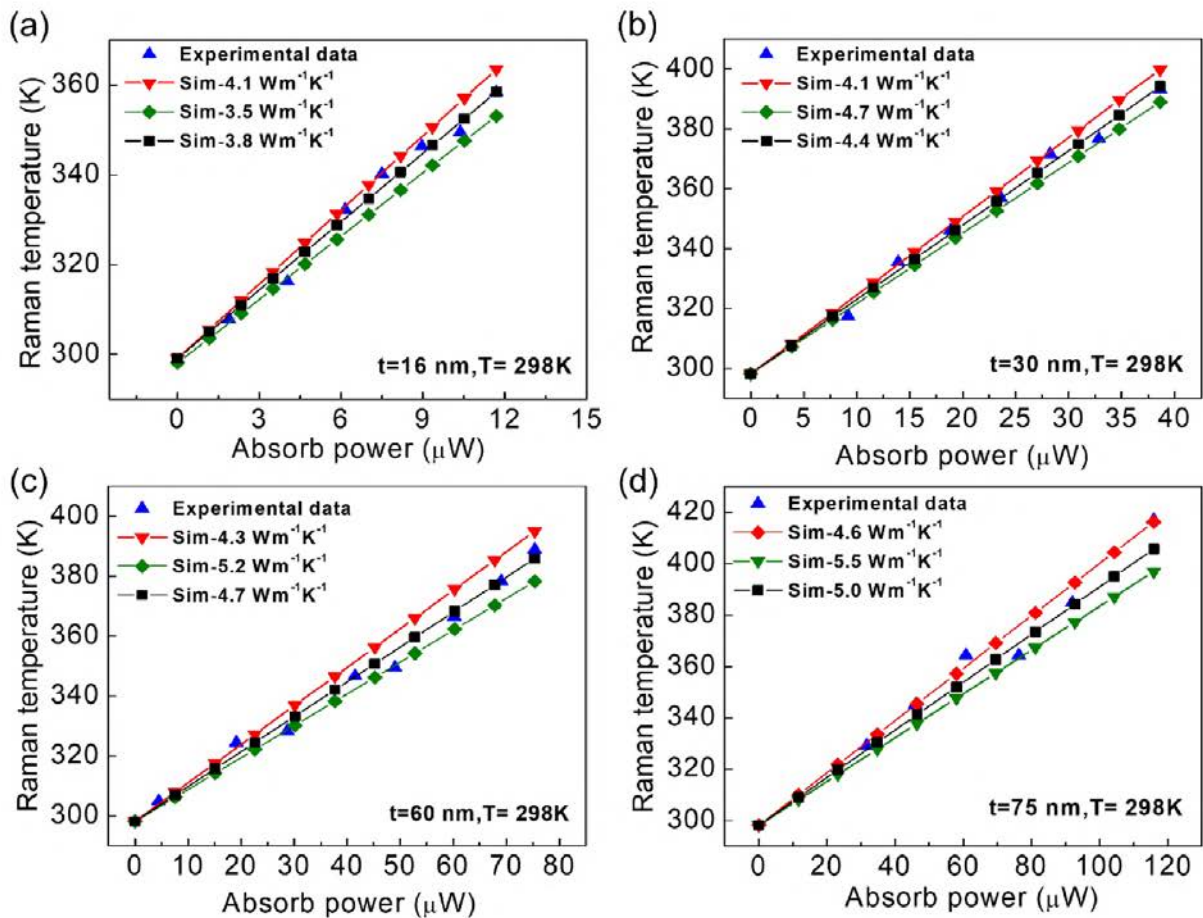


12





**Figure S9.** Transmission (T), Reflection (R) and absorption (A) measurements in SnSe<sub>2</sub> films of different thickness at different ambient temperatures. (a), (e), (i), (m) T, R, and A measurements at constant power ( $P_1 = 10 \mu\text{W}$ ) as a function of different ambient temperatures. (b)-(d), (f)-(h), (j)-(l) and (n)-(p) T, R and A measurements as a function of incident powers. In the inset of each graph we indicate the thickness of the films, the wavelength of the laser and the ambient temperature inside of the cryostat.

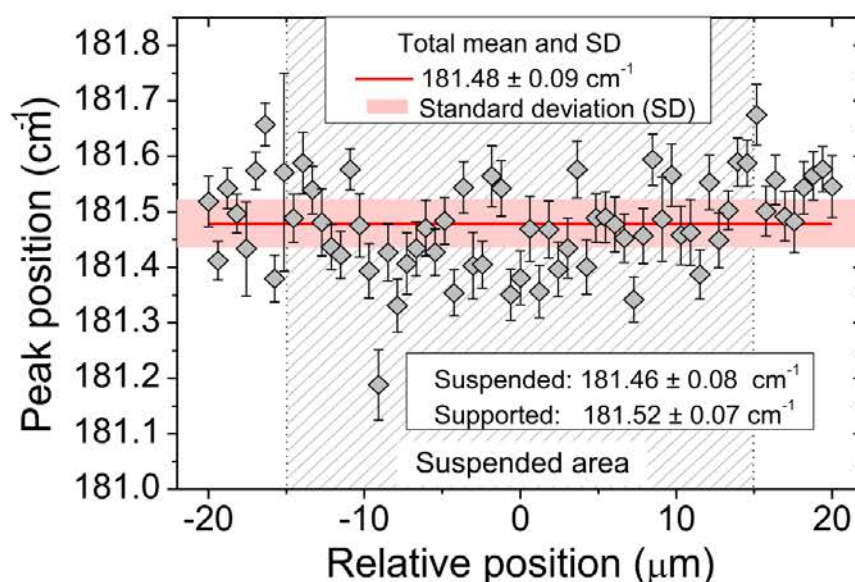


**Figure S10.** Examples of FEM simulations (COMSOL) performed for the case of (a) 16 nm, (b) 30 nm, (c) 60 nm and 75 nm thick SnSe<sub>2</sub> film at the ambient temperature of 298 K. The blue data show the temperature of the films at the laser spots measured by single-laser Raman thermometry at 298 K (see experimental data in Figure S7). In each figure, the red, black and green solid lines show the simulated curves from which we calculated three different thermal

conductivity values. The black solid lines in all the figures give us the best fit to the experimental data.

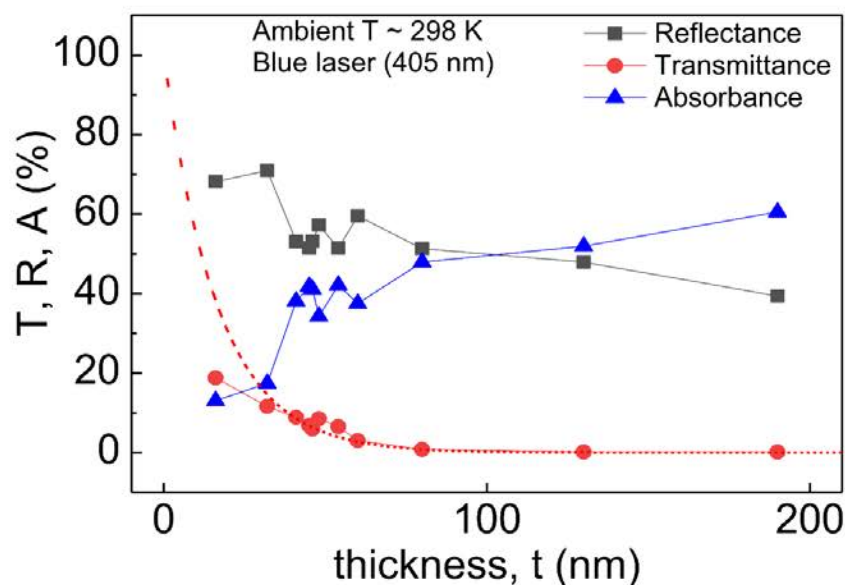
## 6. Effect of strain, defects and non-uniform Raman signal on suspended samples

Due to the exfoliation process, we do not expect to have a significant strain and/or defects to affect the Raman signal. However, any strain, defects or non-uniform areas can be detected through Raman line scans (baselines) using a low power probe laser. Figure S11 shows a representative example of a line scan along a 55 nm thick suspended  $\text{SnSe}_2$  film. We observe that in both suspended and supported areas the  $A_{1g}$  mode is detected at almost the same peak position with a difference of  $0.06 \text{ cm}^{-1}$ , which most likely is attributed to a small heating effect produced by the probe laser. Similar line scans were carried out for each sample and used as reference measurements prior to the in-plane thermal conductivity measurements to ensure the uniform Raman signal across the suspended films.



**Figure S11.** Example of a Raman line scan (reference measurement) in a 55 nm thick free standing  $\text{SnSe}_2$  film.

In addition, Babacic et al.<sup>20</sup> showed that the residual strain created in suspended MoSe<sub>2</sub> films during exfoliation is relatively low (0.022-0.2 GPa, see Table S4 in the SI of Babacic et al.). Nevertheless, even in the case of a slightly non-uniform signal across the film thickness, we do not expect to have a temperature gradient because the quite large absorption coefficient of SnSe<sub>2</sub>  $\sim 2\text{-}3\times 10^4\text{ cm}^{-1}$  and  $4\text{-}8\times 10^4\text{ cm}^{-1}$  at 532 nm<sup>21</sup> and 405 nm,<sup>22</sup> respectively. These values give a penetration depth around 500-300 nm and 250-125 nm, respectively. The large penetration depth suggests that both lasers (405 nm or 532 nm) illuminate homogeneously the samples, therefore, the heating source (or sensor for the case of two-laser) will heat (or probe) homogeneously the full thickness of the films.



**Figure S12.** Transmission (T), Reflection (R) and absorption (A) measurements in SnSe<sub>2</sub> films of different thickness at room temperature ( $T\sim 298\text{ K}$ ). In the inset of the graph we indicate the wavelength of the laser and the ambient temperature inside of the cryostat. The dashed red line shows the exponential fit for the transmitted power ( $T \sim \exp(-\mu \cdot t)$ ), where  $\mu$  is the fitting exponent and  $t$  the thickness of the films.

Thickness (nm)	Incident power ( $\mu\text{W}$ )	Transmission (%)	Reflection (%)	Absorption (%)
16	102	19	68	13
32	126	12	71	17
41	171	9	53	38
45	170	6.8	51	42.2
46	172	6	53	41
48	264	8.5	57	34.5
54	172	6.5	51	42.5
60	265	3.	59	38
80	217	0.7	51	48.3
130	510	0.1	47	52.9
190	523	0.1	39	60.9

**Table S1.** Summary of the thickness-dependent transmission, reflection and absorption measurements at room temperature for all the SnSe<sub>2</sub> films. The incident power was varied in order to reach a sufficient temperature rise (between 100 and 250 K) in the SnSe<sub>2</sub> films.

## References

1. Fuchs, K. The conductivity of thin metallic films according to the electron theory of metals. *Math. Proc. Cambridge Philos. Soc.* **34**, 100–108.
2. Chambers, R. G. The Conductivity of Thin Wires in a Magnetic Field. *Proc. R. Soc. A Math. Phys. Eng. Sci.* **202**, 378–394 (1950).
3. Sondheimer, E. H. *The mean free path of electrons in metals. Advances in Physics* vol. 1 (1952).
4. Asheghi, M., Leung, Y. K., Wong, S. S. & Goodson, K. E. Phonon-boundary scattering in thin silicon layers. *Appl. Phys. Lett.* **71**, 1798 (1997).
5. Zhang, H., Chen, X., Jho, Y.-D. & Minnich, A. J. Temperature-Dependent Mean Free Path Spectra of Thermal Phonons Along the c -Axis of Graphite. *Nano Lett.* **16**, 1643–

- 1649 (2016).
6. Minnich, A. J. Determining Phonon Mean Free Paths from Observations of Quasiballistic Thermal Transport. *Phys. Rev. Lett.* **109**, 205901 (2012).
  7. Cuffe, J. *et al.* Reconstructing phonon mean-free-path contributions to thermal conductivity using nanoscale membranes. *Phys. Rev. B* **91**, 245423 (2015).
  8. Grant, M. & Boyd, S. Graph implementations for nonsmooth convex programs. in *Recent Advances in Learning and Control* (eds. Blondel, V., Boyd, S. & Kimura, H.) 95–110 (Springer-Verlag Limited, 2008).
  9. Grant, M. & Boyd, S. CVX: Matlab Software for Disciplined Convex Programming, version 2.1. *CVX: Matlab Software for Disciplined Convex Programming, version 2.1* (2014).
  10. Hansen, P. C. & O’Leary, D. P. The use of the L-curve in the regularization of discrete ill-posed problems. *SIAM J. Sci. Comput.* **14**, 1487–1503 (1993).
  11. Hansen, P. C. The L-curve and its use in the numerical treatment of inverse problems. in *Computational Inverse Problems in Electrocadiology* (ed. Johnston, P.) 119–142 (WIT press, 2000).
  12. Sanchez-Martinez, M.-Á., Alzina, F., Oyarzo, J., Sotomayor Torres, C. & Chavez-Angel, E. Impact of the Regularization Parameter in the Mean Free Path Reconstruction Method: Nanoscale Heat Transport and Beyond. *Nanomaterials* **9**, 414 (2019).
  13. Schmidt, A. J., Cheaito, R. & Chiesa, M. A frequency-domain thermoreflectance method for the characterization of thermal properties. *Rev. Sci. Instrum.* **80**, 094901

- (2009).
14. Yang, J., Ziade, E. & Schmidt, A. J. Uncertainty analysis of thermoreflectance measurements. *Rev. Sci. Instrum.* **87**, 14901 (2016).
  15. Yang, J. Thermal property measurement with frequency domain thermoreflectance. (Boston University, 2017).
  16. Nemoto, S. Measurement of the refractive index of liquid using laser beam displacement. *Appl. Opt.* **31**, 6690 (1992).
  17. Chávez-Ángel, E. *et al.* Reduction of the thermal conductivity in free-standing silicon nano-membranes investigated by non-invasive Raman thermometry. *APL Mater.* **2**, 012113 (2014).
  18. Sandell, S. *et al.* Thermoreflectance techniques and Raman thermometry for thermal property characterization of nanostructures. *J. Appl. Phys.* **128**, 131101 (2020).
  19. Graczykowski, B. *et al.* Thermal conductivity and air-mediated losses in periodic porous silicon membranes at high temperatures. *Nat. Commun.* **8**, 415 (2017).
  20. Babacic, V. *et al.* Thickness-Dependent Elastic Softening of Few-Layer Free-Standing MoSe<sub>2</sub>. *Adv. Mater.* **33**, 2008614 (2021).
  21. Manou, P., Kalomiros, J. A., Anagnostopoulos, A. N. & Kambas, K. Optical properties of SnSe<sub>2</sub> single crystals. *Mater. Res. Bull.* **31**, 1407–1415 (1996).
  22. Saritha, K., Suryanarayana Reddy, A. & Ramakrishna Reddy, K. T. Investigation on Optical Properties of SnSe<sub>2</sub> Thin Films Synthesized by Two – Stage Process. *Mater. Today Proc.* **4**, 12512–12517 (2017).

## 4. Thermal transport in layered PtSe<sub>2</sub>

### 4.1 Introduction

Atomic thin layered semiconductors have received a lot of attention from the scientific community due to their extraordinary layer-dependent optical, electronic and thermal properties that open new prospects for the microelectronics industry.<sup>56</sup> Vertical devices, which consist of one or several atoms thick 2D material and whose heat transport is usually vertical, already perform well with diode,<sup>57</sup> photodetector,<sup>58</sup> transistors,<sup>59,60</sup> and solar cells.<sup>61</sup> In such devices, the thermal interface properties of atomically thin 2D materials vary widely depending on their thickness, the interaction between layers, and the degree of bonding to the substrate. Therefore, it is important to understand interplane heat transfer and phonon dynamics, especially for precious metal dichalcogenides such as PtSe<sub>2</sub>, as they are likely to be integrated into future high performance 2D devices.<sup>62–65</sup> PtSe<sub>2</sub> exhibits excellent and unique properties such as high charge carrier mobility at room temperature, 8 times higher than MoS<sub>2</sub>,<sup>66</sup> better air stability, and better oxidation resistance than black phosphorus.<sup>60</sup> In addition, PtSe<sub>2</sub> can grow at low temperatures, making it easy to integrate into practical devices.<sup>67</sup> With a widely adjustable bandgap<sup>68</sup> and layer-dependent semiconductor-semimetal transition behaviour,<sup>69</sup> it is considered a promising material for use in many electronic devices,<sup>60</sup> optoelectronic devices,<sup>62</sup> and thermoelectric devices.<sup>70</sup> Recently, band engineering with thickness modulation has been shown to increase the heat output of 2-layer PtSe<sub>2</sub> nanosheets by a factor of 50 compared with bulk PtSe<sub>2</sub>. In addition, the calculation results show that compressive or tensile stresses can induce a significantly improved n-type or p-type Seebeck coefficient in the single-layer PtSe<sub>2</sub>.<sup>71</sup> Despite the great potential of PtSe<sub>2</sub> in thermoelectric applications, there are few experimental studies of the unique thermal properties<sup>72</sup> and phonon dynamics of PtSe<sub>2</sub> films<sup>73</sup> and they are still limited. Accordingly, this task explores the phonon dynamics and thermal properties of supported crystalline and polycrystalline PtSe<sub>2</sub> thin films of various thicknesses (1-40 layers) grown by molecular beam epitaxy (MBE) on zinc oxide (ZnO) substrates. To do. First, a combination of low-frequency Raman and pump-probe coherent phonon spectroscopy was used to study the layer breathing mode (LBM) of



PtSe<sub>2</sub> thin films to extract effective out-of-plane elastic constants, layer-dependent sound velocity, and lifetime of acoustic phonons. Next, we focused on clarifying the effect of crystallinity and size on the thermal conductivity of PtSe<sub>2</sub> thin films supported across the plane, taking into account the interfacial thermal resistance of the multi-layer sample geometry. Finally, the first principle of the Boltzmann transport equation (BTE) was used to study thermal conductivity, and the density general function theory (DFT) was used to calculate the harmonic and non-harmonic constants of the PtSe<sub>2</sub> thin film. We will clarify the microscopic mechanism of heat transport in PtSe<sub>2</sub> thin film.

## 4.2 Material growth, structural characterization, and phonon dynamics

Two PtSe<sub>2</sub> wedges were grown under ultrahigh vacuum (base pressure in the low 10–10 mbar range) in an MBE chamber equipped with a cryo-panel and a reflection high energy electron diffraction (RHEED) setup. Each PtSe<sub>2</sub> monolayer consisted of three atomic sublayers, in which Pt atoms were sandwiched between Se atoms. For the crystalline PtSe<sub>2</sub> wedge, four monolayers of PtSe<sub>2</sub> were deposited by co-evaporating Pt and Se on the ZnO (0001) substrate kept at 450 °C. The resulting RHEED patterns were anisotropic with a 7° of mosaicity, demonstrating the good-crystalline character of the film, and the epitaxy relationship was found to be ZnO (0001)[100]/PtSe<sub>2</sub> (111) [100]. For the polycrystalline PtSe<sub>2</sub> wedge, a 2.4-Å-thick Pt film was first deposited by magnetron sputtering at room temperature and selenized it in the MBE chamber by deposition of Se at room temperature and subsequent annealing at 750 °C under Se flux. The magnetron sputtering reactor and the MBE chamber were connected under ultrahigh vacuum and PtSe<sub>2</sub> films were fully grown in situ. the equivalent PtSe<sub>2</sub> thickness was two monolayers (2 ML) after selenization. Two more PtSe<sub>2</sub> films were finally deposited by co-evaporating Pt and Se at 450 °C to obtain a 4 ML thick polycrystalline film. In a second step, the sample was covered with a motorized mechanical mask except for a thin 1.5-mm-large band at the edge to deposit 14 ML of PtSe<sub>2</sub> by co-evaporating Pt and Se at 450 °C. The mask was then retracted at a constant speed and stopped at 1mm from the edge to evaporate the 0–22 ML PtSe<sub>2</sub> wedge by co-evaporation at the same temperature. The films retained their respective crystalline and polycrystalline character at the end of the growth by checking RHEED.

Both samples were annealed at 750 °C for 10 min under Se flux after the growth to improve their crystalline quality. To avoid the film degradation during air transfer, a ~10-nm-thick amorphous Se layer was deposited on the sample at room temperature. The crystalline, acoustic, and morphological characterizations of the samples were studied by Raman spectroscopy, high-resolution scanning transmission electron microscopy (HR-STEM) measurements. The in-plane lattice constants were found to be  $a=b \approx 0.37$  nm and  $c \approx 0.52$  nm. Additionally, DFT calculations gave  $a=0.377$  nm and  $c=0.486$  nm. with  $a$  being in excellent agreement with our measurements.

Raman spectra of crystalline- and polycrystalline PtSe<sub>2</sub> films of different thicknesses was characterized. The high-frequency modes (170 – 210 cm<sup>-1</sup>) originated from in-plane and out-of-plane vibrations of Se atoms corresponding to E<sub>g</sub> (~180 cm<sup>-1</sup>) and A<sub>1g</sub> (~205 cm<sup>-1</sup>) modes, respectively. In addition, a weak interlayer longitudinal optical (LO) mode could also be observed at ~235 cm<sup>-1</sup>. Specifically, the vibrations detected here were related to the out of-plane displacements of the PtSe<sub>2</sub> layers known as layer breathing modes (LBM). The position of the LBM shifted to lower frequencies as the number of layers increased. For our system, we found  $C_{33} = 31.8 \pm 0.95$  GPa. Furthermore, the phonon dynamics of the crystalline PtSe<sub>2</sub> samples were measured by pump-probe coherent phonon spectroscopy using the asynchronous optical sampling method (ASOPS). The decay time of LBM was measured as a function of the number of layers and the calculated phonon decay due to boundary scattering contribution. Apart from the good agreement between the theory and the experimental data, we observed that the phonon lifetime was not affected by the group velocity (thickness-dependent or constant).

### 4.3 Thermal conductivity and interfacial heat transport measurements

Frequency domain thermo-reflectance (FDTR), a well-established optical pump-probe technique, capable of measuring heat transport in and across interfaces in PtSe<sub>2</sub> thin films. In our study, a customised set up using a reflected probe beam with a wavelength of 532 nm was aligned coaxially with the pump beam and focused with the pump spot to monitor the periodic fluctuations in reflectivity at the sample surface caused by the oscillating sample temperature. All the samples after the MBE growth

were coated with a 100 nm thick Au layer, which was chosen to maximize the coefficient of thermo-reflectance at the probe wavelength ( $\sim 2.36 \times 10^{-4} \text{ K}^{-1}$ ). A lock-in amplifier (Zurich Instruments HF2LI) was used to record the amplitude and phase response of the reflected probe beam to the thermal wave, and the phase lag between the pump and probe beam as the observable quantity. More details on the experimental setup can be found in the following paper.

The cross-plane thermal conductivity ( $k_z$ ) of the PtSe<sub>2</sub> thin films was subsequently extracted by following a multilayer three-dimensional (3D) heat diffusion model that includes the interface thermal conductance between the different layers and anisotropic heat transport.<sup>74</sup> For each experiment, we first quantified the sensitivity of the recorded phase signal to different parameters:  $k_z$ , the volumetric heat capacity ( $C$ ), the thermal conductivity anisotropy ratio ( $k_r/k_z$ ); and the different interface thermal conductance, in a similar manner to that of Schmidt et al.<sup>74</sup> A high-magnification 50x objective lens was used to produce a focused root mean square (rms) laser spot size ( $1/e^2$  radius) of approximately  $\sim 1.5 \mu\text{m}$ . To reduce the uncertainties associated with variations in the laser spot size between measurements on different films, the spot size was measured for each different experiment using the knife's edge method. All the room temperature measurements were performed under both ambient and vacuum conditions.

Before the thermal measurements on thin PtSe<sub>2</sub> films, we performed FDTR measurements on a bulk PtSe<sub>2</sub> crystal coated with 100 nm of Au in order to extract the anisotropy ratio of the thermal conductivities. The thermal conductivity of the deposited Au film was first measured using electrical conductivity. The volumetric specific heat of Au and PtSe<sub>2</sub> were taken from the literature.<sup>65,75</sup> This left us with three unknowns: the  $k_z$  and  $k_r$  of the bulk PtSe<sub>2</sub> crystal and the Au-PtSe<sub>2</sub> interface thermal conductance ( $G_{\text{Au-bulk}}$ ). The anisotropic ratio between  $k_r$  and  $k_z$  was extracted directly from the model fit of the experimental data in the low-frequency range (20 kHz–1 MHz) using a nonlinear least-squares routine. The observed anisotropy ratio of thermal conductivity in PtSe<sub>2</sub> was about 9 with  $k_z = 4.6 \pm 0.7 \text{ W/mK}$  and  $k_r = 41.4 \text{ W/mK}$ , which is similar to the anisotropic ratios of SnSe<sub>2</sub>,<sup>21,37</sup> InSe,<sup>76</sup> and armchair black phosphorous.<sup>77</sup> Our first principles BTE calculations gave  $k_z = 2.84 \text{ Wm}^{-1} \text{ K}^{-1}$  and  $k_r = 39.0 \text{ Wm}^{-1} \text{ K}^{-1}$ ,  $k_r$  was in agreement with the measurement.

We performed FDTR measurements in large-area crystalline and polycrystalline PtSe<sub>2</sub> films of different thicknesses (1–40 ML) on ZnO substrate for studying the impact of

crystallinity and film thickness on the  $k_z$  of PtSe<sub>2</sub> thin films. The thickness of Au and PtSe<sub>2</sub> films in the wedge sample stacks consist of Au/PtSe<sub>2</sub>/ZnO were measured by AFM and low-frequency Raman spectroscopy, respectively. The heat capacities of Au, ZnO, and PtSe<sub>2</sub> were taken from the literature.<sup>65,75,78</sup> Thus, the remaining unknown parameters were the  $k_z$  value of the PtSe<sub>2</sub> films,  $G_1$ (interface thermal conductance between Au and PtSe<sub>2</sub>), and  $G_2$  (interface thermal conductance between PtSe<sub>2</sub> and ZnO).  $k_z$  was estimated by fitting to experimental data in a low-frequency range (20 kHz-1 MHz), and  $G_1$  and  $G_2$  were estimated by fitting the data in a high-frequency range (1 – 20 MHz).

Note that in FDTR measurements of thin films, the diameter of the laser spot compared is usually large than the thermal diffusion length during the modulation of the pump beam. Thus, the heat flow is expected to be mainly one-dimensional in the cross-plane direction.<sup>79</sup> We used the anisotropy ratio extracted from the bulk PtSe<sub>2</sub> experiments. We extracted  $k_z$  value of crystalline and polycrystalline films as a function of thickness, which linear increase with the increasing thickness starting from 2.4 nm (4 ML) up to 10 and 24 nm, respectively. In polycrystalline films with thicknesses  $t > 12$  nm,  $k_z$  showed a plateau, and a maximum  $k_z$  reduction of ~35% was observed compared to the crystalline samples. The  $k_z$  for bulk PtSe<sub>2</sub> and thickness dependent values were obtained from first principles DFT-BTE calculations. We also performed Raman thermometry measurements in a few layers of crystalline PtSe<sub>2</sub> films (2, 3, and 4 layers of PtSe<sub>2</sub>), where we found  $k_z$  values in good agreement with the FDTR results. Next, the room temperature phonon MFP in the cross-plane direction of PtSe<sub>2</sub> was estimated through the data from the FDTR and ASOPS measurement. The  $\Lambda_z$  was about ~5 nm for a ten layers film. But the phonons with  $\Lambda_z > 24$  nm in crystalline PtSe<sub>2</sub> films substantially contribute to the thermal conductivity while in polycrystalline films grain boundary scattering reduces this value to ~12 nm. This is in close agreement with the DFT calculations.

More details are discussed in the following paper Article 2.

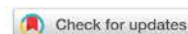
## 4.4 Conclusion

In summary, characterization techniques with a combination of FDTR, low-frequency Raman, and pump-probe coherent phonon spectroscopies, and state-of-the-heat DFT

calculations, were used to study the dynamic properties and heat transport of phonons in MBE-growth crystals and polycrystalline PtSe<sub>2</sub> thin films of various thicknesses (1-40 nm). Our work has shown the ability to quantify the effects of thickness and crystallinity on interplane heat transfer of PtSe<sub>2</sub> thin films. Our results show that the thermal conductivity was reduced by almost 35% with polycrystalline films thicker than 12 nm compared with crystals of the same thickness. Furthermore, from the phonon dynamics study of crystalline PtSe<sub>2</sub>, the out-of-plane elastic constant  $C_{33} = 31.8$  GPa and the layer-dependent group velocities in the range of 1340 ms<sup>-1</sup> for 2-layer to 1873 ms<sup>-1</sup> in 8 layers PtSe<sub>2</sub> were extracted. Finally, we showed that the lifetime of acoustic phonons in PtSe<sub>2</sub> thin films, which are the main thermal carriers of heat in semiconductors, was as short as picoseconds. Our results provide new insights into the heat transport and phonon dynamics of nanoscale layered materials for future design of 2D-based devices for energy harvesting and effective heat dissipation of thermoelectric and optoelectronic devices.

# Article 2

## ARTICLE OPEN

Effect of crystallinity and thickness on thermal transport in layered PtSe<sub>2</sub>

Alexandros El Sachat<sup>1</sup>, Peng Xiao<sup>1,2</sup>, Davide Donadio<sup>3</sup>, Frédéric Bonell<sup>4</sup>, Marianna Sledzinska<sup>5</sup>, Alain Marty<sup>4</sup>, Céline Vergnaud<sup>4</sup>, Hervé Boukari<sup>4</sup>, Matthieu Jamet<sup>4</sup>, Guillermo Arregui<sup>1</sup>, Zekun Chen<sup>3</sup>, Francesc Alzina<sup>1</sup>, Clivia M. Sotomayor Torres<sup>1,5</sup> and Emigdio Chavez-Angel<sup>1</sup>

We present a comparative investigation of the influence of crystallinity and film thickness on the acoustic and thermal properties of layered PtSe<sub>2</sub> films of varying thickness (1–40 layers) using frequency-domain thermo-reflectance, low-frequency Raman, and pump-probe coherent phonon spectroscopy. We find ballistic cross-plane heat transport up to ~30 layers PtSe<sub>2</sub> and a 35% reduction in the cross-plane thermal conductivity of polycrystalline films with thickness larger than 20 layers compared to the crystalline films of the same thickness. First-principles calculations further reveal a high degree of thermal conductivity anisotropy and a remarkable large contribution of the optical phonons to the thermal conductivity in bulk (~20%) and thin PtSe<sub>2</sub> films (~30%). Moreover, we show strong interlayer interactions in PtSe<sub>2</sub>, short acoustic phonon lifetimes in the range of picoseconds, an out-of-plane elastic constant of 31.8 GPa, and a layer-dependent group velocity ranging from 1340 ms<sup>-1</sup> in bilayer to 1873 ms<sup>-1</sup> in eight layers of PtSe<sub>2</sub>. The potential of tuning the lattice thermal conductivity of layered materials with the level of crystallinity and the real-time observation of coherent phonon dynamics open a new playground for research in 2D thermoelectric devices and provides guidelines for thermal management in 2D electronics.

npj 2D Materials and Applications (2022)6:32; <https://doi.org/10.1038/s41699-022-00311-x>

## INTRODUCTION

Atomically-thin 2D semiconductors have attracted immense attention in the scientific community due to their exceptional layer-dependent optical, electronic, and thermal properties that open new prospects in the microelectronics industry<sup>1</sup>. Vertical devices consisting of one- or few-atom thick 2D materials, where heat transport usually occurs in the vertical direction, have already shown excellent performance in diodes<sup>2</sup>, photodetectors<sup>3</sup>, transistors<sup>4,5</sup>, and solar cells<sup>6</sup>. In such devices, the interfacial thermal properties of atomically-thin layered 2D materials significantly vary depending on their thickness, interlayer interactions, and degree of bonding with the substrate. It is therefore essential to understand cross-plane thermal transport and phonon dynamics, particularly in noble metal dichalcogenides, like PtSe<sub>2</sub>, due to their large potential for integration in future high-performance 2D devices<sup>7–10</sup>.

PtSe<sub>2</sub> exhibits outstanding inherent properties, including high carrier mobility at room temperature, which is eight times larger than MoS<sub>2</sub><sup>11</sup>, excellent stability to air, and resistance to oxidation, better than black phosphorus<sup>5</sup>. Moreover, PtSe<sub>2</sub> can be easily integrated into practical devices since it can be grown at low temperatures<sup>12</sup>. Together with its widely tunable bandgap<sup>13</sup> and layer-dependent semiconductor-to-semimetal transition behavior<sup>14</sup>, it is considered a promising material to be employed in many electronic<sup>5</sup>, optoelectronic<sup>7</sup> and thermoelectric devices<sup>15</sup>. For instance, Moon et al.<sup>15</sup> have recently shown that band engineering by thickness modulation leads to a 50-fold enhancement of the thermopower in bilayer PtSe<sub>2</sub> nanosheets with respect to bulk PtSe<sub>2</sub>. Moreover, calculated results have shown that in monolayer PtSe<sub>2</sub> compressive or tensile strain can induce significantly enhanced n- or p-type Seebeck coefficients<sup>16</sup>. Despite the large

potential of PtSe<sub>2</sub> in thermoelectric applications, experimental studies of the intrinsic thermal properties<sup>17</sup> and phonon dynamics of PtSe<sub>2</sub><sup>18</sup> films are few and still limited.

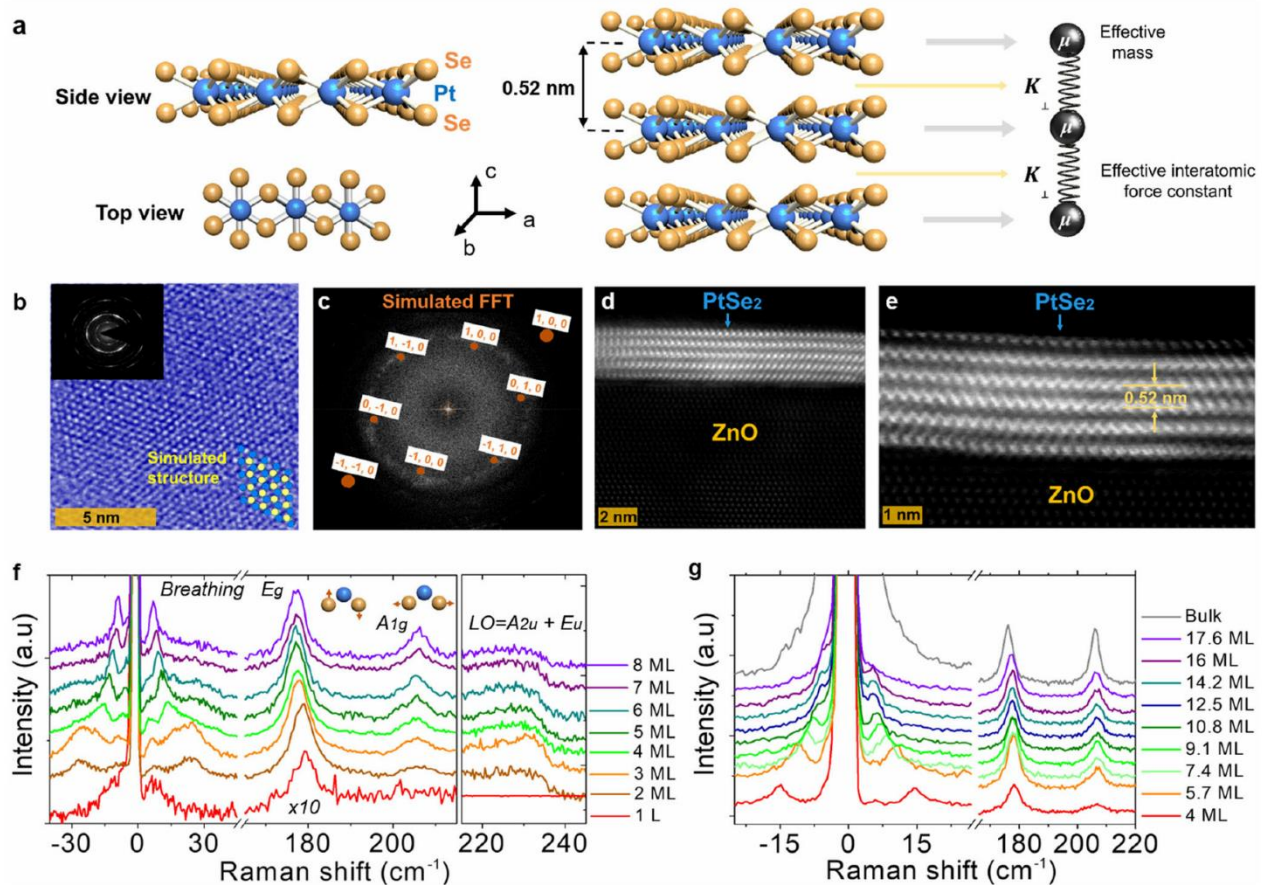
In this work, we study the phonon dynamics and thermal properties of supported crystalline and polycrystalline PtSe<sub>2</sub> thin films of varying thickness (1 to 40 layers), which were grown by molecular beam epitaxy (MBE) on zinc oxide (ZnO) substrates. First, by using a combination of low-frequency Raman and pump-probe coherent phonon spectroscopies we investigate the layer-breathing modes (LBM) in PtSe<sub>2</sub> thin films and extract an effective out-of-plane elastic constant, a layer-dependent sound velocity, and the acoustic phonon lifetimes. Then, we focus on unraveling the impact of crystallinity and size effects on the cross-plane thermal conductivity of supported PtSe<sub>2</sub> thin films taking into account the interfacial thermal resistances in our multilayer sample geometry. Finally, we investigate the thermal conductivity by the first-principles Boltzmann transport equation (BTE) computing the harmonic and anharmonic force constants by density functional theory (DFT) to reveal the microscopic mechanism of heat transport in PtSe<sub>2</sub> thin films.

## RESULTS AND DISCUSSION

## Material growth, structural characterization, and phonon dynamics

Two PtSe<sub>2</sub> wedges were grown under ultrahigh vacuum (base pressure in the low 10<sup>-10</sup> mbar range) in an MBE chamber equipped with a cryo-panel and a reflection high energy electron diffraction (RHEED) setup. For the crystalline PtSe<sub>2</sub> wedge, four monolayers of PtSe<sub>2</sub> were deposited by co-evaporating Pt and Se on the ZnO (0001) substrate kept at 450 °C. The resulting RHEED

<sup>1</sup>Catalan Institute of Nanoscience and Nanotechnology (ICN2), CSIC and BIST, Campus UAB, Bellaterra 08193 Barcelona, Spain. <sup>2</sup>Departamento de Física, Universidad Autónoma de Barcelona, Bellaterra 08193 Barcelona, Spain. <sup>3</sup>Department of Chemistry, University of California, Davis, CA 95616, United States. <sup>4</sup>Université Grenoble Alpes, CNRS, CEA, Grenoble INP, IRIG-Spintec, 38054 Grenoble, France. <sup>5</sup>ICREA, Passeig Lluís Companys 23, 08010 Barcelona, Spain. <sup>✉</sup>email: alexandros.elsachat@icn2.cat; emigdio.chavez@icn2.cat



**Fig. 1** Structural characterization and low-frequency Raman spectroscopy of  $\text{PtSe}_2$ . **a** Side and top views of the  $\text{PtSe}_2$  crystal structure (left), schematics of the side view of a trilayer  $\text{PtSe}_2$  crystal structure (middle), and the one-dimensional linear atomic chain model (right). The blue and orange spheres represent Pt and Se atoms, respectively. **b** HR-STEM images of a 5 ML crystalline  $\text{PtSe}_2$  film and **c** the Fast Fourier transform of the respective image, from which we extract the  $a$  and  $b$  lattice constants,  $a = b \approx 0.37$  nm. **d, e** Cross-sectional TEM images of the as-grown 3 nm (5 ML)  $\text{PtSe}_2$  film, from which we extract the  $c$ -lattice constant,  $c \approx 0.52$  nm. The  $\text{PtSe}_2$  is layered and each layer is parallel to the underlying ZnO substrate. Thickness-dependent Raman spectra of **f** crystalline and **g** polycrystalline  $\text{PtSe}_2$  films deposited on ZnO. The inset in **(f)** shows blue and orange spheres that represent Pt and Se atoms, respectively and arrows that point to the direction of the movement of that layer.

patterns were anisotropic with a  $7^\circ$  of mosaicity (see Supplementary Fig. 1), demonstrating the good-crystalline character of the film, and the epitaxy relationship was found to be ZnO (0001) [100]/ $\text{PtSe}_2$  (111) [100]. Additional characterization of epitaxial ZnO/ $\text{PtSe}_2$  is reported in reference <sup>11</sup>. For the polycrystalline  $\text{PtSe}_2$  wedge, we first deposited a 2.4-Å-thick Pt film by magnetron sputtering at room temperature and selenized it in the MBE chamber by deposition of Se at room temperature and subsequent annealing at 750 °C under Se flux. The magnetron sputtering reactor and the MBE chamber are being connected under ultrahigh vacuum and  $\text{PtSe}_2$  films are fully grown in situ. After selenization, the equivalent  $\text{PtSe}_2$  thickness was two monolayers (2 ML). The RHEED patterns were streaky but isotropic, showing the in-plane polycrystalline character of the film, with a well-defined (0001) surface for all grains but random in-plane crystal orientation. Two more  $\text{PtSe}_2$  films were finally deposited by co-evaporating Pt and Se at 450 °C to obtain a 4 ML thick polycrystalline film (see Supplementary Fig. 1c).

In a second step, we covered the sample with a motorized mechanical mask except for a thin 1.5-mm-large band at the edge to deposit 14 ML of  $\text{PtSe}_2$  by co-evaporating Pt and Se at 450 °C. The mask was then retracted at a constant speed and stopped at 1 mm from the edge to evaporate the 0–22 ML  $\text{PtSe}_2$  wedge by

co-evaporation at the same temperature. We checked by RHEED that the films retained their respective crystalline and polycrystalline character at the end of the growth. The final structure is shown in Supplementary Fig. 1d. Each  $\text{PtSe}_2$  monolayer consists of three atomic sublayers, in which Pt atoms are sandwiched between Se atoms (see Fig. 1a). Both samples were annealed at 750 °C for 10 min under Se flux after the growth in order to improve their crystalline quality. To avoid the film degradation during air transfer, the films were capped by a  $\sim 10$ -nm-thick amorphous Se layer deposited at room temperature.

The crystalline, acoustic and morphological characterizations of the samples were studied by Raman spectroscopy and high-resolution scanning transmission electron microscopy (HR-STEM) measurements. The arrangements of Pt and Se atoms in the planar HR-STEM image (Fig. 1b) and the symmetric diffraction pattern in the fast Fourier transform (FFT) image (Fig. 1c) further support the good crystal structure nature of the films. In addition, the high-magnification cross-sectional HR-STEM images (Fig. 1d, e) show the layered hexagonal honeycomb structure of a five layers  $\text{PtSe}_2$  film, where bright Pt atoms are surrounded by six lighter colored Se atoms. The in-plane and out-of-plane lattice parameters were obtained from the  $(l\ 0\ 0)$  and  $(l\ m\ 0)$  planes of the FFT and image analysis of cross-plane sections of the film (see Fig. 1e), respectively.



The in-plane lattice constants were found to be  $a = b \approx 0.37$  nm and  $c \approx 0.52$  nm in good agreement with previous studies<sup>10,15,19</sup> and in excellent agreement with the ones deduced from our x-ray diffraction measurements (see Supplementary Fig. 2). On the other hand, DFT calculations give  $a = 0.377$  nm and  $c = 0.486$  nm. Whereas  $a$  is in excellent agreement with our measurements,  $c$  is significantly underestimated (6.5%). There may be multiple reasons for this discrepancy, among which the difficulty in the DFT calculations to simulate PtSe<sub>2</sub> and PtSe compounds for all the GGA exchange functionals (e.g., PBEsol, AM05)<sup>20</sup> and even van der Waals functionals (e.g., vdW-DF-C09 and vdW-DF-CX)<sup>21</sup>.

The layered PtSe<sub>2</sub> adopts a T-type hexagonal crystal structure, belonging to the  $P3m1$  space group with a  $D_{3d}$  (-m) point group. The primitive PtSe<sub>2</sub> cell contains 3 atoms, then its vibrational spectrum includes nine modes: three acoustic ( $A_{2u} + E_u$ ) and six optical ( $A_{1g} + E_g + 2A_{2u} + 2E_u$ ). The optical modes can be classified as Raman active ( $E_g$ ,  $A_{1g}$  and LO ( $A_{2u} + E_u$ )) and infrared active ( $2E_u + 2A_u$ ) modes<sup>22</sup>. Fig. 1f, g show the Raman spectra of crystalline- and polycrystalline PtSe<sub>2</sub> films of different thicknesses, respectively. The high-frequency modes (170–210 cm<sup>-1</sup>) are originated from in-plane and out-of-plane vibrations of Se atoms corresponding to  $E_g$  (~180 cm<sup>-1</sup>) and  $A_{1g}$  (~205 cm<sup>-1</sup>) modes, respectively. In addition, a weak interlayer longitudinal optical (LO) mode can be also observed at ~235 cm<sup>-1</sup>. LO is generated by a combination of the in-plane  $E_u$  and out-of-plane  $A_{2u}$  modes from the vibrations of Pt and Se atoms in the opposite phases. The Raman peaks located in the low-frequency regions (–30 to 30 cm<sup>-1</sup>) correspond to interlayer vibrations of PtSe<sub>2</sub> planes<sup>5,18</sup>.

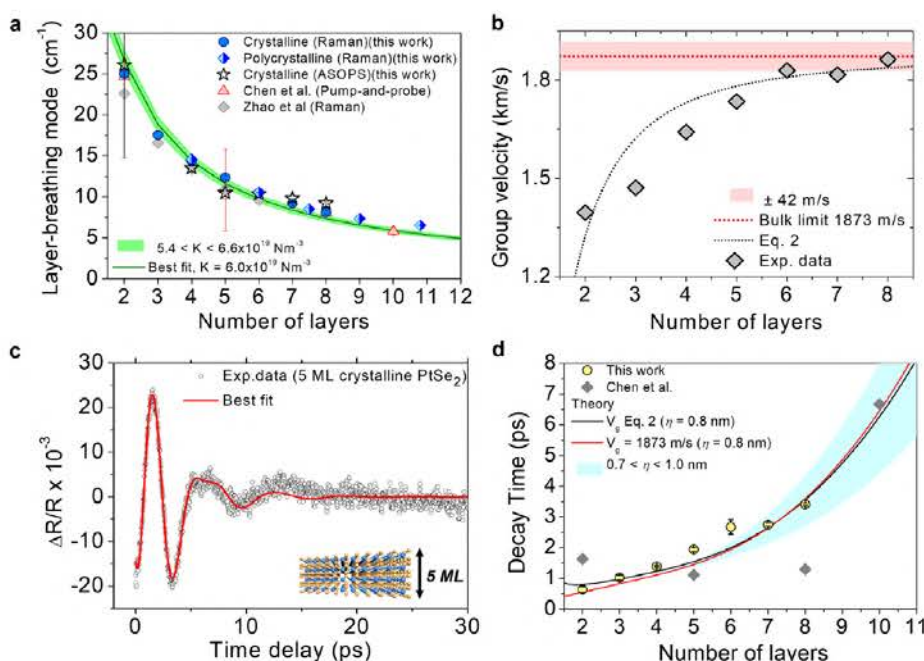
Specifically, the vibrations detected here are related to the out-of-plane displacements of the PtSe<sub>2</sub> layers known as layer-breathing modes (LBM). As shown in Fig. 1f, g, the position of the LBM shifts to lower frequencies as the number of layers increases. The thickness-dependence can be simulated by using a one-dimensional linear atomic chain model<sup>23</sup>. This model considers each PtSe<sub>2</sub> layer as a large atom with an effective mass

per unit area  $\mu = 4.8 \times 10^{-6}$  kg m<sup>-2</sup> connected by a string with an effective interlayer breathing force constant (IBFC) per unit area  $K_{\perp}$  and separated by a distance  $d \approx 0.52$  nm given by the interatomic distance between layers (see Fig. 1a). The solution of the linear chain with vanishing stress as a boundary condition on the free surface is given by:

$$f = \sqrt{\frac{K_{\perp}}{\mu m^2}} \sin\left(\frac{q_{N,j}}{2} d\right) \quad (1)$$

where  $f$  is the vibrational frequency of the mode,  $q_{N,j} = 2\pi/\lambda_{N,j}$  is the acoustic wavevector,  $\lambda_{N,j} = 2Nd/j$  is the phonon wavelength,  $N$  is the number of layers ( $N = 2, 3, \dots$ ) and  $j$  is the index of the acoustic mode ( $j = 1, 2, 3, \dots$ ). The experimental and the fitted thickness-dependence of the first LBM ( $j = 1$ ) is shown in Fig. 2a. The fitted curve was obtained using the IBFC adjustable variable, which is determined to be  $K_{\perp} = 6.0 \pm 0.14 \times 10^{19}$  N m<sup>-3</sup>. A similar value was also obtained by Chen et al.<sup>18</sup> with  $K_{\perp} = 6.2 \times 10^{19}$  N m<sup>-3</sup> using the same approach. Now, if we multiply the IBFC by the interlayer distance, we can also derive the corresponding  $C_{33}$  component of the elastic constant tensor<sup>24,25</sup>.

For our system, we found  $C_{33} = 31.8 \pm 0.95$  GPa, which is in the same range as other 2D materials e.g., 38.7–36.5 GPa for graphite, 54.3 GPa for MoSe<sub>2</sub><sup>26</sup>, 24.5 GPa for h-BN<sup>27</sup>, 52 GPa and 52.1 GPa for MoS<sub>2</sub> and WSe<sub>2</sub>, respectively<sup>25</sup>. It is interesting to notice that the polycrystalline films also follow the same trend as the crystalline samples (see Fig. 2a) thus most likely the granular characteristics of the sample do not affect significantly the interlayers forces. Likewise, it is also possible to obtain the  $C_{44}$  constant using the effective interlayer shear force constant ( $K_{//}$ ). Chen et al.<sup>18</sup> calculated  $K_{//} = 4.6 \times 10^{19}$  N m<sup>-3</sup> for PtSe<sub>2</sub> based on density functional theory simulations from Zhao<sup>5</sup>, giving  $C_{44} = 23$  GPa and  $v_{TA} = 1553$  ms<sup>-1</sup>. In addition, from Eq. (1), it is also possible to



**Fig. 2 Phonon dynamics in PtSe<sub>2</sub>.** **a** Peak position of the first order breathing mode measured in crystalline and polycrystalline PtSe<sub>2</sub> films using low-frequency Raman spectroscopy and ASOPS as a function of the number of layers and comparison with other experimental works. **b** Calculated group velocity as a function of the number of layers. **c** Representative transmission signal obtained with ASOPS in 5 ML PtSe<sub>2</sub> (black open circles) and the best fit (red line). **d** The extracted phonon decay time (yellow dots) vs the number of layers. The red and black curves are theoretical predictions of the phonon lifetimes based on the model proposed by Ziman<sup>30</sup>. The region displayed with light blue shows the impact of roughness in the calculated lifetimes. The gray data points show phonon lifetimes measured by Chen et al.<sup>18</sup>.

extract the group velocity considering that  $v_g = d(2\pi f)/dq$ .

$$v_g = d \sqrt{\frac{K}{\mu}} \cos\left(\frac{\pi j}{2N}\right) \quad (2)$$

In the limit  $N \rightarrow \infty$  and considering the experimental interlayer distance  $d \approx 0.52 \pm 0.01$  nm, Eq. (2) gives the bulk limit for the cross-plane longitudinal velocity  $v_{LA} = 1873 \pm 42$  m s<sup>-1</sup>. A similar value can be obtained using an approximation of  $v_g = \sqrt{\frac{C_{33}}{\rho}} = 1825 \pm 28$  m s<sup>-1</sup> where  $\rho = 9540$  kg m<sup>-3</sup> is the density of PtSe<sub>2</sub> and  $C_{33} = 31.8$  GPa. Using a numerical differentiation, it is also possible to extract the group velocity as a function of the number of layers as shown in Fig. 2b.

Furthermore, the phonon dynamics of the crystalline PtSe<sub>2</sub> samples were measured by pump-probe coherent phonon spectroscopy using the asynchronous optical sampling method (ASOPS)<sup>28,29</sup> (see details in Methods). Figure 2c shows the typical modulation of the reflectivity ( $\Delta R/R$ ) as a function of the time delay (black open circles) and the corresponding best model fit in a 5 ML PtSe<sub>2</sub> crystalline film. The change of reflectivity includes the effects of a fast and slow electronic relaxation process as well as the dynamics of the generated phonons. The time traces are fitted to a damped harmonic oscillator of the form:<sup>18</sup>

$$\Delta R/R = \sum_{i=1}^2 A_i \exp\left(-\frac{t}{\tau_i}\right) + \sum_{j=1}^2 B_j \exp\left(-\frac{t}{\tau_j}\right) \sin(2\pi f_j t + \phi_j) \quad (3)$$

where  $t$  is the time delay between the pump and the probe lasers,  $A$  and  $B$  are the amplitudes,  $\tau_i$  are the decay times,  $f$  the phonon frequency, and  $\phi$  is a phase delay. The first term of Eq. (3) represents the fast and slow relaxation processes of the excited carriers. The second term describes the damped phonon oscillations. The Fast Fourier transforms (FFT) of the

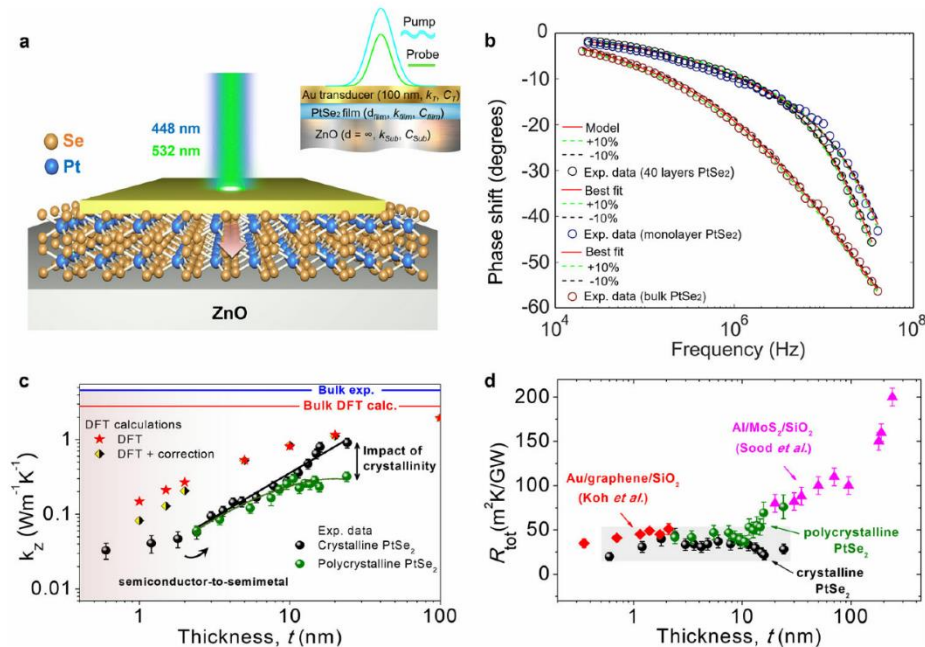
time-domain data for all measured samples are displayed in the Supplementary.

Figure 2d shows the measured decay time of LBM as a function of the number of layers (yellow dots) and the calculated phonon decay due to boundary scattering contribution based on the model proposed by Ziman<sup>30</sup>. This model considers the impact of the roughness ( $\eta$ ) of the film surface through a phenomenological parameter  $p = \exp[-16\pi^2\eta^2/\lambda^2]$ , which modifies the effective mean free path  $\Lambda = (1+p)/(1-p) Nd/v_g$  of the acoustic waves. The black and red curves of Fig. 2d were calculated using a thickness-dependent group velocity (Eq. (2)) and a constant value given by the bulk limit (1873 m s<sup>-1</sup>), respectively, with a constant  $\eta = 0.82$  nm as measured by AFM (see Supplementary Fig. 3).

Apart from the good agreement between the theory and the experimental data, we observe that the phonon lifetime is not affected by the group velocity (thickness-dependent or constant). Similar observations of boundary-limited lifetimes have been reported in suspended MoSe<sub>2</sub> flakes by Soubelet et al.<sup>26</sup>. They measured lifetimes of the order of ~1–41 ps in 2–8 ML limited by boundary effects. While in thicker samples (>20 ML), they observed longer lifetimes (~0.3–10 ns) limited by phonon-phonon scattering. The large difference in lifetimes measured here (1–4 ps) is mainly attributed to the difference in the phonon group velocity which is 1.4 to 1.5 times smaller than MoSe<sub>2</sub>.

### Thermal conductivity and interfacial heat transport measurements

For the thermal measurements, we used a custom-built frequency-domain thermo-reflectance (FDTR) setup, a well-established optical pump-probe technique, capable of measuring heat transport in thin films and across interfaces<sup>31–36</sup>. A schematic representation of the experimental setup is shown in Fig. 3a.



**Fig. 3 Thermal conductivity and interfacial heat transport measurements.** **a** Schematic illustrations of the FDTR technique and the multilayer system. **b** Typical FDTR data measured in bulk PtSe<sub>2</sub> (red circles), 40 layers (black circles), and monolayer (blue circles) crystalline PtSe<sub>2</sub> films and the corresponding best model fits in the whole frequency range. **c** Cross-plane thermal conductivity  $k_z$  of crystalline (black spheres) and polycrystalline (green spheres) PtSe<sub>2</sub> films versus film thickness  $t$ . The uncertainty of the estimated  $k_z$  was calculated based on error propagation for the input parameters. The blue and red lines in (a) display the bulk cross-plane thermal conductivity values obtained by FDTR and DFT calculations, respectively. The black and green curves are a guide for the eye. **d** Total thermal resistance,  $R_{\text{total}} = R_{\text{int}} + R_{\text{PtSe}_2}$ , of crystalline (black spheres) and polycrystalline (green spheres) PtSe<sub>2</sub> thin films, plotted versus film thickness  $t$ . The uncertainty region is displayed as a gray rectangle. The total cross-plane thermal resistance measurements of Au/graphene/SiO<sub>2</sub><sup>47</sup> (red diamonds) and Al/MoS<sub>2</sub>/SiO<sub>2</sub><sup>41</sup> (purple triangles) interfaces are also reported.

A modulated pump beam with a wavelength of 448 nm is focused onto the sample, creating a periodic heat flux with a Gaussian spatial distribution on the sample surface. A reflected probe beam with a wavelength of 532 nm is aligned coaxially with the pump beam and focused with the pump spot to monitor the periodic fluctuations in reflectivity at the sample surface caused by the oscillating sample temperature. All the samples after the MBE growth were coated with a 100 nm thick Au layer, which was chosen to maximize the coefficient of thermo-reflectance at the probe wavelength ( $\sim 2.36 \times 10^{-4} \text{ K}^{-1}$ ). We used a lock-in amplifier (Zurich Instruments HF2LI) to record the amplitude and phase response of the reflected probe beam to the thermal wave, and the phase lag between the pump and probe beam as the observable quantity. More details on the experimental setup can be found elsewhere<sup>35</sup>.

In the present experiments, we obtained frequency-domain measurements by varying the modulation frequency of the pump beam over a wide range (20 kHz–40 MHz). The cross-plane thermal conductivity ( $k_z$ ) of the PtSe<sub>2</sub> thin films was subsequently extracted by following a multilayer three-dimensional (3D) heat diffusion model that includes the interface thermal conductance between the different layers and anisotropic heat transport<sup>31</sup>. For each experiment, we quantified first the sensitivity of the recorded phase signal to different parameters:  $k_z$ , the volumetric heat capacity ( $C$ ), the thermal conductivity anisotropy ratio ( $k_r/k_z$ ), and the different interface thermal conductances, in a similar manner to that of Schmidt et al.<sup>31</sup>. The details about the measurement sensitivity to different combinations of parameters in the model can be found in Supplementary Fig. 4. In all the experiments we used a high-magnification 50× objective lens that produced a focused root mean square (rms) spot size ( $1/e^2$  radius) of approximately  $\sim 1.5 \mu\text{m}$ . To reduce the uncertainties associated with variations in the laser spot size between measurements on different films, the spot size was measured for each different experiment using the knife's edge method, as shown in Supplementary Fig. 6. All the room temperature measurements were performed under both ambient and vacuum conditions.

Before the thermal measurements on thin PtSe<sub>2</sub> films, we performed FDTR measurements on a bulk PtSe<sub>2</sub> crystal coated with 100 nm of Au in order to extract the anisotropy ratio of the thermal conductivities. The thermal conductivity of the deposited Au film was first measured using electrical conductivity and the Wiedemann–Franz law,  $k_{\text{Au}} = 195 \text{ W m}^{-1} \text{ K}^{-1}$  (see details in Supplementary Fig. 7). The volumetric specific heat of Au and PtSe<sub>2</sub> were taken from literature<sup>10,36</sup>. This leaves us with three unknowns: the cross-plane and in-plane thermal conductivity of the bulk PtSe<sub>2</sub> crystal and the Au–PtSe<sub>2</sub> interface thermal conductance ( $G_{\text{Au-bulk}}$ ). The in-plane thermal conductivity was expressed in terms of the anisotropic ratio ( $\alpha$ ) and the cross-plane thermal conductivity  $k_r = \alpha \cdot k_z$ .

However, from the sensitivity analysis, we found that the recorded phase signal has low sensitivity to  $G_{\text{Au-bulk}}$  and only at high frequencies while its sensitivity to the anisotropic heat flow is high in almost the whole frequency range (see Supplementary Fig. 5). This allowed us to extract  $\alpha$  directly from the model fit of the experimental data in the low-frequency range (20 kHz–1 MHz) using a nonlinear least-squares routine, which requires an initial guess to determine the value of the free parameter ( $k_z$ ) (see Supplementary Fig. 11). The inset in Supplementary Fig. 11 shows the numerical errors of the applied model fits as a function of different anisotropy ratios. The minimum value of the fitting error, which gives us the best fit of the FDTR data, corresponds to  $\alpha = 9$ ,  $k_z = 4.6 \pm 0.7 \text{ W m}^{-1} \text{ K}^{-1}$  and  $k_r \approx 41.4 \text{ W m}^{-1} \text{ K}^{-1}$ .

The observed anisotropy ratio between  $k_r$  and  $k_z$  in PtSe<sub>2</sub> is similar to previously reported values of other 2D-layered materials, such as InSe ( $\alpha \sim 10$ )<sup>37</sup>, SnSe<sub>2</sub> ( $\alpha \sim 7$ – $8$ )<sup>35,38</sup>, and armchair black phosphorous ( $\alpha \sim 6$ – $10$ )<sup>39</sup>. Our first-principles BTE calculations give  $k_z = 2.84 \text{ W m}^{-1} \text{ K}^{-1}$  and  $k_r = 39.0 \text{ W m}^{-1} \text{ K}^{-1}$ .  $k_r$  is in excellent

agreement with the measurement, while  $k_z$  is significantly overestimated, possibly due to the discrepancy in the equilibrium  $c$  lattice parameter mentioned above. Nevertheless, we can still use DFT and BTE to analyse the phonon contributions to cross-plane transport in PtSe<sub>2</sub> bulk and the effect of finite thickness in thin films, at least qualitatively.

To study the impact of crystallinity and film thickness on the cross-plane thermal conductivity of PtSe<sub>2</sub> thin films, we performed FDTR measurements in large-area crystalline and polycrystalline PtSe<sub>2</sub> films of different thicknesses (1–40 ML) on ZnO substrate. The wedge sample stacks consist of Au/PtSe<sub>2</sub>/ZnO (see Fig. 3a and Supplementary Fig. 1). Typical examples of the recorded phase signals and the corresponding best model fit for bulk, monolayer, and 40 ML crystalline PtSe<sub>2</sub> are shown in Fig. 3b. Here, the key parameters for the model in our multilayer system are the spot sizes of the pump and probe beams,  $k_z$ , the film thickness  $t$ , the  $C$  of each layer, and the interface thermal conductance (between Au and PtSe<sub>2</sub>,  $G_1$ , and between PtSe<sub>2</sub> and ZnO,  $G_2$ ). The thickness of Au and PtSe<sub>2</sub> films were measured by AFM and low-frequency Raman spectroscopy, respectively (see section above and Supplementary). The heat capacities of Au, ZnO, and PtSe<sub>2</sub> were taken from the literature<sup>10,36,40</sup>. Thus, the remaining unknown parameters were the  $k_z$  value of the PtSe<sub>2</sub> films,  $G_1$  and  $G_2$ .

To extract a unique value of  $k_z$  from a single measurement we followed a fitting approach similar to that suggested in the previous works<sup>31,32,35</sup> and supported by our sensitivity analysis (see Supplementary Fig. 4). First, we estimate  $k_z$  by fitting to experimental data in a low-frequency range (20 kHz–1 MHz), where the measurement sensitivity to the  $G_1$ ,  $G_2$ , and heat capacity of the films is negligible. Then, we fix  $k_z$  and fit experimental data in a high-frequency range (1–40 MHz) to estimate simultaneously  $G_1$  and  $G_2$ . As an initial guess to determine the value of the free parameters ( $k_z$ ,  $G_1$ , and  $G_2$ ) we used previously reported values of similar material systems<sup>41–43</sup>. We also verified that the final fit results are not sensitive to the choice of initial values. The same analysis has been followed to extract  $k_z$ ,  $G_1$ , and  $G_2$  values for all the PtSe<sub>2</sub> films.

In Supplementary Fig. 13 we show all the interface thermal resistance measurements,  $R_1 = 1/G_1$ ,  $R_2 = 1/G_2$ , and  $R_{\text{int}} = R_1 + R_2$ , extracted by the FDTR experiments. The observed variation of  $R_{\text{int}}$  might be attributed to differences in the interface characteristics of Au (transducer)/PtSe<sub>2</sub> and PtSe<sub>2</sub>/ZnO (substrate), which could result in different interfacial energy coupling. The apparent increase of  $R_2$  with increasing film thickness most likely is due to the reduced mechanical coupling of the films to the underlying ZnO resulting from a potential increase in sample stiffness or changes in the vibrational spectra<sup>44</sup>. However, we note that most of the extracted values are within the experimental uncertainty, thus it is not clear if there is a systematic increase of  $R_2$  with thickness. Similarly, a weak thickness-dependent thermal resistance trend has been measured in InSe, MoS<sub>2</sub>, and SnSe<sub>2</sub> thin films<sup>35,37,41</sup>.

It is interesting to note that, in contrast to the bulk case, in FDTR measurements in thin films, the diameter of the laser spot is usually large compared to the thermal diffusion length during the modulation period of the pump beam. Thus, the heat flow is expected to be mainly one-dimensional in the cross-plane direction<sup>32</sup>. This has been confirmed by our sensitivity analysis, where we found that the sensitivity of the recorded phase signal to the in-plane transport is relatively low (see Supplementary Fig. 4c). Therefore, since anisotropic differences in thermal conductivities as a function of the film thickness cannot be resolved, for the data analysis we used the anisotropy ratio extracted from the bulk PtSe<sub>2</sub> experiments. The dependence of the thermal anisotropy with the film thickness has been studied recently in similar material systems, such as supported InSe<sup>37</sup> and SnSe<sub>2</sub><sup>35</sup> films, showing a thickness-independent  $\alpha$  of 10 and 8.4, respectively.

Figure 3c displays the extracted  $k_z$  value of all the PtSe<sub>2</sub> thin films as a function of thickness. In both crystalline (black data points) and polycrystalline films (green data points), we observe a linear increase of  $k_z$  with increasing the film thickness starting from 2.4 nm (4 ML) up to 10 and 24 nm, respectively. In polycrystalline films with thicknesses  $t > 12$  nm,  $k_z$  shows a plateau, and a maximum cross-plane thermal conductivity reduction of ~35% was observed compared to the crystalline samples. This result highlights the strong impact of crystallinity on  $k_z$  and suggests that depending on the film crystallinity phonons with different mean free paths (MFPs) contribute to  $k_z$ . In crystalline PtSe<sub>2</sub> films, heat is propagating through coherent vibrations (phonon modes) that travel distances at least 24 nm (~40 ML) while in polycrystalline samples, they start to decay above 12 nm (~20 ML). This behavior most likely is attributed to the enhanced phonon scattering due to the presence of high-density defective grain boundaries randomly oriented in the polycrystalline film. XRD measurements on polycrystalline films provided in Supplementary Fig. 12 confirmed the random orientation of the grains. On the contrary, as the film thickness becomes thinner ( $t < 12$  nm), thermal phonons (especially long-wavelength phonons) are not strongly scattered by the reduced number of grain boundaries available within the volume of the materials, and both crystalline and polycrystalline films show similar  $k_z$  values.

In Fig. 3c, we also show the  $k_z$  obtained from first-principles DFT-BTE calculations, both, for bulk PtSe<sub>2</sub> and thickness-dependent values as two different sets of data. The first set accounts solely for the finite thickness of the film and gives an overall much larger thermal conductivity than the measured one at the corresponding thickness (red data points). The overestimation of the calculated thermal conductivity for the whole thickness range can be related to the underestimation of the  $c$ -axis compared with the experimental data and the assumption of a perfect single-crystal structure of the films. In addition,  $G_1$  and  $G_2$  were not taken into account in the DFT calculations, which further explains the overestimated values in the calculated thickness-dependence of  $k_z$ . However, we observe that the trend of thickness-dependent of the thermal conductivity is preserved. Finally, correcting the BTE calculation for the observed thickness-dependent reduction of sound velocity provides a better agreement between theory and experiments over the whole range of thickness considered (yellow-black diamonds).

The observed linear dependence of  $k_z$  from four monolayers up to a certain thickness in both sets of samples is consistent with ballistic heat conduction processes, as has been shown in previous works, where the thermal conductivity increased linearly with the characteristic length of the system<sup>41,45,46</sup>. However, in few-layer crystalline PtSe<sub>2</sub> films ( $t < 2-3$  nm), we observe a deviation from the linear thickness-dependence of  $k_z$  (see Fig. 3c, black spheres). Since interfaces might dominate cross-plane heat transport in very thin films, the apparent deviation might be attributed to variations in the total thermal resistance per unit area,  $R_{\text{tot}}$ , of the film (see calculations below), which can be written as the sum of the combined interface thermal resistance,  $R_{\text{int}} = 1/G_1 + 1/G_2$ , and volumetric cross-plane thermal resistance,  $R_{\text{PtSe}_2} = t/k_z$ <sup>41,47</sup>. Note that this expression is not valid in very thin films and  $G_1$  and  $G_2$  should be treated as one diffusive interface instead of two discrete ones<sup>41,47</sup>. Another possible explanation for this deviation is the semiconductor-to-semimetal evolution of PtSe<sub>2</sub> films after 4 monolayers (~2 nm)<sup>48</sup>, which might result in an additional contribution of the electron thermal conductivity to  $k_z$  and/or lower contact resistivity between PtSe<sub>2</sub> and Au<sup>12</sup>.

To quantify the impact of cross-plane ballistic phonon transport on the total thermal resistance of multilayer PtSe<sub>2</sub> films, we plotted the total thermal resistance,  $R_{\text{tot}} = R_{\text{PtSe}_2} + R_{\text{int}}$ , versus film thickness (Fig. 3d). We observe that in crystalline PtSe<sub>2</sub>  $R_{\text{tot}}$  remains almost constant in the entire thickness range (see black

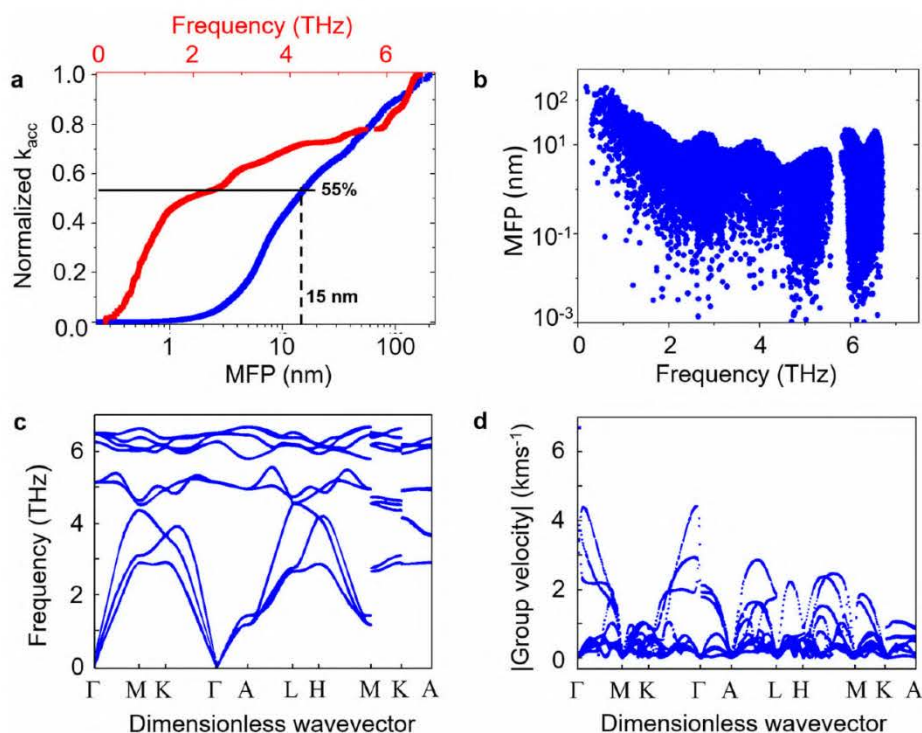
spheres), with values approximately of  $28 \pm 10 \text{ m}^2 \text{ KGW}^{-1}$ , while in polycrystalline samples (see green spheres)  $R_{\text{tot}}$  is constant only up to 12 nm and then starts to increase up to  $75 \pm 10 \text{ m}^2 \text{ KGW}^{-1}$ . The large contribution of the volumetric resistance component,  $R_{\text{PtSe}_2}$ , to  $R_{\text{tot}}$  and the thickness-independent  $R_{\text{tot}}$  in crystalline films indicate ballistic phonon transport along the  $c$ -axis of the films. Similar results has been previously observed in few-layer-graphene and single-crystal MoS<sub>2</sub> flakes that showed a thickness-independent  $R_{\text{tot}}$  for film thicknesses between 0.4–4 nm<sup>47</sup> and 20–40 nm<sup>41</sup>, respectively.

The increased values of  $R_{\text{tot}}$  in polycrystalline films after 12 nm indicate a transition from ballistic to diffusive transport regime most likely due to phonon grain boundary scattering. For comparison, in Fig. 3d we plot our calculated  $R_{\text{tot}}$  (black and green spheres) with previous total cross-plane thermal resistance measurements on different 2D materials, where similar interfacial contributions from the bottom (2D material/substrate) and top (metal/2D material) interfaces were taken into account<sup>41,47</sup>. Our values are in line with these estimations and suggest that in sufficiently thin films, phonons (especially long-wavelength phonons) can directly propagate between the metal and substrate without being strongly scattered by interfaces.

To further confirm the robustness of our approach to measuring the intrinsic cross-plane thermal conductivity of thin films, we performed Raman thermometry measurements in a few layers of crystalline PtSe<sub>2</sub> films (2, 3, and 4 layers of PtSe<sub>2</sub>, see Supplementary Fig. 8), where we found  $k_z$  values in good agreement with the FDTR results (see Supplementary Table 1). The agreement between Raman and FDTR experiments further supports our  $R_{\text{tot}}$  calculations and shows that it is possible to quantify the interfacial thermal contributions in a multilayer structure from a single set of FDTR measurements despite the low phase sensitivity to  $G_1$  and  $G_2$ . Note that in Raman thermometry measurements we have only the contribution of  $R_2$  to the total thermal resistance.

Next, we estimate the room temperature phonon MFP in the cross-plane direction ( $\Lambda_z$ ) using a simplified expression from the kinetic theory,  $k_z \sim (1/3)Cv_s\Lambda_z$ , where  $v_s$  is the averaged sound velocity of cross-plane acoustic modes. For PtSe<sub>2</sub> we used  $C \sim 1.78 \text{ MJ m}^{-3} \text{ K}^{-1}$ <sup>49</sup>, while  $k_z$  and  $v_s$  were determined experimentally ( $k_z \sim 4.6 \text{ Wm}^{-1} \text{ K}^{-1}$ ,  $v_s \sim \sqrt{\frac{1}{3}(\frac{1}{v_{LA}^2} + \frac{2}{v_{TA}^2})}$ ) through our FDTR and ASOPS measurements described above. From this estimation, we found  $\Lambda_z \sim 5$  nm, which corresponds to a thickness of approximately ten layers. However, our FDTR experimental data suggest that in crystalline PtSe<sub>2</sub> films phonons with  $\Lambda_z > 24$  nm substantially contribute to the thermal conductivity (about 37% of the bulk value, from our BTE-DFT calculations) while in polycrystalline films grain boundary scattering reduces this value to ~12 nm (see Fig. 3c). This is in close agreement with our DFT calculations that show that phonons with MFP larger than 15 nm contribute to almost 55% of the total cross-plane bulk thermal conductivity (see Fig. 4a).

In particular, Fig. 4a shows the normalized cumulative thermal conductivity as a function of frequency (red axis) and phonon mean free path (black axis) for bulk PtSe<sub>2</sub>. We observe a quite narrow cross-plane MFP distribution (1–200 nm) but longer than the rough estimation from the kinetic theory ~5 nm. This discrepancy is well known and comes from the fact that each phonon contributes in a different manner to the thermal conductivity<sup>41,50–52</sup>. An averaged value can be misleading and underestimate the real contribution of the phonon MFP to the total thermal conductivity. It is interesting to note also the rather large contribution (~30%) of low-frequency phonons (<1 THz) to the total thermal conductivity. These phonons modes are sensitive to the introduction of additional periodicity and their dispersion relation can be easily tuned through nanofabrication<sup>53,54</sup>. This opens the possibility of exploring alternative ways of tuning



**Fig. 4** First-principles DFT calculations. **a** Normalized thermal conductivity accumulation ( $k_{acc}$ ) as a function of the phonon frequency (red curve) and MFP (blue curve) for bulk PtSe<sub>2</sub>. **b** Calculated bulk phonon mean free as a function of frequency. **c** Phonon dispersion relations and **d** group velocity of bulk PtSe<sub>2</sub> along high-symmetry directions in the Brillouin zone.

thermal conduction through phonon engineering in two-dimensional materials.

Furthermore, in Fig. 4b we show that the MFPs in the cross-plane direction of the acoustic modes may be as high as 200 nm. Remarkably, there is a large number of optical modes with MFPs between 1 to 10 nm. This leads to a significant contribution of the optical modes to the thermal conductivity of bulk and PtSe<sub>2</sub> films, as shown in Fig. 4a and Supplementary Fig. 10. Finally, DFT-BTE calculations provide further insight into the heat transport mechanisms in PtSe<sub>2</sub>. Figure 4c shows the phonon dispersions of bulk PtSe<sub>2</sub> along high-symmetry paths in the Brillouin Zone. As opposed to 2H phases, we observe no gap between the optical and the acoustic modes. It is worth noting that the high-frequency optical modes are unusually dispersive in the  $\Gamma$ -A direction if compared to other layered materials, for which optical phonon dispersions are usually flat<sup>55</sup>. This can be seen in Fig. 4d which displays the group velocities along the same k-point paths. Figure 4d also shows that the speed of sound in the  $\Gamma$ -A direction, averaged over the three acoustic branches, is 1930 m s<sup>-1</sup> ( $v_{LA} = 2120$  m s<sup>-1</sup>).

In conclusion, we have studied phonon dynamic properties and heat transport in MBE-grown crystalline and polycrystalline PtSe<sub>2</sub> thin films of varying thickness (1 to 40 ML) using a combination of characterization techniques, i.e., FDTR, low-frequency Raman, and pump-probe coherent phonon spectroscopies, and state-of-the-art DFT calculations. Our work demonstrates the ability to quantify the influence of thickness and crystallinity on the cross-plane heat propagation in thin layered PtSe<sub>2</sub> films, showing an almost 35% reduction in the thermal conductivity of polycrystalline films with thickness larger than 12 nm in comparison with crystalline films of the same thickness. Moreover, from the phonon dynamic study in crystalline PtSe<sub>2</sub>, we extract an out-of-plane elastic constant  $C_{33} = 31.8$  GPa and a layer-dependent group velocity ranging from 1340 ms<sup>-1</sup> in bilayer PtSe<sub>2</sub> to 1873 ms<sup>-1</sup> in eight layers of PtSe<sub>2</sub>.

Last, we showed that acoustic phonons in PtSe<sub>2</sub> thin films, which are the main carriers of heat in semiconductors, have extraordinarily short lifetimes in the order of picoseconds. Our results provide new insight into the heat transport and phonon dynamics in 2D materials at the nanoscale, with potential implications for the future design of 2D-based devices for energy harvesting and effective heat dissipation in thermoelectric and optoelectronic devices.

## METHODS

### Molecular beam epitaxy growth

Pt and Se were respectively evaporated thanks to an e-gun evaporator and a standard effusion cell. The Pt deposition rate was set to 0.75 Å min<sup>-1</sup> and monitored in real-time by a quartz crystal microbalance. The pressure of Se at the sample position was measured with a retractable ionization gauge and set to  $1.0 \times 10^{-6}$  mbar, which corresponds to a Se:Pt flux ratio of about 15. The MBE reactor is connected under UHV to a magnetron sputtering chamber with a Pt target. The Pt deposition rate was set to 4.7 Å min<sup>-1</sup> thanks to a retractable quartz crystal microbalance, the DC magnetron power was 1 W, and the argon pressure was  $1.2 \times 10^{-2}$  mbar. The ZnO (0001) substrates (CrysTec GmbH) were first etched for 30 s with an HCl 1.8% solution and rinsed with deionized water. This chemical treatment was followed by annealing for 1 h at 900 °C in an O<sub>2</sub> atmosphere, then annealing in UHV for 5 min at ~800 °C.

### X-ray diffraction measurements

Grazing-incidence x-ray diffraction measurements were performed with a SmartLab Rigaku diffractometer. The source is a rotating anode beam tube (Cu K $\alpha = 1.54$  Å) operating at 45 kV and 200 mA. The diffractometer is equipped with a parabolic multilayer mirror and in-plane collimators of 0.5° on both source and detector sides defining the angular resolution. A K $\beta$  filter on the detector side eliminates parasitic radiations.

### Density functional theory calculations

We computed the lattice thermal conductivity of 1 T (octahedral) PtSe<sub>2</sub> by density functional theory (DFT) and the Boltzmann transport equation (BTE). In the DFT calculations, we used a van der Waals density functional with consistent exchange (vdW-DF-CX) that reliably predicts the structural and vibrational properties of several 2D materials, including transition metal dichalcogenides<sup>56,57</sup>. Valence Kohn-Sham wavefunctions are expanded on plane-waves basis set with a cutoff of 40 Ry, and projector augmented pseudopotentials are used to model screened nuclei<sup>58</sup>. A uniform 8 × 8 × 6 mesh of k-points was used to integrate the first Brillouin Zone. Phonon dispersion relations were computed by density functional perturbation theory interpolating a uniform 4 × 4 × 3 q-point mesh<sup>59,60</sup>.

### Boltzmann transport equation

Second-order and third-order force constants for the thermal conductivity calculations were computed by fitting the forces of 80 configurations of the 4 × 4 × 3 PtSe<sub>2</sub> supercells, in which the atoms are randomly displaced with a standard deviation of 0.01 Å using the hiPhive code<sup>61</sup>. Second-order and third-order force constants were cut off at 6.9 and 5.13 Å, respectively. Fitting employed recursive feature elimination with a limit of 300 features (out of 961). The fit gives a root mean square error on the forces of 0.0044 eV/Å with R<sup>2</sup> = 0.999. The solution of the linearized phonon BTE was computed by directly inverting the scattering tensor on a 21 × 21 × 17 mesh of q-points, as implemented in kALDo<sup>62</sup>. The effect of the finite thickness of the samples is taken into account by including the boundary conditions in the scattering term as proposed by Maassen and Lundstrom<sup>63</sup>.

### Asynchronous optical sampling measurements

In this technique, two pulsed lasers (pump and probe beams) are focused on the sample surface. The pump produces a change of reflectivity which is measured by the probe beam as a function of the time delay between the lasers. The absorption of the pump laser causes an increase in the local strain via two separate mechanisms, namely thermal expansion, and the hydrostatic deformation potential. The thermal expansion is a consequence of the anharmonicity of the lattice, whereas the deformation potential is due to the excitation of electrons into binding orbitals. Both mechanisms periodically change the effective volume of the material, which in turn modulates the optical properties of the film that are probed by the second laser. In this experiment, we used 2 fs Ti:sapphire lasers with a repetition rate of ~1 GHz stabilized via an electronic feedback loop to achieve a small repetition rate difference of 2 kHz. The rate difference produces a time delay between the pump and probe pulses without the need for a mechanical delay stage. The delay between the pump pulses is kept at 1 ns, while the pump and probe pulses coincide every 500 ms. The measurements were done at a fixed central wavelength of λ = 790 nm for the pump (~1 mW) and the probe (~0.15 mW) beams, collinearly focused to a ~1-μm-diameter spot on the sample surface.

### DATA AVAILABILITY

All relevant data and codes are available from the corresponding author on request.

Received: 6 December 2021; Accepted: 28 April 2022;

Published online: 23 May 2022

### REFERENCES

- Ferrari, A. C. et al. Science and technology roadmap for graphene, related two-dimensional crystals, and hybrid systems. *Nanoscale* **7**, 4598–4810 (2015).
- Jariwala, D. et al. Gate-tunable carbon nanotube–MoS<sub>2</sub> heterojunction p–n diode. *Proc. Natl Acad. Sci. USA* **110**, 18076–18080 (2013).
- Massicotte, M. et al. Picosecond photoresponse in van der Waals heterostructures. *Nat. Nanotechnol.* **11**, 42–46 (2016).
- Chhowalla, M., Jena, D. & Zhang, H. Two-dimensional semiconductors for transistors. *Nat. Rev. Mater.* **1**, 16052 (2016).
- Zhao, Y. et al. High-electron-mobility and air-stable 2D layered PtSe<sub>2</sub> FETs. *Adv. Mater.* **29**, 1604230 (2017).
- Deng, Y. et al. Black phosphorus–monolayer MoS<sub>2</sub> van der Waals heterojunction p–n diode. *ACS Nano* **8**, 8292–8299 (2014).
- Yu, X. et al. Atomically thin noble metal dichalcogenide: a broadband mid-infrared semiconductor. *Nat. Commun.* **9**, 1545 (2018).
- Liu, Y., Zhang, S., He, J., Wang, Z. M. & Liu, Z. Recent progress in the fabrication, properties, and devices of heterostructures based on 2D materials. *Nano Micro Lett.* **11**, 13 (2019).
- Li, D. et al. Recent progress of two-dimensional thermoelectric. *Mater. Nano Micro Lett.* **12**, 36 (2020).
- Gong, Y. et al. Two-dimensional platinum diselenide: synthesis, emerging applications, and future challenges. *Nano Micro Lett.* **12**, 174 (2020).
- Bonell, F. et al. High carrier mobility in single-crystal PtSe<sub>2</sub> grown by molecular beam epitaxy on ZnO(0001). *2D Mater.* <https://doi.org/10.1088/2053-1583/ac37aa> (2021).
- Yim, C. et al. Electrical devices from top-down structured platinum diselenide films. *npj 2D Mater. Appl.* **2**, 5 (2018).
- Zhang, W., Qin, J., Huang, Z. & Zhang, W. The mechanism of layer number and strain dependent bandgap of 2D crystal PtSe<sub>2</sub>. *J. Appl. Phys.* **122**, 205701 (2017).
- Wang, Y. et al. Monolayer PtSe<sub>2</sub>, a new semiconducting transition-metal-dichalcogenide, epitaxially grown by direct selenization of Pt. *Nano Lett.* **15**, 4013–4018 (2015).
- Moon, H. et al. Strong thermopower enhancement and tunable power factor via semimetal to semiconductor transition in a transition-metal dichalcogenide. *ACS Nano* **13**, 13317–13324 (2019).
- Guo, S.-D. Biaxial strain tuned thermoelectric properties in monolayer PtSe<sub>2</sub>. *J. Mater. Chem. C* **4**, 9366–9374 (2016).
- Yin, S. et al. Thermal conductivity of few-layer PtS<sub>2</sub> and PtSe<sub>2</sub> obtained from optothermal Raman spectroscopy. *J. Phys. Chem. C* **125**, 16129–16135 (2021).
- Chen, X. et al. Direct observation of interlayer coherent acoustic phonon dynamics in bilayer and few-layer PtSe<sub>2</sub>. *Photonics Res.* **7**, 1416 (2019).
- Zhang, K. et al. Experimental evidence for type-II Dirac semimetal in PtSe<sub>2</sub>. *Phys. Rev. B* **96**, 125102 (2017).
- Cooper, V. R. Van der Waals density functional: an appropriate exchange functional. *Phys. Rev. B* **81**, 161104 (2010).
- Terentjev, A. V., Constantin, L. A. & Pitarke, J. M. Dispersion-corrected PBEsol exchange-correlation functional. *Phys. Rev. B* **98**, 214108 (2018).
- O'Brien, M. et al. Raman characterization of platinum diselenide thin films. *2D Mater.* **3**, 021004 (2016).
- Luo, N. S., Ruggerone, P. & Toennies, J. P. Theory of surface vibrations in epitaxial thin films. *Phys. Rev. B* **54**, 5051–5063 (1996).
- Carpinteri, A. *Structural Mechanics* (CRC Press, 2014).
- Zhao, Y. et al. Interlayer breathing and shear modes in few-trilayer MoS<sub>2</sub> and WSe<sub>2</sub>. *Nano Lett.* **13**, 1007–1015 (2013).
- Soubelet, P. et al. The lifetime of interlayer breathing modes of few-layer 2H-MoS<sub>2</sub> membranes. *Nanoscale* **11**, 10446–10453 (2019).
- Jiménez-Riobóo, R. J. et al. In- and out-of-plane longitudinal acoustic-wave velocities and elastic moduli in h-BN from Brillouin scattering measurements. *Appl. Phys. Lett.* **112**, 051905 (2018).
- Elzinga, P. A., Lytle, F. E., Jian, Y., King, G. B. & Laurendeau, N. M. Pump/probe spectroscopy by asynchronous optical sampling. *Appl. Spectrosc.* **41**, 2–4 (1987).
- Bartels, A. et al. Ultrafast time-domain spectroscopy based on high-speed asynchronous optical sampling. *Rev. Sci. Instrum.* **78**, 35107 (2007).
- Ziman, J. M. *Electrons and Phonons. The Theory of Transport Phenomena in Solids* (Oxford Univ. Press, 1960).
- Schmidt, A. J., Cheaito, R. & Chiesa, M. A frequency-domain thermoreflectance method for the characterization of thermal properties. *Rev. Sci. Instrum.* **80**, 094901 (2009).
- Schmidt, A. J., Chen, X. & Chen, G. Pulse accumulation, radial heat conduction, and anisotropic thermal conductivity in pump-probe transient thermoreflectance. *Rev. Sci. Instrum.* **79**, 114902 (2008).
- El Sachat, A., Alzina, F., Sotomayor Torres, C. M. & Chavez-Angel, E. Heat transport control and thermal characterization of low-dimensional materials: a review. *Nanomaterials* **11**, 175 (2021).
- Sandell, S. et al. Thermoreflectance techniques and Raman thermometry for thermal property characterization of nanostructures. *J. Appl. Phys.* **128**, 131101 (2020).
- Xiao, P. et al. Anisotropic thermal conductivity of crystalline layered SnSe<sub>2</sub>. *Nano Lett.* **21**, 9172–9179 (2021).
- Sandell, S. et al. Enhancement of thermal boundary conductance of metal–polymer system. *Nanomaterials* **10**, 670 (2020).
- Rai, A., Sangwan, V. K., Gish, J. T., Hersam, M. C. & Cahill, D. G. Anisotropic thermal conductivity of layered indium selenide. *Appl. Phys. Lett.* **118**, 73101 (2021).
- Wang, H., Gao, Y. & Liu, G. Anisotropic phonon transport and lattice thermal conductivities in tin dichalcogenides SnS<sub>2</sub> and SnSe<sub>2</sub>. *RSC Adv.* **7**, 8098–8105 (2017).
- Jang, H., Wood, J. D., Ryder, C. R., Hersam, M. C. & Cahill, D. G. Anisotropic thermal conductivity of exfoliated black phosphorus. *Adv. Mater.* **27**, 8017–8022 (2015).
- Serrano, J. et al. Heat capacity of ZnO: isotope effects. *Phys. Rev. B* **73**, 94303 (2006).
- Sood, A. et al. Quasi-ballistic thermal transport across MoS<sub>2</sub> thin films. *Nano Lett.* **19**, 2434–2442 (2019).

42. Subramanyan, H., Kim, K., Lu, T., Zhou, J. & Liu, J. On the importance of using exact full phonon dispersions for predicting interfacial thermal conductance of layered materials using diffuse mismatch model. *AIP Adv.* **9**, 115116 (2019).
43. Liu, X., Zhang, G. & Zhang, Y.-W. Thermal conduction across the one-dimensional interface between a MoS<sub>2</sub> monolayer and metal electrode. *Nano Res.* **9**, 2372–2383 (2016).
44. Borlido, P., Huran, A. W., Marques, M. A. L. & Botti, S. Structural prediction of stabilized atomically thin tin layers. *npj 2D Mater. Appl.* **3**, 21 (2019).
45. Hsiao, T.-K. et al. Observation of room-temperature ballistic thermal conduction persisting over 8.3 μm in SiGe nanowires. *Nat. Nanotechnol.* **8**, 534–538 (2013).
46. Vakulov, D. et al. Ballistic phonons in ultrathin nanowires. *Nano Lett.* **20**, 2703–2709 (2020).
47. Koh, Y. K., Bae, M.-H., Cahill, D. G. & Pop, E. Heat conduction across monolayer and few-layer graphenes. *Nano Lett.* **10**, 4363–4368 (2010).
48. Ansari, L. et al. Quantum confinement-induced semimetal-to-semiconductor evolution in large-area ultra-thin PtSe<sub>2</sub> films grown at 400 °C. *npj 2D Mater. Appl.* **3**, 33 (2019).
49. Maregedze, C. N. *Numerical Simulation of Structural Electronic, Optical and Thermal Properties of Platinum Dichalcogenides*. MSc thesis, Univ. of Witwatersrand. (2019).
50. Cuffe, J. et al. Reconstructing phonon mean-free-path contributions to thermal conductivity using nanoscale membranes. *Phys. Rev. B* **91**, 245423 (2015).
51. Henry, A. S. & Chen, G. Spectral phonon transport properties of silicon based on molecular dynamics simulations and lattice dynamic. *J. Comput. Theor. Nanosci.* **5**, 141–152 (2008).
52. Esfarjani, K., Chen, G. & Stokes, H. Heat transport in silicon from first-principles calculations. *Phys. Rev. B* **84**, 085204 (2011).
53. Graczykowski, B. et al. Phonon dispersion in hypersonic two-dimensional phononic crystal membranes. *Phys. Rev. B* **91**, 75414 (2015).
54. Sledzinska, M. et al. 2D phononic crystals: progress and prospects in hypersound and thermal transport engineering. *Adv. Funct. Mater.* **30**, 1904434 (2019).
55. Mortazavi, B. et al. Exploring phononic properties of two-dimensional materials using machine learning interatomic potentials. *Appl. Mater. Today* **20**, 100685 (2020).
56. Berland, K. & Hyldgaard, P. Exchange functional that tests the robustness of the plasmon description of the van der Waals density functional. *Phys. Rev. B* **89**, 035412 (2014).
57. Lindroth, D. O. & Erhart, P. Thermal transport in van der Waals solids from first-principles calculations. *Phys. Rev. B* **94**, 115205 (2016).
58. Blöchl, P. E. Projector augmented-wave method. *Phys. Rev. B* **50**, 17953–17979 (1994).
59. Baroni, S., de Gironcoli, S., Dal Corso, A. & Giannozzi, P. Phonons and related crystal properties from density-functional perturbation theory. *Rev. Mod. Phys.* **73**, 515–562 (2001).
60. Giannozzi, P. et al. Advanced capabilities for materials modelling with Quantum ESPRESSO. *J. Phys. Condens. Matter* **29**, 465901 (2017).
61. Eriksson, F., Fransson, E. & Erhart, P. The hiphive package for the extraction of high-order force constants by machine learning. *Adv. Theory Simul.* **2**, 1800184 (2019).
62. Barbalinardo, G., Chen, Z., Lundgren, N. W. & Donadio, D. Efficient anharmonic lattice dynamics calculations of thermal transport in crystalline and disordered solids. *J. Appl. Phys.* **128**, 135104 (2020).
63. Maassen, J. & Lundstrom, M. Steady-state heat transport: ballistic-to-diffusive with Fourier's law. *J. Appl. Phys.* **117**, 035104 (2015).

## ACKNOWLEDGEMENTS

This work has been supported by the Severo Ochoa program, the Spanish Research Agency (AEI, grant no. SEV-2017-0706), and the CERCA Program/Generalitat de Catalunya.

The authors acknowledge support from the Spanish MICINN project SIP (PGC2018-101743-B-I00), and the EU project NANOPOLY (GA 289061). The LANEF framework (ANR-10-LABX-51-01) is acknowledged for its support of mutualized infrastructure. PX acknowledges support for the Ph.D. fellowship from the EU Marie Skłodowska-Curie COFUND PREBIST (Grant Agreement 754558). AES acknowledges support by the H2020-MSCA-IF project THERMIC-GA No. 101029727. The authors acknowledge Dr. John Cuffe for his critical comments.

## AUTHOR CONTRIBUTIONS

A.E.S. and E.C.-A., conceived the project. A.E.S. and E.C.-A., built the F.D.T.R., setup and performed the thermal measurements and data analysis. A.E.S. performed the A.F.M. measurements. E.C.-A. and P.X., performed the Raman measurements. E.C.-A. and G.A., performed the A.S.O.P.S., measurements and analysis. F.B., A.M., C.V., H.B. and M.J. fabricated the M.B.E. samples and performed the X.R.D., measurements. P.X., M.S., A.E.S. and E.C.-A., performed the T.E.M., measurements and the structural analysis. D.D. and Z.C., performed the D.F.T., calculations and provided support to the theoretical analysis. All authors reviewed and edited the manuscript and have given approval to the final version of the manuscript. The manuscript was written by A.E.S. and E.C.-A., A.E.S. and P.X., contributed equally.

## COMPETING INTERESTS

The authors declare no competing interests.

## ADDITIONAL INFORMATION

**Supplementary information** The online version contains supplementary material available at <https://doi.org/10.1038/s41699-022-00311-x>.

**Correspondence** and requests for materials should be addressed to Alexandros El Sachat or Emigdio Chavez-Angel.

**Reprints and permission information** is available at <http://www.nature.com/reprints>

**Publisher's note** Springer Nature remains neutral with regard to jurisdictional claims in published maps and institutional affiliations.



**Open Access** This article is licensed under a Creative Commons Attribution 4.0 International License, which permits use, sharing, adaptation, distribution and reproduction in any medium or format, as long as you give appropriate credit to the original author(s) and the source, provide a link to the Creative Commons license, and indicate if changes were made. The images or other third party material in this article are included in the article's Creative Commons license, unless indicated otherwise in a credit line to the material. If material is not included in the article's Creative Commons license and your intended use is not permitted by statutory regulation or exceeds the permitted use, you will need to obtain permission directly from the copyright holder. To view a copy of this license, visit <http://creativecommons.org/licenses/by/4.0/>.

© The Author(s) 2022

# Article 2 Supporting Information



## Supplementary Information

### Effect of crystallinity and thickness on thermal transport in layered PtSe<sub>2</sub>

Alexandros El Sachat<sup>\*1</sup>, Peng Xiao<sup>1,2</sup>, Davide Donadio<sup>3,4</sup>, Frédéric Bonell<sup>5</sup>, Marianna Sledzinska<sup>1</sup>, Alain Marty<sup>5</sup>, Céline Vergnaud<sup>5</sup>, Hervé Boukari<sup>5</sup>, Matthieu Jamet<sup>5</sup>, Guillermo Arregui<sup>1</sup>, Zekun Chen<sup>3,4</sup>, Francesc Alzina<sup>1</sup>, Clivia M. Sotomayor Torres<sup>1,6</sup>, Emigdio Chavez-Angel<sup>\*1</sup>

<sup>1</sup> Catalan Institute of Nanoscience and Nanotechnology (ICN2), CSIC and BIST, Campus UAB, Bellaterra, 08193 Barcelona, Spain

<sup>2</sup> Departamento de Física, Universidad Autónoma de Barcelona, Bellaterra, 08193 Barcelona, Spain

<sup>3</sup> Department of Chemistry, University of California, Davis, California 95616, United States

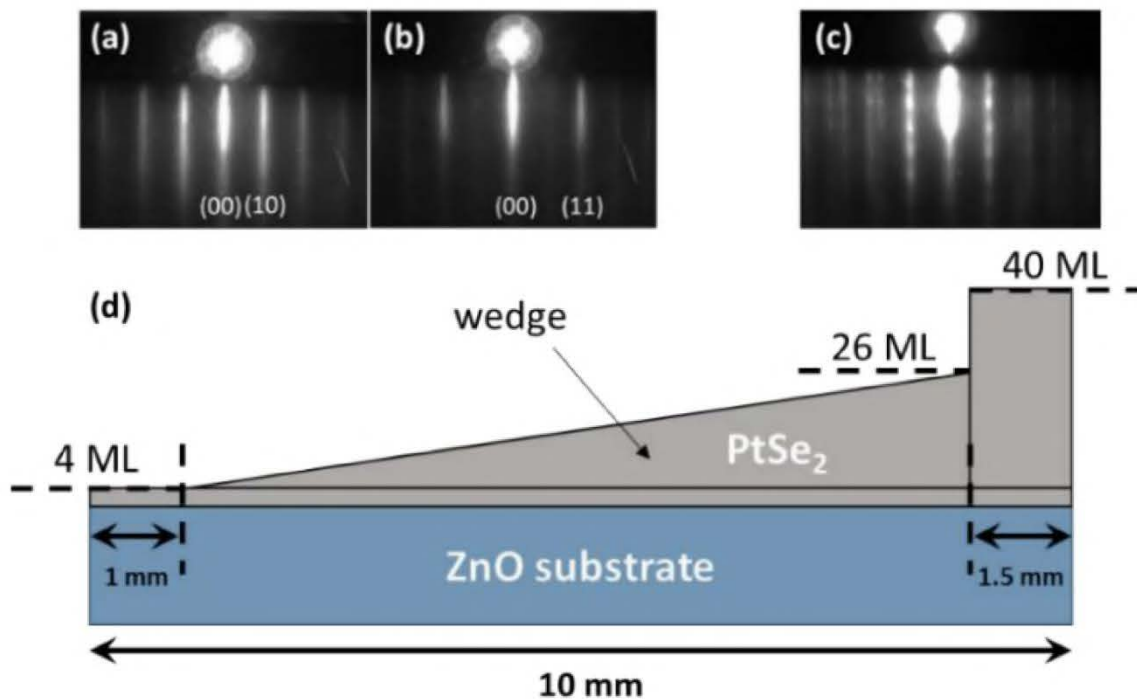
<sup>4</sup> Ikerbasque, Basque Foundation for Science, E-48011 Bilbao, Spain

<sup>5</sup> Université Grenoble Alpes, CNRS, CEA, Grenoble INP, IRIG-Spintec, 38054 Grenoble

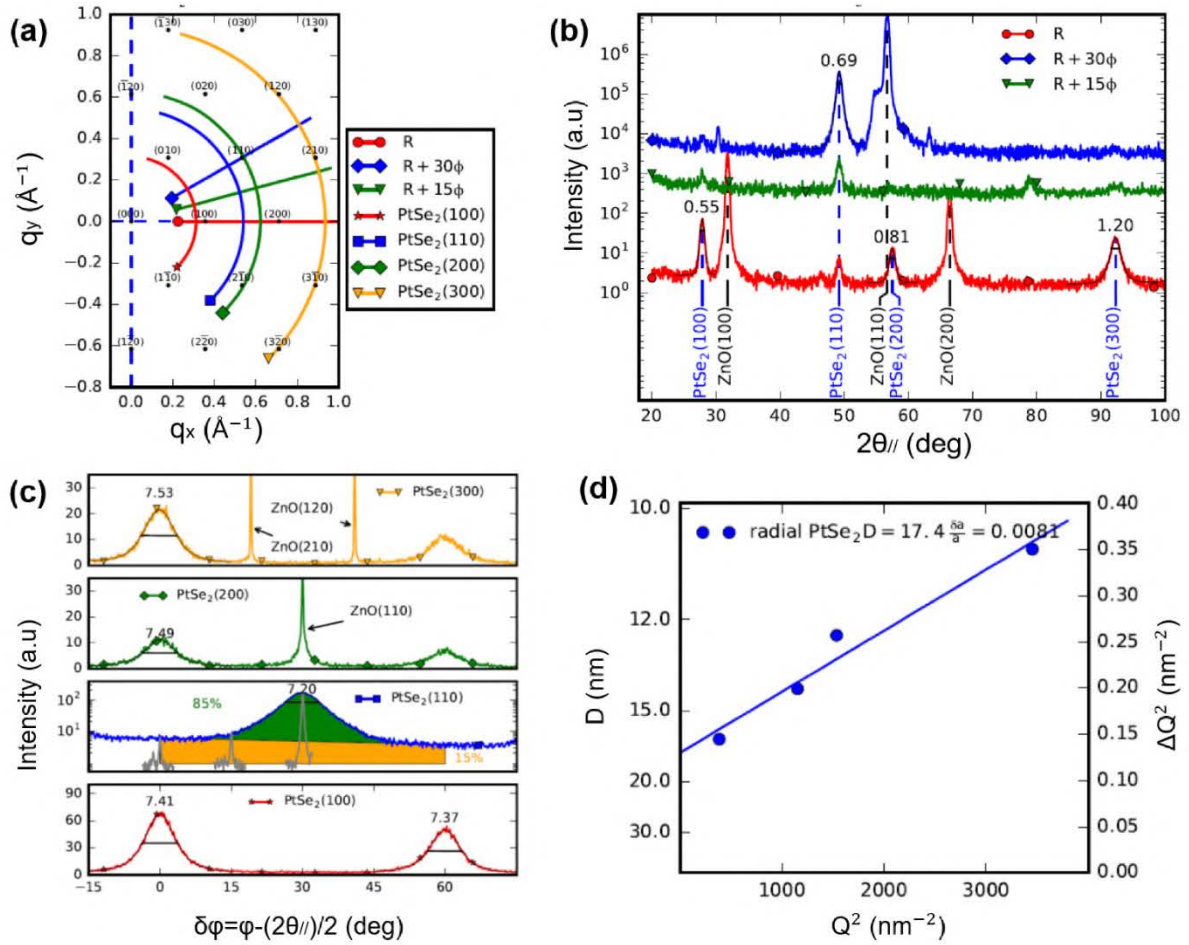
<sup>6</sup> ICREA, Passeig Lluís Companys 23, 08010 Barcelona, Spain

**Keywords:** 2D materials, PtSe<sub>2</sub>, thermal conductivity, phonon lifetimes, frequency domain thermorefectance

**Corresponding authors**

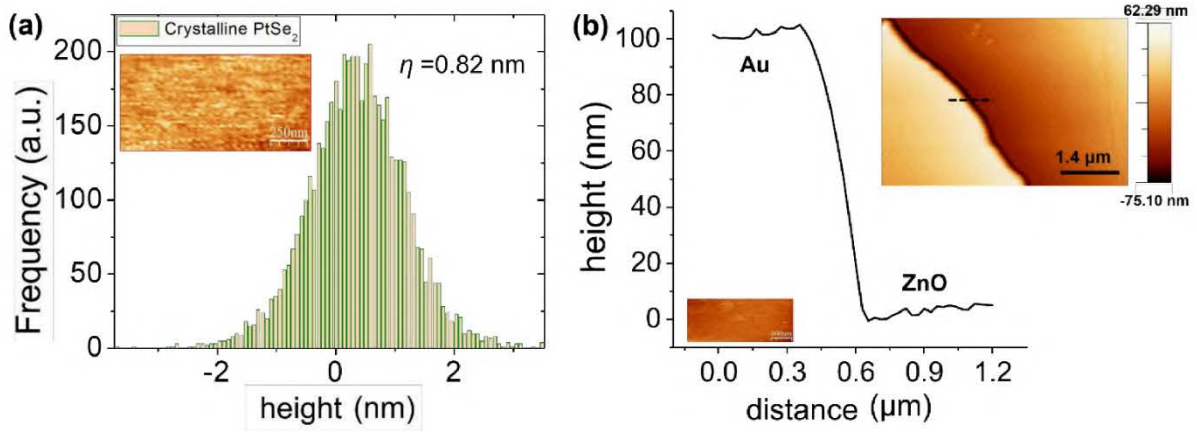


**Supplementary Figure 1. Reflection high energy electron diffraction (RHEED) measurements and the final structure of the PtSe<sub>2</sub> wedge sample. (a) and (b) RHEED patterns of 4 ML PtSe<sub>2</sub> grown by co-evaporation along two different azimuths respectively. (c) RHEED pattern of the polycrystalline PtSe<sub>2</sub> film. Only one azimuth is shown since it is isotropic. (d) Schematic drawing in cross-section of the final structure.**



**Supplementary Figure 2. X-ray diffraction measurements in PtSe<sub>2</sub>.** (a) Schematics of the different scans in the reciprocal space (radial and azimuthal) performed by grazing-incidence x-ray diffraction, (b) XRD radial scans showing the crystalline nature of the PtSe<sub>2</sub> film. (c) Azimuthal scans of the PtSe<sub>2</sub> Bragg peaks, from which we obtain the in-plane mosaic spread (see numbers on top of the peaks corresponding to the FWHM in degrees). (d) The momentum transfer  $Q$  for each radial Bragg diffraction peak can be calculated using  $Q = 4\pi/\lambda \sin(\theta_{//})$ , and the radial and azimuthal peak momentum dispersions using  $\Delta Q_{\text{rad}} = \Delta(2\theta)/2 \cdot 4\pi/\lambda \cos(\theta_{//})$ , where  $\Delta(2\theta)$  are the corresponding FWHM. Plotting  $\Delta Q^2$  as a function of  $Q^2$  for the radial and azimuthal scans, one can determine the domain size  $D$ , the in-plane lattice parameter distribution  $\Delta a/a$ , from the intercept and the slope of the radial scans using the expression:<sup>1</sup>

$$\Delta Q_{\text{rad}}^2 = (2\pi/D)^2 + Q^2 (\Delta a/a)^2.$$



**Supplementary Figure 3. AFM measurements.** (a) Histogram of the height distribution (surface roughness) measured by AFM for crystalline PtSe<sub>2</sub>. The root mean square roughness (RMS),  $\eta$ , is 0.82 nm. The inset shows an AFM image of the crystalline PtSe<sub>2</sub> wedge sample. (b) AFM topography profile of the deposited Au transducer on ZnO substrate taken from the black dashed line depicted in the AFM image (inset in (b)).

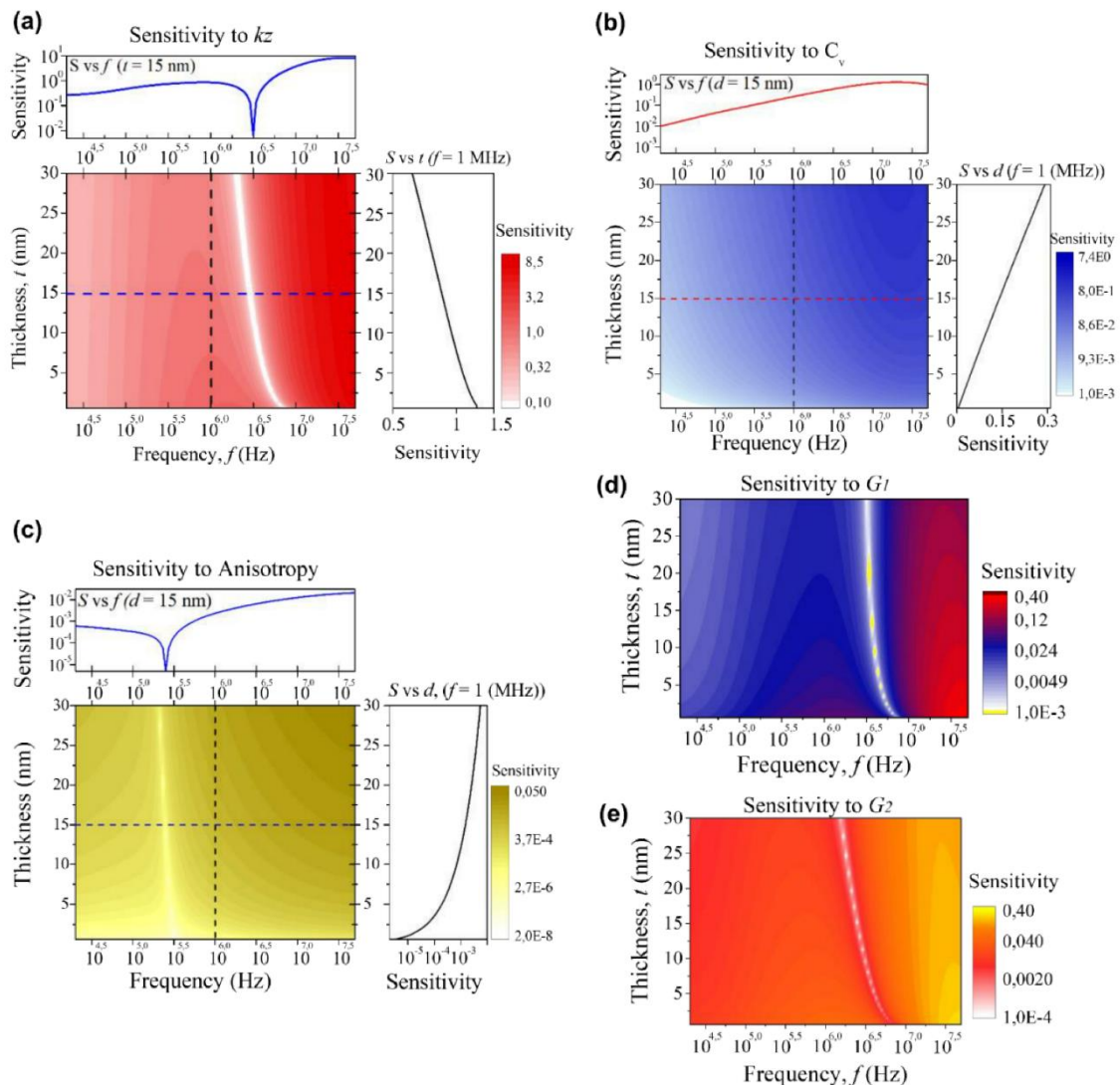
### Supplementary Note 1: FDTR sensitivity analysis

We quantify the phase sensitivity to multiple thermal properties in a similar manner to that of Schmidt *et al.*<sup>2</sup> The calculated phase sensitivity ( $-V_{in}/V_{out}$ ) to multiple parameters ( $k_z$ ,  $C_v$ , anisotropy,  $G_1$  and  $G_2$ ) as a function of thickness and modulation frequency for the case of Au/PtSe<sub>2</sub>/ZnO stacks is shown in Supplementary Figure 4(a-e). For the sensitivity analysis, we fit the experimental thickness dependence of the cross-plane thermal conductivity ( $k_z$ ) using the Fuchs-Sondheimer model considering only cross-plane heat transport described by:<sup>3</sup>

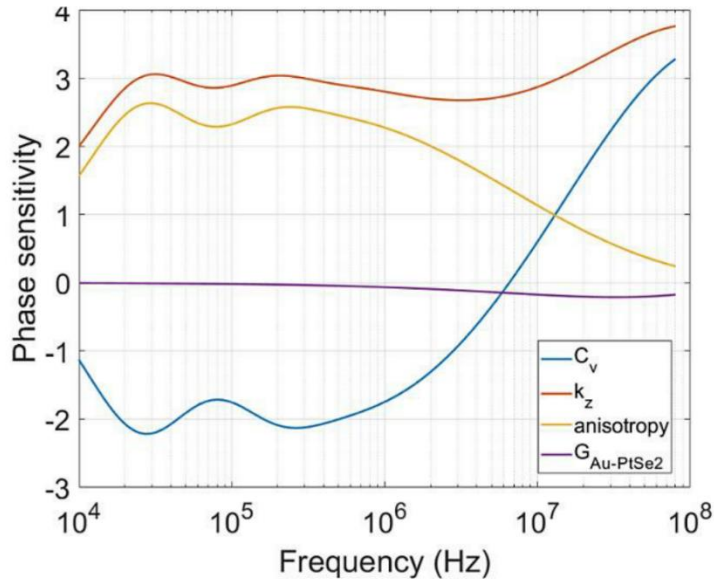
$$\frac{k_{film, z}}{k_{bulk, z}} = S(\chi) = 1 - \chi(1 - \exp[-1/\chi]) \quad (1)$$

where  $k_{bulk, z}$  is the cross-plane thermal conductivity of the film (bulk) sample,  $S(\chi)$  is the suppression function,  $\chi$  is the Knudsen number  $\chi = \Lambda_{bulk}/d$ ,  $\Lambda_{bulk}$  is the bulk MFP (120 nm from the best fit) and  $d$  is the thickness of the film. This fit allows us to have a continuous function to plot the sensitivity as a function of excitation frequency and sample thickness. The degree of

anisotropy or the ratio between in-plane ( $k_r$ ) and cross-plane ( $k_z$ ) thermal conductivities was estimated from the bulk measurements  $k_r/k_z = 9$ . It was assumed constant for all the films. The sensitivity analysis is shown over a frequency range of 20 kHz–40 MHz, where we observed that depending on the frequency range the phase sensitivity to a given parameter varies. For example, the sensitivity to in-plane transport for the thin films is almost zero and it is dominant for cross-plane transport (see Supplementary Figure 4c). Moreover, from Supplementary Figure 4d,e we observe that the sensitivity of the recorded phase signal to  $G_1$  and  $G_2$  is relatively low. However, in the case of bulk PtSe<sub>2</sub> the sensitivity to cross-plane and in-plane transport is high almost in the entire frequency range (see Supplementary Figure 5), thus it is possible to extract the anisotropy ratio between  $k_r$  and  $k_z$  from a data set.



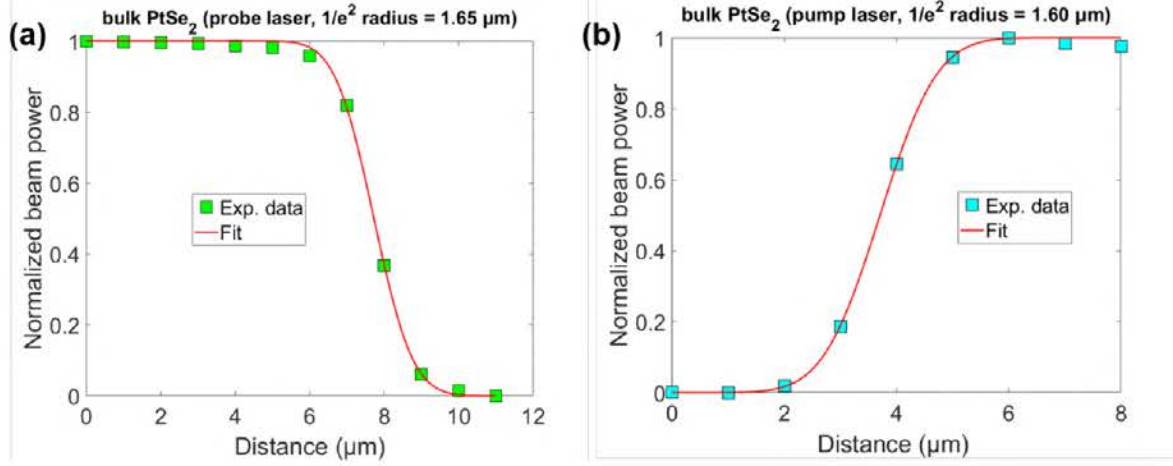
**Supplementary Figure 4. Phase sensitivity analysis for thin PtSe<sub>2</sub> films.** Calculated phase sensitivity to (a)  $k_z$ , (b)  $C_v$ , (c) anisotropy, (d)  $G_1$  and (e)  $G_2$  as a function of thickness and modulation frequency for the case of Au/PtSe<sub>2</sub>/ZnO stacks.



**Supplementary Figure 5. Phase sensitivity analysis for bulk PtSe<sub>2</sub>.** Calculated phase sensitivity to  $k_z$ ,  $C_v$ , anisotropy and  $G_{\text{Au-PtSe}_2}$  as a function of the modulation frequency for the case of bulk PtSe<sub>2</sub> crystal.

### Supplementary Note 2: Spot size measurements

The spot size for each measurement was determined by using the knife's edge method. For the measurements we use the transducer layer as sharp edge and we measured the intensity of the reflected light as a function of the stage position. The beam intensity as a function of the translation distance was fitted to an error function curve<sup>4</sup> and the  $1/e^2$  radius of this curve was taken as the laser spot radius.



**Supplementary Figure 6. Spot size measurements.** Typical examples of measured (a) probe and (b) pump spot sizes in bulk PtSe<sub>2</sub> crystal using the knife's edge method.

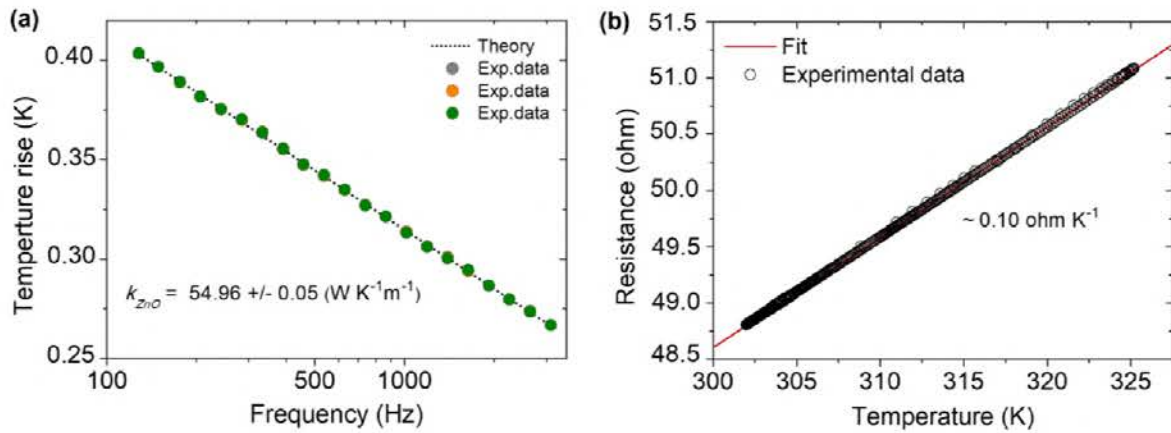
### Supplementary Note 3: Three omega measurements

The measurement of the thermal conductivity of the ZnO substrate was carried out by using the well-known three-omega (3 $\omega$ ) method.<sup>5,6</sup> The 3 $\omega$ -heater strip consisted in a 100 nm-thick gold wire patterned on a 0.5 mm thick ZnO substrate by photolithography and electron beam physical vapour deposition (EBPVD). The width of the heating line was defined as  $2b = 12 \mu\text{m}$  and the length as  $l = 1.3 \text{ mm}$ , the latter considered as the distance between the voltage (inner) pads. The width was estimated by averaging several microscopic images of the heater lines. The thermal conductivity of the substrate was obtained by solving the transient heat conduction equation for a finite width line heater, deposited onto semi-infinite surface of a film-on substrate system. The temperature rise is given by the following equation:

$$\Delta T = \frac{P}{lk\pi} \int_0^{\infty} \frac{\sin^2(xb)}{\sqrt{x^2 + iq^2}} dx \quad (2)$$

where  $P$  is the applied power (20 mW),  $q = 1/\lambda = \sqrt{2\omega/\alpha}$  is the inverse of the thermal penetration depth ( $\lambda$ ), with  $\alpha$  the thermal diffusivity and  $\omega$  the excitation frequency ( $\omega = 2\pi f$ ), and  $k$  is the thermal conductivity of the material. Finally, the thermal conductivity of the

substrate was estimated by fitting the experimental temperature rise of the  $3\omega$  signal (grey, orange and green dots in Supplementary Figure 7a) using the Supplementary Equation 2.



**Supplementary Figure 7. Three omega measurements. (a)** Temperature rise of the  $3\omega$ -heater vs excitation frequency for a 0.5 mm thick ZnO substrate. **(b)** Typical temperature dependence of the electrical resistivity of a  $3\omega$ -heater of the same system.

#### Supplementary Note 4: Raman thermometry measurements

To validate the thermal conductivities obtained by the FDTR measurements, Raman thermometry analysis were carried out in 2, 3 and 4 layer-thick PtSe<sub>2</sub> supported samples. Raman thermometry is a contactless and steady state technique for measuring thermal conductivity. It is based on probing the local temperature using the shift of Raman mode as a thermometer, previously calibrated in a cryostat at a pressure of  $10^{-3}$  mbar. We used the excitation laser (532 nm) as both the heat source and the temperature sensor simultaneously. The local heating was controlled by varying the incident laser power and the thermal conductivity was extracted by solving the heat equation using finite element simulation method (COMSOL). In the simulations, the heat power and thermal properties of the sample were given as inputs, and the resulting temperature profile was calculated. Then, by adjusting the simulated temperature profile to the measured one, the cross-plane thermal conductivity was obtained. The absorbed



power was estimated by using the experimental absorption reported by Chen et al.<sup>7</sup> and extrapolated to our experimental data considering a 10% deviation (x-axis error bar). For the FEM simulations, we used a Gaussian heat source given by:

$$Q = \frac{2AP_I}{\pi d\sigma^2} \exp\left[\frac{-2r^2}{\sigma^2}\right] \quad (3)$$

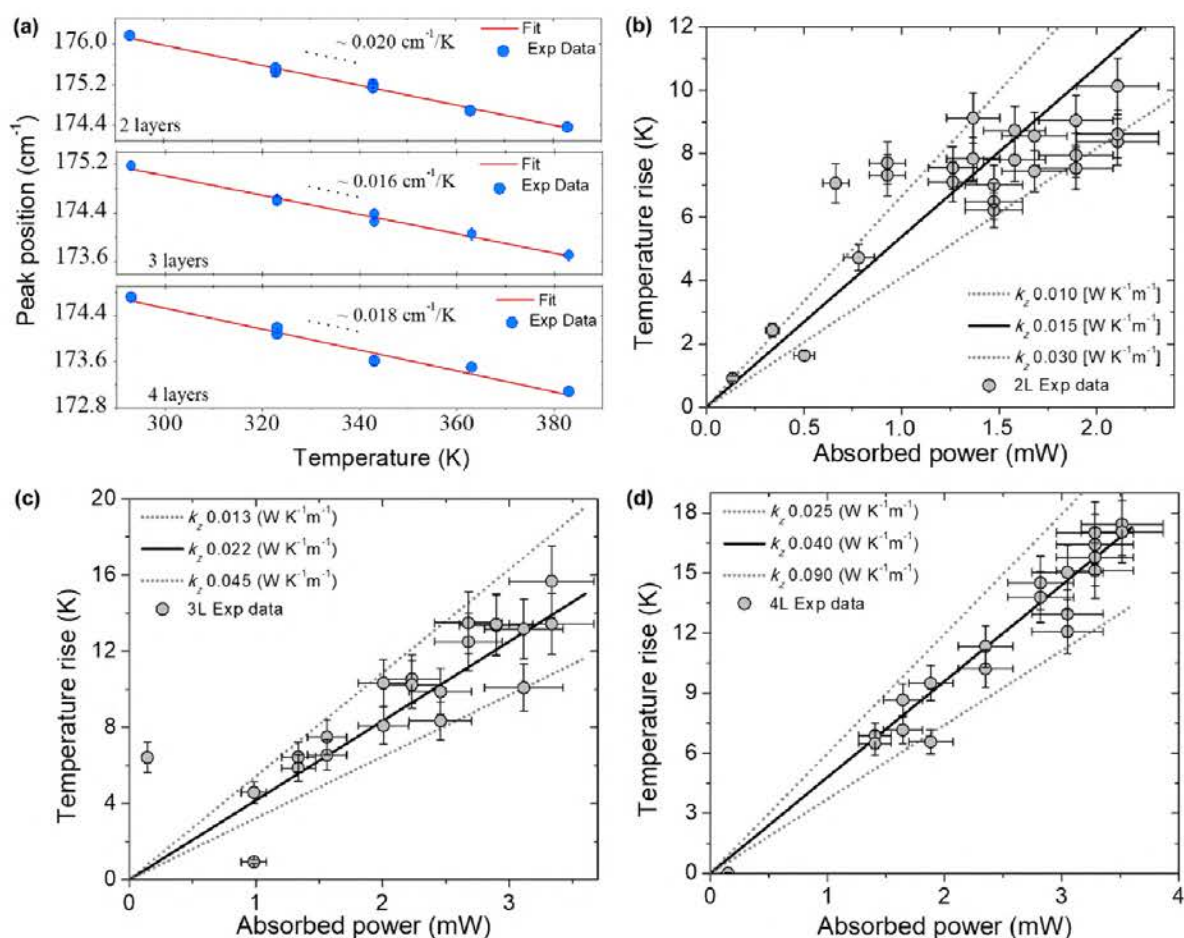
where  $A$  is the absorption coefficient,  $P_I$  is the incident power,  $d$  is the sample thickness and  $\sigma$  is the  $1/e^2$  radius measured in-situ using the knife's edge method. The temperature rise in the film ( $T_m$ ) is averaged considering the real spatial temperature distribution given by:

$$T_m = \frac{\int_0^\infty rT(r) \exp\left[\frac{-2r^2}{\sigma^2}\right] dr}{\int_0^\infty r \exp\left[\frac{-2r^2}{\sigma^2}\right] dr} \quad (4)$$

A comparison of the measured  $k_z$  by Raman thermometry and FDTR is shown in Supplementary Table 1.

Sample	Measured thermal conductivity ( $\text{WK}^{-1}\text{m}^{-1}$ )	
	Raman thermometry	FDTR
2 layers PtSe <sub>2</sub>	0.015	0.04
3 layers PtSe <sub>2</sub>	0.040	0.06
4 layers PtSe <sub>2</sub>	0.09	0.10

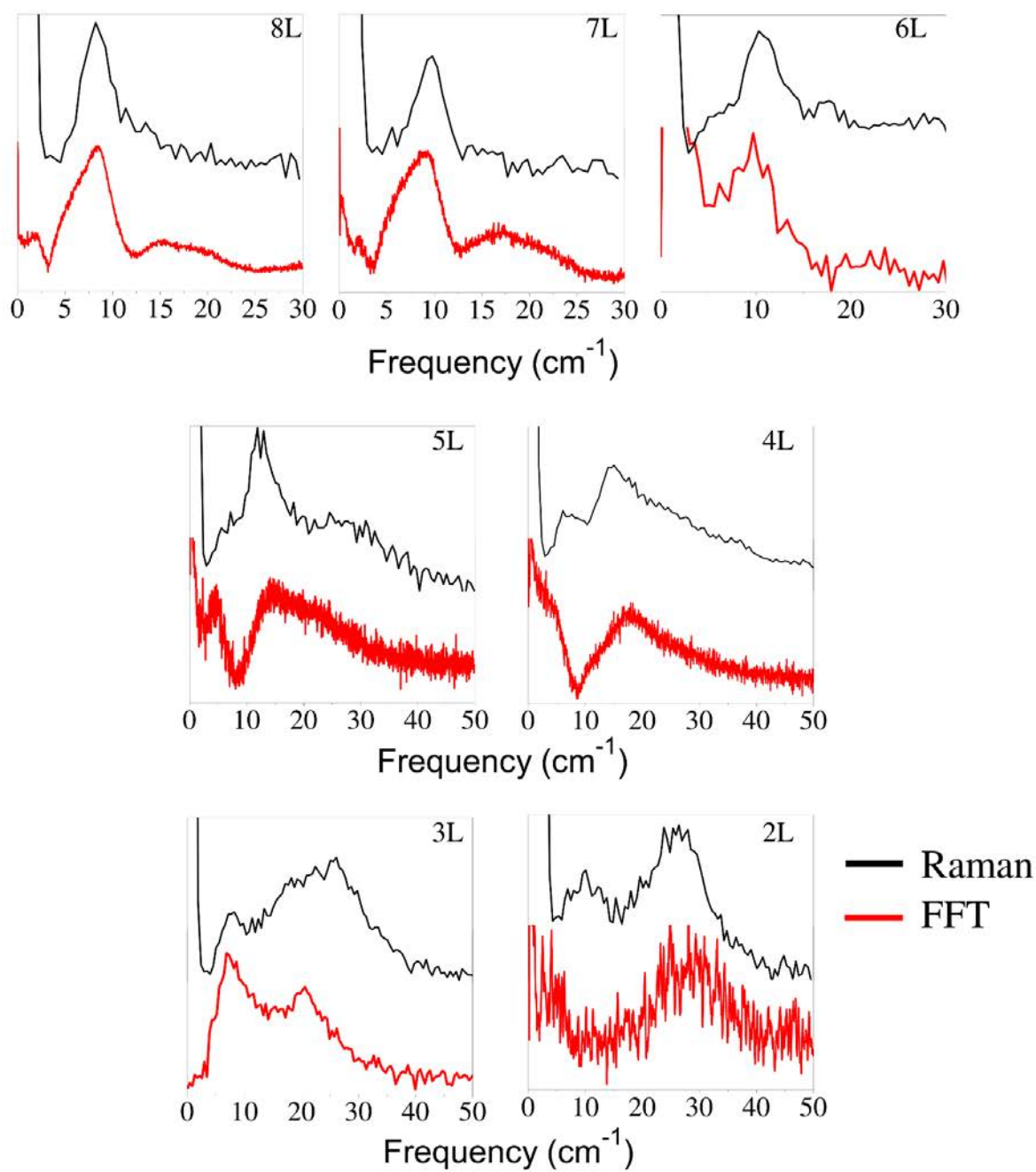
**Supplementary Table 1.** Measured cross-plane thermal conductivity obtained by Raman thermometry and FDTR.



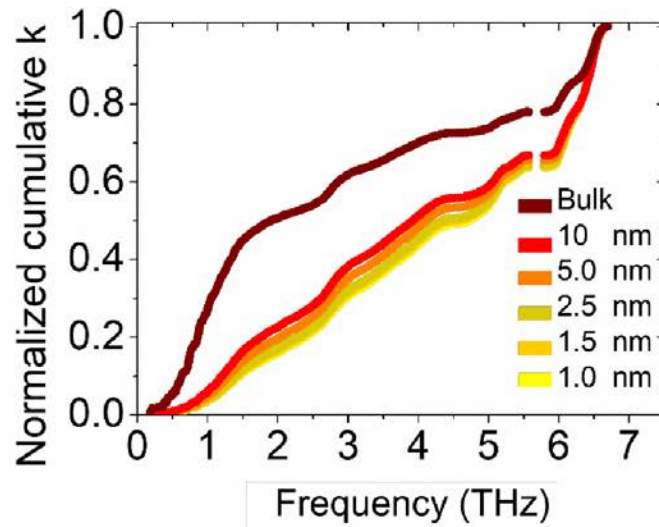
**Supplementary Figure 8. Raman thermometry measurements.** (a) Temperature dependence of the E<sub>g</sub> Raman active mode peak position. (b)-(d) Experimental temperature rise as a function of the absorbed power.

### Supplementary Note 5: Fourier transform from ASOPS data

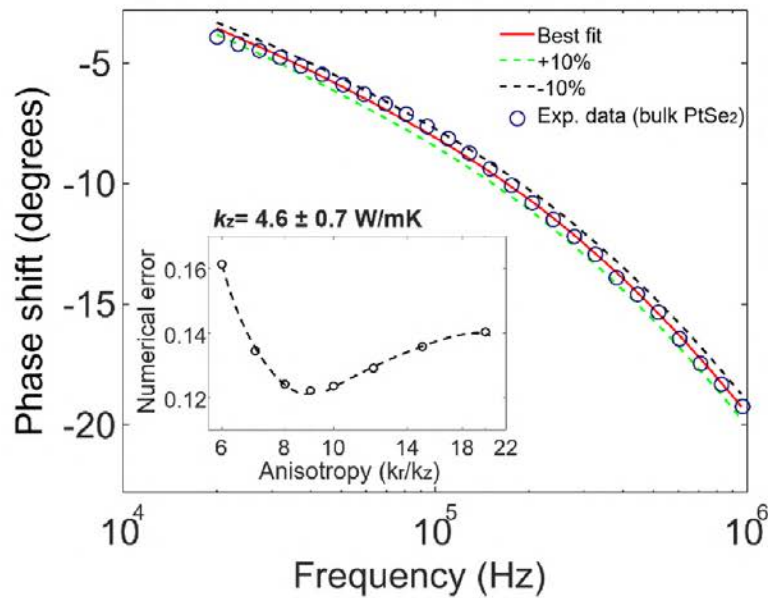
Supplementary Figure 9 shows the Raman spectra and fast Fourier transform of the layered breathing modes for different film thicknesses. From the FFT spectra we can observe a second peak located at higher energy than the LBM. It means that the experimental data should be fitted with two-exponential model as is also shown in the work of Chen et al.<sup>7</sup> The origin of this second peak is associated to a Raman inactive standing wave produced by the interaction of the thin film with the substrate.



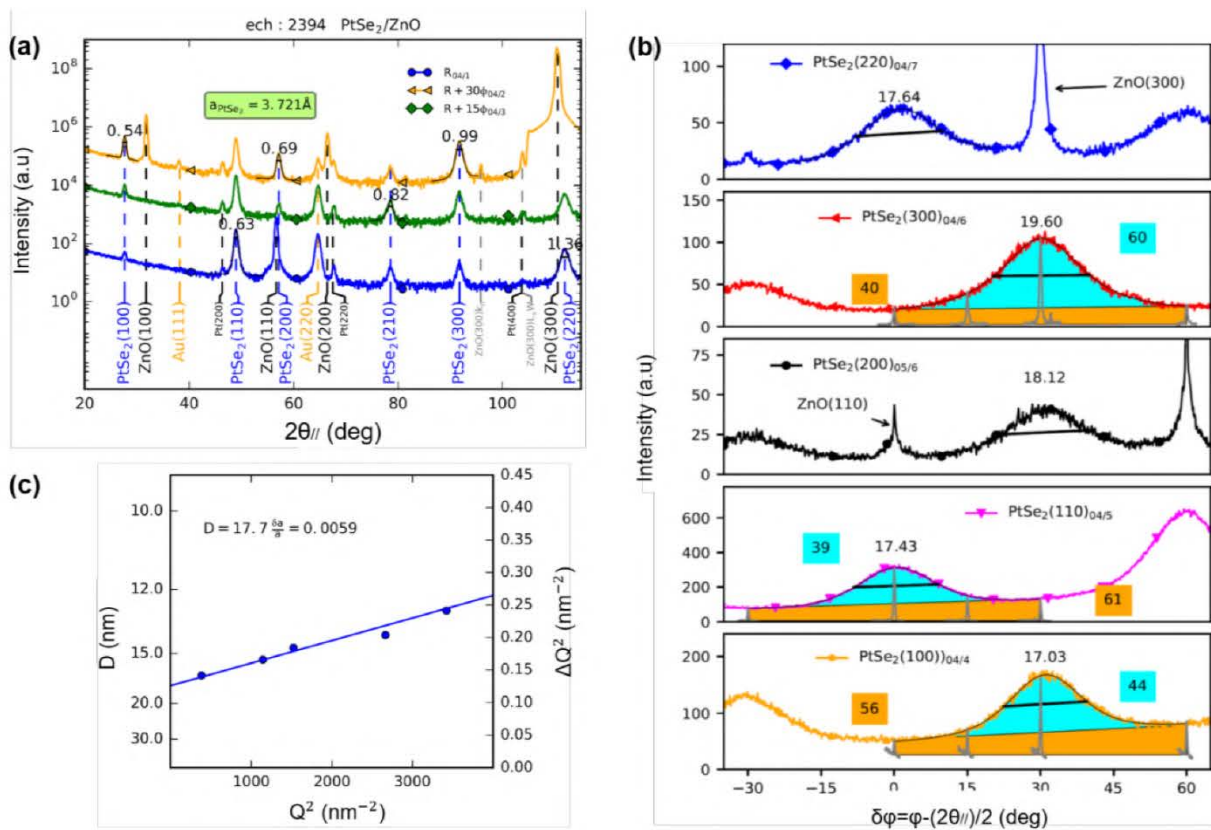
**Supplementary Figure 9. Fast Fourier transform of the layered breathing modes.** Layer-dependent breathing modes measured by Raman spectroscopy (black line) and Fast Fourier transform (FFT) of ASOPS signals (red lines).



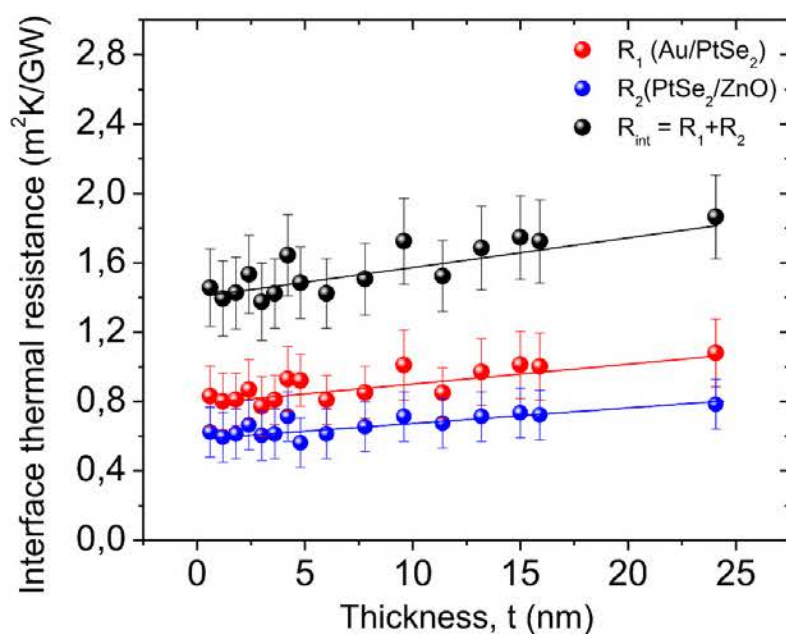
**Supplementary Figure 10. DFT calculations.** Normalized thermal conductivity accumulation as a function of the phonon frequency for thin films of thicknesses ranging from 1 to 10 nm and bulk PtSe<sub>2</sub>.



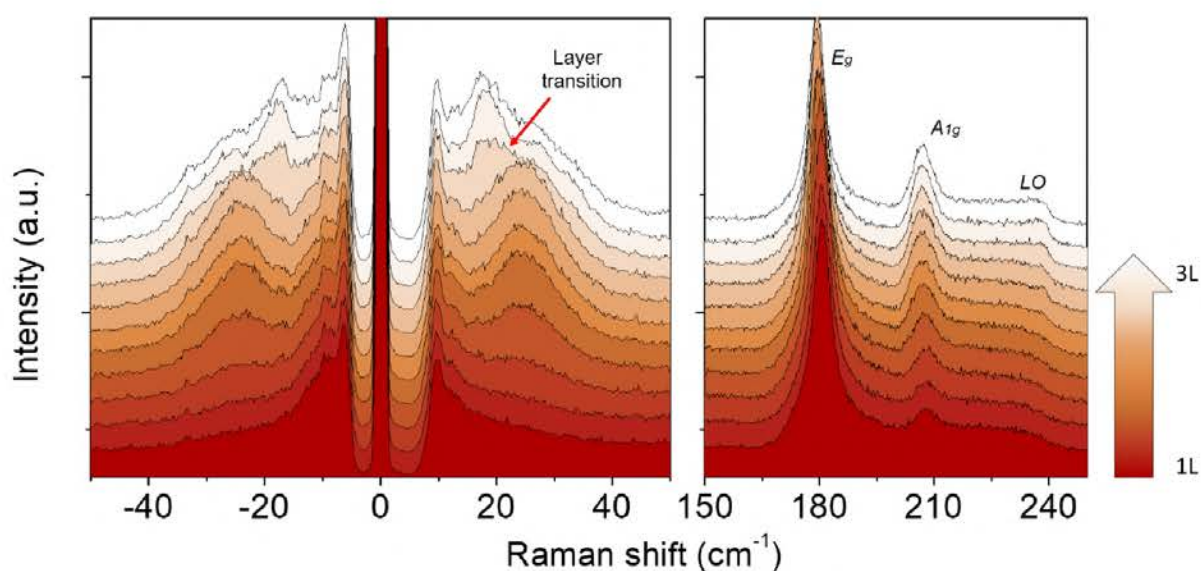
**Supplementary Figure 11.** FDTR data from bulk PtSe<sub>2</sub> crystal and the best model fit in a low frequency range (20 kHz - 1 MHz) for a ratio  $k_r/k_z = 9$ . The inset graph shows the calculated numerical errors of fits with different anisotropies.



**Supplementary Figure 12.** (a) XRD radial scans in the polycrystalline wedge sample showing the polycrystalline nature of the PtSe<sub>2</sub> film. The PtSe<sub>2</sub> peaks are present along the 3 directions showing the isotropic character. We can see Au (covering a large part of the sample surface) since those measurements performed after the FDTR experiments. (b) Azimuthal scans of the PtSe<sub>2</sub> Bragg peaks, from which we obtain broad peaks ( $\sim 18^\circ$ ) and  $\sim 50\%$  of grains are randomly oriented in-plane. Because of the wedge structure, the intensity varies in azimuthal scans. (c)  $\Delta Q^2$  as a function of  $Q^2$  for the radial and azimuthal scans. From the intercept and the slope of the radial scans we can determine the domain size  $D$  and the in-plane lattice parameter distribution  $\Delta a/a$ .



**Supplementary Figure 13. Interface thermal resistance measurements.** The black spheres represent the total interface thermal resistance values,  $R_{\text{int}}$ , taking into account the Au/PtSe<sub>2</sub> (red spheres) and PtSe<sub>2</sub>/ZnO (blue spheres) interface thermal resistances extracted by the FDTR measurements. The errors bars were estimated by the standard deviation of several measurements, including the numerical errors from the fits.



**Supplementary Figure 14. Raman line scan between 1 and 3 ML PtSe<sub>2</sub> in the crystalline wedge sample.**

## Supplementary References

1. Renaud, G., Barbier, A. & Robach, O. Growth, structure, and morphology of the Pd/MgO(001) interface: Epitaxial site and interfacial distance. *Phys. Rev. B* **60**, 5872–5882 (1999).
2. Schmidt, A. J., Cheaito, R. & Chiesa, M. A frequency-domain thermoreflectance method for the characterization of thermal properties. *Rev. Sci. Instrum.* **80**, 094901 (2009).
3. Zhang, H., Chen, X., Jho, Y.-D. & Minnich, A. J. Temperature-Dependent Mean Free Path Spectra of Thermal Phonons Along the c -Axis of Graphite. *Nano Lett.* **16**, 1643–1649 (2016).
4. Nemoto, S. Measurement of the refractive index of liquid using laser beam displacement. *Appl. Opt.* **31**, 6690 (1992).
5. Cahill, D. G. Thermal conductivity measurement from 30 to 750 K: the  $3\omega$  method. *Rev. Sci. Instrum.* **61**, 802 (1990).
6. Cahill, D. G. Erratum: “Thermal conductivity measurement from 30 to 750 K: The  $3\omega$  method” [Rev. Sci. Instrum. 61, 802 (1990)]. *Rev. Sci. Instrum.* **73**, 3701 (2002).
7. Chen, X. *et al.* Direct observation of interlayer coherent acoustic phonon dynamics in bilayer and few-layer PtSe 2. *Photonics Res.* **7**, 1416 (2019).

# 5. Manipulating thermal conductivity of layered MoS<sub>2</sub>

## 5.1 Introduction

Overheating is one of the main reasons for device failure in modern electronics. Managing this excess heat is a challenge and a significant recent research efforts to have been dedicated to control and manipulate heat transport on the nanoscale<sup>80–84</sup>. A viable solution to the issue of thermal engineering and waste heat conversion could be 2D materials. Materials with very high thermal conductivities ( $\kappa$ ) such as graphene (2000 W/mK)<sup>85,86</sup> and hBN (700-450 W/mK)<sup>87,88</sup> already find commercial applications in heat spreading. Materials with lower  $\kappa$ , such as semiconducting transition metal dichalcogenides (TMDs) (25 W/mK - 100 W/mK, for single layer and bulk, respectively<sup>89–93</sup>) have potential for applications in thermoelectric generation<sup>94</sup>, thermal rectification<sup>95</sup> or heat routing, ie blocking or guiding the heat through a precisely defined path<sup>96,97</sup>. Heat routing could have significant implications for 2D material-based electronics, nanoelectromechanical systems, and sensors by enabling the accurately dissipating of heat from hotspots without damaging the underlying structures. However, such devices have not yet been proven using layered materials.

Therefore, with the advent of layered material-based electronics, an understanding of their thermal properties is important to enable the efficient dissipation of excess heat from electronic components. Fourier's law of heat conduction is valid in layered materials for describing heat diffusion, which provide theoretical guidelines for layered materials-based applications.<sup>59,94,98</sup> The previous sections showed that the thermal conductivity of layered materials can be affected by their own factors, such as type of material, thickness, surface roughness, point defects, vacancies, and grain boundaries, etc.<sup>33,99</sup> Additionally, thermal conductivity of materials can be manipulated by changing substrates and annealing. Nanopatterning with periodic holey structures have also been utilized as able to change the thermal conductivity of layered materials because holey structures can give rise to new acoustic dispersions and band structures due to the periodic Bragg scattering as well as localized Mie scattering from



the individuals.<sup>100</sup> These standard nanopatterning techniques, including nanolithography and FIB, have been shown to work efficiently for other materials, such as silicon, as a consequence of a reduction of the acoustic phonon mean free paths (MFPs)<sup>32,101–103</sup>. In the case of MoS<sub>2</sub>, existing theoretical work points to rather short phonon MFPs, on the order of 5–20 nm<sup>89,92,104</sup>. Still, a recent theoretical study indicated that even nanostructures with a periodicity of about 400 nm could already significantly reduce the in-plane  $\kappa$  for monolayer MoS<sub>2</sub><sup>105</sup>. Still, no systematic experimental studies of nanopatterning effects on  $\kappa$  in MoS<sub>2</sub> have been reported.

Here we first studied the annealing effected on the thermal conductivity of MoS<sub>2</sub> nanosheets-based membranes, where their thermal conductivities were increasing with the increased annealing temperature. The next we proposed a structure based on free-standing, few-layer, nanopatterned MoS<sub>2</sub> for thermal routing applications. That is, blocks and conducts heat from a hotspot through a predefined path in the in-plane direction. We started by using an EBL and ICP to fabricate a holey area on a large-area free-standing polycrystalline MoS<sub>2</sub> membrane. Because of the unsolved issue of polymer attached on the surface of 2D materials and the resulting problem of measuring thermal conductivity of MoS<sub>2</sub> membranes nanopatterned by EBL, we only studied the effects of FIB-based nanopatterning on the thermal conductivity of MoS<sub>2</sub> nanosheets-based membranes. Selective patterning of specific areas makes a big difference in thermal conductivity within the same material. Therefore, the patterned area acts as a high thermal resistance. We obtain a thermal resistance of  $4 \cdot 10^{-6}$  m<sup>2</sup>K/W with only four patterned lattice periods of 300 nm, highlighting the significant potential of MoS<sub>2</sub> in thermal management applications.

We arrive at these designs via a thorough study of the in-plane thermal conductivity as a function of thickness, temperature, and porosity in both pristine and nanopatterned MoS<sub>2</sub> membranes. 2LRT was used to measure the thermal conductivity of a series of free-standing MoS<sub>2</sub> flakes with diameters more than 20  $\mu$ m and thicknesses from 5 to 40 nm, resulting in values from 30 to 85 W/mK, respectively. After nanostructuring a square lattice of holes with a diameter of about 100-nm with a FIB, the thermal conductivity decreased by more than 90% in the 500 nm cycle, and a value of less than 1 W/mK was obtained in the 300 nm cycle. The results were supported by EMD for both pristine and nanopatterned MoS<sub>2</sub>.

## 5.2 Improving thermal conductivity of layered MoS<sub>2</sub> by annealing

Because the method of synthesizing large amounts of MoS<sub>2</sub> nanosheets is much easier and cheaper than synthesizing MoS<sub>2</sub> monolayers. MoS<sub>2</sub> nanosheets have been used for the fabrication of optoelectronic,<sup>106</sup> and transistors,<sup>59,98,107</sup> and thermoelectric devices.<sup>64,71,108</sup> In order to study the temperature effects on the thermal conductivity of layered MoS<sub>2</sub> nanosheets-based membranes, in this chapter, we studied the annealing method which used to increase thermal conductivity of MoS<sub>2</sub> nanosheets based membrane by increasing the interface quality among the MoS<sub>2</sub> nanosheets. The aim of the study was to solve the disadvantage of MoS<sub>2</sub> nanosheets based membrane which has a super low thermal conductivity of ~0.1 W/mK. Herein, we studied the thermal conductivity of MoS<sub>2</sub> nanosheets-based membrane affected by annealing in furnaces in the argon environment. The experimental data showed that membranes made from the solution exfoliated MoS<sub>2</sub> nanosheets and annealed at varies temperatures had different thermal conductivities.

There are two main methods used to synthesize MoS<sub>2</sub> nanosheets: lithium-interaction assisted solution exfoliation and ultrasonication exfoliation. In comparison with lithium-interaction, the ultrasonication solution exfoliation method can produce pure MoS<sub>2</sub> nanosheets without additional reagent, especially lithium which can probably increase electrical and thermal conductivity of the materials. Additionally the ultrasonication solution exfoliation method is an environmental friendly.<sup>109</sup> Accordingly, in this study MoS<sub>2</sub> nanosheets were synthesized using the ultrasonication solution exfoliation method as mentioned in Chapter 2. The samples were fabricated by dropping and drying the MoS<sub>2</sub> nanosheets solution on the free-standing 50nm thick and 1mm\*1mm area SiNx membranes, and then annealed at 298 K, 473 K, 573 K, 673 K, and 773 K in the LPCVD system with the gas flow of 200scmm Argon, respectively. The argon gas environment can protect the structure of MoS<sub>2</sub> nanosheets in high temperatures, as it prevents reaction with oxygen or water molecules. The maximum temperature was set as 773 K, because according to previous experience of synthesizing MoS<sub>2</sub> by a CVD system, MoS<sub>2</sub> starts to sublime when the surrounding temperature is higher than 773 K.

The two-laser Raman thermometry system was used to measure the  $k_r$  of these samples. Their original thermal conductivity was measured in a vacuum environment. Based on the analysis of the results of humidity sensors detailed in Chapter 6, water molecules in ambient environment can attach on the surface of MoS<sub>2</sub> nanosheets to build water ions channels that can result in the changes to electrical conductivity. We proposed that ambient humidity could also affect thermal conductivity of MoS<sub>2</sub> nanosheets-based membranes. Consequently, we also measured thermal conductivity of these samples at atmospheric pressure with the relative humidity ~40% (RH-40%) and nitrogen environment, respectively.

Line scanning measurements were made using 2LRT to plot the temperature distribution on the samples. In this work, the excitation power of the green laser applied was about 30  $\mu$ W. In order to get a clear temperature distribution curve, the blue laser energy was increased to 250  $\mu$ W, 500  $\mu$ W, and 500  $\mu$ W for these samples measured in vacuum, RH-40%, and nitrogen, respectively. Where the A<sub>1g</sub> peak position of the Raman spectra of the MoS<sub>2</sub> nanosheets on the heating point was shifted about 1.5 - 2  $\text{cm}^{-1}$ . The incident heating power applied on these samples in vacuum was much lower than the energy applied in atmospheric pressure, because the surrounding gas molecules at room temperature can absorb a lot of energy from the high temperature area. The precise energy of the blue laser absorbed by the samples was measured used four photodetectors, include the incident laser power, the transmitted laser power, the reflected laser power, and the transmitted reflected laser power. After measuring the original thermal conductivity, the samples were annealed at 473 K, 573 K, and 673 K, and then scanned again using 2LRT from -100  $\mu\text{m}$  to 100  $\mu\text{m}$  with a step of 2  $\mu\text{m}$ . The sample annealed at 773 K was scanned in the same process from -150  $\mu\text{m}$  to 150  $\mu\text{m}$  with a step of 5  $\mu\text{m}$ . Temperature coefficient is an important parameter for calculating the temperature distribution of the line scanning curves according to the Raman shift. In this study, we measured the temperature coefficient of these samples in a nitrogen environment only using the green laser with a low energy of ~30  $\mu$ W without heating up the samples. The temperature of substrates was controlled by increasing by current heating or cooling by the flowing of liquid nitrogen, while this can also be easily done at atmospheric pressure, but in a vacuum, it is more difficult due to the poor connection between the sample and substrate. The Raman shifts of the MoS<sub>2</sub> nanosheets based membranes were recorded as the temperature of the

substrates increased from 113 K to 353 K with a step of 40 K. The temperature was maintained for 20 minutes to ensure that all of the MoS<sub>2</sub> membranes reached the temperature setting point.

The curves of two Raman peaks E<sup>1</sup><sub>2g</sub> (~ 380 cm<sup>-1</sup>) and A<sub>1g</sub> (~ 407 cm<sup>-1</sup>) as a function of the temperature were plotted for the calculation of the temperature coefficient for the samples. The data showed that the temperature coefficients of E<sup>1</sup><sub>2g</sub> and A<sub>1g</sub> were ~-0.010 and ~-0.008 ± 0.001 K/cm<sup>-1</sup>, respectively, and these parameters did not change with the annealing temperatures and were applied on the MoS<sub>2</sub> nanosheets-based membranes. We can therefore postulate that the structure of our samples was not changed in the annealing process, as evidenced by our results which showed that annealing the MoS<sub>2</sub> nanosheets-membranes from 473 K – 773 K only enhanced the interface quality of the MoS<sub>2</sub> nanosheets without changing their structures. According to the calculation process of the 2LRT discussed above, the calculation of thermal conductivity is based on the thickness of the MoS<sub>2</sub> nanosheets based membranes, and the slope of the temperature distribution in logarithmic scale of the measurement. Therefore, we calculated and plotted the curves of the temperature distribution as a function with the logarithmic scanning position. As shown in Figure 8, we measured the thermal conductivity of these samples in RH-40%, in nitrogen in atmospheric pressure, and in vacuum. The thickness of MoS<sub>2</sub> nanosheets on the supported area of the samples along a scratch were first measured using scanning thermal microscopy (SThM). However, because the thickness of the supported area on the boundary of the samples was probably not the same as the thickness of the suspended area in the center area of the samples, the calculated thermal conductivity had a relatively large error bar. Herein, we used a FIB system to cut lines in the center area of the membranes for measuring their thickness with more accurately. The pristine MoS<sub>2</sub> nanosheets-based membrane had a similar thermal conductivity of 0.1 W/mK to the sample annealed at 473K. Herein, we only compared the thermal conductivity of samples fabricated under similar conditions. The results show that as the annealed temperature increased from 473 K to 773K, thermal conductivity of these samples measured in vacuum increased from 0.08 ± 0.03 W/mK to 0.2 ± 0.04 W/mK, although the increase in thermal conductivity in RH-40% and nitrogen environment was not obviously.

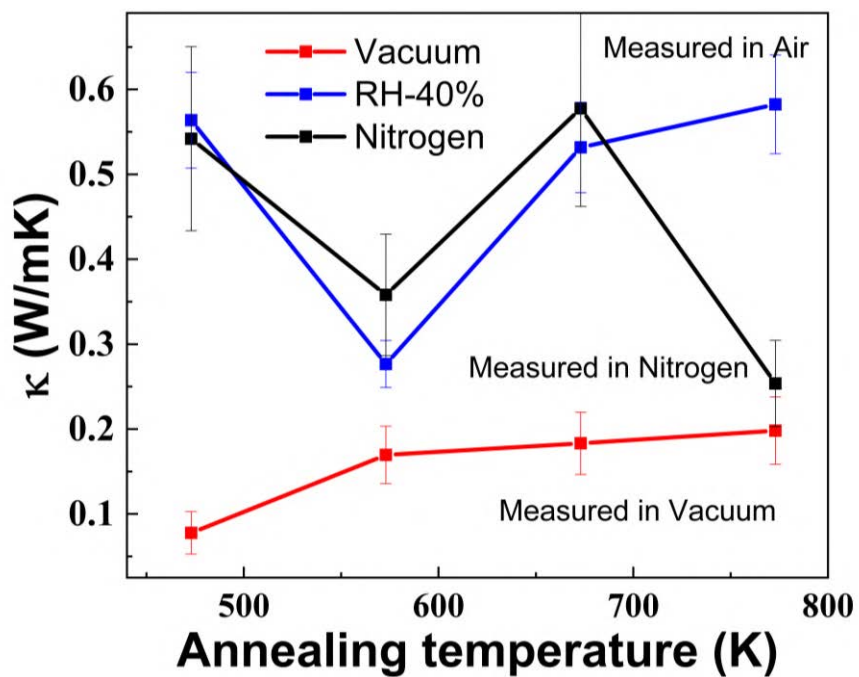


Fig. 8. Thermal conductivity of the MoS<sub>2</sub> nanosheets-based membranes annealing at 473 K, 573 K, 673 K, and 773 K and measured in vacuum, RH-40%, and nitrogen, respectively.

## 5.3 Heat routing in nanopatterned MoS<sub>2</sub>

In this work we have designed, fabricated and tested two heat routing structures: a thermal insulating ring which confines heat in a delimited area, and a heat guiding Z-shape channel which confines heat and conducts it away from a source. The heat routing structures were based on free-standing, single-crystalline MoS<sub>2</sub> membranes with diameter of 30  $\mu\text{m}$  and thickness of 10 nm. The samples were prepared using mechanical exfoliation and dry transfer and FIB was employed to pattern the areas which delimited the heat flow. To measure the temperature distributions of the patterned MoS<sub>2</sub> structures 2LRT set-up was used. The technique has been successfully employed for measuring thermal conductivities of free-standing 2D materials<sup>33,110,111</sup>. In the thermal insulating ring, the thermal boundary conductance of the patterned region  $G = 1/R = 0.25 \text{ MW/m}^2\text{K}$  and thermal conductivity below 1 W/mK. We also measured the temperature distribution inside the Z-channel, decreased from the hotspot towards the heatsink at the membrane edges. These results demonstrated the efficiency of the nanopatterning of layered materials for heat management applications.

These structures were based on measurements, and simulation of thermal transport in few-layer pristine and nanopatterned MoS<sub>2</sub>. We measured the in-plane  $\kappa$  of large-area, free-standing, few-layer MoS<sub>2</sub> membranes with thicknesses from 5 to 40 nm and diameters of 20 and 30  $\mu\text{m}$  using 2LRT. Due to the system symmetry, in 2LRT the line scan Raman spectra can be collected when the probe laser linearly scans the free-standing membrane through the center<sup>32,33,112</sup>. Thermal conductivity of pristine MoS<sub>2</sub> increased from  $34 \pm 3 \text{ W/mK}$  to  $88 \pm 5 \text{ W/mK}$  as the thickness increased from 6 nm to 40 nm. We observed almost linear dependence the  $\kappa$  as a function of thickness. A small minimum observed for the 6 nm thick sample can be explained as competition between the phonon-phonon and surface-phonon scattering<sup>113</sup>. Subsequently, samples with lattice periods ranging 300 to 500 nm were fabricated in these same membranes using a FIB, and their thermal conductivity was re-measured. In comparison, the patterned membranes with  $a = 500 \text{ nm}$  showed a significant, 10-fold reduction of thermal conductivity. An additional sample with  $a = 300 \text{ nm}$  showed an even lower thermal conductivity, below 1 W/mK which approaches the amorphous value<sup>91,102</sup>

We used MD simulations to better understand the thickness and patterning effects on the thermal conductivity of MoS<sub>2</sub>. The thermal conductivity was studied with the EMD method<sup>114</sup> using the LAMMPS package and the REBO-LJ potential<sup>115</sup>. The increase in  $\kappa$  as a function of the MoS<sub>2</sub> thickness obtained with the EMD simulations was in good agreement with the experimental results. The 4 nm thick MoS<sub>2</sub> membranes with  $a = 500$  nm showed an experimental thermal conductivity of about  $3.8 \pm 1$  W/mK. The in-plane thermal conductivity calculated by EMD is  $5.2 \pm 2.3$  W/mK, a value that was in agreement with the experimental values, and hence validates the aforementioned modelling procedure.

Finally, for the high-temperature applications it is crucial to know the temperature dependence of the thermal conductivity  $\kappa(T)$  for both the pristine and patterned MoS<sub>2</sub> membranes. For the pristine membrane a 30% reduction in  $\kappa$  was measured as temperature was increased from 300 to 450 K, similar to the decrease predicted by the EMD. For the patterned MoS<sub>2</sub>, a reduction of about 10% was measured for the same temperature increase. These results confirmed that the temperature more strongly affects the phonon MFPs of the pristine membrane than that of the patterned MoS<sub>2</sub>. For the pristine MoS<sub>2</sub>, Umklapp phonon-phonon and higher order scattering are dominant at higher temperatures. On the contrary, for the patterned MoS<sub>2</sub>, scattering from the holes constitutes the majority of scattering events and thus phonon-phonon interactions are less significant. Even so, at 500 K the five-times difference in  $\kappa$  between the patterned and pristine MoS<sub>2</sub> was observed, validating its potential for applications at high temperatures.

More details are discussed in the following paper Article 3.

## 5.4 Conclusion

In this work, the results showed the thermal conductivity of MoS<sub>2</sub> nanosheets based membrane increased by about 140% by annealing at 673K for 3 hours. The thickness dependent  $\kappa_r$  of layered MoS<sub>2</sub> membrane was also demonstrated and increased from  $30 \pm 3$  W/mK at 4.5 nm to  $88 \pm 3$  W/mK at 40 nm. The thermal conductivity of the nanopatterned area with a period 500nm was reduced by more than 90%. Thermal conductivity of less than 1W/mK was achieved with a period of 300 nm. The results were confirmed with EMD simulations of the pristine membranes and properly reduced

unit cells of nanostructured membranes. We demonstrated that porosity for reducing the same percentage thermal conductivity of layered materials could be much smaller than the other traditional materials such as silicon and silicon carbide. Finally, we designed, fabricated, and validated two heat routing structures: MoS<sub>2</sub> thermal insulator and MoS<sub>2</sub> heat conduction channel. Our findings have the potential to trigger new strategies for heat dissipation and passive cooling in 2D-based electronics operating in high temperatures and high temperature gradients environments.



# Article 3

# Thermal Routing in Nanopatterned MoS<sub>2</sub>

Peng Xiao<sup>1,2\*+</sup>, Alexandros El Sachat<sup>1\*</sup>, Emigdio Chávez Angel<sup>1</sup>, Ryan C. Ng<sup>1</sup>, Giorgos Nikoulis<sup>3</sup>, Joseph Kioseoglou<sup>3</sup>, Konstantinos Termentzidis<sup>4</sup>, Clivia M. Sotomayor Torres<sup>1,5</sup>, and Marianna Sledzinska<sup>1+</sup>

<sup>1</sup>Catalan Institute of Nanoscience and Nanotechnology (ICN2), CSIC and BIST, Campus UAB, Bellaterra, 08193 Barcelona, Spain

<sup>2</sup>Departamento de Física, Universidad Autónoma de Barcelona, Bellaterra, 08193 Barcelona, Spain

<sup>3</sup>Department of Physics, Aristotle University of Thessaloniki, GR-54124 Thessaloniki, Greece

<sup>4</sup>Univ Lyon, CNRS, INSA Lyon, CETHIL, UMR5008 69621 Villeurbanne, France

<sup>5</sup>ICREA, Passeig Lluís Companys 23, 08010 Barcelona, Spain

\*e-mail: [peng.xiao@icn2.cat](mailto:peng.xiao@icn2.cat); [marianna.sledzinska@icn2.cat](mailto:marianna.sledzinska@icn2.cat)

## ABSTRACT

In modern electronics overheating is one of the primary causes of device failure. Recently, 2D materials are emerging in electronics due to their nature atomic thickness and excellent electronic performance, an understanding of their thermal properties is crucial to enable the efficient transfer of excess heat away from the electronic components. In this work we propose structures based on free-standing, few-layer, nanopatterned MoS<sub>2</sub> to route heat flow. Specifically, we demonstrate the creation of a pre-defined path in the in-plane direction through the combination of the blocking and subsequent guiding of heat away from a thermal hotspot. By selective patterning of the MoS<sub>2</sub> surface, we are able to vary and control the thermal conductivity within the same material. The patterned regions act as high thermal resistors: exhibiting a thermal resistance of as large as  $4 \cdot 10^{-6} \text{ m}^2\text{K/W}$  resulting from as few as four patterned lattice periods with 300 nm spacing, highlighting the significant potential of MoS<sub>2</sub> for thermal management applications. The in-plane thermal conductivity as a function of thickness, porosity, and temperature in both pristine and nanopatterned MoS<sub>2</sub> membranes were measured using a Two-laser Raman thermometry. After nanopatterning with a focused ion beam we have obtained a greater than ~10-fold and ~88-fold reduction of the thermal conductivities for the patterned period of 500 nm and 300 nm, respectively. Notably, the layered MoS<sub>2</sub> shows higher sensitive to nanopatterning than silicon and silicon carbide by reducing thermal conductivity with a small porosity. The results were supported by equilibrium molecular dynamic simulations for both pristine and nanopatterned MoS<sub>2</sub>.

**Keywords:** MoS<sub>2</sub>, thermal conductivity, heat routing, heat guiding, nanopatterning

Electrons move increasingly faster through increasingly smaller silicon circuits to enrich the capacity and speed chips. However, their performance is often limited by excessive heat generation during device operation, which threatens their proper function. Managing this excess heat is a challenge and significant recent research efforts have been devoted to control and manipulate heat transport on the nanoscale<sup>1-5</sup>. A viable avenue towards improved thermal engineering solutions and waste heat conversion could be 2D materials. Materials with very

high thermal conductivities ( $\kappa$ ) such as graphene (2000 W/mK)<sup>6,7</sup> and hexagonal boron nitride (hBN) (700-450 W/mK)<sup>8,9</sup> have already found commercial applications in heat spreading, due to their ability to efficiently transfer and disperse heat. Materials with lower  $\kappa$ , such as semiconducting transition metal dichalcogenides (TMDs) (25 W/mK - 100 W/mK, for single layer and bulk materials, respectively<sup>10-14</sup>) have potential for applications in thermoelectric generation<sup>15</sup>, thermal rectification<sup>16</sup> or heat routing. This lattermost application focuses on the ability to direct heat along a precisely defined path through a combination of blocking and subsequent guiding of the heat<sup>17,18</sup>. Heat routing could have significant implications for 2D material-based electronics, nano-electromechanical systems (NEMS) and sensing devices by enabling the precise dissipation of heat away from hotspots without damaging subjacent structures. However, such devices have yet to be demonstrated using TMDs.

One obstacle to the incorporation of TMDs for heat routing applications is the requirement of a *local* control of  $\kappa$ . While the  $\kappa$  of MoS<sub>2</sub> can be decreased by introducing defects or grain boundaries<sup>19,20</sup>, there are no existing systematic studies on locally engineering the  $\kappa$ . One strategy to reduce  $\kappa$  is via nanostructuring of the material, such as by patterning periodically arranged holes. These structures can be achieved using standard nanofabrication techniques, such as electron beam lithography and dry etching or focused ion beam (FIB). These standard techniques have been shown to work efficiently in other materials, such as silicon, due to the reduction of the acoustic phonon mean free paths (MFPs)<sup>21,22</sup>. In the case of MoS<sub>2</sub>, existing theoretical work points to rather short phonon MFPs, on the order of 5–20 nm<sup>10,13,23</sup>. A recent theoretical study indicated that even nanostructures with a periodicity of about 400 nm could already significantly reduce the in-plane  $\kappa$  for monolayer MoS<sub>2</sub><sup>24</sup>, although no systematic experimental studies of nanopatterning effects on  $\kappa$  in MoS<sub>2</sub> have been reported to date.

Additionally, nanostructuring has been proposed to reduce the thermal conductivity of materials such as silicon and silicon carbide for improving their thermoelectric performance.<sup>25</sup> It is difficult to reduce  $\kappa$  of silicon (Si) and silicon carbide (SiC) crystalline by nanostructuring, normally a porosity of 0.2 – 0.5 of nanostructuring was applied for reducing their half  $\kappa$ ,<sup>22,26,27</sup> however, which resulting in a limited improvement of thermoelectric performance because a large electrical conductivity is reduced for the large porosity. Layered materials, including MoS<sub>2</sub>, show the large anisotropic thermal conductivities,<sup>28,29</sup> are expected to be more sensitive to the nanostructuring for better thermoelectric performance.

In this work we have designed, fabricated, and tested two heat routing structures: a thermal insulating ring which confines heat in a delimited area, and a heat guiding channel which confines heat and conducts it away from a source. We measured the in-plane  $\kappa$  of large-area, free-standing, few-layer MoS<sub>2</sub> membranes using two-laser Raman thermometry (2LRT). Subsequently, samples with lattice periods ranging 300 to 500 nm were fabricated in these same membranes using a focused ion beam (FIB), and their  $\kappa$  was re-measured. The effect of sample thickness and temperature on the  $\kappa$  of pristine and nanopatterned MoS<sub>2</sub> were calculated via equilibrium molecular dynamics (EMD) based on the auto correlation function of the heat flux. Our results indicate that nanopatterning technique in layered materials is a promising platform for thermal management applications and thermoelectric.

## RESULTS AND DISCUSSION

### MoS<sub>2</sub> thermal insulator and heat conduction channel

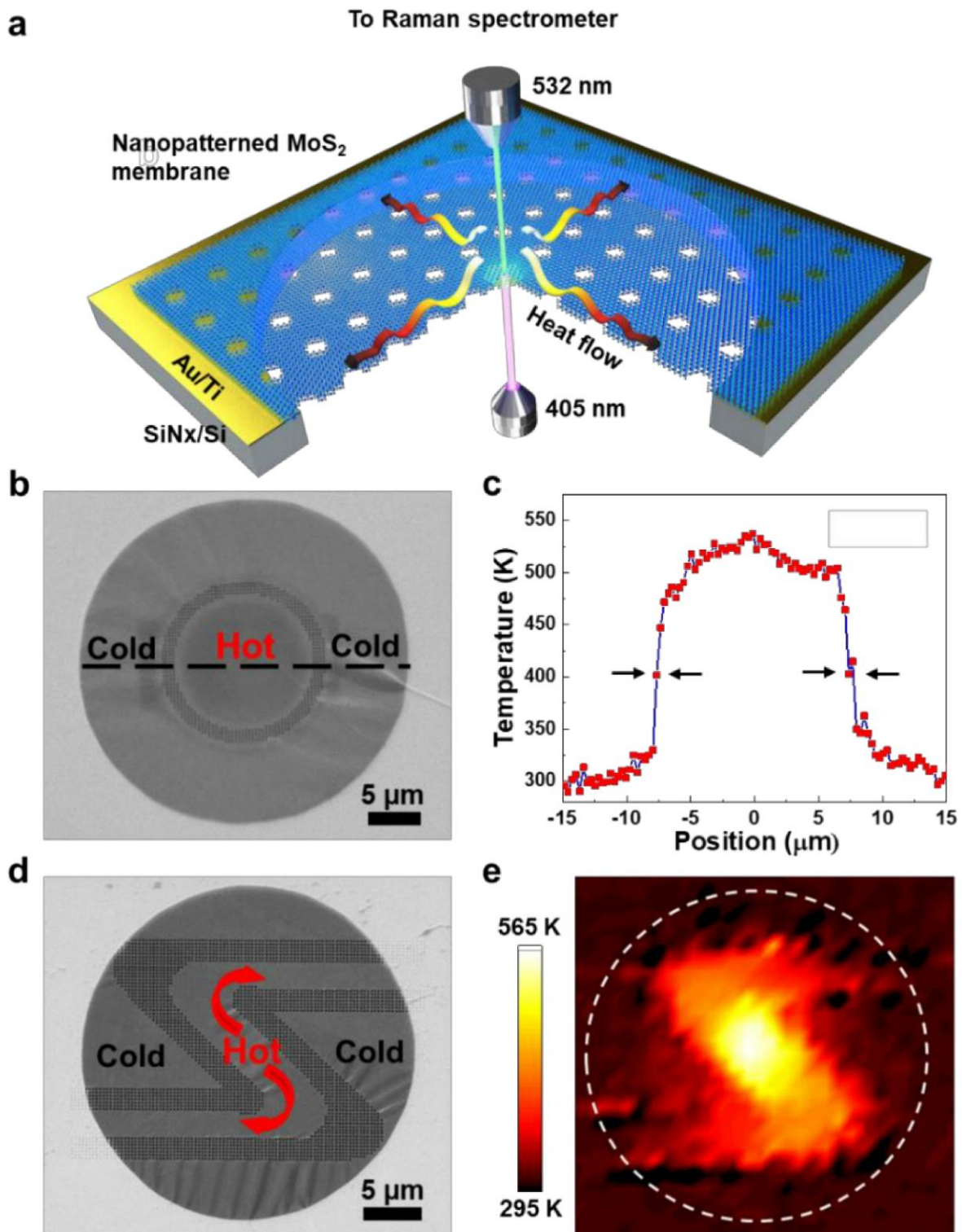
The heat routing devices are based on free-standing, single-crystalline MoS<sub>2</sub> membranes with a diameter of 30  $\mu\text{m}$  and a thickness of 10 nm. The samples were prepared using mechanical exfoliation and dry transfer, followed by FIB to pattern the areas that delimit the heat flow. A schematic of the sample and experimental set-up is shown in Figure. 1a. Details of the nanofabrication and measurements are described in the *Materials and Methods* section.

To measure the temperature distributions of the patterned MoS<sub>2</sub> devices, a 2LRT set-up was used. This technique has previously been successfully employed for measuring thermal conductivities of free-standing 2D materials<sup>19,29,30</sup>. A high power, heating laser (405 nm) couples to the sample from the bottom, creating a temperature gradient that translates to a shift in the frequency of the Raman active modes E<sub>2g</sub> and A<sub>1g</sub> of MoS<sub>2</sub>. The modes are measured using a low-power probe laser (532 nm,  $P_{probe} \sim 10 \mu\text{W}$ ) coupled to the Raman spectrometer. The A<sub>1g</sub> peak frequency change is converted to temperature, using previously acquired calibration curves (Figure. S1 and Table T1 in *Supporting Information*).

A heat insulating ring with radius  $r = 7.5 \mu\text{m}$  and four lattice periods  $a = 300 \text{ nm}$  was patterned on a free-standing MoS<sub>2</sub> membrane and is shown in Figure 1b and S2. The heating laser was focused onto the center of the membrane to create a hotspot. The temperature profile for the absorbed heating power  $P = 28.4 \mu\text{W}$  was recorded, along the dashed line in Figure 1b. The center of the membrane, i.e., inside the ring, maintained the temperature at approximately 500 K. A sharp drop of the temperature down to 330 K was recorded between the inner and outer parts of the ring, indicating that the ring blocked most of the heat flow from the center to the edges of the membrane, as shown in Figure 1c. The temperature of the outer part of the MoS<sub>2</sub> was almost unaffected by the heating and maintained a temperature between 300 and 330 K.

All the measurements were performed in vacuum with no convection or heat transfer to air. Therefore, no other dissipation channels were available and the only path for the heat to follow was through the patterned area. The corresponding thermal resistance  $R$  of the patterned region can be calculated from  $Q = \Delta T/R$ , where  $Q$  is the heat flux and  $\Delta T$  is the temperature drop. The calculated  $R$  is  $4 \cdot 10^{-6} \text{ m}^2\text{K/W}$ , which corresponds to a thermal boundary conductance  $G = 1/R = 0.25 \text{ MW/m}^2\text{K}$  and a  $\kappa$  below  $1 \text{ W/mK}$ .

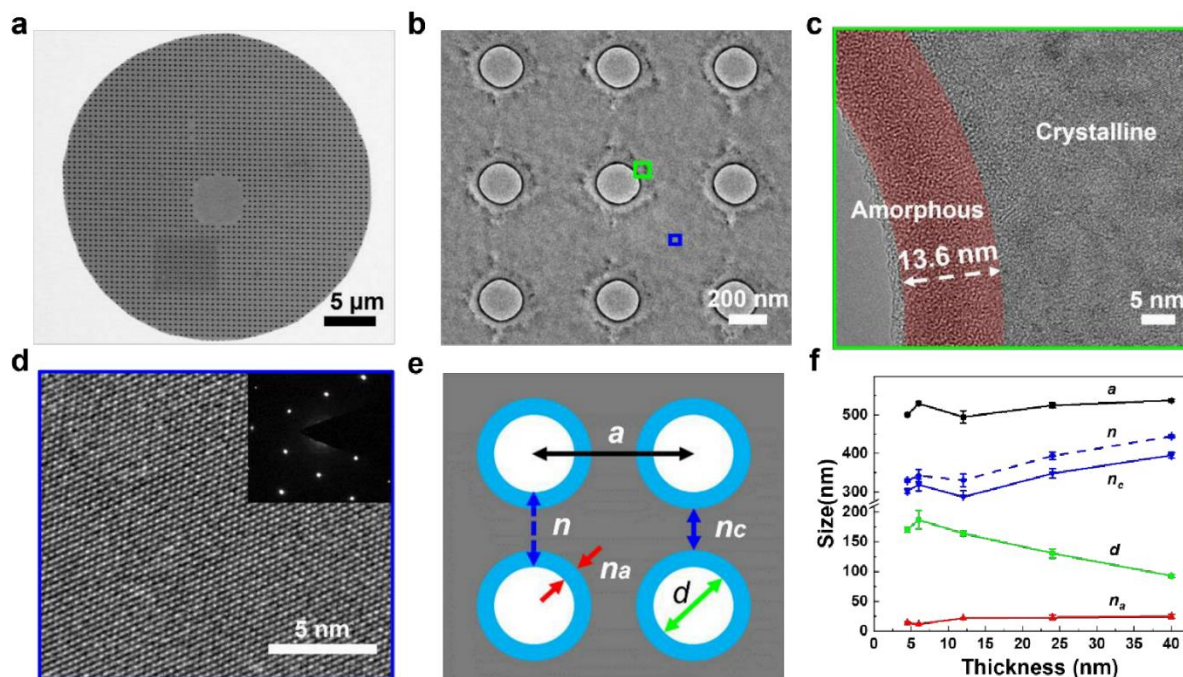
We further extended this idea by fabricating a Z-shaped heat guiding channel ( $a = 300 \text{ nm}$ , patterned area width  $w = 2.1 \mu\text{m}$ , channel width  $w = 3.6 \mu\text{m}$ ) on the MoS<sub>2</sub> membrane (Figure 1d and S3). The heating laser was focused on the center of the membrane, creating a hotspot with temperature of 560 K, and a corresponding temperature map of this membranes is shown in Figure 1e. The temperature inside the channel, decreased from the hotspot towards the heatsink at the membrane edges. Thus, the lateral heat flow was delimited by the patterned area and the free-standing area outside the channel was protected from the high temperatures. These results demonstrate the efficiency of the nanopatterning of TMDs for heat management applications.



**Figure 1. MoS<sub>2</sub> thermal insulator and heat conduction channel. (a) Schematic of the 2LRT set-up. (b) SEM image of a free-standing MoS<sub>2</sub> with a thermal insulator ring. Dashed line indicates the scan direction. (c) Corresponding temperature profile for the absorbed power  $P = 28.4 \mu\text{W}$  focused on the center of the sample. Arrows point to the heat insulating ring. (d) SEM image of a free-standing MoS<sub>2</sub> membrane with Z-shape heat conduction channel. (e) Corresponding temperature map for the absorbed power  $P = 8.5 \mu\text{W}$  focused on the center of the sample. Dashed line corresponds to the membrane edge.**

## Thermal conductivity of the pristine and patterned MoS<sub>2</sub>

Neck size and period of holey array always consider as the main parameters for estimate the thermal conductivity of nanopatterned materials. For examples,  $\kappa$  of nanopatterned Si and SiC were reported decreased with the decreasing neck size and period, and their  $\kappa$  decreased about ~50% than their pristine membranes after nanopatterned a hole array with a neck size down to ~50 nm or a period down to ~300 nm.<sup>22,26,27</sup> Due to the unique layered structured of MoS<sub>2</sub>, which the bulk material was reported has an in-plane and cross-plane  $\kappa$  of ~110 W/mK and ~2 W/mK, respectively.<sup>28,31–33</sup> The nanopatterned holey area perpendicular to the plane of MoS<sub>2</sub>



**Figure 2.** Characterization of the nanopatterned, free-standing MoS<sub>2</sub>. (a) SEM image of a suspended MoS<sub>2</sub> after FIB nanopatterning. (b) High resolution TEM image of a part of the holey array on a 4.5 nm thick nanopatterned MoS<sub>2</sub> membrane. (c) TEM image of the hole edge at the region that corresponds to the green square in panel (b). (d) High resolution TEM image of the crystalline neck at the region that corresponds to the blue square in panel (b) and the corresponding electron diffraction pattern. (e) Schematic of the unit cell of the patterned sample with period  $a$ , hole diameter  $d$ , neck  $n$ , crystalline neck  $n_c$ , amorphous width  $n_a$ , where  $n = a - d = n_c + n_a$ . (f) Unit cell parameters as a function of the MoS<sub>2</sub> thickness.

was estimated to only reduce the in-plane  $\kappa$  rather than the cross-plane  $\kappa$ . To confirm the underlying mechanism and rationalize the measured performance of the thermal management devices, and the implanted holey area effects on thermal properties of layered MoS<sub>2</sub>, we examined  $\kappa$  of free-standing MoS<sub>2</sub> membranes before and after nanopatterning of holey area with different periods. We fabricated a set of eight pristine MoS<sub>2</sub> membranes with thicknesses ranging from 5 to 40 nm and with diameters of 20 and 30  $\mu\text{m}$  (Figure S4), which the large area, thin free-standing membranes with a large ratio between radius and thickness of ~5000 times are good for the in-plane  $\kappa$  measurement with more accurate results. After measuring their  $\kappa$  using a 2LRT, holey arrays were subsequently patterned through the membrane using FIB with

two kinds of hole lattice period  $a$  of  $\sim 500$  nm and  $\sim 300$  nm. The central area was intentionally left unpatterned to be used to focus the heating laser for creating a stable hot spot, corresponding to the edged gold-coated substrate as a good heat sink (Figure 2a, b).

FIB patterning is known to damage crystalline structure and introduce amorphisation in processed samples, which has strong implications on thermal transport<sup>34</sup>. To minimize the damage and reduce other potential influencing factors, a low gallium ion current (2 pA) was used in this work to mill holes the MoS<sub>2</sub> membranes. In the TEM, the boundary region of the membrane near to holes can be seen to be amorphous (Figure 2c), the remaining area between the holes maintained its crystalline structure, as confirmed by TEM and electron diffraction (Figure 2d). Interface between the amorphous and crystalline phase is not sharp, the two phases are mixed in a small region. Figure 2e illustrates the lattice unit-cell, where  $a$  is the lattice parameter and  $d$  is the pore/hole diameter. A summary of the dimensional parameters of all the samples and corresponding TEM images are shown in Figure 2f and Figure S5. By keeping the value of  $a$  around 500 nm, the amorphous width  $n_a$  increased from  $\sim 10$  nm to  $\sim 25$  nm with the increasing membrane thickness, the hole diameter  $d$  decreased from  $\sim 190$  nm to  $\sim 90$  nm with the increasing membrane thickness, and correspondingly, neck size  $n$  and  $n_c$  both increased with the increasing of thickness. This is because the focused ion beam size was not changed by applying the same beam current, and the ion beam intensity conforms to Gaussian distribution with low-energy ions at its boundary. With the increase of membrane thickness, the energy at the edges of the ion beam was not enough gradually to etch MoS<sub>2</sub> but changed its structure. Therefore, the size of holes and the amorphous were decreased and increased with the increasing membrane thickness, respectively. A very small presence of Ga ions resulting from the FIB patterning was detected only in the 40 nm-thick sample, and almost no signal of Ga was detected in the 4.5 nm-thick sample (Figure S3) and thus is not expected to significantly affect the thermal transport. The size of the amorphous region around the holes patterned using the FIB is comparable to other fabrication techniques, such as laser ablation. As shown in Figure. S7, an apparent amorphous region induced by a high-power laser beam suggests that the amorphous MoS<sub>2</sub> can be generated by high temperature.

Thermal transport in 2D free-standing membranes is dominated by the in-plane thermal conductivity, which can be calculated using Fourier's law:  $P/(2\pi r t) = -\kappa dT/dr$  where  $P$  is the heating power absorbed by the sample,  $r$  is the distance from center hot spot to edged heat sink, and  $t$  is the membrane thickness. By taking  $r dT/dr = dT/d(\ln r)$  the following expression for  $\kappa$  was obtained:  $\kappa = -P/(2\pi t \frac{dT}{d(\ln r)})$ . Due to the system symmetry, in 2LRT the line scan Raman spectra can be collected when the probe laser linearly scans the free-standing membrane through the center<sup>19,22,35</sup>. An example of the experimental procedure for the 4.5-nm thick pristine and patterned MoS<sub>2</sub> is discussed in the *Supporting Information* and shown in Figure S8.

Thermal conductivity as a function of the thickness of MoS<sub>2</sub> is shown in Figure 3a. The  $\kappa$  of pristine MoS<sub>2</sub> increased from  $28 \pm 3$  W/mK to  $87 \pm 5$  W/mK as the thickness increased from 6 nm to 40 nm. We observed almost linear dependence the  $\kappa$  as a function of thickness. The surface defect-phonon scattering effects on the in-plane  $\kappa$  of MoS<sub>2</sub> become relatively weaker with the increasing membrane thickness, resulting in the increasing trends of  $\kappa$ . However, a minimum  $\kappa$  observed for the 6 nm thick sample, smaller than 4.5 nm samples with a  $\kappa$  of  $29 \pm 3$  W/mK, can be explained as competition between the phonon-phonon and surface-phonon

scattering. This result, previously observed also for supported MoS<sub>2</sub>, was reported at around 6.6 nm-thick sample,<sup>32,36</sup> in agreement with the results in this work.

The nanopatterned membranes followed the same trend as the pristine ones, which  $\kappa$  increased from  $2.8 \pm 0.6$  W/mK to  $6.5 \pm 0.9$  W/mK with the membrane thickness increased from 6 nm to 40 nm. The 4.5 nm thick sample show a  $\kappa$  of  $3.8 \pm 1.4$  W/mK and high than the  $\kappa$  of the 6 nm-thick sample. Herein, the increasing trend of  $\kappa$  of MoS<sub>2</sub> is consistent before and after nanopatterning. Besides, an additional sample with a smaller period  $a = 300$  nm showed an even lower  $\kappa$ , below 1 W/mK which approaches the amorphous value<sup>12</sup>. In Figure 3 b and c we compared the  $\kappa$  of nanopatterned MoS<sub>2</sub> as functions of the neck size and porosity. For  $a = 500$  nm  $\kappa$  decreased almost linearly with the increasing neck size and decreasing porosity, respectively. However, for  $a = 300$  nm we observed a sharp drop in  $\kappa$ , which might be similar to the effect observed previously for patterned silicon membranes<sup>37</sup>. These results show a high efficiency of nanopatterning on reducing the  $\kappa$  of MoS<sub>2</sub>, which can be extended to other layered materials. Finally, to evaluate the impact of nanopatterning on  $\kappa$ , a reduction factor  $R$  was simply defined as  $R = \kappa_p / \kappa$  to observe the magnitude of the decrease of  $\kappa$  in MoS<sub>2</sub>, where  $\kappa_p$  and  $\kappa$  are thermal conductivities of the pristine and patterned MoS<sub>2</sub>, respectively. In comparison, as shown in Figure 3d,  $R$  of the nanopatterned MoS<sub>2</sub> with  $a = 500$  nm is  $\sim 10$ , which increased to  $\sim 80$  when  $a = 300$  nm. Interestingly, for the nanopatterned samples with period  $a = 500$  nm, their  $R$  was plotted as a function of thickness as shown in Figure S10, the 4.5 nm thick sample with a  $R$  value of 7.7 is smaller than other samples with  $R > 10$ . This further confirms the predominant role of the hole boundary scattering. Such large  $R$  explained the previous discussion that nanopatterned MoS<sub>2</sub> was applied for the heat blocking and insulator applications.

Additionally, the changing porosity of these samples was used to evaluate the  $\kappa$  reduction efficiency of MoS<sub>2</sub>, which  $R$  increased from  $\sim 10$  to  $\sim 80$  when the porosity increased from  $\sim 0.09$  to  $\sim 0.27$ . The results were compared to the other reported nanopatterned Si and SiC membranes which needs a large porosity ( $> 0.3$ ) for realizing a low reductions factor ( $< 5$ ).<sup>26,27,38</sup> The nanopatterned MoS<sub>2</sub> membrane show a larger reduction factor than Si and SiC. Because nanopatterning technique normally only reduce the in-plane  $\kappa$  of materials when the holey array is induced perpendicular to the material surface. MoS<sub>2</sub>, one of the layered materials have a large anisotropic  $\kappa$ , which  $\kappa$  can be reduced efficiently by reducing its in-plane  $\kappa$  using the holey array. However, the anisotropic  $\kappa$  ratio in silicon is less than 2<sup>39</sup>, and resulting in the low reduction factor although using a nanostructure with a large porosity, which is also happened for SiC.

According to the figure of merit  $ZT$ , which is defined as  $ZT = S^2 \sigma T / \kappa$ , where  $S$  is the Seebeck coefficient,  $\sigma$  is the electric conductivity,  $T$  is the absolute temperature, is employed to evaluate the efficiency of thermoelectric. The large porosity of holey array applied in Si and SiC can reduce their  $\kappa$  and  $\sigma$  at the same time, because volume of the materials was removed too much, which the  $ZT$  improvement was limited. For the layered MoS<sub>2</sub>, the nanopatterning with small porosity can reduce the  $\kappa$  easily without too large effect on its  $\sigma$ , since small volume material was removed from the materials, and the electron mean free path is much smaller than the neck size of holey array<sup>40</sup>. Since MoS<sub>2</sub> and other layered materials by nanopatterning are expected to show better thermoelectric performance.



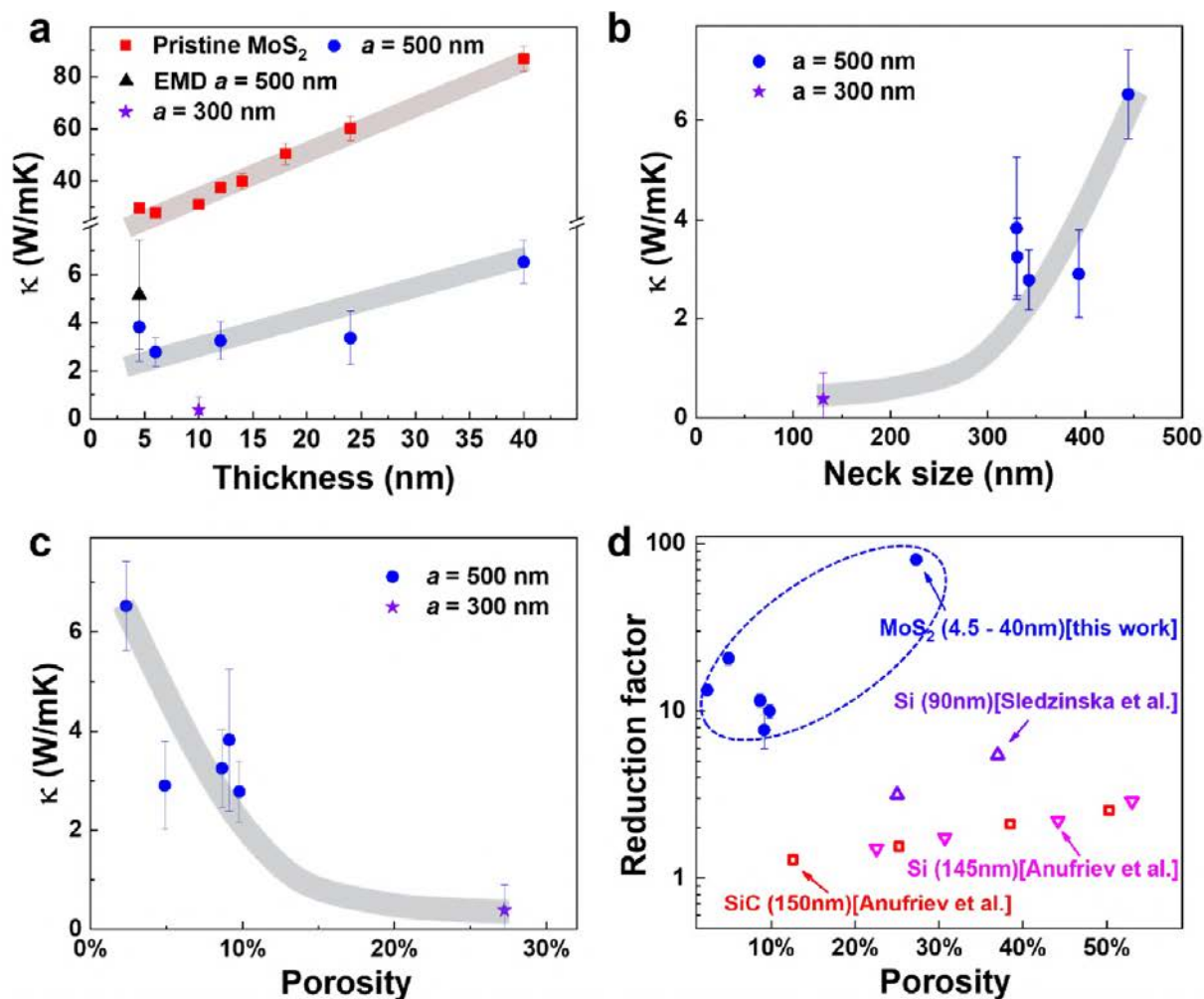


Figure 3. Thermal conductivity of the pristine and patterned MoS<sub>2</sub>. (a) Comparison between the thermal conductivities of the pristine and nanopatterned MoS<sub>2</sub> measured using 2LRT and simulated using EMD. (b, c) Thermal conductivity of the nanopatterned MoS<sub>2</sub> as a function of the neck size and porosity, respectively. (d) Thermal conductivity reduction factor as a function of porosity and thickness (inset). Lines serve as guides to the eye.

## NEMD simulations of pristine and patterned MoS<sub>2</sub>

We used EMD simulations to better understand the thickness and patterning effects on the thermal conductivity of MoS<sub>2</sub> (*Materials and Methods*). The  $\kappa$  was studied with the EMD method<sup>41</sup> using the LAMMPS package and the REBO-LJ potential<sup>42</sup>. In previous studies using the REBO-LJ potential and the homogeneous non-equilibrium EMD the highest  $\kappa$  value was found for the single-layer MoS<sub>2</sub> (100 W/mK), which further decreased with increasing thickness and reached the bulk value for three layers<sup>43</sup>. In the current study, using the EMD method, we found that the in-plane  $\kappa$  increased from  $\sim 9$  W/mK to 24 W/mK, for the 4- and 10-nm thick MoS<sub>2</sub>, respectively. For the 10 nm thick MoS<sub>2</sub>, its  $\kappa$  already reached 62% of the bulk value. The increase in  $\kappa$  as a function of the MoS<sub>2</sub> thickness obtained with the EMD simulations was in good agreement with the experimental results (Figure. S7 and *EMD simulations in Supporting information*).

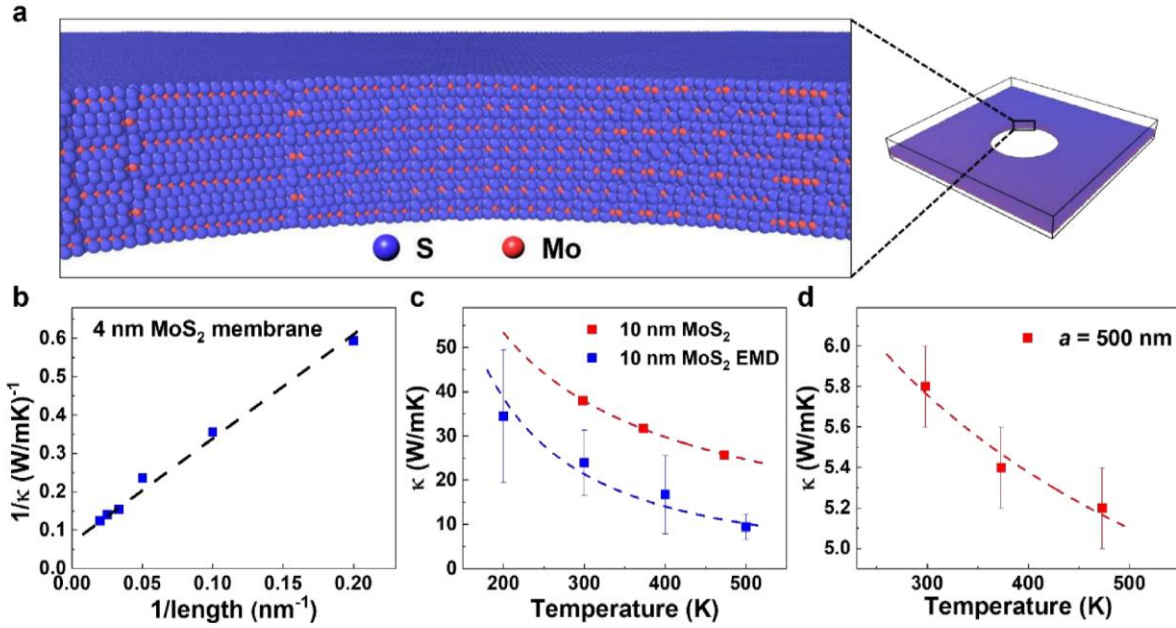
To calculate the phonon MFPs in the in-plane direction of the thinnest measured sample, 4 nm thick MoS<sub>2</sub>, non-equilibrium molecular dynamics (NEMD) simulations were performed following the methodology described in Ref<sup>9</sup>. The inverse  $\kappa$  versus the inverse length of the atomistic model showed a linear dependence (Figure. 4b), from which the MFP was calculated to be about 41 nm. A similar value of 30 nm for bulk MoS<sub>2</sub> was obtained using the MFP reconstruction method. The reconstruction method was applied to the experimental results assuming diffusive thermal transport governed by the Fuchs-Sondheimer approach (Figure S9)<sup>44,45</sup>. An extended description of this method can be found elsewhere<sup>29,46-48</sup>.

The results of the phonon MFP calculations were used to scale down the atomistic model of the nanopatterned samples that have been investigated experimentally. The thickness of the atomistic model of the MoS<sub>2</sub> was kept at 4 nm, while the dimensions along the x and y directions were scaled down five times. Regardless, the distance between two consecutive holes was larger than the average phonon MFP (Table T3 in *Supporting Information*). Thus, we could study the effect of nanostructuring of the membranes without large error by scaling down the model structure. It should be noted that the full-sized atomistic model would contain about 60,000,000 atoms and our initial calculations concluded that a study on such a model would have been inaccurate and computationally inefficient.

In Figure 4a the atomistic configuration of the unit cell of the nanopatterned MoS<sub>2</sub> is presented<sup>49</sup>. The inset shows a zoomed-in region on the surface atoms of the hole. The sulfur atoms are irregularly displayed on the hole surface, due to their higher mobility with respect to the molybdenum atoms and the hole's surface is partially covered with sulfur atoms.

The 4 nm thick MoS<sub>2</sub> membranes with  $a = 500$  nm showed an experimental  $\kappa$  of about  $3.8 \pm 1$  W/mK. For the scaled down atomistic model from Figure 3a, the in-plane  $\kappa$  calculated by EMD is  $5.2 \pm 2.3$  W/mK, a value that is in agreement with the experimental values, and hence validates the aforementioned modeling procedure. The difference between the experimental and theoretical value can be attributed to the presence of the amorphous ring around the perforated holes. In previous studies, the presence of a native oxide or amorphous phase above the nano-membranes or on the walls of the holes in the patterned nanomembranes were shown to have significant impact on the effective  $\kappa$  of such nanostructures<sup>50-52</sup>. For the case of

patterned membranes, the reduction due to the presence of an amorphous shell around the holes has been estimated to be on the order of 50-75%<sup>51</sup>.



**Figure 4. EMD simulations and temperature-dependent thermal conductivity of the 10 nm-thick, free-standing MoS<sub>2</sub>.** (a) System size dependence of  $1/\kappa$  leading to the calculation of the phonon mean free path at 300 K for a 4 nm thick MoS<sub>2</sub> membrane. (b) Atomistic configuration of the 4 nm thick MoS<sub>2</sub> nanopatterned membrane containing 2,037,703 atoms; 97.32 nm along x direction and 97.14 nm along y direction. Inset: surface atoms of the hole. (c) Comparison between experiment and EMD simulations of temperature-dependent thermal conductivity of a free-standing 10-nm thick MoS<sub>2</sub>. (d) Experimental temperature-dependent thermal conductivity of the same membrane after nanopatterning. Dashed lines are guides to the eye.

### Temperature-dependent thermal conductivity

For the high-temperature applications, it is crucial to know the temperature dependence of the thermal conductivity for both the pristine and patterned MoS<sub>2</sub> membranes. An example of the results for the 10 nm-thick MoS<sub>2</sub> are shown in Figure 4. The calculations were only performed for the pristine membranes due to the aforementioned computational limitations. For the pristine membrane a 30% reduction in  $\kappa$  was measured as the temperature was increased from 300 to 450 K, similar to the decrease predicted by the EMD. For the patterned MoS<sub>2</sub>, a reduction of about 10% was measured for the same temperature increase. These results confirm that the temperature more strongly affects the phonon MFPs of the pristine membrane than that of the patterned MoS<sub>2</sub>. For the pristine MoS<sub>2</sub>, Umklapp phonon-phonon and higher order scattering are dominant at higher temperatures. On the contrary, for the patterned MoS<sub>2</sub>, scattering from the holes constitutes the majority of scattering events and thus phonon-phonon interactions are less significant. Even so, at 500 K at five-fold difference in  $\kappa$  between the patterned and pristine MoS<sub>2</sub> was observed, indicating its potential for applications at high temperatures.

## CONCLUSION

In this work we designed and fabricated two heat routing structures in MoS<sub>2</sub> membranes, a thermal insulator and a heat conduction channel. The proposed designs pave the way for efficient heat manipulation using 2D materials, with possible applications in 2D electronics for free-standing NEMS. These structures were enabled by the large difference in  $\kappa$  between the nanopatterned and unpatterned parts of the membranes, which is maintained even at high temperatures. We have obtained a more than 10-fold reduction of  $\kappa$  for hole arrays with a period of 500 nm (porosity < 0.1), easily accessible with standard nanofabrication tools. A  $\kappa$  below 1 W/mK was obtained when the membranes were patterned with a period of 300 nm. The results show that layered MoS<sub>2</sub> is more sensitive to nanostructuring with small porosity than Si and SiC. The results were confirmed by the EMD simulations for the pristine membranes and on an adequately reduced unit cell for the nanopatterned membranes. We have shown that even though the phonon MFPs are on the order of tens of nms, the  $\kappa$  is strongly suppressed by structures with periodicities of a few hundred nm's. The study of the effect of the temperature on  $\kappa$  showed that the main scattering process for pristine membranes is the Umklapp phonon-phonon scattering, while for the perforated membranes scattering along the phonon-hole-walls becomes more important. This approach to reduce the MoS<sub>2</sub>  $\kappa$  can also be extended to other layered materials, especially the layered SnSe<sub>2</sub> with high Seebeck coefficient for high-performance thermoelectric applications. Our findings may enable new strategies for heat dissipation and passive cooling in 2D-based electronics operating at environmental conditions involving temperature to ~600 K and temperature gradients of 100 K.

## METHODS

### Sample preparation and characterization

An Au/Ti (95 nm/5 nm) layer was deposited on a holey SiN<sub>x</sub> substrate (Norcada, Canada) by e-beam metal deposition. A 2-mm thick Polydimethylsiloxane (PDMS) film was created using a 10 to 1 ratio of silicon base to curing agent (Sylgard ®184, Dow Corning, USA) and cured at room temperature for 24 hours. The PDMS film was used to mechanically exfoliate MoS<sub>2</sub> membranes from bulk MoS<sub>2</sub> crystals (Graphene Supermarket, USA), and the MoS<sub>2</sub> membranes were dry-transferred onto the Au/Ti coated holey substrate leaving a the free-standing MoS<sub>2</sub> membrane. A Focused Ion Beam (FIB) (Zeiss 1560XB Cross Beam, Germany) was used to etch periodic holes into the MoS<sub>2</sub> membrane with a beam current of 2 pA, a voltage of 30 kV, and an etch time of 10 ms. An unetched center area with a diameter of ~5  $\mu$ m to be used as a heating island.

### Thermal conductivity measurements

#### *Two-laser Raman Thermometry*

As the peak position of a Raman peak depends on the material temperature, it can be used to probe the material temperature. The A<sub>1g</sub> peak position of the MoS<sub>2</sub> Raman spectrum was used to probe the temperature of MoS<sub>2</sub> membrane in this work, as its peak intensity is much stronger than that of the E<sub>2g</sub><sup>1</sup> peak. A probe laser (532 nm, Cobolt) and a heating laser (405 nm, Cobolt) were focused on the center of a free-standing membrane from the topside and bottom-side,

respectively. The heating laser and the free-standing membrane were fixed on a motorized stage (Marzhauser), which sets their relative position and preventing a change in the position of the violet laser during measurement to ensure a stable and uncontacted heating source. The probe laser was coupled to the Raman spectrometer (T64000) and scanned at various points on the sample. The probe laser spot size was 1.2  $\mu\text{m}$ . Laser power absorbed by the membranes was measured *in-situ* using the configuration described elsewhere<sup>19,22</sup>. All the samples were measured in a temperature-controlled, vacuum chamber at a pressure of  $\sim 3 \times 10^{-3}$  mTorr (Linkam). The gold layer also acted as a heat sink to ensure that the MoS<sub>2</sub> temperature in the supported area is the same as that of the environment. For calculating the  $\kappa$ , a temperature distribution around the heating source on the free-standing membrane was required. The 2LRT experiment consists of two consecutive scans: 1) No heating applied ('baseline'). This measurement also helps to assess the sample quality (strain, contamination, etc.). 2) Heating applied using a 405 nm wavelength laser coupled from below the sample. The A<sub>1g</sub> peak position difference between the background scan and heating scan was divided by the A<sub>1g</sub> peak's temperature coefficient of each sample and converted to the temperature (Figure S1 and Table T1 in *Supporting Information*). The profiles of regions near the heat-sink could be well fitted by the constant  $\kappa$  (Figure s8) where the slope of the fitting lines corresponds to the  $dT/d(\ln r)$ . The spectra are collected every 0.5  $\mu\text{m}$  using a Märzhäuser stage with Tango controller, which provides repeatability  $< 1 \mu\text{m}$  (bidirectional) and a resolution of 0.01  $\mu\text{m}$  (smallest step size).

### *One-laser Raman Thermometry*

A heating-probe laser (532nm, Cobolt) was used to heat the samples at the center as well as collect the corresponding Raman spectra. All the measurements were performed in a temperature-controlled vacuum chamber (Linkam) and the laser power absorbed by the samples was measured *in-situ* using the configuration described elsewhere<sup>20</sup>.

### *Temperature-dependent thermal conductivity*

The measurements were performed in a temperature-controlled vacuum chamber (Linkam) where the heatsink temperature was varied from 123 K to 473 K. The samples were characterized using the 1LRT.

## **Molecular dynamics simulations**

### *EMD*

The thermal conductivity was investigated using the equilibrium molecular dynamics (EMD) method<sup>41</sup> and the Non-equilibrium Molecular Dynamics (NEMD). All simulations were conducted using LAMMPS<sup>42</sup> and the REBO-LJ potential. The MoS<sub>2</sub> parameterization of the REBO-LJ potential was considered from ref<sup>53</sup>, while the Lennard-Jones parameters for the S-S pair was adapted from ref<sup>54</sup> as it was motivated by room-temperature (300 K) calculations whereas ref<sup>53</sup> was motivated by zero-temperature calculations. The REBO-LJ potential for MoS<sub>2</sub> has been extensively tested on thermal property calculations in comparison with all the available interatomic potentials and has been shown to be the most reliable one<sup>43</sup>. Several systems are modeled with various thicknesses and temperatures. For each specific atomic model and temperature, the  $\kappa$  was calculated by averaging 10 different EMD runs with 10 different initialization seeds for random velocity distributions (Figure S12). The first step was to equilibrate the system with an NVT run for 400 ps at the temperature under investigation.

This step is to heat up the system prior to the EMD run to reach the linear (or equilibrated) region faster during the EMD. For the simulations under REBO-LJ potential, a time step of 0.5 fs was used and the EMD method for 1200 ps (2400000 steps) was performed. Finally, the average of 10 different cases, each with a different initial distribution of atomic velocities, was considered to calculate the mean curve of the  $\kappa$  vs time plot.

### *NEMD*

In order to calculate the phonon MFP of the 4-nm thick 2D MoS<sub>2</sub>, non-equilibrium Molecular Dynamics (NEMD) simulations at 300 K were performed. 2D atomistic configurations with lengths ranging from 5 to 50 nm were considered and the thermal conductivity of each was calculated. The two fixed regions and two thermostat regions together have a length of 0.5 nm. Following NEMD, a phonon travels in the crystal between the two cold and hot reservoirs at temperatures of 270K and 330K, respectively. It is known that phonons can exhibit at least two kinds of scattering procedures: they can be scattered by other phonons travelling in the material, or they can be scattered by the reservoirs, which are considered by the phonon as a different material with an almost infinite  $\kappa$ .

## Notes

The authors declare no competing financial interests.

## ACKNOWLEDGMENTS

This work has been supported by the Severo Ochoa program, the Spanish Research Agency (AEI, grant no. SEV-2017-0706) and the CERCA Programme/Generalitat de Catalunya. MS, ECA and CMST acknowledge support from Spanish MICINN project SIP (PGC2018-101743-B-I00), H2020-FET project NANOPOLY (GA No. 289061), ERC-ADG project LEIT (GA No. 885689). P.X. acknowledges support by a Ph.D. fellowship from the EU Marie Skłodowska-Curie COFUND PREBIST project (GA No. 754558). A.E.S acknowledges support by the H2020-MSCA-IF project THERMIC (GA No. 101029727). R.C.N. acknowledges funding from the EU-H2020 research and innovation programme under the Marie Skłodowska Curie Individual Fellowship (Grant No. 897148). The work was supported by computational time granted from the National Infrastructures for Research and Technology S.A. (GRNET) in the National HPC facility - ARIS - under the project NOUS (pr010034).

## AUTHOR CONTRIBUTIONS

P.X. M.S. A.E.S. C.M.S.T conceived the project. P.X. performed sample fabrication. P.X. A.E.S E.C.A. conducted the thermal conductivity measurements under the supervision of M.S. and C.M.S.T. K.T. J.K. G.N. performed the theoretical simulation. P.X. A.E.S. E.C.A. compiled and analyzed the data, with input from K.T. J.K. G.N. developed the model that simulated the experiments. P.X. and M.S. wrote the paper, with input from all authors. P.X., and A.E.S. contributed equally.

## REFERENCES

- (1) Cui, Y.; Li, M.; Hu, Y. Emerging Interface Materials for Electronics Thermal Management: Experiments, Modeling, and New Opportunities. *J. Mater. Chem. C* **2020**, *8* (31), 10568–10586. <https://doi.org/10.1039/C9TC05415D>.
- (2) Fu, Y.; Hansson, J.; Liu, Y.; Chen, S.; Zehri, A.; Samani, M. K.; Wang, N.; Ni, Y.; Zhang, Y.; Zhang, Z.-B.; Wang, Q.; Li, M.; Lu, H.; Sledzinska, M.; Torres, C. M. S.; Volz, S.; Balandin, A. A.; Xu, X.; Liu, J. Graphene Related Materials for Thermal Management. *2D Mater.* **2019**, *7* (1), 012001. <https://doi.org/10.1088/2053-1583/ab48d9>.
- (3) Lohrasbi, S.; Hammer, R.; Essl, W.; Reiss, G.; Defregger, S.; Sanz, W. A Comprehensive Review on the Core Thermal Management Improvement Concepts in Power Electronics. *IEEE Access* **2020**, *8*, 166880–166906. <https://doi.org/10.1109/ACCESS.2020.3021946>.
- (4) Song, H.; Liu, J.; Liu, B.; Wu, J.; Cheng, H.-M.; Kang, F. Two-Dimensional Materials for Thermal Management Applications. *Joule* **2018**. <https://doi.org/10.1016/j.joule.2018.01.006>.
- (5) Licht, A.; Pfister, N.; DeMeo, D.; Chivers, J.; Vandervelde, T. E. A Review of Advances in Thermophotovoltaics for Power Generation and Waste Heat Harvesting. *MRS Adv.* **2019**, *4* (41–42), 2271–2282. <https://doi.org/10.1557/adv.2019.342>.
- (6) Balandin, A. A.; Ghosh, S.; Bao, W.; Calizo, I.; Teweldebrhan, D.; Miao, F.; Lau, C. N. Superior Thermal Conductivity of Single-Layer Graphene. *Nano Lett.* **2008**, *8* (3), 902–907. <https://doi.org/10.1021/nl0731872>.
- (7) El Sachat, A.; Köenemann, F.; Menges, F.; Del Corro, E.; Garrido, J. A.; Sotomayor Torres, C. M.; Alzina, F.; Gotsmann, B. Crossover from Ballistic to Diffusive Thermal Transport in Suspended Graphene Membranes. *2D Mater.* **2019**, *6* (2), 025034. <https://doi.org/10.1088/2053-1583/ab097d>.
- (8) Jo, I.; Pettes, M. T.; Kim, J.; Watanabe, K.; Taniguchi, T.; Yao, Z.; Shi, L. Thermal Conductivity and Phonon Transport in Suspended Few-Layer Hexagonal Boron Nitride. *Nano Lett.* **2013**, *13* (2), 550–554. <https://doi.org/10.1021/nl304060g>.
- (9) Cai, Q.; Scullion, D.; Gan, W.; Falin, A.; Zhang, S.; Watanabe, K.; Taniguchi, T.; Chen, Y.; Santos, E. J. G.; Li, L. H. High Thermal Conductivity of High-Quality Monolayer Boron Nitride and Its Thermal Expansion. *Sci. Adv.* **2019**, *5* (6), eaav0129. <https://doi.org/10.1126/sciadv.aav0129>.
- (10) Yuan, P.; Wang, R.; Wang, T.; Wang, X.; Xie, Y. Nonmonotonic Thickness-Dependence of in-Plane Thermal Conductivity of Few-Layered MoS<sub>2</sub>: 2.4 to 37.8 Nm. *Phys. Chem. Chem. Phys.* **2018**, *20* (40), 25752–25761. <https://doi.org/10.1039/C8CP02858C>.
- (11) Yarali, M.; Wu, X.; Gupta, T.; Ghoshal, D.; Xie, L.; Zhu, Z.; Brahmi, H.; Bao, J.; Chen, S.; Luo, T.; Koratkar, N.; Mavrokefalos, A. Effects of Defects on the Temperature-Dependent Thermal Conductivity of Suspended Monolayer Molybdenum Disulfide Grown by Chemical Vapor Deposition. *Adv. Funct. Mater.* **2017**, *27* (46), 1704357. <https://doi.org/10.1002/adfm.201704357>.
- (12) Aiyiti, A.; Hu, S.; Wang, C.; Xi, Q.; Cheng, Z.; Xia, M.; Ma, Y.; Wu, J.; Guo, J.; Wang, Q.; Zhou, J.; Chen, J.; Xu, X.; Li, B. Thermal Conductivity of Suspended Few-Layer MoS<sub>2</sub>. *Nanoscale* **2018**, *10* (6), 2727–2734. <https://doi.org/10.1039/C7NR07522G>.
- (13) Bae, J. J.; Jeong, H. Y.; Han, G. H.; Kim, J.; Kim, H.; Kim, M. S.; Moon, B. H.; Lim, S. C.; Lee, Y. H. Thickness-Dependent in-Plane Thermal Conductivity of Suspended MoS<sub>2</sub> Grown by Chemical Vapor Deposition. *Nanoscale* **2017**, *9* (7), 2541–2547. <https://doi.org/10.1039/C6NR09484H>.
- (14) Gu, X.; Li, B.; Yang, R. Layer Thickness-Dependent Phonon Properties and Thermal Conductivity of MoS<sub>2</sub>. *J. Appl. Phys.* **2016**, *119* (8), 085106. <https://doi.org/10.1063/1.4942827>.
- (15) Zhao, Y.; Cai, Y.; Zhang, L.; Li, B.; Zhang, G.; Thong, J. T. L. Thermal Transport in 2D Semiconductors—Considerations for Device Applications. *Adv. Funct. Mater.* **2020**, *30* (8), 1903929. <https://doi.org/10.1002/adfm.201903929>.
- (16) Wang, H.; Hu, S.; Takahashi, K.; Zhang, X.; Takamatsu, H.; Chen, J. Experimental Study of Thermal Rectification in Suspended Monolayer Graphene. *Nat. Commun.* **2017**, *8* (1), 15843. <https://doi.org/10.1038/ncomms15843>.

- (17) Kurşun, B.; Sivrioğlu, M. Heat Transfer Enhancement Using U-Shaped Flow Routing Plates in Cooling Printed Circuit Boards. *J. Braz. Soc. Mech. Sci. Eng.* **2018**, *40* (1), 13. <https://doi.org/10.1007/s40430-017-0937-z>.
- (18) Song, J.; Lu, L.; Li, B.; Zhang, B.; Hu, R.; Zhou, X.; Cheng, Q. Thermal Routing via Near-Field Radiative Heat Transfer. *Int. J. Heat Mass Transf.* **2020**, *150*, 119346. <https://doi.org/10.1016/j.ijheatmasstransfer.2020.119346>.
- (19) Sledzinska, M.; Graczykowski, B.; Placidi, M.; Reig, D. S.; Sachat, A. E.; Reparaz, J. S.; Alzina, F.; Mortazavi, B.; Quey, R.; Colombo, L.; Roche, S.; Torres, C. M. S. Thermal Conductivity of MoS<sub>2</sub> polycrystalline Nanomembranes. *2D Mater.* **2016**, *3* (3), 035016. <https://doi.org/10.1088/2053-1583/3/3/035016>.
- (20) Sledzinska, M.; Quey, R.; Mortazavi, B.; Graczykowski, B.; Placidi, M.; Reig, D. S.; Navarro-Urrios, D.; Alzina, F.; Colombo, L.; Roche, S.; Torres, C. M. S. *Record Low Thermal Conductivity of Polycrystalline MoS<sub>2</sub> Films: Tuning the Thermal Conductivity by Grain Orientation*. <https://pubs.acs.org/doi/abs/10.1021/acsami.7b08811> (accessed 2019-05-08). <https://doi.org/10.1021/acsami.7b08811>.
- (21) Sledzinska, M.; Graczykowski, B.; Maire, J.; Chavez-Angel, E.; Sotomayor-Torres, C. M.; Alzina, F. 2D Phononic Crystals: Progress and Prospects in Hypersonic and Thermal Transport Engineering. *Adv. Funct. Mater.* **2020**, *30* (8), 1904434. <https://doi.org/10.1002/adfm.201904434>.
- (22) Graczykowski, B.; El Sachat, A.; Reparaz, J. S.; Sledzinska, M.; Wagner, M. R.; Chavez-Angel, E.; Wu, Y.; Volz, S.; Wu, Y.; Alzina, F.; Sotomayor Torres, C. M. Thermal Conductivity and Air-Mediated Losses in Periodic Porous Silicon Membranes at High Temperatures. *Nat. Commun.* **2017**, *8* (1), 415. <https://doi.org/10.1038/s41467-017-00115-4>.
- (23) Cai, Y.; Lan, J.; Zhang, G.; Zhang, Y.-W. Lattice Vibrational Modes and Phonon Thermal Conductivity of Monolayer MoS<sub>2</sub>. *Phys. Rev. B* **2014**, *89* (3), 035438. <https://doi.org/10.1103/PhysRevB.89.035438>.
- (24) Zulfiqar, M.; Zhao, Y.; Li, G.; Li, Z.; Ni, J. Intrinsic Thermal Conductivities of Monolayer Transition Metal Dichalcogenides MX<sub>2</sub> (M = Mo, W; X = S, Se, Te). *Sci. Rep.* **2019**, *9* (1), 4571. <https://doi.org/10.1038/s41598-019-40882-2>.
- (25) Lim, J.; Wang, H.-T.; Tang, J.; Andrews, S. C.; So, H.; Lee, J.; Lee, D. H.; Russell, T. P.; Yang, P. Simultaneous Thermoelectric Property Measurement and Incoherent Phonon Transport in Holey Silicon. *ACS Nano* **2016**, *10* (1), 124–132. <https://doi.org/10.1021/acsnano.5b05385>.
- (26) Anufriev, R.; Maire, J.; Nomura, M. Reduction of Thermal Conductivity by Surface Scattering of Phonons in Periodic Silicon Nanostructures. *Phys. Rev. B* **2016**, *93* (4), 045411. <https://doi.org/10.1103/PhysRevB.93.045411>.
- (27) Anufriev, R.; Wu, Y.; Ordonez-Miranda, J.; Nomura, M. Nanoscale Limit of the Thermal Conductivity in Crystalline Silicon Carbide Membranes, Nanowires, and Phononic Crystals. *NPG Asia Mater.* **2022**, *14* (1), 35. <https://doi.org/10.1038/s41427-022-00382-8>.
- (28) Sood, A.; Xiong, F.; Chen, S.; Cheaito, R.; Lian, F.; Asheghi, M.; Cui, Y.; Donadio, D.; Goodson, K. E.; Pop, E. Quasi-Ballistic Thermal Transport Across MoS<sub>2</sub> Thin Films. *Nano Lett.* **2019**, *19* (4), 2434–2442. <https://doi.org/10.1021/acs.nanolett.8b05174>.
- (29) Xiao, P.; Chavez-Angel, E.; Chaitoglou, S.; Sledzinska, M.; Dimoulas, A.; Sotomayor Torres, C. M.; El Sachat, A. Anisotropic Thermal Conductivity of Crystalline Layered SnSe<sub>2</sub>. *Nano Lett.* **2021**, *21* (21), 9172–9179. <https://doi.org/10.1021/acs.nanolett.1c03018>.
- (30) Arrighi, A.; Corro, E. D.; Urrios, D. N.; Costache, M. V.; Sierra, J. F. F.; Watanabe, K.; Taniguchi, T.; Garrido, J. A.; Valenzuela, S. O.; Torres, C. M. S.; Sledzinska, M. Heat Dissipation in Few-Layer MoS<sub>2</sub> and MoS<sub>2</sub>/HBN Heterostructure. *2D Mater.* **2021**. <https://doi.org/10.1088/2053-1583/ac2e51>.
- (31) Liu, J.; Choi, G.-M.; Cahill, D. G. Measurement of the Anisotropic Thermal Conductivity of Molybdenum Disulfide by the Time-Resolved Magneto-Optic Kerr Effect. *J. Appl. Phys.* **2014**, *116* (23), 233107. <https://doi.org/10.1063/1.4904513>.
- (32) Bae, J. J.; Jeong, H. Y.; Han, G. H.; Kim, J.; Kim, H.; Kim, M. S.; Moon, B. H.; Lim, S. C.; Lee, Y. H. Thickness-Dependent in-Plane Thermal Conductivity of Suspended MoS<sub>2</sub> Grown by Chemical Vapor Deposition. *Nanoscale* **2017**, *9* (7), 2541–2547. <https://doi.org/10.1039/C6NR09484H>.




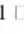
- (33) Gu, X.; Li, B.; Yang, R. Layer Thickness-Dependent Phonon Properties and Thermal Conductivity of MoS<sub>2</sub>. *J. Appl. Phys.* **2016**, *119* (8), 085106. <https://doi.org/10.1063/1.4942827>.
- (34) Giannuzzi, L. A.; Prenitzer, B. I.; Kempshall, B. W. Ion - Solid Interactions. In *Introduction to Focused Ion Beams: Instrumentation, Theory, Techniques and Practice*; Giannuzzi, L. A., Stevie, F. A., Eds.; Springer US: Boston, MA, 2005; pp 13–52. [https://doi.org/10.1007/0-387-23313-X\\_2](https://doi.org/10.1007/0-387-23313-X_2).
- (35) Reparaz, J. S.; Chavez-Angel, E.; Wagner, M. R.; Graczykowski, B.; Gomis-Bresco, J.; Alzina, F.; Sotomayor Torres, C. M. A Novel Contactless Technique for Thermal Field Mapping and Thermal Conductivity Determination: Two-Laser Raman Thermometry. *Rev. Sci. Instrum.* **2014**, *85* (3), 034901. <https://doi.org/10.1063/1.4867166>.
- (36) Yuan, P.; Wang, R.; Wang, T.; Wang, X.; Xie, Y. Nonmonotonic Thickness-Dependence of in-Plane Thermal Conductivity of Few-Layered MoS<sub>2</sub>: 2.4 to 37.8 Nm. *Phys. Chem. Chem. Phys.* **2018**, *20* (40), 25752–25761. <https://doi.org/10.1039/C8CP02858C>.
- (37) Kasprzak, M.; Sledzinska, M.; Zaleski, K.; Iatsunskiy, I.; Alzina, F.; Volz, S.; Sotomayor Torres, C. M.; Graczykowski, B. High-Temperature Silicon Thermal Diode and Switch. *Nano Energy* **2020**, *78*, 105261. <https://doi.org/10.1016/j.nanoen.2020.105261>.
- (38) Sledzinska, M.; Graczykowski, B.; Alzina, F.; Melia, U.; Termentzidis, K.; Lacroix, D.; Sotomayor Torres, C. M. Thermal Conductivity in Disordered Porous Nanomembranes. *Nanotechnology* **2019**, *30* (26), 265401. <https://doi.org/10.1088/1361-6528/ab0ecd>.
- (39) Jeong, C.; Datta, S.; Lundstrom, M. Thermal Conductivity of Bulk and Thin-Film Silicon: A Landauer Approach. *J. Appl. Phys.* **2012**, *111* (9), 093708. <https://doi.org/10.1063/1.4710993>.
- (40) Park, K. T.; Richards-Babb, M.; Freund, M. S.; Weiss, J.; Klier, K. Surface Structure of Single-Crystal MoS<sub>2</sub> (0002) and Cs/MoS<sub>2</sub> (0002) by X-Ray Photoelectron Diffraction. *J. Phys. Chem.* **1996**, *100* (25), 10739–10745. <https://doi.org/10.1021/jp9605865>.
- (41) Termentzidis, K. *Nanostructured Semiconductors Amorphization and Thermal Properties*; 2017.
- (42) Plimpton, S. Fast Parallel Algorithms for Short- Range Molecular Dynamics. *J. Comput. Phys.* **1995**, *117* (1), 44. <https://doi.org/10.1006/jcph.1995.1039>.
- (43) Xu, K.; Gabourie, A. J.; Hashemi, A.; Fan, Z.; Wei, N.; Farimani, A. B.; Komsa, H.-P.; Krasheninnikov, A. V.; Pop, E.; Ala-Nissila, T. Thermal Transport in MoS<sub>2</sub> from Molecular Dynamics Using Different Empirical Potentials. *Phys. Rev. B* **2019**, *99* (5), 054303. <https://doi.org/10.1103/PhysRevB.99.054303>.
- (44) Fuchs, K. The Conductivity of Thin Metallic Films According to the Electron Theory of Metals. *Math. Proc. Camb. Philos. Soc.* **1938**, *34* (1), 100–108. <https://doi.org/10.1017/S0305004100019952>.
- (45) Sondheimer, E. H. The Mean Free Path of Electrons in Metals. *Adv. Phys.* **1952**, *1* (1), 1–42. <https://doi.org/10.1080/00018735200101151>.
- (46) Minnich, A. J. Determining Phonon Mean Free Paths from Observations of Quasiballistic Thermal Transport. *Phys. Rev. Lett.* **2012**, *109* (20), 205901. <https://doi.org/10.1103/PhysRevLett.109.205901>.
- (47) Chavez-Angel, E.; Zarate, R. A.; Fuentes, S.; Guo, E. J.; Kläui, M.; Jakob, G. Reconstruction of an Effective Magnon Mean Free Path Distribution from Spin Seebeck Measurements in Thin Films. *New J. Phys.* **2017**, *19* (1), 013011. <https://doi.org/10.1088/1367-2630/aa5163>.
- (48) Sanchez-Martinez, M.-Á.; Alzina, F.; Oyarzo, J.; Sotomayor Torres, C. M.; Chavez-Angel, E. Impact of the Regularization Parameter in the Mean Free Path Reconstruction Method: Nanoscale Heat Transport and Beyond. *Nanomaterials* **2019**, *9* (3), 414. <https://doi.org/10.3390/nano9030414>.
- (49) NanoMaterialsCAD: Flexible Software for the Design of Nanostructures. <https://doi.org/10.1002/adts.202000232>.
- (50) Neogi, S.; Reparaz, J. S.; Pereira, L. F. C.; Graczykowski, B.; Wagner, M. R.; Sledzinska, M.; Shchepetov, A.; Prunnila, M.; Ahopelto, J.; Sotomayor-Torres, C. M.; Donadio, D. Tuning Thermal Transport in Ultrathin Silicon Membranes by Surface Nanoscale Engineering. *ACS Nano* **2015**, *9* (4), 3820–3828. <https://doi.org/10.1021/nn506792d>.
- (51) Verdier, M.; Lacroix, D.; Didenko, S.; Robillard, J.-F.; Lampin, E.; Bah, T.-M.; Termentzidis, K. Influence of Amorphous Layers on the Thermal Conductivity of Phononic Crystals. *Phys.*

- (52) Verdier, M.; Lacroix, D.; Termentzidis, K. Roughness and Amorphization Impact on Thermal Conductivity of Nanofilms and Nanowires: Making Atomistic Modeling More Realistic. *J. Appl. Phys.* **2019**, *126* (16), 164305. <https://doi.org/10.1063/1.5108618>.
- (53) Stewart, J. A.; Spearot, D. E. Atomistic Simulations of Nanoindentation on the Basal Plane of Crystalline Molybdenum Disulfide ( $\text{MoS}_2$ ). *Model. Simul. Mater. Sci. Eng.* **2013**, *21* (4), 045003. <https://doi.org/10.1088/0965-0393/21/4/045003>.
- (54) Liang, T.; Phillpot, S. R.; Sinnott, S. B. Parametrization of a Reactive Many-Body Potential for Mo-S Systems. *Phys. Rev. B* **2009**, *79* (24), 245110. <https://doi.org/10.1103/PhysRevB.79.245110>.

# Article 3 Supporting Information

## Supporting Information

### Thermal routing in nanopatterned MoS<sub>2</sub>

Peng Xiao<sup>1,2\*</sup> , Alexandros El Sachat<sup>1</sup>, Emigdio Chávez Angel<sup>1</sup>, Ryan C. Ng<sup>1</sup>, Giorgos Nikoulis<sup>3</sup>, Joseph Kioseoglou<sup>3</sup>, Konstantinos Termentzidis<sup>4</sup>, Clivia M. Sotomayor Torres<sup>1,5</sup>, and Marianna Sledzinska<sup>1</sup> 


<sup>1</sup>Catalan Institute of Nanoscience and Nanotechnology (ICN2), CSIC and BIST, Campus UAB, Bellaterra, 08193 Barcelona, Spain

<sup>2</sup>Departamento de Física, Universidad Autónoma de Barcelona, Bellaterra, 08193 Barcelona, Spain

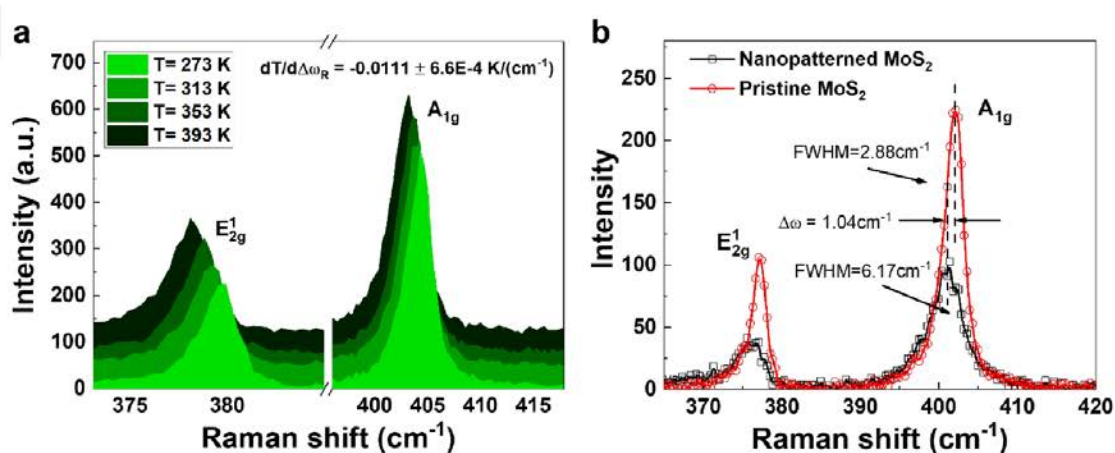
<sup>3</sup>Department of Physics, Aristotle University of Thessaloniki, GR-54124 Thessaloniki, Greece

<sup>4</sup>Univ Lyon, CNRS, INSA Lyon, CETHIL, UMR5008 69621 Villeurbanne, France

<sup>5</sup>ICREA, Passeig Lluís Companys 23, 08010 Barcelona, Spain

 e-mail: [peng.xiao@icn2.cat](mailto:peng.xiao@icn2.cat); [marianna.sledzinska@icn2.cat](mailto:marianna.sledzinska@icn2.cat)

## 1. Temperature calibration of MoS<sub>2</sub>

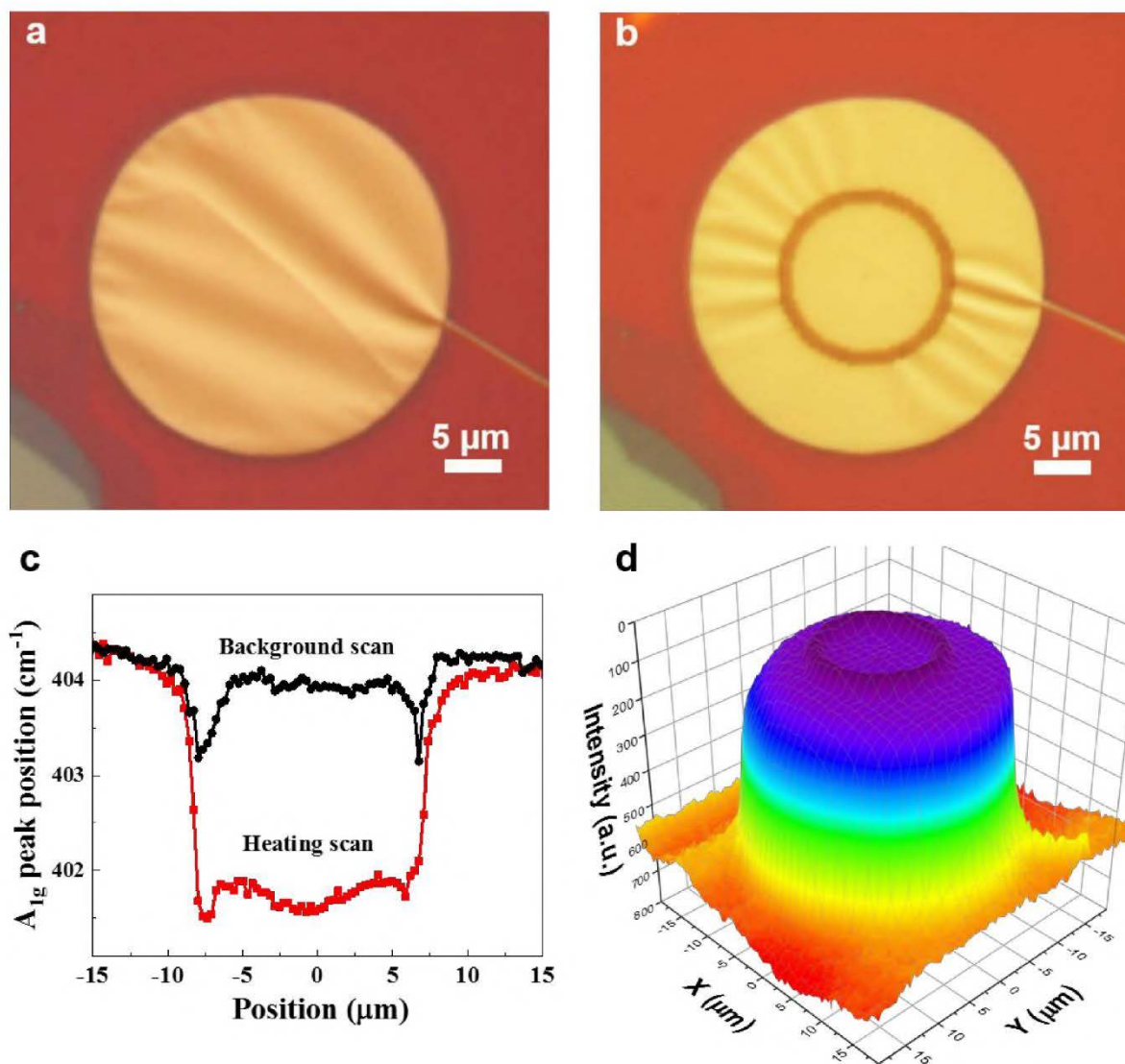


**Fig. S1.** **a**, Temperature-dependent Raman spectra of the MoS<sub>2</sub>. **b**, Raman spectra of the pristine and nanopatterned MoS<sub>2</sub>.

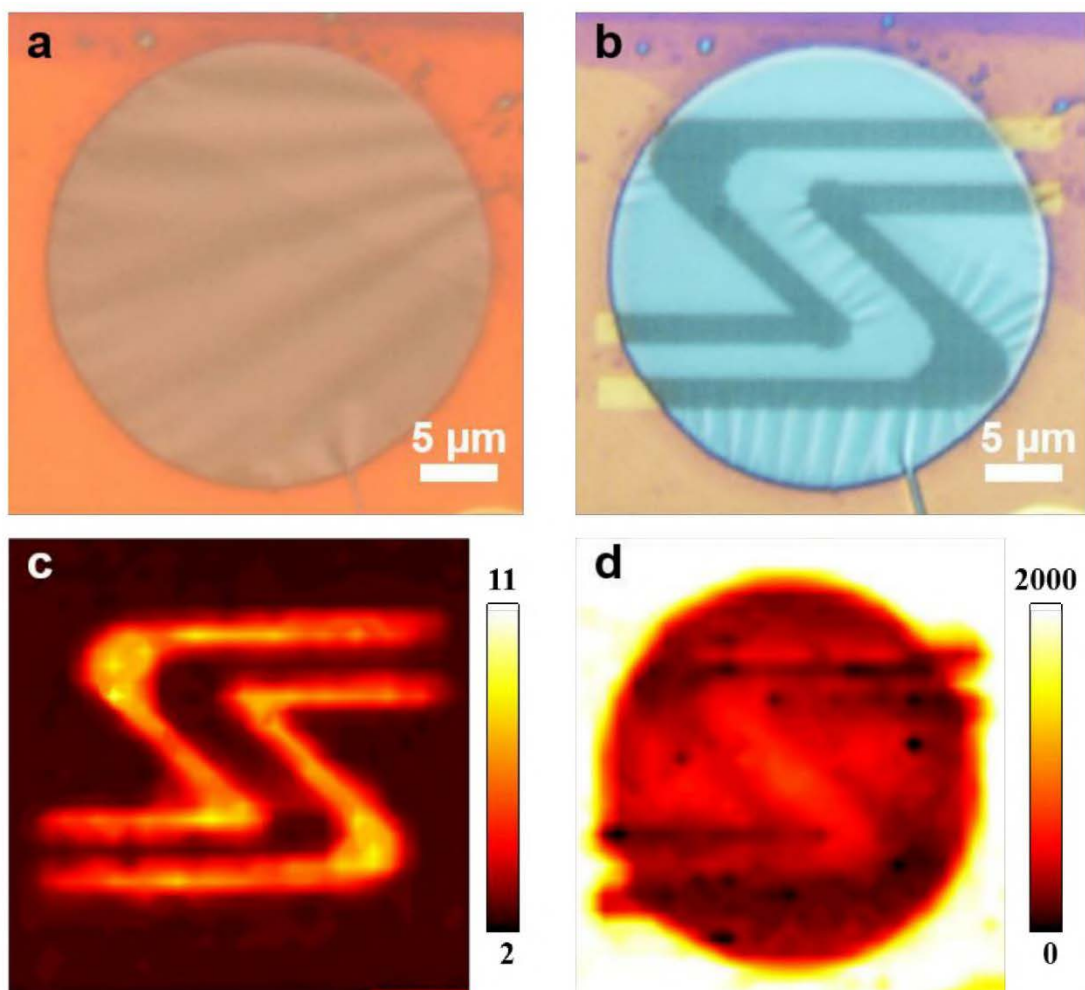
$\frac{dT}{d\Delta\omega_R}$ (K/cm <sup>-1</sup> )		Measured area (Supported/suspended)			
		MoS <sub>2</sub> A <sub>1g</sub> <sup>-</sup> (Supported)	MoS <sub>2</sub> A <sub>1g</sub> <sup>-</sup> (Suspended)	MoS <sub>2</sub> E <sub>2g</sub> <sup>1/2</sup> (Supported)	MoS <sub>2</sub> E <sub>2g</sub> <sup>1/2</sup> (Suspended)
Thickness (nm)	4.5	-0.0112 ± 9.0E-4	-0.0111 ± 6.6E-4	-0.0127 ± 6.7E-4	-0.0125 ± 5.3E-4
	6	-0.0088 ± 6.3E-4	-0.0102 ± 2.7E-4	-0.0104 ± 1.1E-4	-0.0117 ± 0.7E-4
	10	-0.0085 ± 8.5E-4	-0.0090 ± 1.9E-4	-0.0010 ± 13E-4	-0.0101 ± 6.3E-4
	12	-0.0099 ± 3.9E-4	-0.0097 ± 6.1E-4	-0.0108 ± 3.2E-4	-0.0114 ± 9.1E-4
	14	-0.0093 ± 27E-4	-0.0108 ± 26E-4	-0.0133 ± 4.3E-4	-0.0146 ± 17E-4
	18	-0.01 ± 3.1E-4	-0.01 ± 2.2E-4	-0.0117 ± 6.1E-4	-0.0109 ± 3.5E-4
	24	-0.0096 ± 10E-4	-0.0085 ± 4.7E-4	-0.0090 ± 22E-4	-0.0121 ± 17E-4
	40	-0.0107 ± 1.3E-4	-0.0107 ± 1.2E-4	-0.012 ± 4.6E-4	-0.0124 ± 4.7E-4

**Table T1.** Temperature dependence of the MoS<sub>2</sub> A<sub>1g</sub> and E<sub>2g</sub> Raman peak positions for the samples used in this study.

## 2. MoS<sub>2</sub> thermal insulator and heat conduction channel



**Fig. S2.** Optical images of **a**, pristine **b**, nanopatterned MoS<sub>2</sub>. **c**, A<sub>1g</sub> Raman peak position with and without heating. **d**, A<sub>1g</sub> Raman peak intensity as a function of position.



**Fig. S3.** Optical images of **a**, pristine **b**, nanopatterned MoS<sub>2</sub>. **c**, A<sub>1g</sub> Raman peak FWHM. **d**, A<sub>1g</sub> Raman peak intensity as a function of position.

### 3. Sample characterization

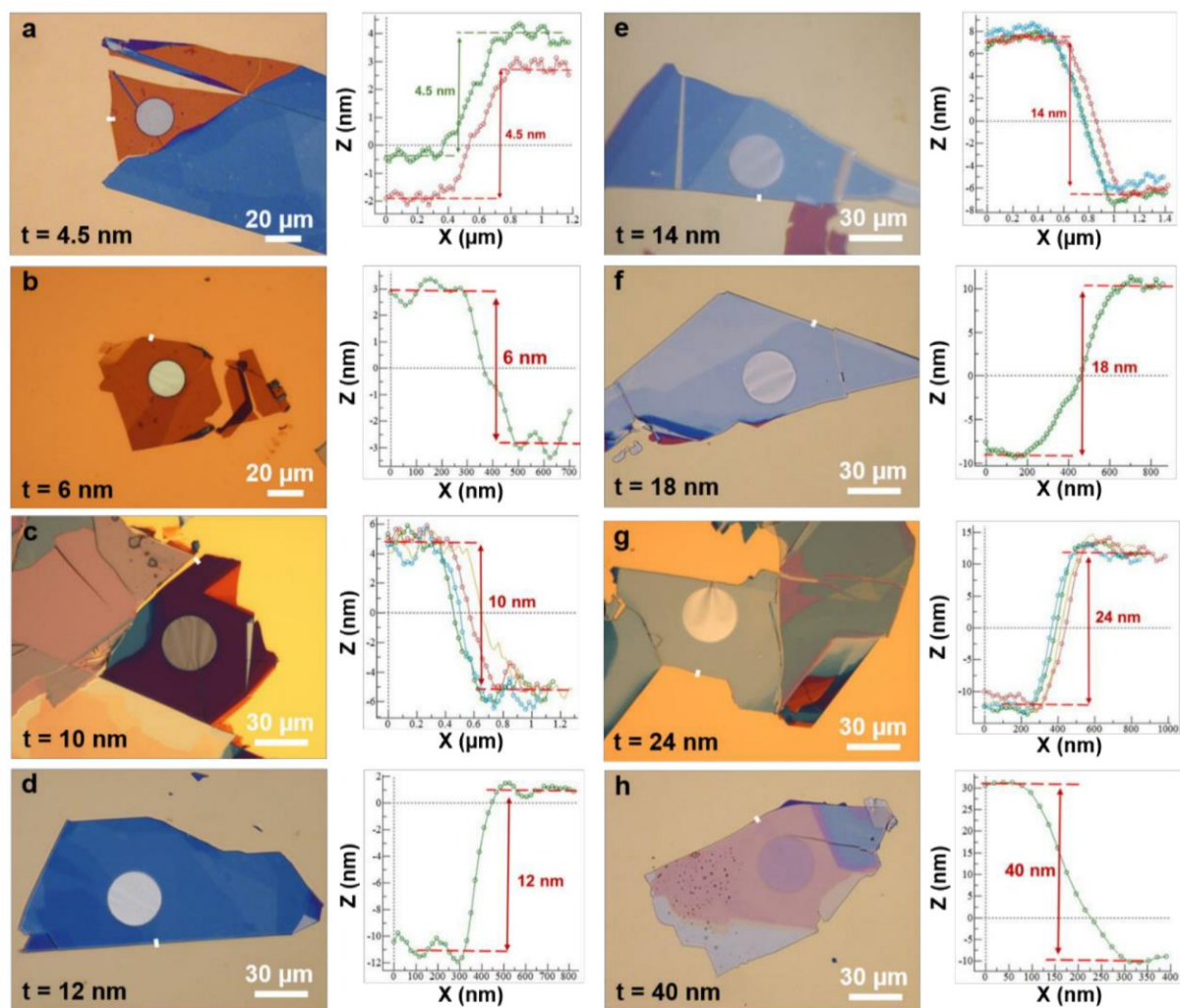
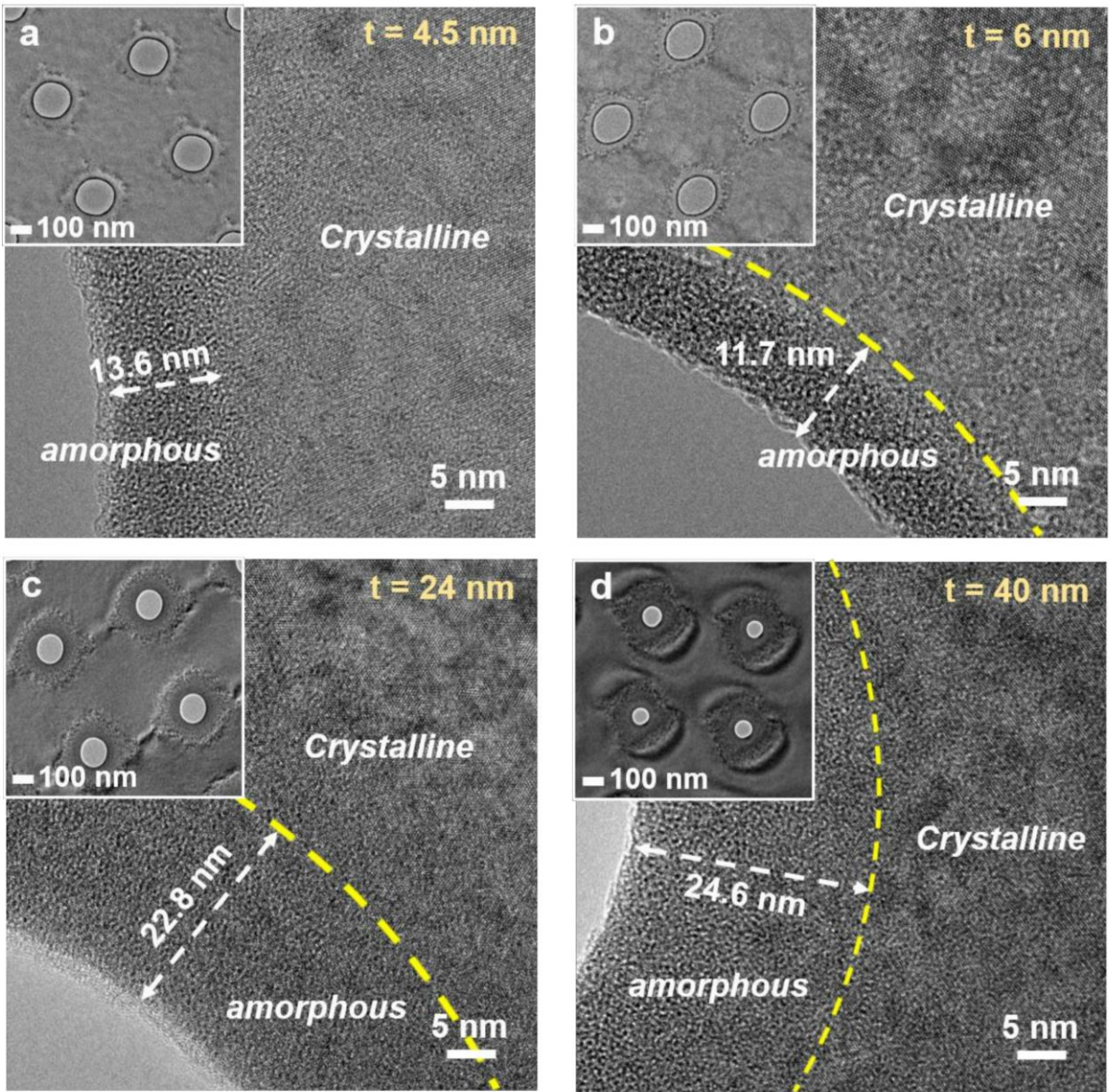
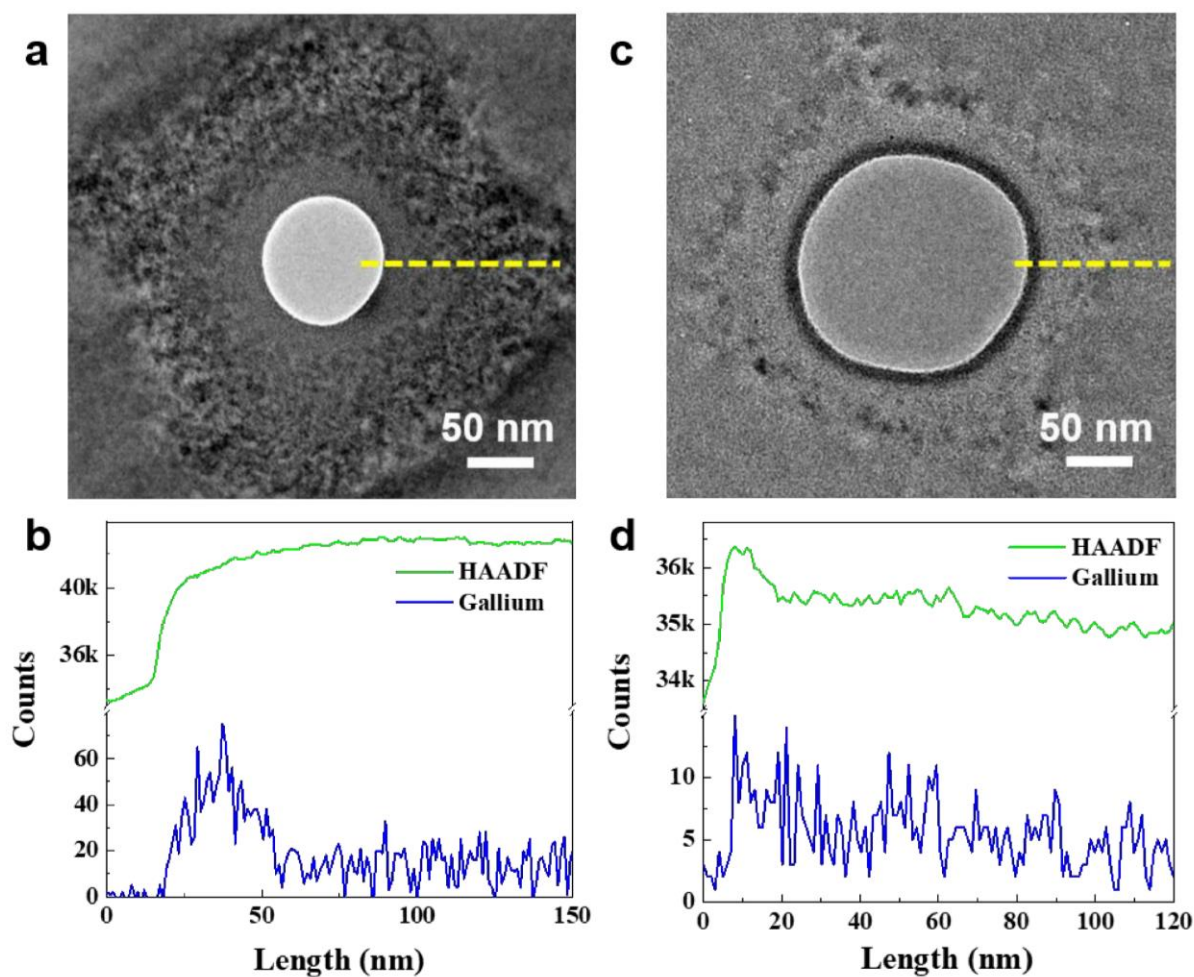


Fig. S4. a-h, Optical images, and atomic force microscopy profiles of the MoS<sub>2</sub> samples.

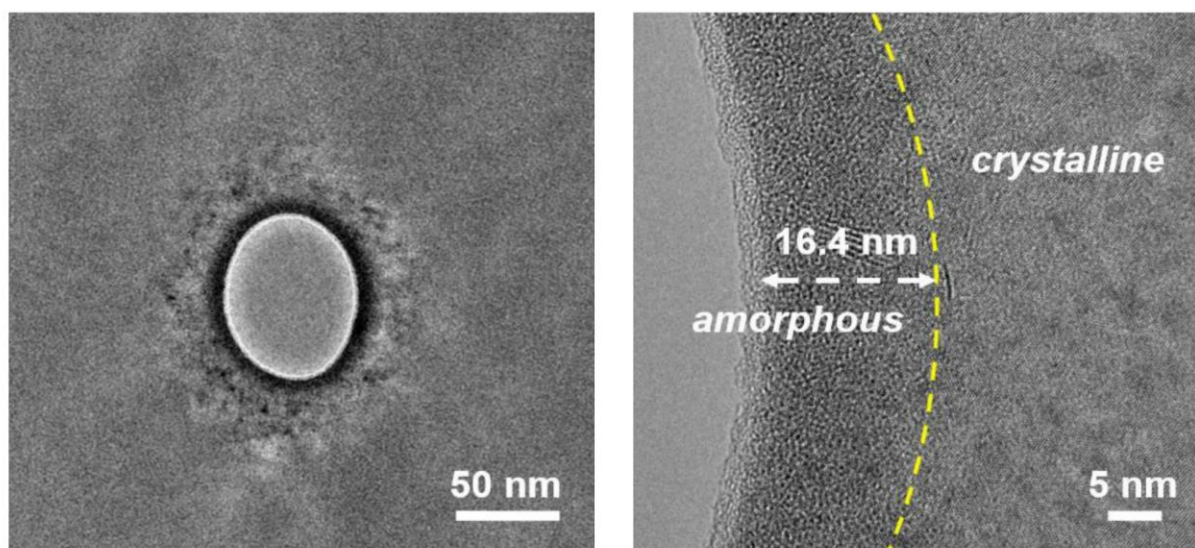


**Fig. S5.** a-d, TEM images of the patterned MoS<sub>2</sub> samples.





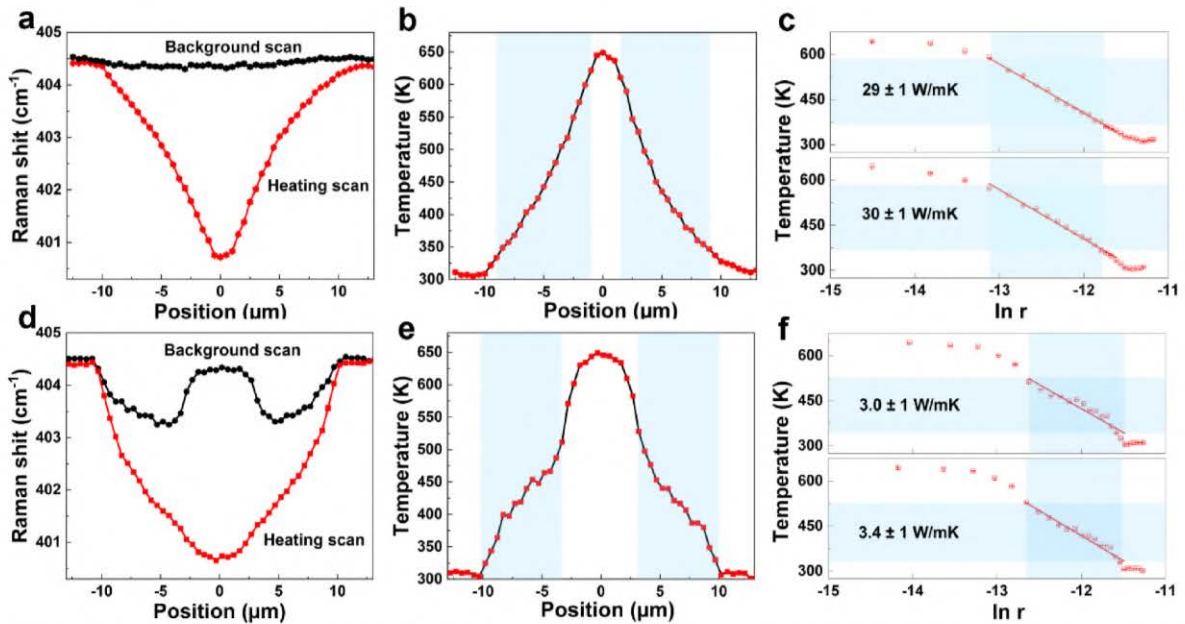
**Fig. S6.** STEM and High-angle annular dark-field imaging (HAADF) profiles and gallium atoms trace for MoS<sub>2</sub> patterned samples with thickness of **a,b** 40 nm; **c,d** 4.5 nm.



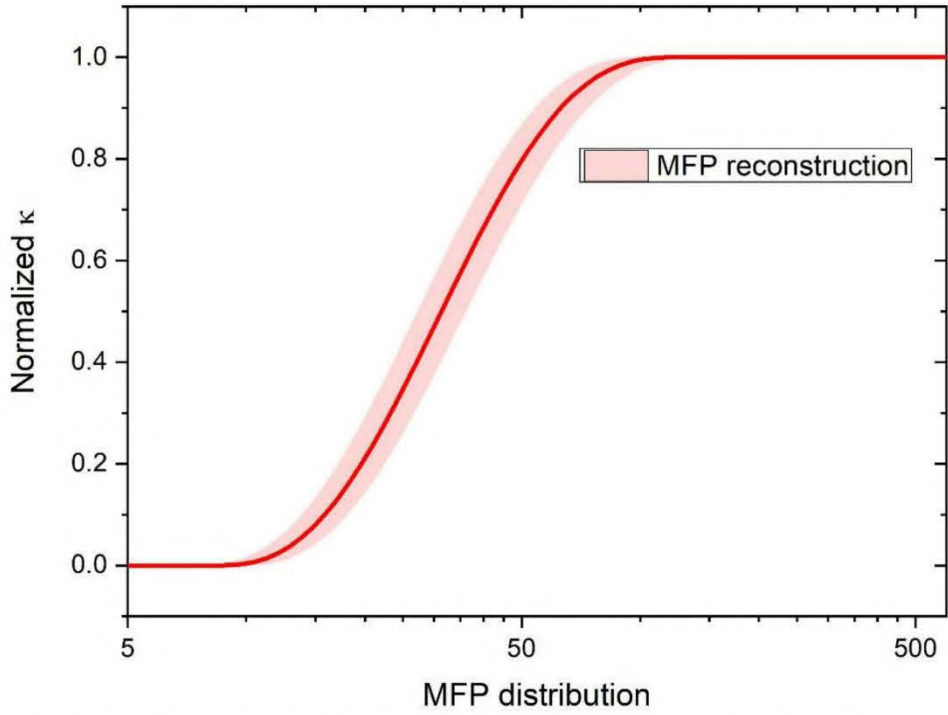
**Fig. S7.** TEM images of the 10 nm thick MoS<sub>2</sub> sample, where the hole was made by laser heating.

#### 4. Experimental procedure for calculation of thermal conductivity

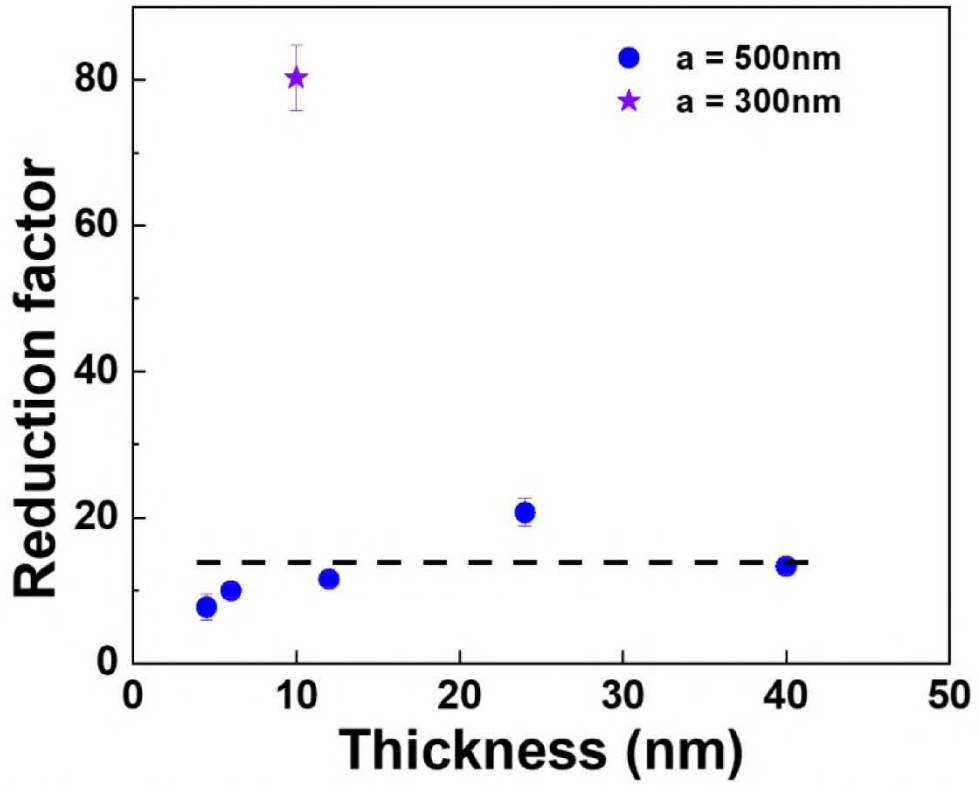
An example of the experimental procedure is shown in Fig. S8 for the 4.5-nm thick pristine MoS<sub>2</sub>. First, the background scan was performed with the heating laser  $P = 0 \mu\text{W}$  and the probe laser set to a low power ( $P_{probe} \sim 10 \mu\text{W}$ ). Next, the heating scan was performed with the heating laser power absorbed by the sample  $P = 137.5 \mu\text{W}$ . The A<sub>1g</sub> peak position for both of the scans is shown in Fig. S8a. The background scan curve shows the constant peak position at 405 cm<sup>-1</sup>, indicating no significant strain is present in the sample. The heating scan curve shows symmetric temperature decay from the center of the samples to the heatsink, where it reaches room temperature. The A<sub>1g</sub> peak position difference between the background scan and heating scan was divided by the A<sub>1g</sub> peak's temperature coefficient of each sample and converted to the temperature (Fig. S1 and Table T1). Near the heat-sink, the profiles could be well fitted by the constant  $\kappa$ , as shown in Fig. 3c, where the slope of the fitting lines in corresponds to the  $dT/d(\ln r)$ . Thermal conductivity of the 4.5-nm thick pristine MoS<sub>2</sub> membrane was calculated about  $29.5 \pm 1 \text{ W/mK}$ . The patterned membranes were measured in the same way as their pristine counterparts. For the patterned 4.5 nm-thick MoS<sub>2</sub> membrane with a nanopatterned period  $a$  of 500 nm, the intensity of the probe laser was reduced to  $6.8 \mu\text{W}$ , while the heating laser power absorbed by the sample  $P$  was  $15.8 \mu\text{W}$  (Fig. S8.d-f). Thermal conductivity of this 4.5-nm thick MoS<sub>2</sub> membrane was calculated about  $3.2 \pm 1 \text{ W/mK}$ . To extract the intrinsic thermal conductivity of the patterned MoS<sub>2</sub>, the experimental value was corrected using a volume correction factor  $\varepsilon$ , which takes into account the volume reduction of the patterned samples, where  $\varepsilon = (1 - \sigma)/(1 + \sigma)$  and the porosity  $\sigma = \pi d^2/4a^2$ .<sup>1</sup> This membrane's thermal conductivity was increased to  $3.8 \pm 1 \text{ W/mK}$ .



**Fig. S8** Thermal conductivity of the 4.5 nm-thick, free-standing pristine and nanopatterned MoS<sub>2</sub>. **a-c**, The thermal conductivity results of the MoS<sub>2</sub> pristine membrane. **a**, *Background and Heating scans* were acquired by the 2LRT. **b**, Temperature profile on the sample, extracted from **(a)**. **c**, Temperature profile as a function of  $\ln(r)$ . The solid line represents a linear fit of the experimental points. **d-f**, The results of the MoS<sub>2</sub> patterned membrane. **d**, *Background and Heating scans* were acquired by the 2LRT. **e**, Temperature profile on the sample, extracted from **(d)**. **f**, Temperature profile as a function of  $\ln(r)$ .



**Figure S9.** Normalized accumulated thermal conductivity as a function of the phonon MFP.



**Figure S10.** Normalized accumulated thermal conductivity as a function of the phonon MFP.

## 5. MD simulations

Concerning the dependence of the thermal conductivity with the layer thickness, three sizes have been investigated; a 4nm (7 tri-layers), 10nm (17 tri-layers) and a bulk system at 300K as there are presented in Figure 1. It should be noticed that even for 10nm, the bulk conductivity has not been reached in contrast to ref <sup>2</sup> argued that from 3 tri-layers (about 1.8 nm) the thermal conductivity reaches the bulk values. The discrepancy is based on the fact that in the present study, the well-established EMD method is used extensively (averaging the results of 10 different cases having random initial distribution of atomic velocities) while in ref <sup>2</sup> the authors have used the homogeneous nonequilibrium MD (HNEMD) method<sup>3,4</sup> in the recently developed form, which is constructed in order the HNEMD method to become efficient for general many-body potentials, including the REBO potential<sup>5</sup>. The current outcome using the EMD method supports the validity of the aforementioned used methodology in combination with the selected interatomic potential owing to the agreement with the experimental results.

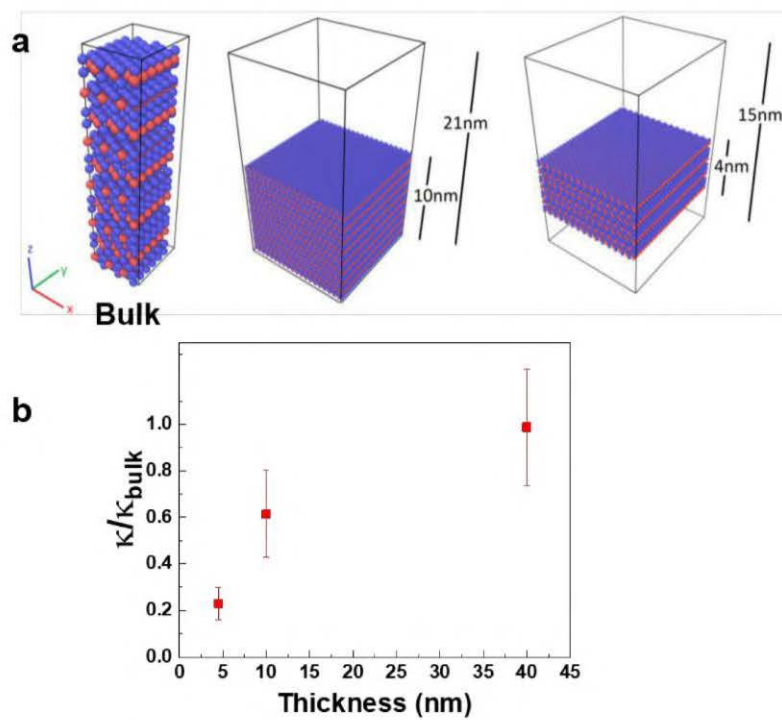
Thickness (nm)	Temperature (K)	Thermal conductivity (W/mK)			
		in-plane	RMSE	out-plane	RMSE
4	300	8.95	2.66	0.012	0.006
10	130	43.83	52.43	0.14	0.14
10	200	34.45	14.92	0.076	0.030
10	300	23.97	7.33	0.044	0.019
10	400	16.73	8.85	0.058	0.023
10	500	9.46	2.93	0.04	0.02
bulk	300	38.52	9.76	1.32	0.36

**Table T2.** Thickness dependence of thermal conductivity of MoS<sub>2</sub>.

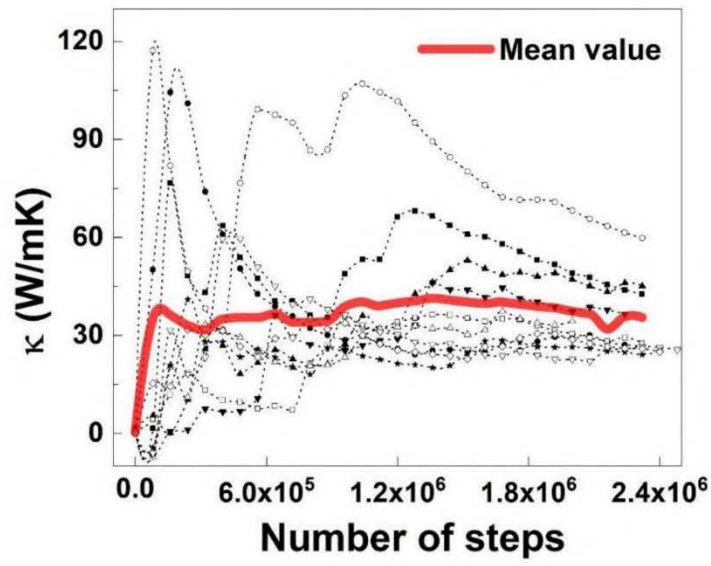
For the main focus of our work, we scaled down the nanopatterned thin film for computational optimization, in order to study its thermal conductivity. Table T3 shows the information about the original pristine system and the scaled down system we studied. To make sure the scaled down system is acceptable for our simulation, we took into account the PMFP. The crystalline surface of the system should be large enough, so it does not restrict the phononic vibrations. Therefore, the smallest path between two consecutive holes is equal to the periodicity minus the hole diameter. That evaluates to 62.4 nm which is larger than the PMFP = 41 nm and hence, the scale down of the system does not restrict the thermal conductivity in any way. The in-plane thermal conductivity was calculated equal to 5.2 W/mK which compares well with our experimental results.

	Thickn ess (nm)	Hole dimeter (nm)	Periodici ty (nm)	Amorphou s size (nm)	Number of atoms	x axis (nm)	y axis (nm)
Original	4	177	489	13.5	58.958.892	489	489
Scaled down	4	35.4	97.8	3	2.037.703	97.32	97.14

Table T3. Information for the Original and the scaled down porous systems.



**Fig. S11.** EMD simulations **a**, Three atomistic configurations: bulk, 10 nm, and 4 nm thick. **b**, Normalized thermal conductivity as a function of thickness.



**Fig. S12** EMD simulation for 10nm pristine film at 200K temperature. The plot shows the in-plane results for y-direction (010) and the mean value was calculated using 10 random seeds.

## References

1. Hashin, Z. & Shtrikman, S. A Variational Approach to the Theory of the Effective Magnetic Permeability of Multiphase Materials. *Journal of Applied Physics* **33**, 3125–3131 (1962).
2. Xu, K. *et al.* Thermal transport in  $\text{MoS}_2$  from molecular dynamics using different empirical potentials. *Phys. Rev. B* **99**, 054303 (2019).
3. Evans, D. J. Homogeneous NEMD algorithm for thermal conductivity—Application of non-canonical linear response theory. *Physics Letters A* **91**, 457–460 (1982).
4. Statistical Mechanics of Nonequilibrium Liquids - 1st Edition.  
<https://www.elsevier.com/books/statistical-mechanics-of-nonequilibrium-liquids/evans/978-0-12-244090-8>.
5. Fan, Z., Dong, H., Harju, A. & Ala-Nissila, T. Homogeneous nonequilibrium molecular dynamics method for heat transport and spectral decomposition with many-body potentials. *Phys. Rev. B* **99**, 064308 (2019).

# 6. MoS<sub>2</sub>- and WS<sub>2</sub>-nanosheets based humidity sensors

## 6.1 Introduction

Fast developments towards smart homes and cities have led to an increased demand for environmental monitoring of living, working and recreational spaces and is pushing the study of the high-performance environmental sensors. Managing optimum indoor humidity is a priority for every homeowner as it directly affects comfort and wellbeing, as well as the proper functioning of heating and air conditioning units. In electronic systems, especially the ones operating outdoors, humidity affects both performance and lifetime. In the past decades humidity sensors were mainly developed with materials such as metal oxides or ceramics<sup>116</sup> due to their high mechanical and chemical stability and fast response to the changes of humidity. Recently, new humidity sensing materials including two-dimensional (2D) materials, such as graphene, black phosphorus, and transition metal dichalcogenides, especially MoS<sub>2</sub> and WS<sub>2</sub>.<sup>117–120</sup> have been considered for sensing applications because of their chemically active edges, high surface-to-volume ratio, easy-fabrication methods, and good electrical performance.<sup>117</sup> TMD-based humidity sensors have shown excellent humidity sensing properties with fast response and high responsivity,<sup>121,122</sup> and substantial progress has been made on improving device flexibility and sensitivity.<sup>123–125</sup>

However, some humidity sensors have been shown to exhibit a decrease of impedance with increasing humidity (defined as the *positive* response)<sup>126–129</sup> while other works have shown an increase of the impedance with increasing humidity (defined as the *negative* response).<sup>119,122</sup> The *positive* humidity sensing mechanism is usually interpreted as invoking the proton hopping process (Grotthuss mechanism)<sup>130,131</sup>. This process describes the proton transport through the hydrogen bonds of water molecules or other hydrogen-bonded liquids, between nanosheets in the film, which results in an increase in the conductance with increasing humidity. On the other hand, the negative response can be explained by the electrons trapping



process<sup>132,133</sup> whereby water molecules absorbed by the material can trap free charges, which results in a conductance decrease with increasing humidity. The electrical response of 2D-based moisture sensors has been reported to be ambiguous showing responses with opposite signs for the same material. For example, Zhao et al. claimed that electrons transfer from MoS<sub>2</sub> film to the absorbed water molecule resulted in the negative response of the MoS<sub>2</sub> film based humidity sensor.<sup>119</sup> Additionally, Mondal et al. reported that MoS<sub>2</sub> nanosheets based humidity sensor showed a positive response attributed to the electron transfer from water molecule to MoS<sub>2</sub> at low humidity, and proton hopping process at high humidity.<sup>129</sup> Water associated protons and water trapped electrons both exist when water molecules are attached on the surface of materials, but so far, only limited research has been carried out to discuss these effects appropriately.<sup>134–137</sup> While 2D materials have the potential to be applied in mass production, the reversing process can cause a certain risk and can be dangerous if surrounding things react with the materials, which can fully reverse the measurement results. Therefore, the sensing mechanisms should be taken into consideration to further avoid the risk of the device aging and performance reversal of sensing applications in the complex working environment.

In addition, the ability to extend 2D sensing materials by using non typical layered materials has further expand the variety of options for ultimate control over the desired properties. An alternative approach to structural optimization in TMDs is to introduce dopants such as transition metal compounds in order to modify the electronic structure in an attempt to further manage humidity sensing behaviours. For example, Burman et al. reported an increase in humidity response of MoS<sub>2</sub> flakes by using hexachloroplatinic acid (H<sub>2</sub>PtCl<sub>6</sub>), which induced Pt nanoparticles by increasing the number of active adsorption sites on the surface of the MoS<sub>2</sub> flakes.<sup>138</sup> Similarly, Wang et al. have reported a soft method to align the MoS<sub>2</sub> lattice using metal chloride CuCl<sub>2</sub> due to the strong interactions with the hexagonal 2D lattice structure.<sup>139</sup>

## 6.2 Fast-response humidity sensors based on TMDs-nanosheets and metal ion composites

In order to characterize the humidity sensing performance of humidity sensors based on TMDs materials, including MoS<sub>2</sub>- and WS<sub>2</sub> nanosheets, MoS<sub>2</sub> monolayer and few-layers, we designed and fabricated a simple humidity sensor measurement system. Figure 9 shows the schematic and photos of the homemade first-generation humidity sensors measurement setup. Our humidity sensor was investigated against a commercial humidity sensor (HIH-5031-001) in the humidity chamber. The chamber had two separate inlet lines for nitrogen gas and humid air. The humidity in the chamber was controlled by changing the proportion of nitrogen and humid air. The humidity was changed in the range of 4-80% with a period of 120s. Current response of all sensors was measured as a function of the RH under DC bias. The data was collected by a Keysight 34461A Multimeter controlled by computer with a MATLAB code.

However, with the understanding of the humidity sensors and the measurement technique. We developed the humidity sensing measurement system with a higher exchange ratio between water vapor and nitrogen gas to allow a more accurate measurement of the fast response and recovery time of our sensors. In the newest system, we used two voltage sources with program-controlled output voltage to control the two input gas lines for the water vapor and nitrogen. The sensors and the reference humidity sensor were placed a smaller box (50 mm \* 50 mm \* 10 mm) in the main chamber and all cables and input gas lines were connected to our sensors and the reference humidity sensor through holes on the wall of the small box. Using the small box enabled faster and more accurate control of the humidity environment because controlling humidity changes in the small space inside the box was easier. All TMDs-based humidity sensors were measured in this humidity sensing measurement system. In order to fabricate a higher sensitivity humidity sensor, the humidity sensing behaviours of MoS<sub>2</sub>- and WS<sub>2</sub> nanosheets were characterized and the results are shown in figure. 10. All nanosheets-based humidity sensors showed excellent repeatability after working for 15 hours. Figure. 10, (A-C), (D-F), and (G-I) show the I-V plots of humidity sensors based for WS<sub>2</sub> nanosheets formed floating membranes,

WS<sub>2</sub> nanosheets precipitate, and the composite of WS<sub>2</sub>- and MoS<sub>2</sub> nanosheets, respectively. The response and recovery times of these sensors with the other related parameters are listed in table 2. Metal ions can form metal nanoparticles on the surface of MoS<sub>2</sub> nanosheets to enhance the quality of MoS<sub>2</sub> nanosheets-based membranes, especially their electrical conductivity. Therefore, we found that MoS<sub>2</sub> nanosheets which could absorb more silver nanoparticles were faster to precipitate, and this could be a potential method to extract MoS<sub>2</sub> nanosheets with a small difference of particle sizes. Figure. 11, (A, B), and (C, D) show the humidity sensing performance of the MoS<sub>2</sub>@Cu and MoS<sub>2</sub>@Ag nanosheets based humidity sensors against a commercial humidity sensor (HIH-5031-001), respectively. To measure our devices, 1 mA current was applied on the sensors, and then the output voltage of the devices was detected. The sampling frequency was 0.8s per point. Figure. 11, (A) shows the V-T plot of the MoS<sub>2</sub>@Cu nanosheets-based humidity sensor, which shows the stability of its humidity sensing behavior in about a 140-minute measurement process. Figure. 11, (B) shows the individual V-T plot of Figure.11, (A), from which the response and recovery time of the device can be determined by counting the sampling points. Here, the response/recovery times of the MoS<sub>2</sub>/Cu sensor and MoS<sub>2</sub>/Ag sensor are also listed in Table 2. It is noticeable that the MoS<sub>2</sub>/Ag sensor shows a better performance than the MoS<sub>2</sub>/Cu sensor.

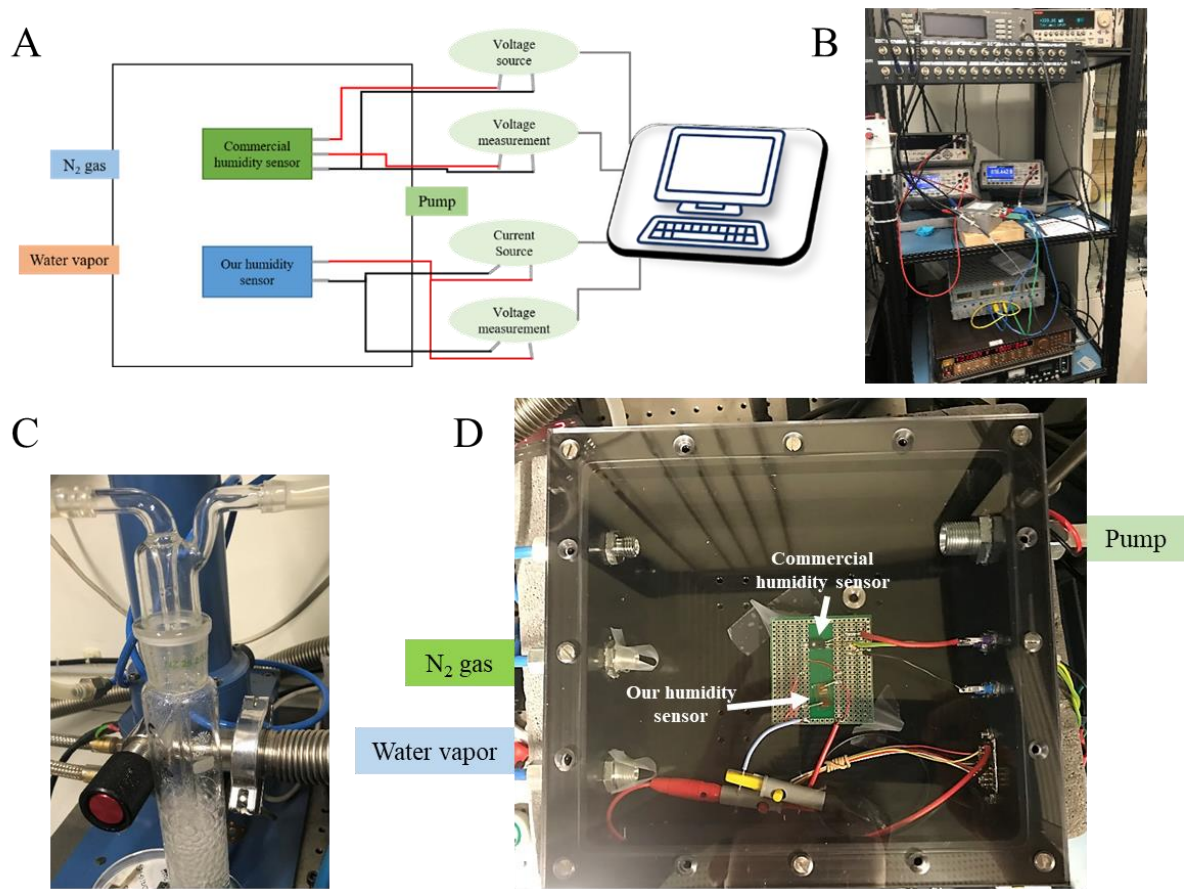


Fig. 9. Humidity sensor measurement setup. (A) Schematic of the humidity sensor measurement setup, (B) photo image of the measurement setup, (C) Water vapor supply unit, and (D) Photo image of the humidity test chamber.

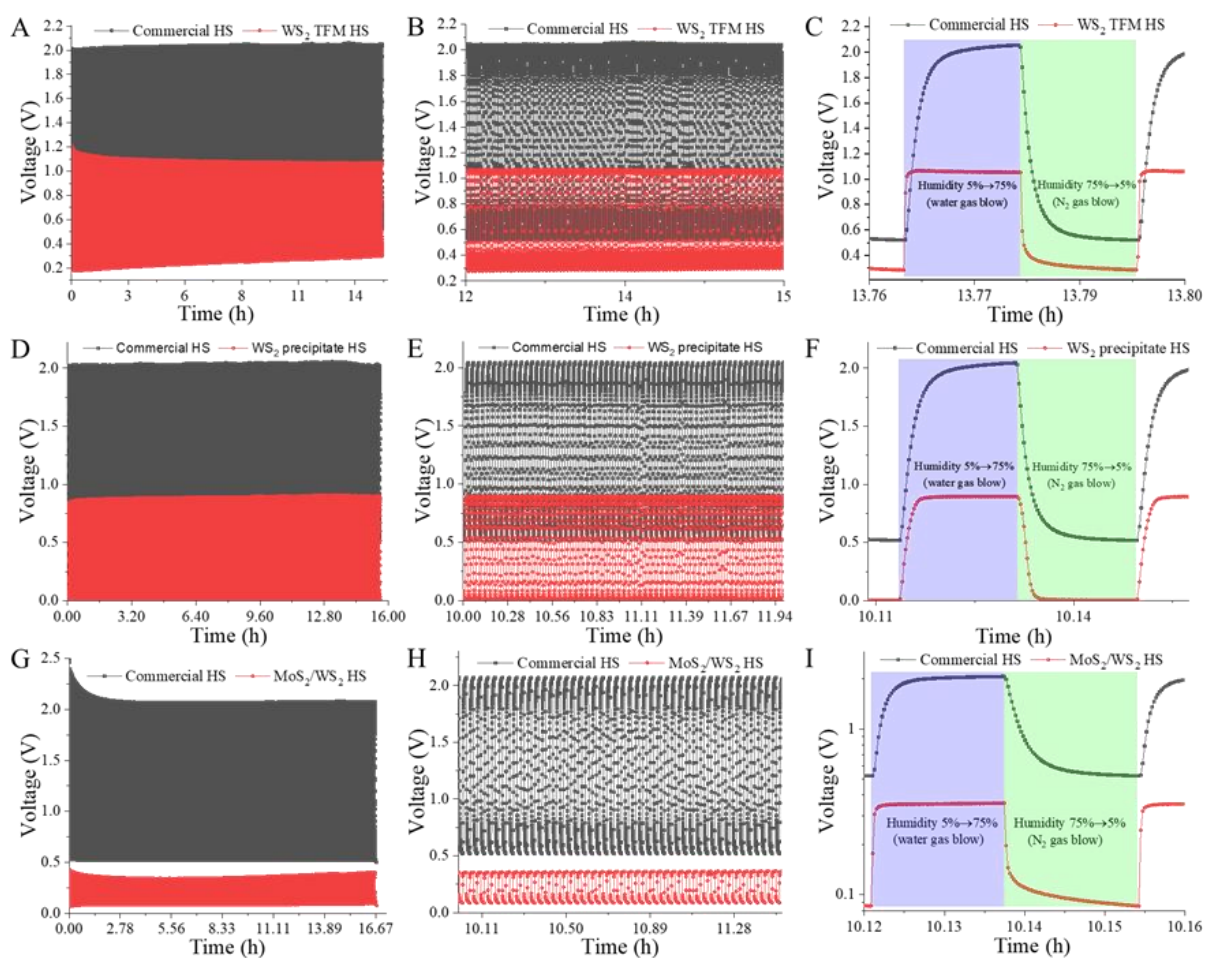


Fig. 10. The humidity sensitivity measurement of  $\text{MoS}_2$ - and  $\text{WS}_2$  nanosheets-based humidity sensors against a commercial sensor. (A-C), (D-F), and (G-I) show the whole range, one part, and an individual v-t curve of humidity sensing measurement for a  $\text{WS}_2$  nanosheets-based floating membrane humidity sensor, a nanosheets-based thick  $\text{WS}_2$  humidity sensor, and a mixed  $\text{MoS}_2$  and  $\text{WS}_2$  nanosheets-based humidity sensor, respectively.

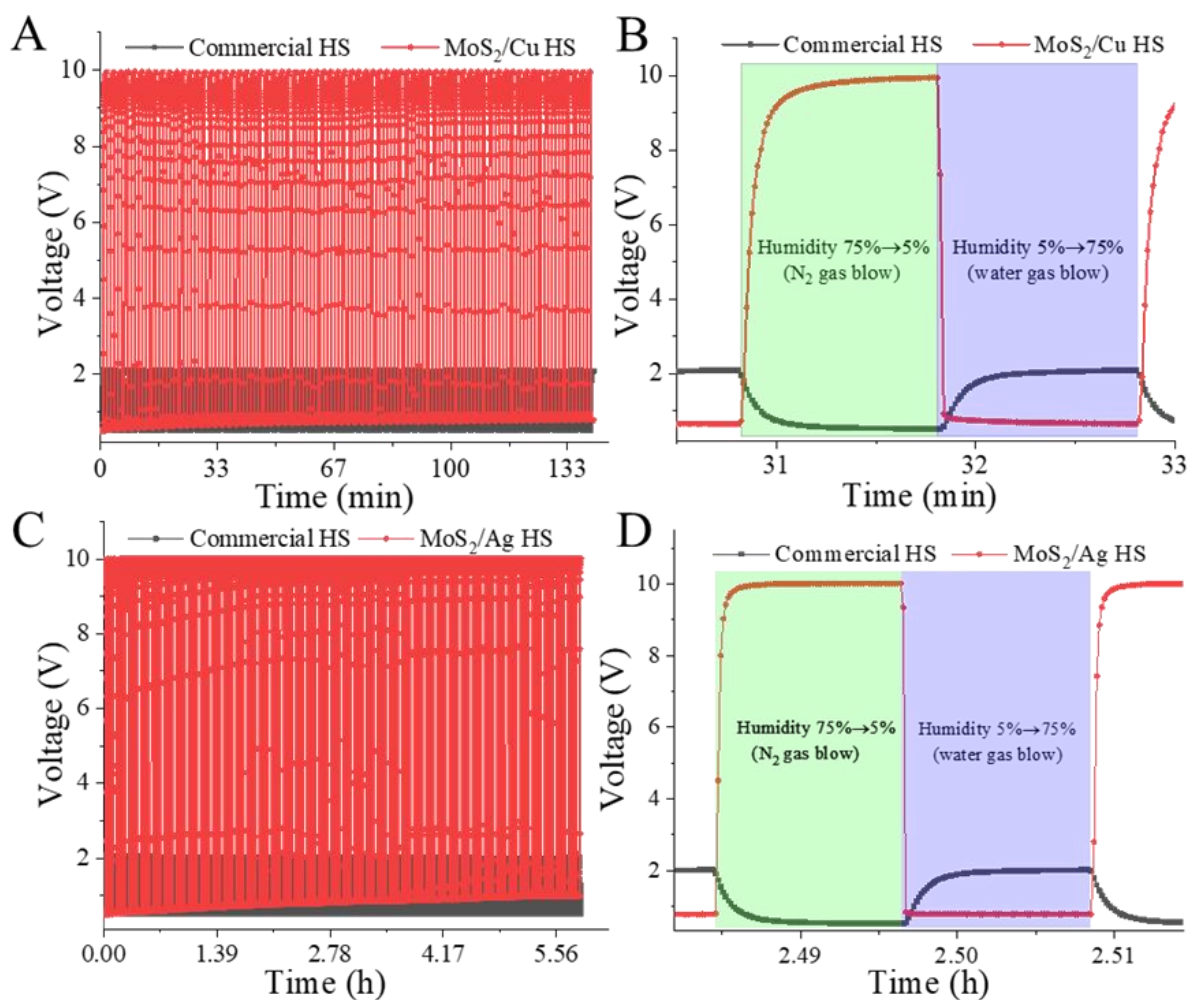


Fig. 11. The humidity sensitivity measurement of metal salts coated MoS<sub>2</sub> nanosheets-based humidity sensors against a commercial sensor. (A) and (B) show the entire range and individual v-t curves, respectively, of humidity sensing measurement for a copper-coated MoS<sub>2</sub> nanosheets-based humidity sensor, respectively. (C) and (D) show the entire range and individual v-t curves, respectively, of humidity sensing measurement for a silver-coated MoS<sub>2</sub> nanosheets-based humidity sensor, respectively.

		Recovery time (humidity 75% -5%)	Response time (humidity 5% -75%)	Test duration	Output voltage (V)
1	Commercial HS	~12 s	~12 s	---	0.5-2.1
2. Fig. 7. A-B	MoS <sub>2</sub> @Cu HS	~9.6 s	~1.6 s	133 min	0.64-9.95
3. Fig. 7. C-D	MoS <sub>2</sub> @Ag HS	~5.6 s	~1.6 s	5.86 h	0.78-10
4. Fig. 8. A-C	WS <sub>2</sub> TFM	~5.6 s	~2.4 s	15 h	0.28-1.06
5. Fig. 8. D-F	WS <sub>2</sub> precipitate	~8 s	~8.8 s	15 h	0.01-0.89
6. Fig. 8. G-I	MoS <sub>2</sub> /WS <sub>2</sub> TFM	~10 s	~2.4 s	16.7 h	0.08-0.36

Table 2: Response and recovery time of TMDs nanosheets-based RH sensors.

The mechanisms of humidity sensors have been widely studied based on different materials, such as graphene<sup>140</sup>, graphene oxide<sup>141</sup>, and MoS<sub>2</sub><sup>142</sup>, WS<sub>2</sub><sup>143</sup>, and SiC NSs,<sup>144</sup> and the composite of graphene oxide and MoS<sub>2</sub>.<sup>145</sup> We surveyed the main 2D layered materials-based humidity sensors and analyzed their advantages and disadvantages. Our findings were that the water and gas molecules attached on the surface and interface of sensing materials could affect the resistance and capacitance of the sensors. The humidity sensor was monitored in a chamber by changing the relative humidity (abbreviated as RH), which is stated as a percentage and determined by the expression:

$$RH\% = \left( \frac{P_v}{P_s} \right) \times 100\%$$

where  $P_v$  and  $P_s$  are the actual partial pressure and saturated pressure of moist air at the same given temperature, respectively. The MoS<sub>2</sub> nanosheets-based humidity sensor has some important parameters such as grain size, thickness, conductivity, dielectric constants, which could change the devices' output electric properties. The output voltage of the humidity sensor is given by:

$$V = I * n * R_s = I * n * \left( \frac{\rho}{t} \right) \left( \frac{L}{W} \right)$$

where  $I$  is the current applied on the humidity sensor,  $n$  is the number of humidity sensing areas,  $R_s$  is the sheets resistance of single humidity sensing area and  $\rho$  is resistivity of the humidity sensing materials, which will be changed by the environmental humidity.  $t$  is the thickness of the humidity sensing materials,  $L$  and  $W$  is the length and width of the single humidity sensing area, which could be easily controlled to adjust the output voltage of the devices.

Therefore, one way of adjusting the humidity sensing behaviors of MoS<sub>2</sub> nanosheets based membrane is by changing the nanosheets size (grain size) of the MoS<sub>2</sub> nanosheets-based membrane. Because MoS<sub>2</sub> nanosheets with different particle sizes have different absorbability of water molecular and resistivity, one of the most critical factors of a fast-response humidity sensor is the thickness of the humidity sensing materials. The sheet resistivity of a MoS<sub>2</sub> nanosheets-based membrane is dependent on its thickness. Because water molecules have difficulty entering the center of the membrane in a short time, the response and recovery time of the humidity sensor and

its thickness are inversely proportional. Therefore, synthesis of a low-roughness and thickness-controllable membrane is emerging. In this work, we developed a new method to synthesize a one-layer MoS<sub>2</sub> nanosheets-based membrane on the surface of water, and then lift up the floating membrane using a glass substrate. The thickness of the membrane could be controlled by repeating the transfer process, independent of the thickness of single MoS<sub>2</sub> nanosheets. Metal nanoparticles, including silver and copper nanoparticles, were introduced into the MoS<sub>2</sub> nanosheets-based membranes in order to adjust their conductivity and dielectric constant and optimize the humidity sensitivity of the devices. Due to the intervention of metal nanoparticles, the water absorbed ability of the composite was also modified, which also affected the response and recovery times of the devices.

To compare the humidity sensing performance of the precipitate-based humidity sensor, the sensor was fabricated using a floating membrane and showed short response and recovery times because of the lower thickness and surface roughness of the membranes. High-quality MoS<sub>2</sub> nanosheets-based thin membranes as humidity sensing materials are essential for our humidity sensors. Recently, a roll-to-roll deposition method has been reported to synthesis thin MoS<sub>2</sub> nanosheets-based membranes.<sup>146</sup> However, the experiment process used a lot toxic solvent, including ethylene glycol and n-hexane. Herein, a simple and environmentally friendly heat-solution method was developed in our lab for synthesizing floating MoS<sub>2</sub> nanosheets-based membranes on ethanol solution surface by heating. The floating membrane can be lifted up and placed on a glass substrate with electrodes to fabricate a fast-response humidity sensor. An interesting observation is that the MoS<sub>2</sub> nanosheets- and WS<sub>2</sub> nanosheets-based humidity sensors showed inverse humidity sensing mechanisms. This phenomenon is further discussed in the next part of this chapter.

### 6.3 Reversing the humidity response of MoS<sub>2</sub>- and WS<sub>2</sub>-based sensors with metal coatings

We report here for the first time that in MoS<sub>2</sub> and WS<sub>2</sub> nanosheets-based humidity sensors the sensing mechanism can be reversed by using transition metal salts, such



as  $\text{CuCl}_2$  and  $\text{AgNO}_3$ . For the  $\text{CuCl}_2$  modified sensors the initial humidity response was positive. However, after 40 minutes the response was reversed to negative and remained that way over several measurement cycles. This signal reversal of the electrical response was attributed to the formation of a continuous film on the  $\text{MoS}_2$  and  $\text{WS}_2$  nanosheets in the humidity measurement process under a voltage drive in the highly repeated humid environment. In contrast, pure  $\text{MoS}_2$  and  $\text{WS}_2$  sensors showed a positive response throughout the whole measurement cycle.

The most common TMDs solution-exfoliation methods include lithium-intercalation and high-power sonication.<sup>147</sup> To avoid the effects of lithium or any other chemical compound on the humidity sensing performance, the  $\text{MoS}_2$  and  $\text{WS}_2$  micro-crystals were exfoliated in an alcohol solution using a high-power sonication probe. The morphology changes of  $\text{CuCl}_2$  and  $\text{AgNO}_3$  modified  $\text{MoS}_2$  nanosheets was studied with scanning transmission electron microscopy (STEM), scanning electron microscopy (SEM), energy-dispersive X-ray spectroscopy (EDX) and X-ray photoemission spectroscopy (XPS). All fabricated sensors showed excellent performance with high sensitivity and short response and recovery times.

To analyse the origin of the humidity sensing mechanism reversal, the  $\text{MoS}_2$  and  $\text{WS}_2$ -based devices were monitored against a commercial relative humidity (RH) sensor with RH changes from 4 to 80% for over 1000 minutes. The effect of  $\text{CuCl}_2$  decoration on the humidity sensing response of  $\text{MoS}_2$  was investigated and we studied the RH sensors based on pure  $\text{MoS}_2$  and on  $\text{CuCl}_2$ -coated  $\text{MoS}_2$ . As expected, the current increased from 1 nA to 600  $\mu\text{A}$  with increasing Cu decoration levels. The pure  $\text{MoS}_2$  humidity sensor showed the highest response value of  $R \sim 74$ . The response values of  $\text{MoS}_2@x\text{Cu}$  humidity sensors decreased gradually from 10 to 0.5 with increasing amount of copper. The response and recovery times were defined as the times needed by the sensor to reach 90% of its saturation output current under increasing and decreasing environmental humidity. The response time of the devices was typically around 1 second, however, the recovery time increased from 1 s, for the pure  $\text{MoS}_2$ , to tens of seconds, for  $\text{CuCl}_2$ -coated  $\text{MoS}_2$ . This indicates that the detachment rate of water molecules from  $\text{CuCl}_2$ -coated  $\text{MoS}_2$  is slower than from pure  $\text{MoS}_2$  nanosheet surfaces. The humidity sensing properties of the  $\text{CuCl}_2$ -coated  $\text{WS}_2$  nanosheets-based devices were also investigated. Pure  $\text{WS}_2$ ,  $\text{WS}_2@100\text{Cu}$  and  $\text{WS}_2@150\text{Cu}$  sensors were characterized under 0.5 V bias voltage in the testing chamber, and the

reversal in the humidity sensing mechanism was observed for all the  $\text{CuCl}_2$ -coated  $\text{WS}_2$  nanosheets-based humidity sensors. To clarify the role of  $\text{CuCl}_2$ , a humidity sensor based on pure  $\text{CuCl}_2$  salt solution was fabricated and characterized. Its I-t curve was found to exhibit a positive response, which proves that the humidity sensing properties of pure  $\text{CuCl}_2$  do not determine the sensing characteristics of  $\text{CuCl}_2$ -coated  $\text{MoS}_2$  or  $\text{WS}_2$  TMDs. Thus, we postulated that there is an interaction between the  $\text{CuCl}_2$  and  $\text{MoS}_2/\text{WS}_2$  in the presence of humidity and under electrical bias which leads to the reversal in the humidity response. Finally, we studied the effect of Ag nanoparticles on the humidity sensing mechanisms of  $\text{MoS}_2$  and  $\text{WS}_2$  nanosheets. The  $\text{MoS}_2@100\text{Ag}$  and  $\text{WS}_2@200\text{Ag}$  sensors were fabricated and measured using the same procedure as described above and in Experimental Methods. They showed a negative response after stabilisation of the reversal process during the measurement. To summarize, the pure  $\text{MoS}_2$  and  $\text{WS}_2$  based sensors exhibited a stable positive response to humidity. In contrast,  $\text{MoS}_2$ - and  $\text{WS}_2$  nanosheets with  $\text{CuCl}_2$  and  $\text{AgNO}_3$  coatings-based humidity sensors exhibited a reversal in the humidity sensing behaviour from positive to negative.

In order to understand the reversal in the humidity response we performed a detailed structural characterization of the devices before and after the measurements. SEM and EDX maps yielded the morphology and elemental distribution. From the preceding characterisation we suggested that a continuous low porosity film was formed due to formation of  $\text{Cu}(\text{OH})_x\text{Cl}$  among both the  $\text{MoS}_2$  and  $\text{WS}_2$  nanosheets. In the as-prepared sensors, copper chloride was presented on the nanosheets. When the voltage was applied in the highly repetitive humid environment,  $\text{Cu}^{2+}$  move slowly towards the negative electrode. During these cycles, the Cu atoms form the  $\text{Cu}(\text{OH})_x\text{Cl}$  that fill the gaps in the porous layer and, in general, created a uniform coating on the nanosheets. The chemical state of the main elements in the  $\text{MoS}_2@MCs$ - and  $\text{WS}_2@MCs$ -based humidity sensors was determined by analysis of XPS spectra and showed the Cu-S bonds formed in  $\text{WS}_2@300\text{Cu}$  sensing film. After the humidity measurement, the high intensity peak appeared as same as the  $\text{MoS}_2@Cu$  sensing film. It also confirmed that an interface material was formed among the  $\text{WS}_2$  nanosheets under the voltage drive in the repeated high humidity environment. These results were corroborated by Raman scattering spectroscopy. The spectra did not show a significant change of the  $E_{12g}$  and  $A_{1g}$  modes of TMDs

before and after measurement, confirming the high stability of such materials in the humidity measurement.

According to the results of the characterization, we proposed a mechanism to explain the inversion of the sensing mechanisms and consequently an appropriate lumped circuit to reproduce it. The deposition of copper chloride onto the MoS<sub>2</sub> nanosheets occurs due to the coordination of copper with sulfur, which causes the precipitation of nanosheets from the colloidal dispersion. This ionic coating is responsible for the positive response in the first minutes of the measurements: when the humidity increases, the ions dissolve in the water channel and enhance the conductivity due to an extra ionic conductivity channel. This facilitates a slow cations migration to the negative electrode of the device. Meanwhile, the excess water leads to copper cations hydration and facilitates the conversion to Cu(OH)<sub>x</sub>Cl, which is poorly soluble in water. This conversion produces a rapid decrease of ionic conductivity and results in formation of an insoluble dielectric coating on the MoS<sub>2</sub> film. Furthermore, the decreasing porosity of the film inhibits the formation of water channels. Thus, the inversion from the positive to a negative mechanism reflects the evolution and conversion of copper from cations to hydroxychloride. In the last part of the measurements, when the mechanism was purely negative, water molecules attached on the surface of the copper coating and under an applied voltage, the charge was trapped in the water film mediated by the newly formed continuous film. Based on the sensing mechanism explained above, an equivalent circuit with two resistances varying with time R<sub>1</sub>(t) and R<sub>2</sub>(t) in parallel with two inductors L<sub>1</sub> and L<sub>2</sub> is proposed. Thus, this simple model works well to explain the sensing mechanism. The inversion from positive to negative response of the sensor was well represented by the domination of R<sub>1</sub> and R<sub>2</sub> over time.

To further understand the reversal in the humidity sensing mechanism in our devices a comparison between our sensors and previously published reports was made. Overall, the positive MoS<sub>2</sub> humidity sensors were mainly fabricated using overlapping MoS<sub>2</sub> nanosheets. In such a loose and porous structures water molecules attaching to nanosheet edges and surface can form the proton transport channels between the overlapping nanosheets, according to the Grotthuss mechanism.<sup>131,148</sup> Due to the high contact resistance between the nanosheets, the proton transport channels dominate the conductance in the structure. The proton transport channels conductance can be

affected by the water content and thus results in a decrease of the film impedance with increasing humidity. On the contrary, the negative MoS<sub>2</sub>-based humidity sensors were fabricated by various methods, using CVD growth, sulfurization, annealing, and the mechanical exfoliation.<sup>119,122,124,149,150</sup> Sensor-based on the polycrystalline films were mainly prepared by the CVD growth, sulfurization and annealing methods at high temperature (300-1000 °C). After annealing, a continuous film was formed by the improvement of the adhesion and contact quality among their grains or nanosheets. The mechanical exfoliated single crystals original has good material quality. Compared to the positive MoS<sub>2</sub> humidity sensors, the key difference is that the negative humidity sensors were fabricated using continuous films, either single- or polycrystalline. These films have an insignificant concentration of structural gaps or active edges, unlike the MoS<sub>2</sub> nanosheets-based film. In such a case, the possibility of water forming proton transport channels in the film becomes limited. The electrons present in the continuous film were trapped by water molecules attached to the surface of the nanomaterial especially in the high humidity environment and this results in a negative humidity sensing behaviour, with the impedance increasing with increasing humidity.<sup>98,151</sup> Similarly, some representative WS<sub>2</sub> nanosheets-based positive humidity sensors, mainly fabricated using solution-exfoliation, tungsten sulfurization and hot-wire chemical vapour deposited WS<sub>2</sub> nanoparticles were also discussed here. We suggest that the negative humidity mechanism can be explained in the same way as for the negative MoS<sub>2</sub> humidity sensors.

More details are discussed in the following paper Article 4.

## 6.4 Conclusion

In conclusion, we fabricated a humidity sensor measurement system. Pure MoS<sub>2</sub> Nanosheets, MoS<sub>2</sub>@Ag Nanosheets, MoS<sub>2</sub>@Cu Nanosheets, and pure WS<sub>2</sub> Nanosheets based humidity sensors were characterized and showed better humidity sensitivity performance than the usual commercial humidity sensors, and most of our sensors showed a low humidity response and recovery time of few seconds. MoS<sub>2</sub>- and WS<sub>2</sub> nanosheets have proved the possibility to fabricate fast response humidity sensors with long-term work stability. Up to now, our best humidity sensor has been

the MoS<sub>2</sub>@Ag nanosheets-based humidity sensor with a short response and recovery time of ~5.6 s and ~1.6 s, respectively when humidity of the chamber changes rapidly in the humidity range of 5% to 75%, and the sampling frequency of output voltage of the equipment is about 1.25 Hz (0.8 s). While this is not fast enough, it can reach the requirement for the first-step humidity measurement of our first-generation humidity sensor. The inversed WS<sub>2</sub>- and MoS<sub>2</sub> nanosheets-based sensors were also considered to fabricate a Winston bridge for high robust humidity sensors.

A simple method for synthesizing CuCl<sub>2</sub> and AgNO<sub>3</sub> modified MoS<sub>2</sub> and WS<sub>2</sub> nanosheets was presented. These nanosheets were used in the manufacture of high-performance RH sensors. The sensor is easy to manufacture, has high sensitivity and long-term stability, and is suitable for applications in a wide range of environments. A simple and effective way to adjust the electrical conductivity of the sensor by controlling the amount of metal salts, especially CuCl<sub>2</sub>, has also been proposed. This work is the first observation to show the reversal of the moisture response from a TMD-based device. The pristine TMD-based sensor showed a positive moisture response, while the MoS<sub>2</sub>@MC and WS<sub>2</sub>@MC-based films showed that the moisture detection mechanism reverses from positive to negative in the first few minutes of measurement. From the analysis of morphology, composition, and real-time I-t curves, this inversion process can be explained by the formation of a continuous membrane under driving voltage in long-term moisture detection measurements. This study shows that metal salts help improve the adhesion of loose MoS<sub>2</sub> and WS<sub>2</sub> nanosheets, resulting in a continuous film with low porosity. The reversal of positive to negative behavior of a humidity sensor can be explained in the context of the sensor's "hydrogen bond network" to "charge acceptor" drive driven by changes in film morphology. This mechanism is supported by simulating sensor activity with a lumped circuit-based model. This work helps to better understand the moisture detection behavior of TMD-based applications, and its morphology and metal decoration are important for producing high performance sensors with controllable and reliable moisture detection mechanisms and gives a new perspective on aging and performance reversal of nanosheet-based devices in complex working environments.

# Article 4

# Reversing the Humidity Response of MoS<sub>2</sub>- and WS<sub>2</sub>-Based Sensors Using Transition-Metal Salts

Peng Xiao,\* Davide Mencarelli, Emigdio Chavez-Angel, Christopher Hardly Joseph, Antonino Cataldo, Luca Pierantoni, Clivia M. Sotomayor Torres, and Marianna Sledzinska



Cite This: *ACS Appl. Mater. Interfaces* 2021, 13, 23201–23209



Read Online

ACCESS |



Metrics & More



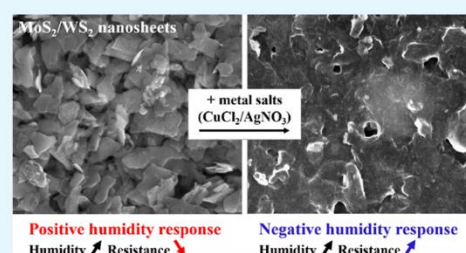
Article Recommendations



Supporting Information

**ABSTRACT:** Two-dimensional materials, such as transition-metal dichalcogenides (TMDs), are attractive candidates for sensing applications due to their high surface-to-volume ratio, chemically active edges, and good electrical properties. However, their electrical response to humidity is still under debate and experimental reports remain inconclusive. For instance, in different studies, the impedance of MoS<sub>2</sub>-based sensors has been found to either decrease or increase with increasing humidity, compromising the use of MoS<sub>2</sub> for humidity sensing. In this work, we focus on understanding the interaction between water and TMDs. We fabricated and studied humidity sensors based on MoS<sub>2</sub> and WS<sub>2</sub> coated with copper chloride and silver nitrate. The devices exhibited high chemical stability and excellent humidity sensing performance in relative humidity between 4 and 80%, with response and recovery times of 2 and 40 s, respectively. We have systematically investigated the humidity response of the materials as a function of the type and amount of induced metal salt and observed the reverse action of sensing mechanisms. This phenomenon is explained based on a detailed structural analysis of the samples considering the Grotthuss mechanism in the presence of charge trapping, which was represented by an appropriate lumped-element model. Our findings open up a possibility to tune the electrical response in a facile manner and without compromising the high performance of the sensor. They offer an insight into the time-dependent performance and aging of the TMD-based sensing devices.

**KEYWORDS:** humidity sensors, sensing mechanisms, tmds, MoS<sub>2</sub>, WS<sub>2</sub>, transition-metal salts



## INTRODUCTION

Fast development toward smart homes and cities leads to an increasing demand for environmental monitoring of living, working, and recreational spaces and pushes the study of the high-performance environmental sensors. Managing optimum indoor humidity is a priority for every homeowner as it directly affects the comfort and wellbeing as well as the proper functioning of heating and air conditioning units. In electronic systems, especially the ones operating outdoors, humidity affects both the performance and the lifetime. In the past few decades, humidity sensors were mainly developed with materials such as metal oxides or ceramics<sup>1</sup> due to their high mechanical and chemical stability and fast response to the changes of humidity. Interestingly, some humidity sensors have been shown to exhibit a decrease of impedance with increasing humidity (defined as a positive response),<sup>2–5</sup> while other works have shown an increase of the impedance with increasing humidity (defined as a negative response).<sup>6,7</sup> The positive humidity sensing mechanism is usually interpreted as invoking the proton hopping process (Grotthuss mechanism).<sup>8,9</sup> This process describes the proton transport through the hydrogen bonds of water molecules or other hydrogen-bonded liquids, between nanosheets in the film, which results in an increase in the conductance with increasing humidity. On the other hand, the negative response can be

explained by the electron trapping process<sup>10,11</sup> whereby water molecules absorbed by the material can trap free charges, which results in a conductance decrease with increasing humidity.

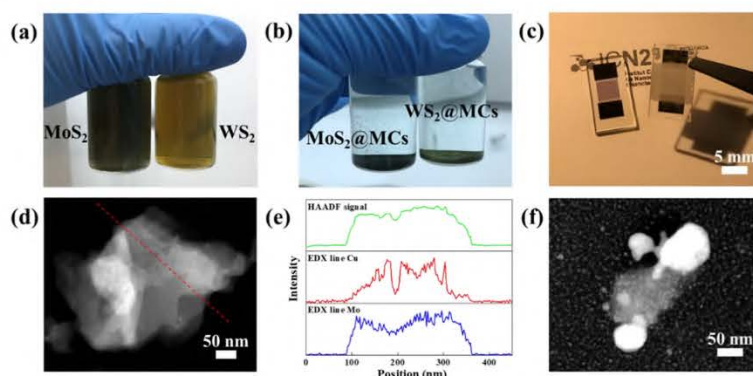
In the recent years, new humidity sensing materials are being considered including two-dimensional (2D) materials such as graphene, black phosphorus, and transition-metal dichalcogenides (TMDs), especially MoS<sub>2</sub> and WS<sub>2</sub>.<sup>6,12–14</sup> These materials are attractive for sensing applications because of their chemically active edges, easy fabrication methods, and good electrical performance.<sup>12</sup> The TMD-based humidity sensors showed excellent humidity sensing properties with a fast response and high responsivity.<sup>7,15</sup> Substantial progress has been made in improving the device flexibility and sensitivity.<sup>16–18</sup> However, the electrical response of 2D-based moisture sensors has been reported to be ambiguous showing responses with opposite signs for the same material. For example, Zhao et al. claimed that electron transfer from a MoS<sub>2</sub> film to the absorbed water

Received: February 26, 2021

Accepted: April 23, 2021

Published: May 5, 2021





**Figure 1.** TMD film preparation and structural characterization. Optical images of (a) stable MoS<sub>2</sub> and WS<sub>2</sub> nanosheet solutions, (b) MoS<sub>2</sub> and WS<sub>2</sub> solutions mixed with metal-containing salts, (c) gold/titanium (95 nm/5 nm) electrodes on a glass substrate (left) and a nanosheet-based humidity sensor (right). STEM images of (d) MoS<sub>2</sub>@Cu nanoparticle and (e) corresponding EDX line scanning curves for the HAADF signal and elemental distributions of Cu and Mo. STEM images of (f) MoS<sub>2</sub>@Ag nanoparticle.

molecule results in a negative response of the MoS<sub>2</sub> film-based humidity sensor.<sup>6</sup> On the other hand, Mondal et al. reported that a MoS<sub>2</sub> nanosheet-based humidity sensor shows a positive response attributed to the electron transfer from a water molecule to MoS<sub>2</sub> at low humidity and a proton hopping process at high humidity.<sup>5</sup> Water-associated protons and water-trapped electrons both exist when water molecules are attached on the surface of materials, but so far limited research has been carried out to appropriately discuss these effects.<sup>19–22</sup> While 2D materials have the potential to be applied in mass production, the reversing process can cause a certain risk and is dangerous if the surrounding things reacted with the materials and can fully reverse the measurement results. Therefore, both sensing mechanisms should be taken into consideration to further avoid the risk of device aging and performance reversal of sensing applications in a complex working environment.

In addition, the ability to extend 2D sensing materials by using the not typically layered materials would further expand the variety of options for an ultimate control over the desired properties. An alternative approach to structural optimization in TMDs is to introduce dopants such as transition-metal compounds in order to modify the electronic structure in an attempt to further manage the humidity sensing behaviors. For example, Burman et al. reported that the humidity response of MoS<sub>2</sub> flakes increased on using hexachloroplatinic acid (H<sub>2</sub>PtCl<sub>6</sub>), which was because Pt nanoparticles increase the number of active adsorption sites on the surface of the MoS<sub>2</sub> flakes.<sup>23</sup> Wang et al. reported a soft method to align the MoS<sub>2</sub> lattice using metal chloride CuCl<sub>2</sub> due to the strong interactions with the hexagonal 2D lattice structure.<sup>24</sup>

We report here for the first time that in MoS<sub>2</sub> and WS<sub>2</sub> nanosheet-based humidity sensors, the sensing mechanism can be reversed using transition-metal salts such as CuCl<sub>2</sub> and AgNO<sub>3</sub>. For these CuCl<sub>2</sub>-modified sensors, the initial humidity response was positive. However, after 40 min, the response was reversed to negative and remained the same over several measurement cycles. This signal reversal of the electrical response was attributed to the formation of a continuous film on the MoS<sub>2</sub> and WS<sub>2</sub> nanosheets in the humidity measurement process under a voltage drive in the highly repeated humid environment. In contrast, pure MoS<sub>2</sub> and WS<sub>2</sub> sensors showed a positive response throughout the whole measurement cycle. This process was clarified by studying the morphological changes of the hybrid composites with scanning transmission

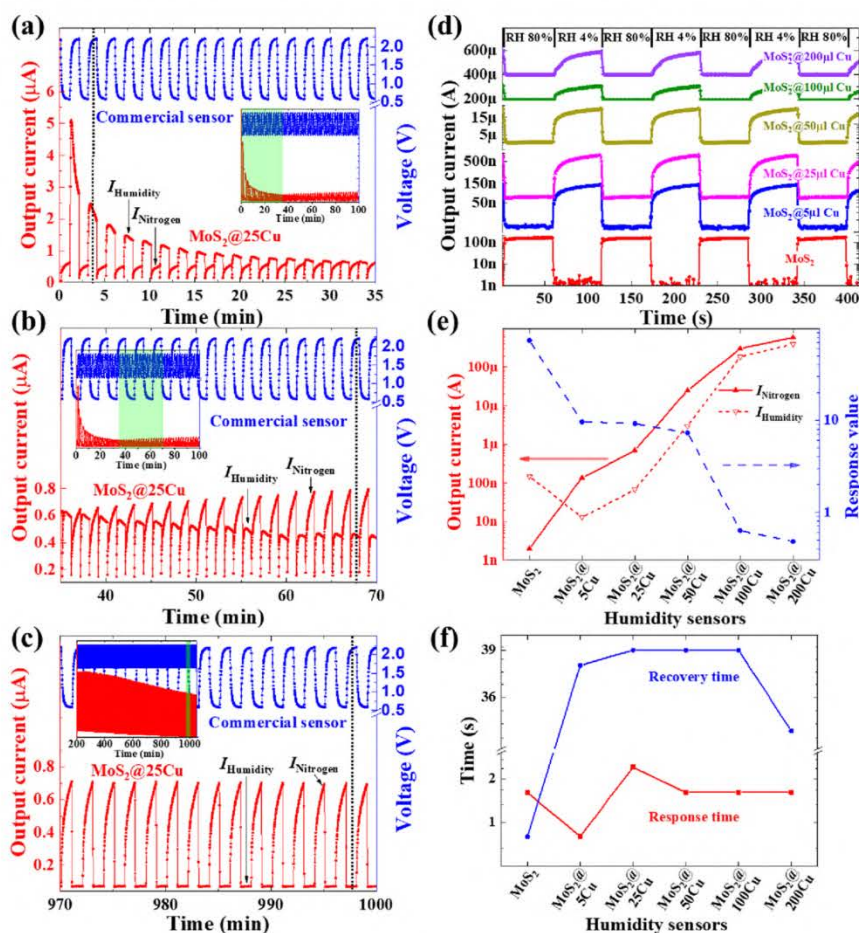
electron microscopy (STEM), scanning electron microscopy (SEM), energy-dispersive X-ray spectroscopy (EDX), and X-ray photoelectron spectroscopy (XPS). All fabricated sensors showed excellent performance with high sensitivity and short response and recovery times. Moreover, by changing the concentration of the metal salts, one can effectively change the decorating level of the sensing film and thereby adjust its impedance. The sensing cycle and its inversion were simulated using a lumped circuit. Finally, we summarize the humidity sensing mechanisms of the reported MoS<sub>2</sub>- and WS<sub>2</sub>-based humidity sensors to demonstrate the morphology effect on their humidity sensing behaviors.

## RESULTS

The most common TMD solution exfoliation methods include lithium intercalation and high-power sonication.<sup>25</sup> To avoid the effects of lithium or any other chemical compound on the humidity sensing performance, the MoS<sub>2</sub> and WS<sub>2</sub> microcrystals were exfoliated in an alcohol solution using a high-power sonication probe. The nanosheet-containing solutions showed a very stable behavior under ambient environmental conditions (see Figure 1a); however, their equilibrium could be broken by adding transition-metal salt solutions such as CuCl<sub>2</sub> and AgNO<sub>3</sub>. The aggregation of metal salts in the dispersion produces precipitation of MoS<sub>2</sub> and WS<sub>2</sub> nanosheets with metal salt coatings (MoS<sub>2</sub>@MCs and WS<sub>2</sub>@MCs) within 24 h as shown in Figure 1b. The humidity sensors were fabricated by drop-casting the precipitates on prefabricated electrodes. The average sizes of these MoS<sub>2</sub> and WS<sub>2</sub> nanosheets were ~258 and ~154 nm, respectively (see Figure S1). The thickness of MoS<sub>2</sub> and WS<sub>2</sub> nanosheets were in the range of 2.5–25 and 30–65 nm, respectively (see Figure S2). The final device is shown in Figure 1c, and the details of the fabrication process are provided in the Experimental Methods.

The morphology of CuCl<sub>2</sub>- and AgNO<sub>3</sub>-modified MoS<sub>2</sub> nanosheets was studied by STEM. The image of a MoS<sub>2</sub> nanosheet with CuCl<sub>2</sub> (MoS<sub>2</sub>@Cu) is shown in Figure 1d. An EDX line scan of the MoS<sub>2</sub>@Cu nanosheet along the red-dotted line and the corresponding curves for high-angle annular dark-field (HAADF) element distribution of Cu and Mo are shown in Figure 1e. The corresponding EDX spectra show that chloride still exists in the new compounds (see Figure S3 in the Supporting Information). They indicate that the majority of MoS<sub>2</sub>@Cu nanosheets were evenly covered by CuCl<sub>2</sub>. Wang et





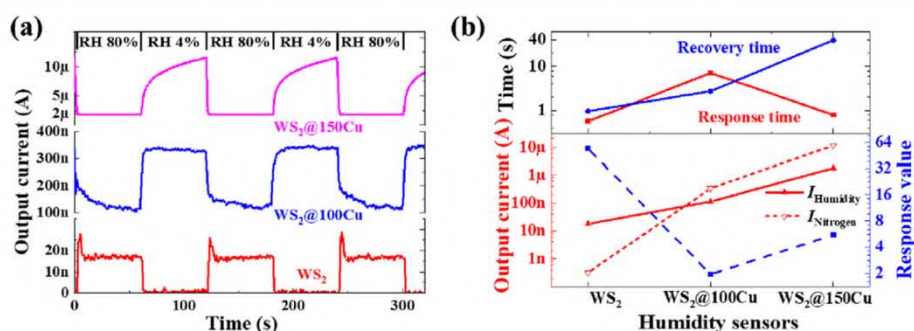
**Figure 2.** MoS<sub>2</sub>-based humidity sensor. Real-time measurement of the humidity sensor MoS<sub>2</sub>@25Cu under repeated RH between 4 and 80% including a comparison to a commercial sensor in the insets of panels (a–c). (a) Positive humidity sensing response in the first 35 min. (b) Positive humidity sensing mechanism reversed to negative in the subsequent 35 min. (c) Stable negative humidity response in the last 30 min of the 1000 min measurement cycle. The dotted vertical lines in panels (a–c) also denote the sensor's  $I_{\text{Humidity}}$ . (d) I–t curves of the MoS<sub>2</sub> nanosheet-based humidity sensors with different Cu decorating levels. (e) Corresponding output current and response values and (f) response and recovery times of these sensors.

al. demonstrated the formation of ionic metal chloride nanocrystals on the surface of MoS<sub>2</sub> using CuCl<sub>2</sub> solution.<sup>24</sup> The heterostructure is mainly coupled via a strong Cu–S chemical bonding rather than weak van der Waals interactions due to the high reactivity of unsaturated Cu atoms at the interface. Figure 1f shows the STEM image of a MoS<sub>2</sub>@Ag nanosheet. The silver ions could be directly reduced and deposited on the surface of MoS<sub>2</sub> nanosheets in the form of metallic silver nanoparticles where MoS<sub>2</sub> acts as a photocatalyst.<sup>26</sup> The smaller (~5 nm) Ag nanoparticles were coated on the surface of MoS<sub>2</sub>, while the larger (~50 nm) Ag nanoparticles were attached to its edges. Due to the large amount of bigger metallic Ag nanoparticles attached to the MoS<sub>2</sub> nanosheet edges, the MoS<sub>2</sub>@Ag-based film has higher electrical conductivity than the MoS<sub>2</sub>@Cu ones.

To analyze the origin of reversal of the humidity sensing mechanism, the MoS<sub>2</sub> and WS<sub>2</sub>-based devices were monitored against a commercial relative humidity (RH) sensor for over 1000 min. A voltage of 1 V was applied to the sensor placed in a humidity testing chamber and 500 cycles of RH changes from 4 to 80% were carried out during a 1000 min measurement interval. The output voltage of the commercial sensor increased

from 0.58 to 2.19 V as the RH increased from 4 to 80%, and its sensing performance was noted as positive. A detailed description of the testing chamber and the RH cycles is given in the **Experimental Methods**.

Figure 2a–c shows the temporal dependence of the electrical current (I–t curves) of a CuCl<sub>2</sub>-coated MoS<sub>2</sub> humidity sensor. The preparation of the RH sensor-labeled MoS<sub>2</sub>@25Cu took place in a solution of 15 mL of MoS<sub>2</sub> with 25 μL of 0.1 g/mL of CuCl<sub>2</sub> (see **Experimental Methods** for details). The RH was changed by flowing different proportions of nitrogen and humid air in the humidity chamber. In the first 35 min, the sensor showed a positive humidity response. However, the output current  $I_{\text{Humidity}}$  (current under high humidity) decreased sharply with time until it was almost equal to  $I_{\text{Nitrogen}}$  (current in a nitrogen environment) in 20 min. Until that moment, the humidity sensing mechanism was not clear and both currents had similar values,  $I_{\text{Nitrogen}} \approx I_{\text{Humidity}}$ . After 35 min,  $I_{\text{Nitrogen}}$  increased and become larger than  $I_{\text{Humidity}}$  and the humidity response reversed to negative. From Figure 2c, it is observed that the humidity sensing performance gradually became stable with a negative response although  $I_{\text{Nitrogen}}$  decreased slightly during



**Figure 3.** WS<sub>2</sub> humidity sensors. Real-time measurement of (a) pure WS<sub>2</sub>, WS<sub>2</sub>@100Cu, and WS<sub>2</sub>@150Cu nanosheet-based humidity sensors and the corresponding (b) sensor response/recovery time and output current/response values.

the test from 200 to 1050 min. The noise in  $I_{\text{Humidity}}$  was not detectable and the signal was flat and stable.

To investigate the effect of CuCl<sub>2</sub> decoration on the humidity sensing response, we studied RH sensors based on pure MoS<sub>2</sub> and CuCl<sub>2</sub>-coated MoS<sub>2</sub>, MoS<sub>2</sub>@*x*Cu, where *x* varied from 5 to 200 μL (see Figure 2d). First of all, the pure MoS<sub>2</sub> humidity sensor showed a positive sensing response with a low output current in the range of 1 to 25 nA, which was maintained during the whole experiment lasting 1000 min. On the other hand, the humidity response of all the MoS<sub>2</sub>@*x*Cu sensors was reversed from positive to negative within a few to tens of minutes. All the output currents remained stable after the reversal process was complete. The output currents increased with the increasing amount of Cu. Figure 2e shows the output currents  $I_{\text{Humidity}}$  and  $I_{\text{Nitrogen}}$  and the response value  $R$  calculated as  $R = (I_{\text{Max}} - I_{\text{min}}) / I_{\text{min}}$ . The values of  $I_{\text{Max}}$  and  $I_{\text{min}}$  are the maximum and minimum currents, respectively, after the output current stabilizes in the measurement. As expected, the currents increased from 1 nA to 600 μA with increasing Cu decoration levels. The pure MoS<sub>2</sub> humidity sensor showed the highest response value of  $R \sim 74$ . The response values of MoS<sub>2</sub>@*x*Cu humidity sensors decreased gradually from 10 to 0.5 with the increasing amount of copper.

The response and recovery times are defined as the times needed by the sensor to reach 90% of its saturation output current under increasing and decreasing environmental humidity. The response time of the devices was typically around 1 s; however, the recovery time increased from 1 s for the pure MoS<sub>2</sub> to tens of seconds for CuCl<sub>2</sub>-coated MoS<sub>2</sub>, as shown in Figure 2f. This result indicates that the detachment rate of water molecules from CuCl<sub>2</sub>-coated MoS<sub>2</sub> is slower than that from pure MoS<sub>2</sub> nanosheet surfaces.

To investigate the humidity sensing properties of the CuCl<sub>2</sub>-coated WS<sub>2</sub> nanosheet-based devices, pure WS<sub>2</sub>, WS<sub>2</sub>@100Cu, and WS<sub>2</sub>@150Cu sensors were characterized under a 0.5 V bias voltage in the testing chamber. As shown in Figure 3a, the pure WS<sub>2</sub>-based sensor showed a positive response to humidity during the 1000 min measurement cycle, with the output current ranging from 0 to 25 nA. Once the water vapor was let into the chamber, the device showed a sharp peak in  $I_{\text{Humidity}}$  and then became stable, which was possibly caused by the release of electrons accumulated in WS<sub>2</sub>.

The reversal in the humidity sensing mechanism was observed for all the CuCl<sub>2</sub>-coated WS<sub>2</sub> nanosheet-based humidity sensors. The response of WS<sub>2</sub>@150Cu was reversed from positive to negative in the first 40 min of the cycle (see Figure S4 in the Supporting Information), similar to that for MoS<sub>2</sub>@Cu as discussed above. The measured output current was in the range of 1.7 to 12 μA. Figure 3b shows the changes in the response

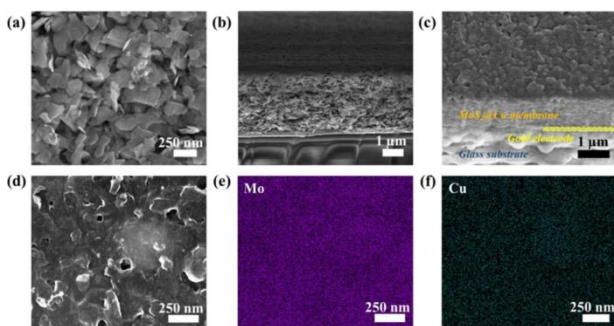
values,  $I_{\text{Humidity}}$  and  $I_{\text{Nitrogen}}$  of these devices with the increasing amount of CuCl<sub>2</sub>. The trend is consistent with the CuCl<sub>2</sub>-coated MoS<sub>2</sub>-based humidity sensor. The pure WS<sub>2</sub> showed the highest response value of 60, the lowest  $I_{\text{Humidity}}$  and  $I_{\text{Nitrogen}}$ , and the slowest response and recovery time compared to the CuCl<sub>2</sub>-coated WS<sub>2</sub> humidity sensors.

To clarify the role of CuCl<sub>2</sub>, a humidity sensor based on a pure CuCl<sub>2</sub> salt solution was fabricated and characterized. Its  $I$ - $t$  curve was found to exhibit a positive response (see Figure S5 in the Supporting Information), which proves that the humidity sensing properties of pure CuCl<sub>2</sub> do not determine the sensing characteristics of CuCl<sub>2</sub>-coated MoS<sub>2</sub> or WS<sub>2</sub> TMDs. Thus, we postulate that there is an interaction between CuCl<sub>2</sub> and MoS<sub>2</sub>/WS<sub>2</sub> in the presence of humidity and under electrical bias that leads to the reversal in the humidity response.

Finally, we studied the effect of Ag nanoparticles on the humidity sensing mechanisms of MoS<sub>2</sub> and WS<sub>2</sub> nanosheets. The MoS<sub>2</sub>@100Ag and WS<sub>2</sub>@200Ag sensors were fabricated and measured using the same procedure as described above and in Experimental Methods. They showed a negative response after stabilization of the reversal process during the measurement (see Figure S6a,b in the Supporting Information). The output currents of the MoS<sub>2</sub>@100Ag and WS<sub>2</sub>@200Ag sensors were in the range of 8–15 and 10–100 mA, respectively. The current is much higher than for the CuCl<sub>2</sub>-coated sensors due to the excellent electrical conductivity of the rather large size of the Ag nanoparticles. The  $I_{\text{Humidity}}$  and  $I_{\text{Nitrogen}}$  response values, and response/recovery times of the two devices were compared, and the results are shown in Table S1. The WS<sub>2</sub>@200Ag sensor shows a higher output current due to the higher charge concentration of Ag compared to the MoS<sub>2</sub>@100Ag sensor. However, the MoS<sub>2</sub>@100Ag humidity sensor has a more stable sensing characteristic with a higher response value of 1.29 and shorter response and recovery times. To summarize, the pure MoS<sub>2</sub>- and WS<sub>2</sub>-based sensors exhibit a stable positive response to humidity. In contrast, MoS<sub>2</sub> and WS<sub>2</sub> nanosheets with CuCl<sub>2</sub> and AgNO<sub>3</sub> coating-based humidity sensors exhibit a reversal in the humidity sensing behavior from positive to negative.

## DISCUSSION

In order to understand the reversal in the humidity response, we performed a detailed structural characterization of the devices before and after the measurements. SEM and EDX maps yielded the morphology and elemental distribution. The original MoS<sub>2</sub>@Cu has a porous structure based on loosely overlapping nanosheets without a tight connection, as shown in Figure 4a,b. As shown in Figure 4c,d, the cross-sectional and top-view SEM

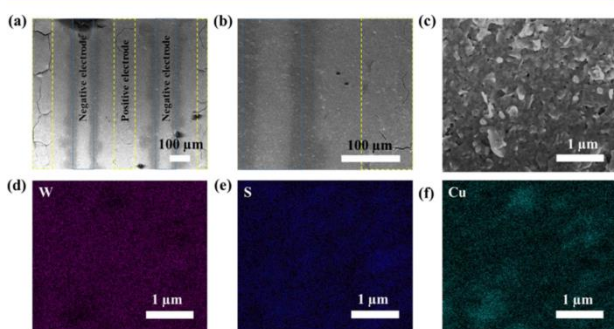


**Figure 4.** Structural characteristics of the as-fabricated MoS<sub>2</sub>@25Cu humidity sensor. (a) Cross-sectional and (b) top-view SEM images of the humidity sensor. (c) Cross-sectional and (d) top-view SEM images after a measurement over 1000 min. Corresponding EDX mapping of (e) Mo and (f) Cu in panel (d).

images of MoS<sub>2</sub>@Cu show that a continuous film of MoS<sub>2</sub>@Cu nanosheets was formed after the 1000 min measurement cycle. The film is clearly less porous and more uniform compared to the as-fabricated MoS<sub>2</sub>@Cu film.

Figure 4c shows a MoS<sub>2</sub>@Cu-based sensor of thickness ~800 nm. The 100 nm-thick gold electrode deposited on the glass substrate is highlighted by the box indicated by the dashed yellow lines. Figure 4e,f shows the corresponding EDX maps of the elements Mo and Cu shown in Figure 4d. Figure S7a,b in the Supporting Information show the SEM image of the pure MoS<sub>2</sub> nanosheets with the corresponding EDX mapping images. The EDX analysis confirmed that the Mo and Cu elements were uniformly distributed in the MoS<sub>2</sub>@Cu film.

The formation of a continuous film after the measurements was also observed in the WS<sub>2</sub>-based humidity sensors. Interestingly, darker areas were visible in the SEM image alongside the negative electrodes of the WS<sub>2</sub>@100Cu sensor after a 1000 min measurement cycle, as shown in Figure 5a,b.



**Figure 5.** Structural characteristics of the as-fabricated WS<sub>2</sub>@100Cu humidity sensor. (a,b) SEM images of the WS<sub>2</sub>@100Cu humidity sensor after a 1000 min measurement. (c) Detail of the negative electrode edge showing an almost continuous film of WS<sub>2</sub> nanosheets. The corresponding EDX mapping of (d) W, (e) S, and (f) Cu.

The color change indicates the migration of Cu<sup>2+</sup> and the ensuing hydration by humidity under the voltage drive during the measurements.<sup>27</sup> Figure 5c shows the SEM image of the dark area, where the WS<sub>2</sub> nanosheets are seen to be well connected forming a continuous film of uniform distribution of the constituting elements (see Figure 5d–f).

From the preceding characterization, we suggest that a continuous low porosity film is formed due to the formation of

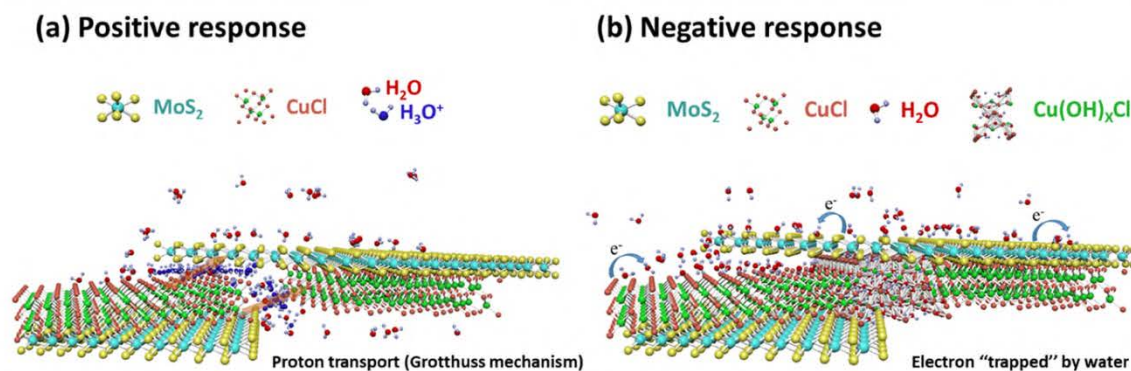
Cu(OH)<sub>x</sub>Cl among both the MoS<sub>2</sub> and WS<sub>2</sub> nanosheets. In the as-prepared sensors, copper chloride is present on the nanosheets. When a voltage is applied in the highly repeated humid environment, Cu<sup>2+</sup> ions move slowly toward the negative electrode. During these cycles, the Cu atoms form Cu(OH)<sub>x</sub>Cl that fills the gaps in the porous layer, and in general, creates a uniform coating on the nanosheets.

To determine the chemical state of the main elements in the MoS<sub>2</sub>@MC- and WS<sub>2</sub>@MC-based humidity sensors, the XPS spectra of pure MoS<sub>2</sub> and MoS<sub>2</sub>@300Cu before and after measurements were analyzed (see Figure S8). The peaks of Cu–S (932.85 eV) and CuCl<sub>2</sub> (935.05 eV) were found in the MoS<sub>2</sub>@Cu sensing film before measurement, which indicates the strong bond formed between MoS<sub>2</sub> and CuCl and that CuCl<sub>2</sub> remains in the humidity sensing film.<sup>24</sup> It is deduced that the Cu salt coating does not affect the chemical states or binding energy peaks of MoS<sub>2</sub>. After humidity measurement, the two main peaks of CuCl<sub>2</sub> at 935.20 and 954.95 eV become broader, and both their positions shifted by about 0.33 eV to higher energies at 935.53 and 955.27 eV, respectively. This change can be attributed to a large amount of hydroxides captured by copper under a voltage drive in the highly repeated humidity environment.<sup>28</sup>

The XPS spectra of pure WS<sub>2</sub> and WS<sub>2</sub>@300Cu before and after measurements were also obtained, and they show the Cu–S bonds formed in the WS<sub>2</sub>@300Cu sensing film. After the humidity measurement, the high intensity peak appeared as same as that for the MoS<sub>2</sub>@Cu sensing film. It is also confirmed that an interface material was formed among the WS<sub>2</sub> nanosheets under the voltage drive in the highly repeated humidity environment. The XPS survey spectra of MoS<sub>2</sub> and WS<sub>2</sub> are shown in Figure S9. The percentages of the main elements including molybdenum, tungsten, sulfur, and copper in the humidity sensors were calculated based on the XPS data. The data confirm a stable ratio between molybdenum and sulfur in the sensors. As expected, the percentage of copper increases with the increasing amount of copper chloride (see Table S2).

These results were corroborated by Raman scattering spectroscopy (see Figure S10). The spectra did not show a significant change in the E<sub>2g</sub><sup>1</sup> and A<sub>1g</sub> modes of TMDs before and after measurements, confirming the high stability of such materials in the humidity measurement.

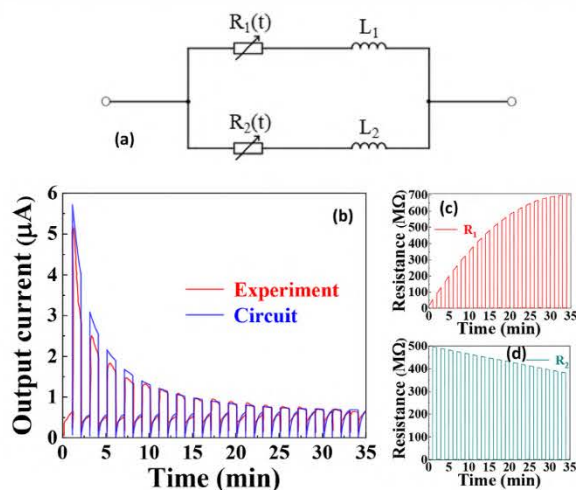
According to the results of the characterization, we propose a mechanism to explain the inversion of the sensing mechanisms (see Figure 6) and consequently an appropriate lumped circuit to reproduce it. The deposition of copper chloride onto the MoS<sub>2</sub> nanosheets occurs due to the coordination of copper with sulfur, which causes precipitation of nanosheets from the colloidal dispersion. This ionic coating is responsible for the positive response in the first minutes of the measurements: when the humidity increases, the ions dissolve in the water channel and enhance the conductivity due to an extra ionic conductivity channel. This facilitates a slow cation migration to the negative electrode of the device. Meanwhile, the excess water leads to copper cation hydration and facilitates the conversion to Cu(OH)<sub>x</sub>Cl, which is poorly soluble in water. This conversion produces a rapid decrease of ionic conductivity and results in the formation of an insoluble dielectric coating on the MoS<sub>2</sub> film. Furthermore, the decreasing porosity of the film inhibits the formation of water channels. Thus, the inversion from the positive to a negative mechanism reflects the evolution and conversion of copper from cations to hydroxychloride. In the last part of the measurements, when the mechanism is purely



**Figure 6.** Schematic of the two humidity sensing mechanisms. (a) Positive response dominated by the proton transport and (b) negative response dominated by the electron trapped by water.

negative, water molecules attach on the surface of the copper coating and under an applied voltage, the charges are trapped in the water film mediated by the newly formed continuous film.

Based on the sensing mechanism explained above, an equivalent circuit with two resistances varying with time  $R_1(t)$  and  $R_2(t)$  in parallel with two inductors  $L_1$  and  $L_2$  is proposed and is shown in Figure 7a. It is postulated that the  $R_1(t)/L_1$



**Figure 7.** Circuit analysis for the humidity sensor. (a) Equivalent circuit model. (b) Comparison of the experimental output current with the circuit analysis. (c) Time dependence of  $R_1$  and (d) time dependence of  $R_2$ .

mesh could be related to the positive sensing response. In the proposed circuit, the low resistance is associated with the presence of copper ions dissolved in the water channels and the low inductance value to the formation of water channels. The ion migration and copper hydroxide formation increase  $R_1(t)$  and decrease  $R_2(t)$  up to the sensing response conversion. The  $R_2(t)/L_2$  mesh would then reproduce the negative sensing response. The dominant values of  $R_2(t)$  are then related to the formation of a continuous film, which inhibits the formation of a water channel. The high values of  $L_2$  confirm the change in the sensing mechanism, if the slow rate of material property modification due to the formation of a water film on the device surface is taken into account.  $R_1(t)$  increases linearly with time, while  $R_2(t)$  is more stable and decreases slowly with time, with a linear slope. The proposed equivalent circuit results are in reasonable agreement with the experimental results. Figure 7b

shows the comparison of the circuit fitting with the experimental output current values. Figure 7c,d shows the time-varying  $R_1(t)$  and  $R_2(t)$  responses. Both  $R_1$  and  $R_2$  have high and low values in time to account for the switching in time of humid and dry conditions. Thus, this simple model works well to explain the sensing mechanism. The inversion from a positive to negative response of the sensor is well represented by the domination of  $R_1$  and  $R_2$  over time.

To further understand the reversal in the humidity sensing mechanism in our devices, a comparison between our sensors and previously published reports was made. Table 1 shows a review of  $\text{MoS}_2$ -based resistive humidity sensor data indicating whether a positive and negative sensing mechanism was observed. From Table 1, it is seen that positive humidity  $\text{MoS}_2$ -based sensors were mainly fabricated using solution-exfoliated  $\text{MoS}_2$  nanosheets in an ambient environment.<sup>2,3,5</sup> The dendritic  $\text{MoS}_2$ -based humidity sensor, which was synthesized at a high temperature, showed a positive humidity sensing behavior since it was dissolved in a NaOH solution prior to the device fabrication, resulting in a similar structure to the solution-exfoliated  $\text{MoS}_2$  nanosheets. Overall, the positive  $\text{MoS}_2$  humidity sensors were mainly fabricated using overlapping  $\text{MoS}_2$  nanosheets. In such loose and porous structures, water molecules attaching to the nanosheet edges and surface can form proton transport channels between the overlapping nanosheets, according to the Grotthuss mechanism.<sup>9,29</sup> Due to the high contact resistance between the nanosheets, the proton transport channels dominate the conductance in the structure. The proton transport channel's conductance can be affected by the water content and thus results in a decrease of the film impedance with increasing humidity.

On the contrary, the negative  $\text{MoS}_2$ -based humidity sensors were fabricated by various methods such as using CVD growth, sulfurization, annealing, and mechanical exfoliation.<sup>6,7,17,30,31</sup> Sensors based on the polycrystalline films were mainly prepared using CVD growth, sulfurization, and annealing methods at high temperatures (300–1000 °C). After annealing, a continuous film is formed by the improvement of the adhesion and contact quality among their grains or nanosheets. The mechanically exfoliated single crystals have a good material quality. Compared to the positive  $\text{MoS}_2$  humidity sensors, the key difference is that the negative humidity sensors were fabricated using continuous films, either single or polycrystalline. These films have an insignificant concentration of structural gaps or active edges, unlike the  $\text{MoS}_2$  nanosheet-based film. In such a case, the possibility of water-forming proton transport channels in the

Table 1. Summary of Humidity Sensing Mechanism of Different MoS<sub>2</sub> Humidity Sensors

materials	preparation methods	mechanisms	response ( $\Omega$ )	RR time (s)	RH range (%)	references
MoS <sub>2</sub> @Cu nanosheets	MoS <sub>2</sub> @Cu by voltage drive	negative	$7.3 \times 10^6 - 7.7 \times 10^8$	1.6/34	4–80	this work
MoS <sub>2</sub> @Ag nanosheets	MoS <sub>2</sub> @Ag by voltage drive	negative	$7.5 \times 10^1 - 1.8 \times 10^2$	4.1/0.9	4–80	this work
MoS <sub>2</sub> film	CVD	negative	$1.0 \times 10^7 - 1.0 \times 10^{13}$	10/60	0–35	Zhao et al. <sup>6</sup>
MoS <sub>2</sub> monolayer	CVD	negative	$8.0 \times 10^{10} - 4.5 \times 10^{11}$		5–63	Guo et al. <sup>17</sup>
MoS <sub>2</sub> nanosheets	annealed at 400 °C	negative		9/17		Zhang et al. <sup>30</sup>
MoS <sub>2</sub> nanosheets	annealed at 400 °C on alumina substrates	negative		9/17	0–60	Zhang et al. <sup>7</sup>
MoS <sub>2</sub> thin film	CVD sulfurization at 1000 °C	negative	$3.3 \times 10^5 - 3.5 \times 10^5$		25–40	Guo et al. <sup>31</sup>
MoS <sub>2</sub>	mechanical exfoliation of single-crystal 2-layer MoS <sub>2</sub>	negative	$6.0 \times 10^{12} - 4.5 \times 10^{13}$		4–84	Late et al. <sup>32</sup>
MoS <sub>2</sub>	PECVD (300 °C) polycrystalline	negative	$4.0 \times 10^4 - 5.5 \times 10^5$		15–90	Ahn et al. <sup>35</sup>
MoS <sub>2</sub> QDs	ultrasonication	positive	$2.0 \times 10^8 - 5.0 \times 10^6$	14/172	0–97	Yadav et al. <sup>3</sup>
MoS <sub>2</sub> nanosheets	SiO <sub>2</sub> microsphere	positive	$4.0 \times 10^3 - 1.0 \times 10^1$	1.5/1.5	0–97	Li et al. <sup>2</sup>
few-layer MoS <sub>2</sub>	CVD, dissolve in NaOH for dendritic MoS <sub>2</sub>	positive	$1.0 \times 10^6 - 1.0 \times 10^0$		0–97	Ren et al. <sup>4</sup>
MoS nanotube	MoS nanotube in an AAO membrane	positive	$2.0 \times 10^8 - 7.7 \times 10^6$	0.5 / 0.8	20–85	Mondal et al. <sup>5</sup>

film becomes limited. The electrons present in the continuous film are trapped by water molecules attached to the surface of the nanomaterial especially in the high humidity environment and this results in a negative humidity sensing behavior, with the impedance increasing with the increasing humidity.<sup>32,33</sup>

Similarly, Table S3 shows results for the representative WS<sub>2</sub> nanosheet-based positive humidity sensors, mainly fabricated using solution exfoliation, tungsten sulfurization, and hot-wire chemical vapor-deposited WS<sub>2</sub> nanoparticles. However, a high-temperature-synthesized polycrystalline WS<sub>2</sub> sensor exhibits a positive humidity sensing behavior, most probably caused by the oxygen attached to the surface of the WS<sub>2</sub> film.<sup>34</sup> Only a few studies discuss the negative humidity sensing behavior. The table also lists negative humidity sensors fabricated using single-crystal WS<sub>2</sub> monolayer and polymer-connected WS<sub>2</sub> nanoparticles. We suggest that the negative humidity mechanism can be explained in the same way as for the negative MoS<sub>2</sub> humidity sensors.

## CONCLUSIONS

A facile methodology to synthesize MoS<sub>2</sub> and WS<sub>2</sub> nanosheets modified using CuCl<sub>2</sub> and AgNO<sub>3</sub> has been presented. These nanosheets were used to fabricate high-performance RH sensors. The sensors are easy to produce and exhibit high sensitivity and long-time stability, making them suitable for applications in a variety of environments. A simple and effective method to adjust the sensor's electrical conductance by controlling the amount of metal salts, especially CuCl<sub>2</sub>, is also proposed.

This work is the first observation showing the reversal in the humidity response of TMD-based devices. While pristine TMD-based sensors show a positive humidity response, MoS<sub>2</sub>@MC- and WS<sub>2</sub>@MC-based films show a reversal in the humidity sensing mechanism, from positive to negative, in the first few minutes of the measurement. From the analysis of the morphology, composition, and real-time I–t curves, this reversal process can be explained by the formation of a continuous film under a driving voltage in a long-time humidity sensing measurement. This work reveals that metal salts can help to improve the adhesion of the loose MoS<sub>2</sub> and WS<sub>2</sub> nanosheets, resulting in a continuous film with low porosity. The inversion from a positive to negative behavior of the humidity sensors can be explained in the context of the change from a “hydrogen bond network” to “charge acceptors” in the sensors driven by the change in the film morphology. The mechanism is supported by

the simulation of the sensor activity by a lumped circuit-based model. This work helps to improve the understanding of the humidity sensing behavior of TMD-based applications and proves that morphology and metal decoration are crucial to fabricate high-performance sensors with controllable and reliable humidity sensing mechanisms and gives a new perspective on aging and performance reversal of nanosheet-based devices in complex working environments.

## EXPERIMENTAL METHODS

**Preparation of MoS<sub>2</sub> and WS<sub>2</sub> Nanosheets.** A solution exfoliation method was used to synthesize the MoS<sub>2</sub> and WS<sub>2</sub> nanosheets.<sup>36</sup> MoS<sub>2</sub> (WS<sub>2</sub>) microcrystals (500 mg) (99.5%, Sigma-Aldrich) were dissolved in 250 mL of 50% ethanol solution and sonicated using a high-power sonication probe (400 W, Fisher brand FB505) with 80% amplitude and an 8 s/8 s ON/OFF pulse for 10 h. The solution was centrifuged at a rotation speed of 7000 rpm for 10 min. The suspension consisting of MoS<sub>2</sub> (WS<sub>2</sub>) nanosheets was used for the subsequent experiments.

**Synthesis of MoS<sub>2</sub> and WS<sub>2</sub> Nanosheets with the Metal Coatings.** Cu nanoparticles were coated on the surface of MoS<sub>2</sub> nanosheets using a CuCl<sub>2</sub> solution.<sup>37</sup> Various volumes of 0.1 g/mL CuCl<sub>2</sub> (99.8%, Labbox) salt solution were mixed with 15 mL of MoS<sub>2</sub> nanosheet solutions in a dark environment for 24 h to synthesize the MoS<sub>2</sub>@Cu nanosheets. Then, Cu-coated MoS<sub>2</sub> nanosheets were dropped and they formed a precipitate at the bottom of the solution. Finally, the precipitate consisted of Cu-coated MoS<sub>2</sub> nanosheets and was collected by the removal of the upper transparent solution. WS<sub>2</sub>@Cu, MoS<sub>2</sub>@Ag, and WS<sub>2</sub>@Ag nanosheets were prepared by the same procedure using the same CuCl<sub>2</sub> and AgNO<sub>3</sub> (99.8%, Labbox), respectively.

**Fabrication of Humidity Sensors.** The Au/Ti (95/5 nm) interdigitated electrodes with a finger width and an interspacing of 100  $\mu$ m were patterned on glass substrates by laser lithography followed by e-beam metal deposition and lift-off. The humidity sensing area size was 5  $\times$  5 mm<sup>2</sup>. The humidity sensors were fabricated using the drop-casting method. The MoS<sub>2</sub>@Cu precipitates were dropped and dried on the glass electrode substrates as a humidity sensing film. Metal-coated (metal-decorated) samples were prepared by adding  $x$   $\mu$ L of 0.1 g/mL CuCl<sub>2</sub> to 15 mL of MoS<sub>2</sub> suspension, with  $x$  varying in the range of 5–200  $\mu$ L. Hereafter, for convenience, sample names will be shortened by omitting “ $x$   $\mu$ L of 0.1 g/mL CuCl<sub>2</sub>.” Here, volumes of 0, 5, 25, 50, 100, and 200  $\mu$ L of CuCl<sub>2</sub> solution-based humidity sensors were written as pure MoS<sub>2</sub>, MoS<sub>2</sub>@5Cu, MoS<sub>2</sub>@25Cu, MoS<sub>2</sub>@50Cu, MoS<sub>2</sub>@100Cu, and MoS<sub>2</sub>@200Cu humidity sensors, respectively. Other humidity sensors such as WS<sub>2</sub>@100Cu, MoS<sub>2</sub>@100Ag, and WS<sub>2</sub>@150Ag were also realized and named in the same way. Finally, the devices were dried at 80 °C for 10 min in an ambient atmosphere.

**Real-Time Measurement of Humidity Sensors.** A home-made humidity sensing chamber was used to investigate the humidity sensors, and it was compared against a commercial humidity sensor (HIH-5031-001). The chamber had two separate inlet lines, one for nitrogen gas and the other for humid air. The humidity in the chamber was controlled by changing the proportion of nitrogen and humid air. The RH was changed between 4 and 80% in a period of 120 s. The response current of all the sensors was measured as a function of RH under a DC bias. The data were collected using a Keysight 34461A multimeter controlled by a MATLAB code.

**Characterization.** A dynamic light scattering instrument (DLS, Malvern Zetasizer) was used to characterize the lateral dimension of the nanosheets. Atomic force microscopy (AFM, NanoScope IV controller and Dimension 3100 head, Veeco) images were obtained for analyzing the thickness of MoS<sub>2</sub> and WS<sub>2</sub> nanosheets. A scanning transmission electron microscope (STEM, FEI Tecnai G2 F20) and a scanning electron microscope (SEM, FEI Magellan 400L) were used to characterize the surface morphology of the single Cu- or Ag-coated MoS<sub>2</sub> nanosheet and the humidity sensing films. The element distribution in the film was characterized by an X-Max Ultim Extreme EDX (FEI Magellan 400L). Raman scattering spectra were obtained using a Horiba T64000 Raman spectrometer with a 532 nm laser line. XPS measurements were performed with a Phoibos analyzer (SPECS GmbH, Germany) to determine the chemical state of the MoS<sub>2</sub>@Cu and WS<sub>2</sub>@Cu composites before and after the measurement.

## ■ ASSOCIATED CONTENT

### SI Supporting Information

The Supporting Information is available free of charge at <https://pubs.acs.org/doi/10.1021/acsami.1c03691>.

DLS, AFM, SEM, EDX, I–t curves, XPS, and Raman spectra characterization of the humidity sensing membranes and tables of element percentages and the sensing performance of these sensors (PDF)

All photos/artwork used in the figures, including the TOC graphic, are original work of the authors and not taken from another source.

## ■ AUTHOR INFORMATION

### Corresponding Author

Peng Xiao – Catalan Institute of Nanoscience and Nanotechnology (ICN2), CSIC and BIST, 08193 Barcelona, Spain; Departamento de Física, Universidad Autónoma de Barcelona, 08193 Barcelona, Spain; [orcid.org/0000-0002-4711-2566](https://orcid.org/0000-0002-4711-2566); Email: [peng.xiao@icn2.cat](mailto:peng.xiao@icn2.cat)

### Authors

Daide Mencarelli – Department of Information Engineering, Polytechnic University of Marche, 60131 Ancona, Italy; INFN-Laboratori Nazionali di Frascati, 00044 Frascati, Italy

Emigdio Chavez-Angel – Catalan Institute of Nanoscience and Nanotechnology (ICN2), CSIC and BIST, 08193 Barcelona, Spain; [orcid.org/0000-0002-9783-0806](https://orcid.org/0000-0002-9783-0806)

Christopher Hardly Joseph – Department of Information Engineering, Polytechnic University of Marche, 60131 Ancona, Italy

Antonino Cataldo – Department of Information Engineering, Polytechnic University of Marche, 60131 Ancona, Italy; INFN-Laboratori Nazionali di Frascati, 00044 Frascati, Italy

Luca Pierantoni – Department of Information Engineering, Polytechnic University of Marche, 60131 Ancona, Italy; INFN-Laboratori Nazionali di Frascati, 00044 Frascati, Italy

Clivia M. Sotomayor Torres – Catalan Institute of Nanoscience and Nanotechnology (ICN2), CSIC and BIST,

08193 Barcelona, Spain; ICREA, 08010 Barcelona, Spain;

[orcid.org/0000-0001-9986-2716](https://orcid.org/0000-0001-9986-2716)

Marianna Sledzinska – Catalan Institute of Nanoscience and Nanotechnology (ICN2), CSIC and BIST, 08193 Barcelona, Spain; [orcid.org/0000-0001-8592-1121](https://orcid.org/0000-0001-8592-1121)

Complete contact information is available at: <https://pubs.acs.org/doi/10.1021/acsami.1c03691>

## Notes

The authors declare no competing financial interest.

## ■ ACKNOWLEDGMENTS

The Catalan Institute of Nanoscience and Nanotechnology (ICN2) is funded by the CERCA program/Generalitat de Catalunya and is supported by the Severo Ochoa program from Spanish MINECO (Grant No. SEV-2017-0706). We acknowledge support from the EU Project Nanosmart (H2020 ICT-07-2018) and ICN2 members acknowledge the Spanish MINECO project SIP (PGC2018-101743-B-I00). P.X. acknowledges support by a PhD fellowship from the EU Marie Skłodowska-Curie COFUND PREBIST project (Grant Agreement No. 754558).

## ■ REFERENCES

- (1) Chen, Z.; Lu, C. Humidity Sensors: A Review of Materials and Mechanisms. *Sens. Lett.* **2005**, *3*, 274–295.
- (2) Li, N.; Chen, X.-D.; Chen, X.-P.; Ding, X.; Zhao, X. Fast-Response MoS<sub>2</sub>-Based Humidity Sensor Braced by SiO<sub>2</sub> Microsphere Layers. *IEEE Electron Device Lett.* **2018**, *39*, 115–118.
- (3) Yadav, S.; Chaudhary, P.; Uttam, K. N.; Varma, A.; Vashistha, M.; Yadav, B. C. Facile Synthesis of Molybdenum Disulfide (MoS<sub>2</sub>) Quantum Dots and Its Application in Humidity Sensing. *Nanotechnology* **2019**, *30*, 295501.
- (4) Ren, J.; Guo, B.; Feng, Y.; Yu, K. Few-Layer MoS<sub>2</sub> Dendrites as a Highly Active Humidity Sensor. *Phys. E Low-Dimens. Syst. Nanostructures* **2020**, *116*, No. 113782.
- (5) Mondal, S.; Kim, S. J.; Choi, C.-G. Honeycomb-like MoS<sub>2</sub> Nanotube Array-Based Wearable Sensors for Noninvasive Detection of Human Skin Moisture. *ACS Appl. Mater. Interfaces* **2020**, *12*, 17029–17038.
- (6) Zhao, J.; Li, N.; Yu, H.; Wei, Z.; Liao, M.; Chen, P.; Wang, S.; Shi, D.; Sun, Q.; Zhang, G. Highly Sensitive MoS<sub>2</sub> Humidity Sensors Array for Noncontact Sensation. *Adv. Mater.* **2017**, *29*, No. 1702076.
- (7) Zhang, S.-L.; Choi, H.-H.; Yue, H.-Y.; Yang, W.-C. Controlled Exfoliation of Molybdenum Disulfide for Developing Thin Film Humidity Sensor. *Curr. Appl. Phys.* **2014**, *14*, 264–268.
- (8) Agmon, N. The Grotthuss Mechanism. *Chem. Phys. Lett.* **1995**, *244*, 456–462.
- (9) Geissler, P. L. Autoionization in Liquid Water. *Science* **2001**, *291*, 2121–2124.
- (10) Barsan, N.; Weimar, U. Conduction Model of Metal Oxide Gas Sensors. *J. Electroceramics* **2001**, *7*, 143–167.
- (11) Kim, W.; Javey, A.; Vermesh, O.; Wang, Q.; Li, Y.; Dai, H. Hysteresis Caused by Water Molecules in Carbon Nanotube Field-Effect Transistors. *Nano Lett.* **2003**, *3*, 193–198.
- (12) Smith, A. D.; Elgammal, K.; Niklaus, F.; Delin, A.; Fischer, A. C.; Vaziri, S.; Forsberg, F.; Räsander, M.; Hugosson, H.; Bergqvist, L.; Schröder, S.; Kataria, S.; Östling, M.; Lemme, M. C. Resistive Graphene Humidity Sensors with Rapid and Direct Electrical Readout. *Nanoscale* **2015**, *7*, 19099–19109.
- (13) Late, D. J. Liquid Exfoliation of Black Phosphorus Nanosheets and Its Application as Humidity Sensor. *Microporous Mesoporous Mater.* **2016**, *225*, 494–503.
- (14) Guo, H.; Lan, C.; Zhou, Z.; Sun, P.; Wei, D.; Li, C. Transparent, Flexible, and Stretchable WS<sub>2</sub> Based Humidity Sensors for Electronic Skin. *Nanoscale* **2017**, *9*, 6246–6253.

- (15) He, P.; Brent, J. R.; Ding, H.; Yang, J.; Lewis, D. J.; O'Brien, P.; Derby, B. Fully Printed High Performance Humidity Sensors Based on Two-Dimensional Materials. *Nanoscale* **2018**, *10*, 5599–5606.
- (16) Duan, Z.; Jiang, Y.; Yan, M.; Wang, S.; Yuan, Z.; Zhao, Q.; Sun, P.; Xie, G.; Du, X.; Tai, H. Facile, Flexible, Cost-Saving, and Environment-Friendly Paper-Based Humidity Sensor for Multifunctional Applications. *ACS Appl. Mater. Interfaces* **2019**, *11*, 21840–21849.
- (17) Guo, J.; Wen, R.; Liu, Y.; Zhang, K.; Kou, J.; Zhai, J.; Wang, Z. L. Piezotronic Effect Enhanced Flexible Humidity Sensing of Monolayer MoS<sub>2</sub>. *ACS Appl. Mater. Interfaces* **2018**, *10*, 8110–8116.
- (18) Awais, M.; Khan, M. U.; Hassan, A.; Bae, J.; Chattha, T. E. Printable Highly Stable and Superfast Humidity Sensor Based on Two Dimensional Molybdenum Diselenide. *Sci. Rep.* **2020**, *10*, 5509.
- (19) Fournier, J. A.; Carpenter, W. B.; Lewis, N. H. C.; Tokmakoff, A. Broadband 2D IR Spectroscopy Reveals Dominant Asymmetric H<sub>5</sub>O<sub>2</sub><sup>+</sup> Proton Hydration Structures in Acid Solutions. *Nat. Chem.* **2018**, *10*, 932–937.
- (20) Zundel, G. Hydrogen Bonds with Large Proton Polarizability and Proton Transfer Processes in Electrochemistry and Biology. In *Advances in Chemical Physics*; Prigogine, I., Rice, S. A., Eds.; John Wiley & Sons: Hoboken, NJ, 2007; pp 1–217.
- (21) Shkrob, I. A.; Schlueter, J. A. Can a Single Molecule Trap the Electron? *Chem. Phys. Lett.* **2006**, *431*, 364–369.
- (22) Mozumder, A. Conjecture on Electron Trapping in Liquid Water. *Int. J. Radiat. Appl. Instrum. Part C Radiat. Phys. Chem* **1988**, *32*, 287–291.
- (23) Burman, D.; Santra, S.; Pramanik, P.; Guha, P. K. Pt Decorated MoS<sub>2</sub> Nanoflakes for Ultrasensitive Resistive Humidity Sensor. *Nanotechnology* **2018**, *29*, 115504.
- (24) Wang, S.; Li, H.; Zhang, J.; Guo, S.; Xu, W.; Grossman, J. C.; Warner, J. H. Epitaxial Templating of Two-Dimensional Metal Chloride Nanocrystals on Monolayer Molybdenum Disulfide. *ACS Nano* **2017**, *11*, 6404–6415.
- (25) Fan, X.; Xu, P.; Zhou, D.; Sun, Y.; Li, Y. C.; Nguyen, M. A. T.; Terrones, M.; Mallouk, T. E. Fast and Efficient Preparation of Exfoliated 2H MoS<sub>2</sub> Nanosheets by Sonication-Assisted Lithium Intercalation and Infrared Laser-Induced 1T to 2H Phase Reversion. *Nano Lett.* **2015**, *15*, 5956–5960.
- (26) Daeneke, T.; Carey, B. J.; Chrimes, A. F.; Ou, J. Z.; Lau, D. W. M.; Gibson, B. C.; Bhaskaran, M.; Kalantar-zadeh, K. Light Driven Growth of Silver Nanoplatelets on 2D MoS<sub>2</sub> Nanosheet Templates. *J. Mater. Chem. C* **2015**, *3*, 4771–4778.
- (27) Cudennec, Y.; Riou, A.; Gérault, Y.; Lecerf, A. Synthesis and Crystal Structures of Cd(OH)Cl and Cu(OH)Cl and Relationship to Brucite Type. *J. Solid State Chem.* **2000**, *151*, 308–312.
- (28) Yoshida, T.; Yamasaki, K.; Sawada, S. An X-Ray Photoelectron Spectroscopic Study of Biuret Metal Complexes. *Bull. Chem. Soc. Jpn.* **1978**, *51*, 1561–1562.
- (29) Fan, R.; Huh, S.; Yan, R.; Arnold, J.; Yang, P. Gated Proton Transport in Aligned Mesoporous Silica Films. *Nat. Mater.* **2008**, *7*, 303–307.
- (30) Zhang, S.-L.; Jung, H.; Huh, J.-S.; Yu, J.-B.; Yang, W.-C. Efficient Exfoliation of MoS<sub>2</sub> with Volatile Solvents and Their Application for Humidity Sensor. *J. Nanosci. Nanotechnol.* **2014**, *14*, 8518–8522.
- (31) Guo, S.; Arab, A.; Krylyuk, S.; Davydov, A. V.; Zaghoul, M.E. Fabrication and Characterization of Humidity Sensors Based on CVD Grown MoS<sub>2</sub> Thin Film. In *2017 IEEE 17th International Conference on Nanotechnology (IEEE-NANO)*; IEEE: Pittsburgh, PA, 2017; pp. 164–167.
- (32) Late, D. J.; Huang, Y.-K.; Liu, B.; Acharya, J.; Shirodkar, S. N.; Luo, J.; Yan, A.; Charles, D.; Waghmare, U. V.; Dravid, V. P.; Rao, C. N. R. Sensing Behavior of Atomically Thin-Layered MoS<sub>2</sub> Transistors. *ACS Nano* **2013**, *7*, 4879–4891.
- (33) Yue, Q.; Shao, Z.; Chang, S.; Li, J. Adsorption of Gas Molecules on Monolayer MoS<sub>2</sub> and Effect of Applied Electric Field. *Nanoscale Res. Lett.* **2013**, *8*, 425.
- (34) Qian, J.; Peng, Z.; Shen, Z.; Zhao, Z.; Zhang, G.; Fu, X. Positive Impedance Humidity Sensors via Single-Component Materials. *Sci. Rep.* **2016**, *6*, 25574.
- (35) Ahn, C.; Lee, J.; Kim, H.-U.; Bark, H.; Jeon, M.; Ryu, G. H.; Lee, Z.; Yeom, G. Y.; Kim, K.; Jung, J.; Kim, Y.; Lee, C.; Kim, T. Low-Temperature Synthesis of Large-Scale Molybdenum Disulfide Thin Films Directly on a Plastic Substrate Using Plasma-Enhanced Chemical Vapor Deposition. *Adv. Mater.* **2015**, *27*, 5223–5229.
- (36) Forsberg, V.; Zhang, R.; Bäckström, J.; Dahlström, C.; Andres, B.; Norgren, M.; Andersson, M.; Hummelgård, M.; Olin, H. Exfoliated MoS<sub>2</sub> in Water without Additives. *PLoS One* **2016**, *11*, No. e0154522.
- (37) Betancourt-Galindo, R.; Reyes-Rodríguez, P. Y.; Puente-Urbina, B. A.; Avila-Orta, C. A.; Rodríguez-Fernández, O. S.; Cadenas-Pliego, G.; Lira-Saldivar, R. H.; García-Cerda, L. A. Synthesis of Copper Nanoparticles by Thermal Decomposition and Their Antimicrobial Properties. *J. Nanomater.* **2014**, *2014*, 1–5.

# Article 4 Supporting information



# Supporting Information

## Reversing the humidity response of MoS<sub>2</sub>- and WS<sub>2</sub>-based sensors using transition metal salts

Peng Xiao<sup>1,2\*</sup>, Davide Mencarelli<sup>4,5</sup>, Emigdio Chavez-Angel<sup>1</sup>, Christopher Hardly Joseph<sup>4</sup>, Antonino Cataldo<sup>4,5</sup>, Luca Pierantoni<sup>4,5</sup>, Clivia M. Sotomayor Torres<sup>1,3</sup> and Marianna Sledzinska<sup>1</sup>

<sup>1</sup> Catalan Institute of Nanoscience and Nanotechnology (ICN2), CSIC and BIST, Campus UAB, Bellaterra, 08193 Barcelona, Spain

<sup>2</sup> Departamento de Física, Universidad Autónoma de Barcelona, Bellaterra, E-08193 Barcelona, Spain

<sup>3</sup> ICREA, Pg. Lluís Companys 23, 08010 Barcelona, Spain

<sup>4</sup> Department of Information Engineering, Polytechnic University of Marche, Via Brecce Bianche, 1, 60131 Ancona, Italy

<sup>5</sup> INFN-Laboratori Nazionali di Frascati, via E. Fermi 40, 00044 Frascati, Italy

\*Corresponding author: peng.xiao@icn2.cat

### Outline

Figure S1 The lateral dimension distributions of MoS<sub>2</sub> and WS<sub>2</sub> nanosheets.

Figure S2 AFM analysis of MoS<sub>2</sub> on SiO<sub>2</sub>/Si wafer substrates.

Figure S3 EDX spectra of MoS<sub>2</sub> nanosheets modified using transition metal salts.

Figure S4 Real time measurement of the humidity sensor WS<sub>2</sub>@150Cu against the commercial humidity sensor.

Figure S5 The CuCl<sub>2</sub>.nH<sub>2</sub>O film-based sensor.

Figure S6 Real time measurement of Ag coated MoS<sub>2</sub> and WS<sub>2</sub> humidity sensors against the commercial humidity sensor.

Figure S7 SEM and EDX images.

Figure S8 XPS spectra of pure MoS<sub>2</sub> nanosheets, MoS<sub>2</sub>@Cu, WS<sub>2</sub> nanosheets and WS<sub>2</sub>@300Cu before and after humidity measurements.

Figure S9 XPS survey spectra.

Figure S10 Raman spectra.

Table S1 The Ag coated sensors output current, response/recovery time, and response value.

Table S2 The percentage of the main elements appeared in the MoS<sub>2</sub> and WS<sub>2</sub> nanosheets based humidity sensors.

Table S3 Summary of humidity sensing mechanism of WS<sub>2</sub> humidity sensors.

A standard dynamic scattering (DLS) instrument was applied to characterize the lateral dimensions of MoS<sub>2</sub> and WS<sub>2</sub> nanosheets, as shown in Figure S1, and their average sizes were about 258 nm and 154 nm, respectively. The thickness of MoS<sub>2</sub> and WS<sub>2</sub> nanosheets were characterized by the Atomic Force Microscopy (AFM) randomly, and their thickness are in the range of 2.5-25 nm and 30-65 nm, respectively (Figure S2).

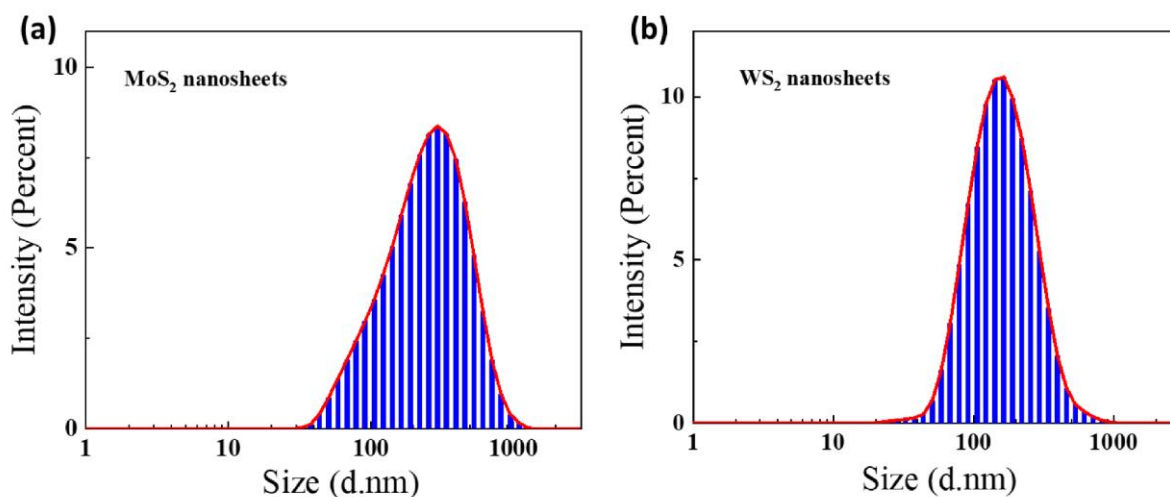


Figure S1. The lateral dimension distributions of nanosheets. (a) MoS<sub>2</sub>, (b) the WS<sub>2</sub>.

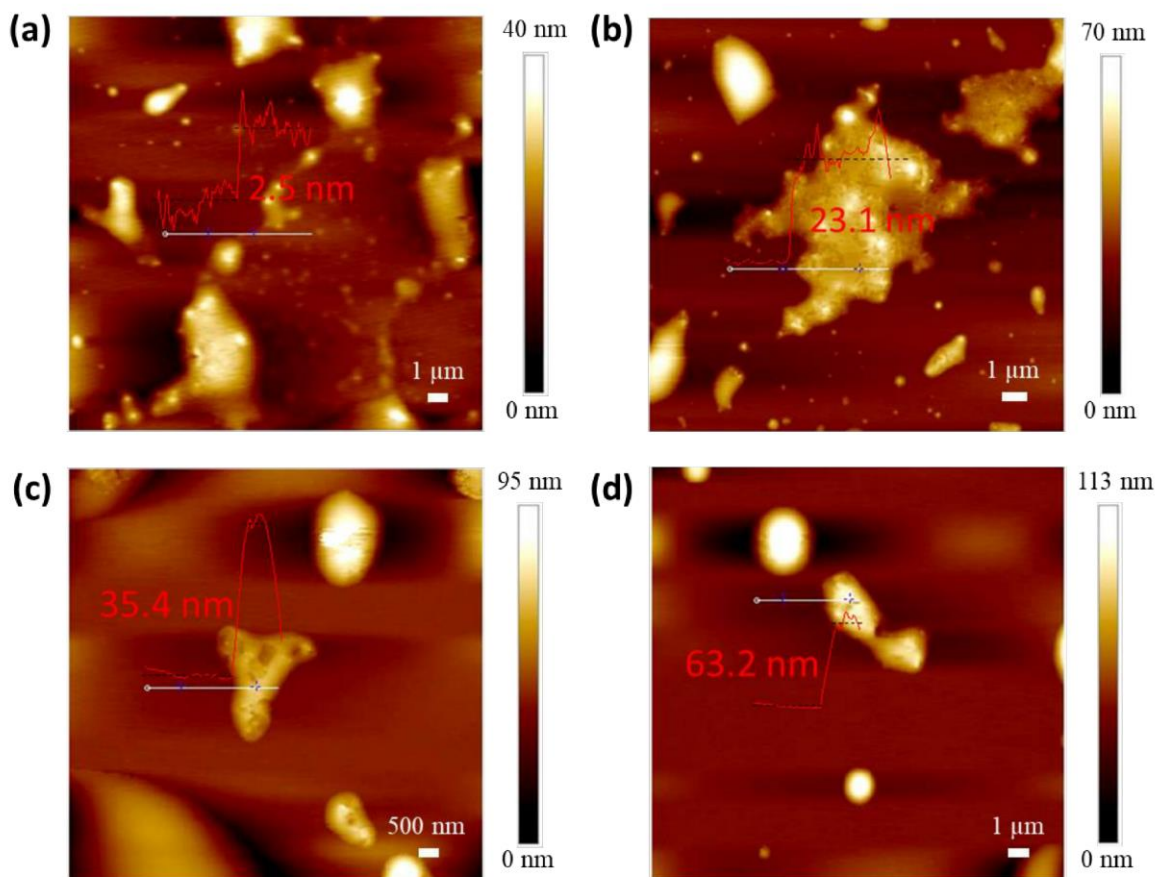
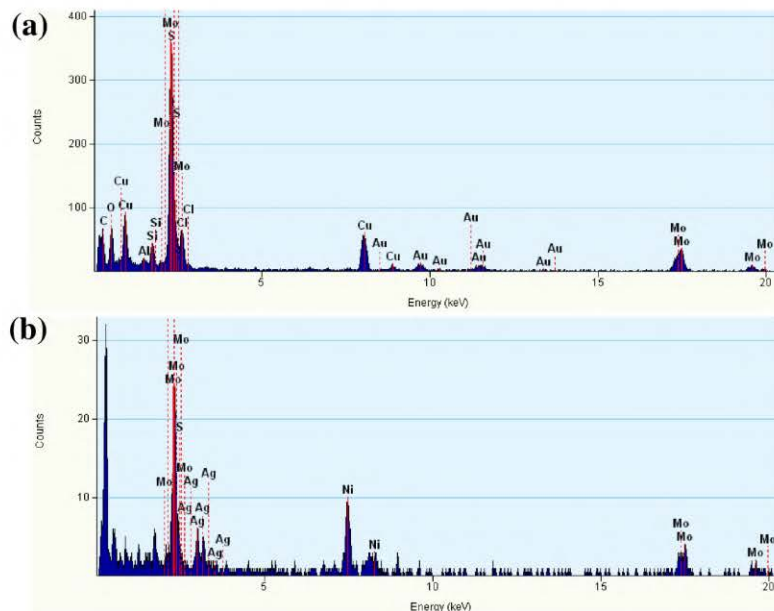


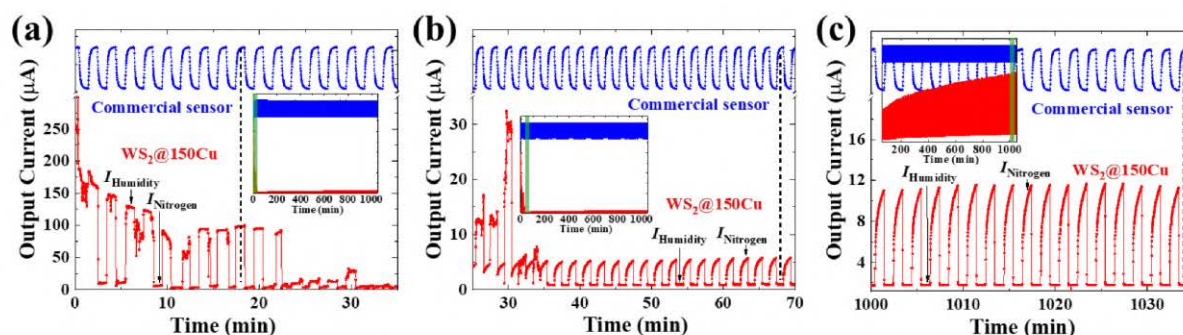
Figure S2. AFM analysis of MoS<sub>2</sub> on SiO<sub>2</sub>/Si wafers. (a) a three layer MoS<sub>2</sub> with the thickness of ~2.5 nm, (b) a ~23.1 nm thick MoS<sub>2</sub> nanosheet, (c) a 35.4 nm thick WS<sub>2</sub> nanosheet, and (d) a 63.2 nm thick WS<sub>2</sub> nanosheet.

The aggregation of metal salts  $\text{CuCl}_2$  and  $\text{AgNO}_3$  to the dispersion produces the precipitation of  $\text{MoS}_2$  and  $\text{WS}_2$  nanosheets after 24 hours, which compounds were studied by transmission electron microscopy (TEM). Figure S3 shows the EDX spectra of  $\text{MoS}_2$  nanosheets modified using  $\text{CuCl}_2$  and  $\text{AgNO}_3$ . The elements of copper and chloride are in the precipitate of  $\text{MoS}_2$  nanosheets with  $\text{CuCl}_2$ . The precipitate of  $\text{MoS}_2$  nanosheets with  $\text{AgNO}_3$  contains the silver.



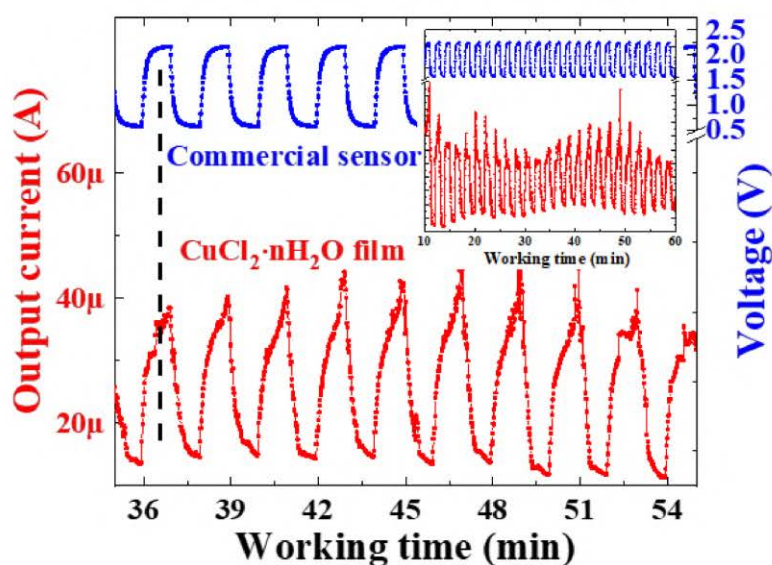
**Figure S3. EDX spectra of  $\text{MoS}_2$  nanosheets modified using transition metal salts.** (a) the precipitate of  $\text{MoS}_2$  nanosheets reacted with  $\text{CuCl}_2$ . (b) the precipitate of  $\text{MoS}_2$  nanosheets reacted with  $\text{AgNO}_3$ .

The reversal in the humidity sensing mechanism was also observed for all the  $\text{CuCl}_2$  modified  $\text{WS}_2$  nanosheets-based humidity sensors, see Figure S4.  $\text{WS}_2@150\text{Cu}$  was reversed from positive to negative in the first 40 minutes of the whole cycle, similar to the  $\text{MoS}_2@Cu$  based humidity sensor.



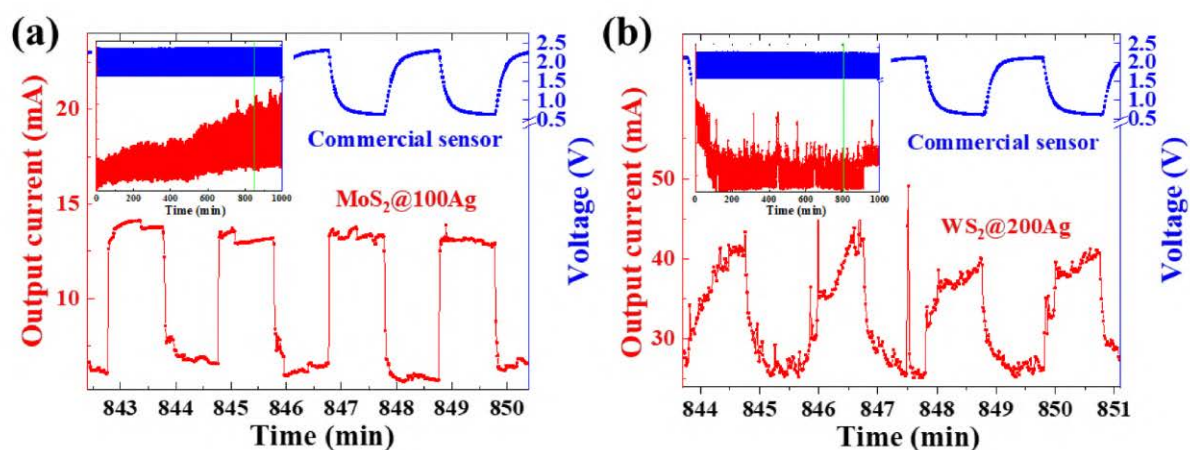
**Figure S4. Real time measurement of the humidity sensor  $\text{WS}_2@150\text{Cu}$  against the commercial humidity sensor.** (a) the sensor showed positive humidity sensing performance under repeated RH between 4 and 80% at the first 35 minutes. (b) the positive humidity sensing mechanism of the  $\text{WS}_2@150\text{Cu}$  sensor reversed to negative in the period of 25 - 60 minutes. (c) The stable negative humidity performance of the sensor at the first 35 minutes after the 1000 minutes' measurement.

Figure S5 shows the humidity sensing performance of the pure  $\text{CuCl}_2$  salt based film, which film exhibits the positive humidity sensing response. Therefore, the humidity sensing properties of  $\text{CuCl}_2$  does not determine the sensing characteristics of  $\text{CuCl}_2$  modified  $\text{MoS}_2$  or  $\text{WS}_2$  TMDs.



**Figure S5. The  $\text{CuCl}_2 \cdot n\text{H}_2\text{O}$  film based sensor.** Real time measurement of the humidity sensing performance of  $\text{CuCl}_2 \cdot n\text{H}_2\text{O}$  film against the commercial humidity sensor.

The humidity sensing performance of  $\text{AgNO}_3$  modified TMDs nanosheets based humidity sensors were also studied. The  $\text{MoS}_2@100\text{Ag}$  and  $\text{WS}_2@200\text{Ag}$  sensors both showed the negative response after stabilisation of the reversal process during the measurement (see Figure S6a, b). The output currents of the  $\text{MoS}_2@100\text{Ag}$  and  $\text{WS}_2@200\text{Ag}$  sensors were in the range of 8 to 15 mA and 10 to 100 mA, respectively. The output current is much higher than the sensor based on the  $\text{CuCl}_2$  modified nanosheets, due to the excellent electrical conductivity of metallic silver. The  $I_{\text{Humidity}}$  and  $I_{\text{Nitrogen}}$ , response values and response/recovery times of the two devices are compared in Table S1.

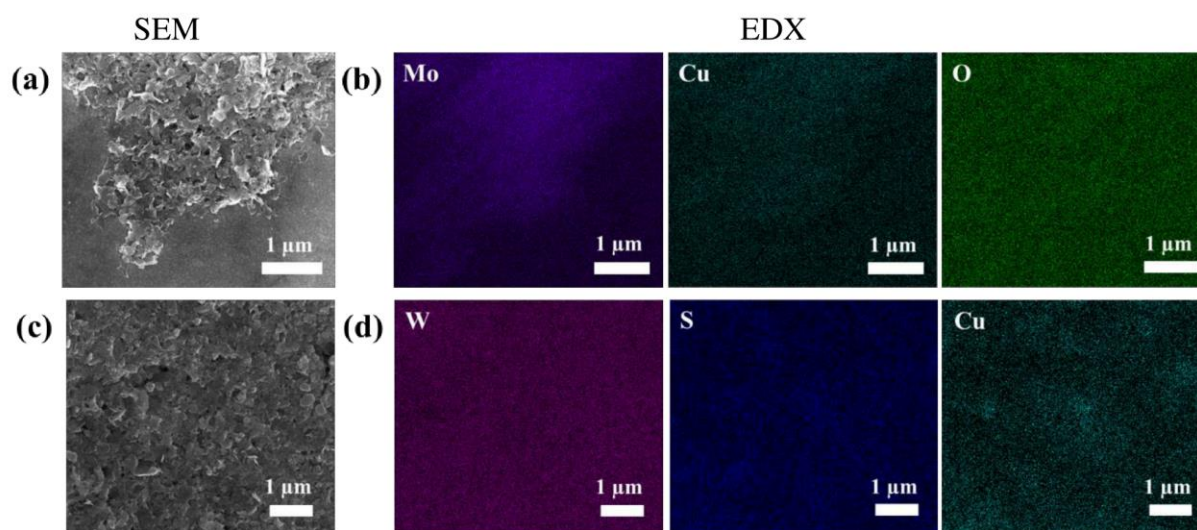


**Figure S6.** Real time measurement of Ag coated  $\text{MoS}_2$  and  $\text{WS}_2$  humidity sensors against the commercial humidity sensor. (a)  $\text{MoS}_2@100\text{Ag}$ , and (b)  $\text{WS}_2@200\text{Cu}$ .

Table S1. The Ag coated sensors output current, response/recovery time, and response value.

Sensors	$I_{\text{Humidity}}$ (mA)	$I_{\text{Nitrogen}}$ (mA)	Response time (s)	Recovery time (s)	Response value
$\text{MoS}_2@100\text{Ag}$	5.69	13.03	4.1	0.9	1.29
$\text{WS}_2@200\text{Ag}$	25.57	41.22	20.8	35.3	0.61

Figures S7a and c show the SEM image of the pure MoS<sub>2</sub> and WS<sub>2</sub> nanosheets with the corresponding EDX mapping images, Figures S7b and d, respectively. The EDX analysis confirmed that Mo and Cu elements were uniformly distributed in the MoS<sub>2</sub>@Cu film.



**Figure S7. SEM and EDX images.** (a) MoS<sub>2</sub>@25Cu humidity sensor before measurement, and (b) the corresponding EDX mapping of elements for Mo, Cu, and O. (c) WS<sub>2</sub>@100Cu humidity sensor before measurement, and (d) the corresponding EDX mapping of elements for W, S, and Cu.

The chemical states of the main elements in the MoS<sub>2</sub>@MCs- and WS<sub>2</sub>@MCs-based humidity sensors were characterized using the Photoemission spectroscopy (XPS). These XPS spectra were recorded in pure MoS<sub>2</sub> and in MoS<sub>2</sub>@300Cu before and after measurements. Figures S8a-c show XPS spectra of the core level of Mo 3d, S 2p, and Cu 2p, respectively. The Mo 3d core level spectra show two main peaks at 232.78, and 229.63 eV, assigned to the Mo 2d<sub>3/2</sub> and Mo 3d<sub>5/2</sub> species in MoS<sub>2</sub>, respectively. The low intensity peaks at 236.04 and 232.92 eV were assigned to the Mo 2d<sub>3/2</sub>, Mo 3d<sub>5/2</sub> species of MoO<sub>3</sub> the content of which increased after the measurements. The peak at 226.81 eV corresponds to the S 2s emission from defect-free regions of MoS<sub>2</sub>.<sup>1</sup> The XPS S 2p core level spectra remained stable during the measurements. The two main peaks at 163.63, and 162.45 eV, are ascribed to the S 2p<sub>1/2</sub>, and S 2p<sub>3/2</sub> species in MoS<sub>2</sub>, respectively. As expected, no trace of Cu is detected in pure MoS<sub>2</sub>. The XPS spectrum of the MoS<sub>2</sub>@300Cu before the measurement shows four main peaks at 932.85/952.60 and 935.05/954.74 eV, which are assigned to the Cu 2p<sub>1/2</sub> and Cu 2p<sub>3/2</sub> species in Cu<sup>2+</sup> and Cu<sup>+</sup> cations, respectively. The Cu<sup>2+</sup> and Cu<sup>+</sup> cations mainly come from CuCl<sub>2</sub> and Cu<sub>2</sub>S, respectively.<sup>2,3</sup> After humidity measurement, the two main peaks of CuCl<sub>2</sub> at 935.20 eV and 954.95 eV become broader, and their positions both shifted about 0.33 eV to the higher energy at 935.53 eV and 955.27 eV, respectively, which probably caused for that a lot of hydroxides captured by copper under a voltage drive in the high repeated humid environment.<sup>4</sup>

XPS spectra of pure WS<sub>2</sub> and WS<sub>2</sub>@300Cu before and after the sensor measurements were compared. In Figure S8d, the W 4f core level spectrum of the pure WS<sub>2</sub> is deconvoluted into four main peaks at 38.18, 36.01, 34.95, and 32.78 eV, assigned to the W 4f<sub>5/2</sub> and W 4f<sub>7/2</sub> species in WO<sub>3</sub> and WS<sub>2</sub>, respectively. The four peaks remain stable after a CuCl<sub>2</sub> coating forms on WS<sub>2</sub>. The WS<sub>2</sub> peaks positions did not change significantly after the measurements, except that the WO<sub>3</sub> peak shifted ~0.3 eV to lower energy. The low intensity peaks at 33.99 and 31.82 eV, are assigned to metallic W4f<sub>5/2</sub> and W4f<sub>7/2</sub> in WS<sub>2</sub>, respectively. It was also found that the spectral feature associated to pure WS<sub>2</sub> had the same intensity as WO<sub>3</sub> in the film, but the WO<sub>3</sub> content increased in the process of the CuCl<sub>2</sub> coating and the humidity measurement, consistent with previous measurements reported on annealed WS<sub>2</sub> nanosheets.<sup>5</sup> The above confirms the humidity enhanced oxidation process in the sensing film. The S 2p core level spectra show two main peaks at 163.58 and 162.42 eV, corresponding to S 2p<sub>1/2</sub> and S 2p<sub>3/2</sub> of WS<sub>2</sub>, respectively (Figure S8e). The peaks of the S=O bond at 170.13 and 168.97 eV disappear after CuCl<sub>2</sub> coating and reappear again after the measurement. On the contrary, the expected XPS S 2p spectral signature of MoS<sub>2</sub>@300Cu is actually flat around 169 eV, from which it is inferred that MoS<sub>2</sub> is more stable and does not easily oxidize. Finally, two low intensity peaks at 161.64 and 164.00 eV correspond to S 2p<sub>3/2</sub> in Cu<sub>2</sub>S and S 2p in WSO, respectively.

Figure S8f confirms that pure WS<sub>2</sub> does not have detectable Cu traces. The XPS spectra of WS<sub>2</sub>@300Cu before measurements have two main peaks at 952.37 and 932.62 eV corresponding to Cu 2p<sub>1/2</sub> and Cu 2p<sub>3/2</sub> of Cu<sub>2</sub>O, while the other two low intensity peaks at 954.49 and 934.40 eV are assigned to the Cu 2p<sub>1/2</sub> and Cu 2p<sub>3/2</sub> of Cu<sup>2+</sup> cations. After the measurements the spectra of WS<sub>2</sub>@300Cu presents both Cu<sup>+</sup> (952.54 and 932.79 eV for Cu2p<sub>3/2</sub> and Cu2p<sub>1/2</sub>, respectively) and Cu<sup>2+</sup> (955.25 and 935.50 eV for Cu2p<sub>3/2</sub> and Cu2p<sub>1/2</sub>, respectively) chemical states. The XPS spectra show that the Cu salt coating does not affect chemical states or binding energy peaks of the MoS<sub>2</sub> and WS<sub>2</sub>. Figure S9 (a) and (b) show the

XPS survey spectra of MoS<sub>2</sub> and WS<sub>2</sub>, which corresponds to the spectra of MoS<sub>2</sub> and WS<sub>2</sub> in Figure S8. The percentage of the main elements include the molybdenum, tungsten, sulfur, and copper appeared in the humidity sensors were calculated based on the XPS data, and listed in the table S2. Which data shows the stable elemental ratio between Molybdenum and sulfur, and the percentage of copper was increasing with the decorated levels of copper chloride. By contrast, the ratio between tungsten and sulfur changes significantly before and after the humidity measurement, because the capturing of hydroxides by copper is effective in WS<sub>2</sub>-based sensors due to the high chemical reactivity of WS<sub>2</sub>.

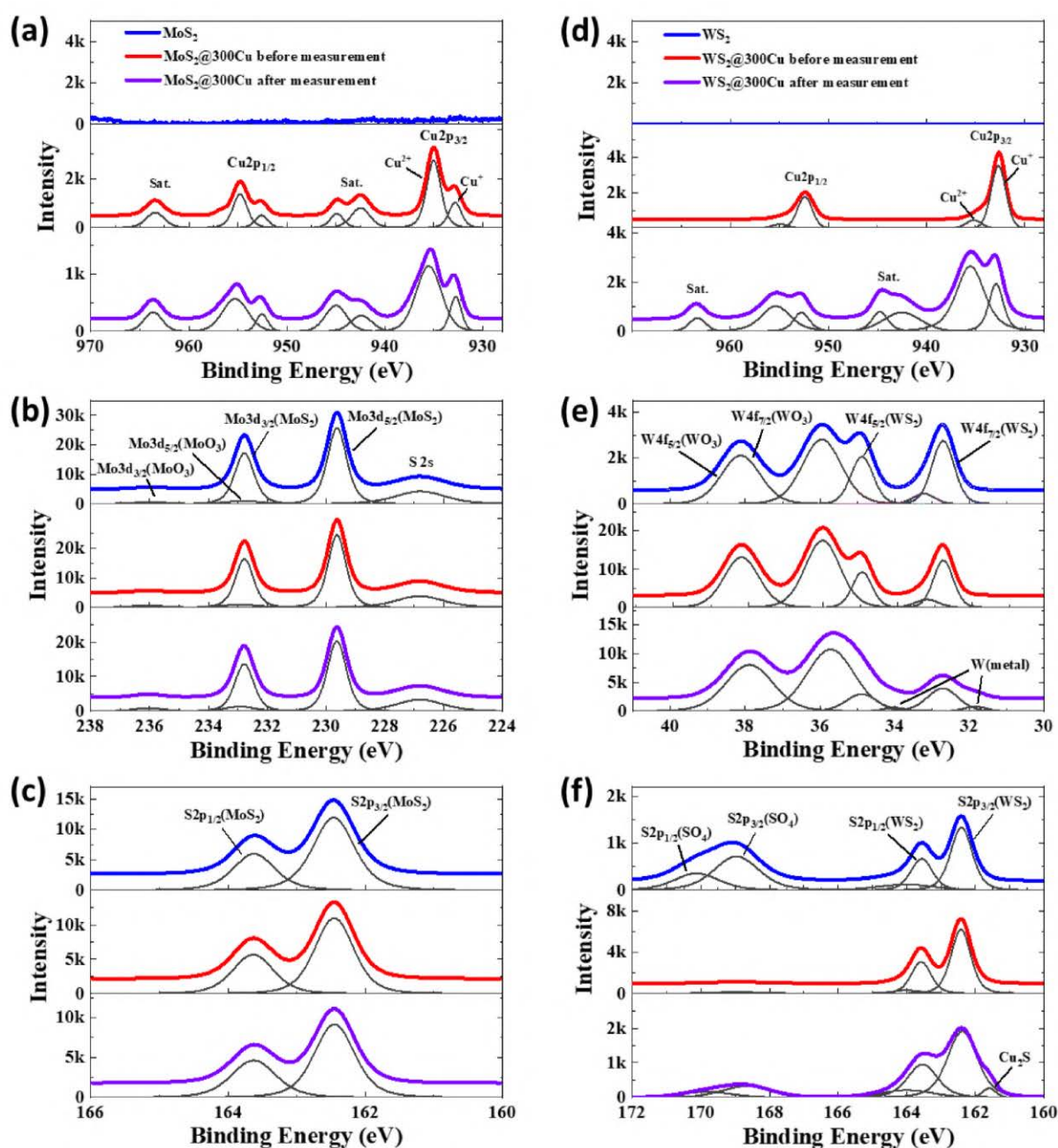
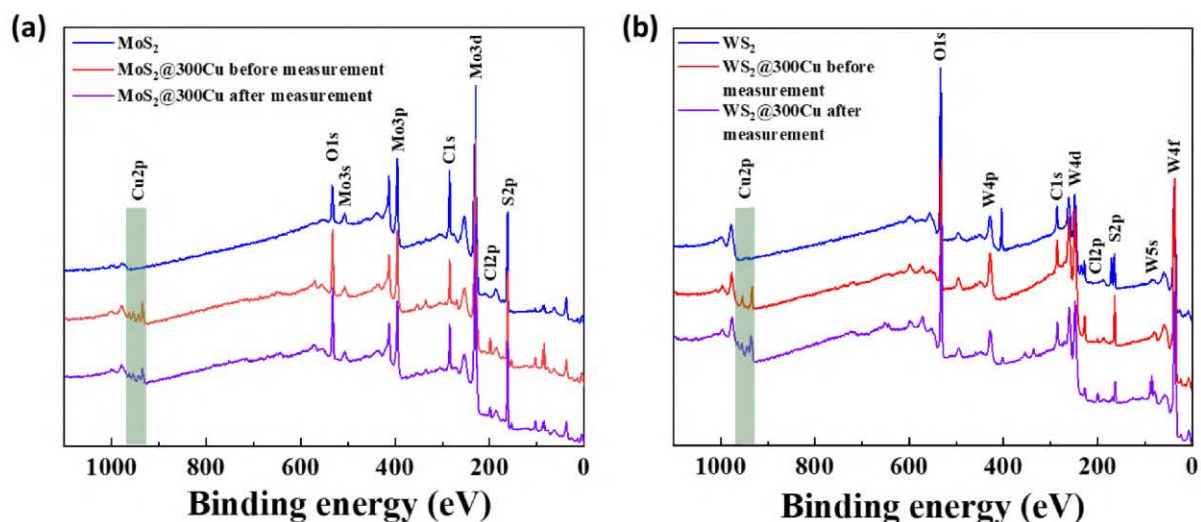


Figure S8. XPS spectra of pure MoS<sub>2</sub> nanosheets, MoS<sub>2</sub>@Cu, WS<sub>2</sub> nanosheets and WS<sub>2</sub>@300Cu before and after humidity measurements. (a) Mo3d, (b) S2p and (c) Cu2p core levels, (d) W4f, (e) S2p, and (f) Cu2p core levels.



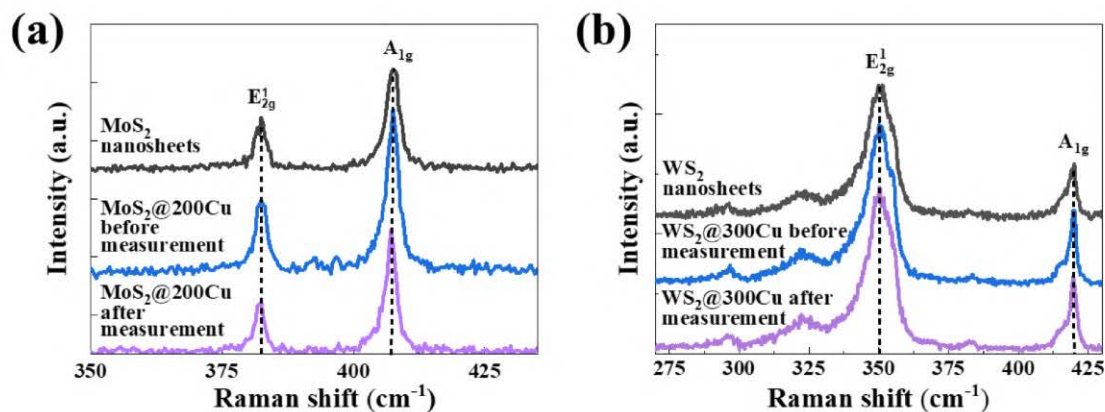


**Figure S9. XPS survey spectra.** (a) include the pure MoS<sub>2</sub> nanosheets, MoS<sub>2</sub>@300Cu before and after humidity measurements, (b) include the pure WS<sub>2</sub> nanosheets, WS<sub>2</sub>@300Cu before and after humidity measurements.

Table S2. The percentage of the main elements appeared in the MoS<sub>2</sub> and WS<sub>2</sub> nanosheets based humidity sensors.

	Mo	S	Cu
MoS <sub>2</sub>	33.47%	66.53%	-
MoS <sub>2</sub> @5Cu after measurement	31.35%	67.70%	0.96%
MoS <sub>2</sub> @25Cu after measurement	32.34%	65.97%	1.69%
MoS <sub>2</sub> @300Cu after measurement	31.70%	61.60%	6.69%
MoS <sub>2</sub> @300Cu before measurement	31.59%	60.64%	7.77%
	W	S	Cu
WS <sub>2</sub>	31.27%	68.73%	-
WS <sub>2</sub> @300Cu before measurement	49.30%	44.00%	6.70%
WS <sub>2</sub> @300Cu after measurement	49.69%	34.61%	15.70%

The MoS<sub>2</sub> and WS<sub>2</sub> based sensing film is systematically studied using a Raman scattering spectroscopy (see Figure S10). The spectra did not show a significant change of the E<sub>2g</sub><sup>1</sup> and A<sub>1g</sub> modes of TMD<sub>s</sub> before and after measurement, confirming the high stability of such materials.



**Figure S10. Raman spectra.** (a) pristine MoS<sub>2</sub> nanosheets, and the MoS<sub>2</sub>@200Cu humidity sensor before and after measurement; (b) pristine WS<sub>2</sub> nanosheets, and WS<sub>2</sub>@300Cu humidity sensor before and after humidity sensors.

We also reviewed the sensing response of the previously published WS<sub>2</sub> based humidity sensors. Table S3 shows results for representative WS<sub>2</sub> nanosheets-based positive humidity sensors, mainly fabricated using solution-exfoliation, tungsten sulfurization and hot-wire chemical vapour deposited WS<sub>2</sub> nanoparticles. But the high-temperature synthesized polycrystalline WS<sub>2</sub> sensors exhibit a positive humidity sensing behaviour, most probably caused by oxygen attached to the surface of the WS<sub>2</sub> film.<sup>6</sup> Only a few publications discuss the negative humidity sensing behaviour. The table also lists negative humidity sensors fabricated using single-crystal WS<sub>2</sub> monolayer and polymer-connected WS<sub>2</sub> nanoparticles. We suggest that the negative humidity mechanism can be explained in the same way as for the negative MoS<sub>2</sub> humidity sensors.

Table S3. Summary of humidity sensing mechanism of WS<sub>2</sub> humidity sensors.

Materials	Preparation methods	Mechanisms	Response ( $\Omega$ )	RR time (s)	RH range	Reference
<b>WS<sub>2</sub>@Cu nanosheets</b>	<b>WS<sub>2</sub>@Cu by voltage drive</b>	<b>Negative</b>	$4.3 \times 10^1 - 2.8 \times 10^2$	<b>0.8/38.8</b>	<b>4-80%</b>	<b>This work</b>
<b>WS<sub>2</sub>@Ag nanosheets</b>	<b>WS<sub>2</sub>@Ag by voltage drive</b>	<b>Negative</b>	$6.3 \times 10^0 - 5.9 \times 10^1$	<b>20.8/30.3</b>	<b>4-80%</b>	<b>This work</b>
WS <sub>2</sub> aerogel	-	Negative	$1.7 \times 10^7 - 1.9 \times 10^7$	-	0-40%	Yan <sup>7</sup>
Li-solution exfoliation	WS <sub>2</sub> (PEO) <sub>1.4</sub> nanocomposites	Negative	$1.0 \times 10^4 - 8.0 \times 10^4$	-	0-90%	Frindt <sup>8</sup>
WS <sub>2</sub> monolayer	CVD	Negative	$2.0 \times 10^{11} - 2.0 \times 10^{13}$	-	0.1Pa to 1atm	Lan <sup>9</sup>
Polycrystalline WS <sub>2</sub> films	Tungsten metal sulfurization	Positive	$5.0 \times 10^{10} - 2.9 \times 10^8$	5/6	20-90%	Guo <sup>10</sup>
WS <sub>2</sub> nanoparticles	Hot-wire chemical vapour deposition	Positive	$5.0 \times 10^9 - 5.3 \times 10^6$	12/13	11-97%	Pawbake <sup>11</sup>
WS <sub>2</sub> /WSe <sub>2</sub> nanohybrids	Sonication	Positive	-	40/65	25-80%	Jha <sup>12</sup>
WS <sub>2</sub> /SnO <sub>2</sub> nanocomposite	Sulfurized Na <sub>2</sub> WO <sub>4</sub> and dissolved in water	positive	$1.0 \times 10^9 - 4.4 \times 10^5$	-	11-95%	Chen <sup>13</sup>
WS <sub>2</sub> -SnO <sub>2</sub> nanocomposite	Na <sub>2</sub> WO <sub>4</sub> facile hydrothermal route	Positive	$1.0 \times 10^8 - 1.0 \times 10^3$	-	11-85%	Zhang <sup>14</sup>
WS <sub>2</sub> nanosheets	Sonication	Positive	-	13/17	40-80%	Jha <sup>15</sup>

## References

- (1) Syari'ati, A.; Kumar, S.; Zahid, A.; Ali El Yumin, A.; Ye, J.; Rudolf, P. Photoemission Spectroscopy Study of Structural Defects in Molybdenum Disulfide (MoS<sub>2</sub>) Grown by Chemical Vapor Deposition (CVD). *Chem. Commun.* **2019**, 55 (70), 10384–10387.
- (2) P. Vasquez, R. CuCl<sub>2</sub> by XPS. *Surf. Scuebce Spectra* **1993**, 2, 160.
- (3) Strohmeier, B. R.; Leyden, D. E.; Scottfield, R.; Hercules, D. M. Surface Spectroscopic Characterization of Cu/Al<sub>2</sub>O<sub>3</sub>. *J. Catal.* **1985**, 94, 514-530.
- (4) Yoshida, T.; Yamasaki, K.; Sawada, S. An X-Ray Photoelectron Spectroscopic Study of Biuret Metal Complexes. *Bull. Chem. Soc. Jpn.* **1978**, 51 (5), 1561–1562.
- (5) Paolucci, V.; Emamjomeh, S. M.; Nardone, M.; Ottaviano, L.; Cantalini, C. Two-Step Exfoliation of WS<sub>2</sub> for NO<sub>2</sub>, H<sub>2</sub> and Humidity Sensing Applications. *Nanomaterials* **2019**, 9 (10), 1363.
- (6) Qian, J.; Peng, Z.; Shen, Z.; Zhao, Z.; Zhang, G.; Fu, X. Positive Impedance Humidity Sensors via Single-Component Materials. *Sci. Rep.* **2016**, 6 (1), 25574.
- (7) Yan, W.; Harley-Trochimczyk, A.; Long, H.; Chan, L.; Pham, T.; Hu, M.; Qin, Y.; Zettl, A.; Carraro, C.; Worsley, M. A.; Maboudian, R. Conductometric Gas Sensing Behavior of WS<sub>2</sub> Aerogel. *FlatChem* **2017**, 5, 1–8.
- (8) Frindt, R. F.; Yang, D. Restacked WS<sub>2</sub>(PEO)<sub>1.4</sub> Nanocomposites. *Mol. Cryst. Liq. Cryst. Sci. Technol. Sect. Mol. Cryst. Liq. Cryst.* **1998**, 311 (1), 367–375.
- (9) Lan, C.; Li, C.; Yin, Y.; Liu, Y. Large-Area Synthesis of Monolayer WS<sub>2</sub> and Its Ambient-Sensitive Photo-Detecting Performance. *Nanoscale* **2015**, 7 (14), 5974–5980.
- (10) Guo, H.; Lan, C.; Zhou, Z.; Sun, P.; Wei, D.; Li, C. Transparent, Flexible, and Stretchable WS<sub>2</sub> Based Humidity Sensors for Electronic Skin. *Nanoscale* **2017**, 9 (19), 6246–6253.
- (11) Pawbake, A. S.; Waykar, R. G.; Late, D. J.; Jadkar, S. R. Highly Transparent Wafer-Scale Synthesis of Crystalline WS<sub>2</sub> Nanoparticle Thin Film for Photodetector and Humidity-Sensing Applications. *ACS Appl. Mater. Interfaces* **2016**, 8 (5), 3359–3365.
- (12) Jha, R. K.; Guha, P. K. Humidity Sensing Properties of Coexfoliated Heterogeneous WS<sub>2</sub> /WSe<sub>2</sub> Nanohybrids. *IEEE Trans. Nanotechnol.* **2018**, 17 (3), 582–589.
- (13) Chen, Y.; Pei, Y.; Jiang, Z.; Shi, Z.; Xu, J.; Wu, D.; Xu, T.; Tian, Y.; Wang, X.; Li, X. Humidity Sensing Properties of the Hydrothermally Synthesized WS<sub>2</sub>-Modified SnO<sub>2</sub> Hybrid Nanocomposite. *Appl. Surf. Sci.* **2018**, 447, 325–330.
- (14) Zhang, D.; Cao, Y.; Li, P.; Wu, J.; Zong, X. Humidity-Sensing Performance of Layer-by-Layer Self-Assembled Tungsten Disulfide/Tin Dioxide Nanocomposite. *Sens. Actuators B Chem.* **2018**, 265, 529–538.
- (15) Pristine WS<sub>2</sub> Nanosheets for Ultrasensitive and Highly Stable Chemiresistive Humidity Sensors. *Nanotechnology* **2016**, 27 (47), 475503.

## 7. Conclusions and perspectives

Here we summarise the main results of this thesis and the possible future work to further understand and manage the heat transport in the layered materials.

Since good thermal management is required to maintain the specific functions of their prospective electronic devices based on layered materials in order to avoid overheating. In this thesis, we have identified layered materials for thermal management and humidity sensing applications. In order to better understand the related properties of layered materials and obtain the high-quality samples, we studied the materials starting from the synthesis process. As shown in the Chapter 2, the layered materials studied in this thesis were prepared and measured in our laboratory, except the PtSe<sub>2</sub> layered polycrystalline film which was grown by a molecular beam epitaxy in the group of Dr. Jamet Matthieu. Monolayers and few-layers MoS<sub>2</sub> and WS<sub>2</sub> were synthesized by chemical vapor deposition. Both SnSe<sub>2</sub> and MoS<sub>2</sub> multilayers suspended membranes were prepared by a combination of mechanical exfoliation and dry-transfer method. MoS<sub>2</sub> and WS<sub>2</sub> layered nanosheets were synthesized by solution exfoliation method. In-plane and cross-plane thermal conductivities of these materials were obtained using contactless laser Raman thermometry and frequency-domain thermoreflectance, respectively. In this thesis, two main research stands were followed in the quest to enhance the thermal management of layered materials.

First, we investigated the thermal conductivity of novel and rarely studied layered materials (SnSe<sub>2</sub> and PtSe<sub>2</sub>) that vary due to their structural factors, such as thickness and crystallinity, and environmental factors, such as temperature, pressure, and surrounding gases including N<sub>2</sub> and H<sub>2</sub>O (humidity). In Chapter 3, we demonstrated that the  $k_r$  and  $k_z$  of the layered SnSe<sub>2</sub> increased with increasing thickness, with an anisotropic ratio of about 8.4. The strong temperature dependence of the thermal conductivity became gradually weaker with decreasing thickness due to the dominant role of phonon boundary scattering. The MFP reconstruction method showed that the main heat-carrying phonons that contribute to  $k_r$  and  $k_z$  have mean free paths of several tens of nanometers. In Chapter 4, we studied phonon dynamic properties and heat transport in MBE-grown crystalline and polycrystalline PtSe<sub>2</sub> thin film with a

thickness varying from 1 to 40 layers. The methods were FDTR, low-frequency Raman scattering, pump-probe coherent phonon spectroscopy, and state-of-the-art DFT calculations. The  $k_z$  of polycrystalline PtSe<sub>2</sub> with a thickness above 12 nm was almost 35% lower compared to the same thickness crystalline films. The phonon dynamic study of the crystalline PtSe<sub>2</sub>, showed an out-of-plane elastic constant  $C_{33} = 31.8$  GPa and a layer-dependent group velocity ranging from 1340 ms<sup>-1</sup> in the bilayer to 1873 ms<sup>-1</sup> in an eight-layers sample. The acoustic phonons in PtSe<sub>2</sub> had extraordinarily short lifetimes on the order of picoseconds. Additionally, in Chapter 5, we found that the MoS<sub>2</sub> nanosheets-based membrane with a low crystallinity shows a low thermal conductivity of  $0.08 \pm 0.03$  W/mK in vacuum and increased to  $0.55 \pm 0.03$  W/mK in ambient conditions. The kind of the surrounding gases (N<sub>2</sub>, O<sub>2</sub>, H<sub>2</sub>O, etc.) effects on thermal conductivity of the membrane was not obvious, which should be further studied. We also demonstrated that thickness going from 4.5 to 40 nm, result in an increase of the  $k_r$  of layered MoS<sub>2</sub> membranes from  $30 \pm 3$  W/mK to  $88 \pm 3$  W/mK.

Second, we actively intervened in the thermal conductivity of the layered materials for better utilizing of these materials in devices, the external techniques including annealing and nanopatterning were explored to control the thermal conductivity of MoS<sub>2</sub>. Therefore, In Chapter 5, we found that the thermal conductivity of the MoS<sub>2</sub> nanosheets-based film and layered MoS<sub>2</sub> supporting membrane changed by annealing and nanopatterning, respectively. We demonstrated that  $k_r$  of the MoS<sub>2</sub> nanosheets-based film increased by about 140% after annealing at 673K for 3 hours. The thickness-dependent  $k_r$  of layered MoS<sub>2</sub> membrane was determined and shown to increase from  $30 \pm 3$  W/mK at 4.5 nm to  $88 \pm 3$  W/mK at 40 nm. The thermal conductivity of these samples was dropped by about 90% after nanopatterning with a 500 nm periodic hole array, and by 99% after nanopatterning with a period of 300 nm periodic hole array. We demonstrated that the level of porosity to reduce the same percentage thermal conductivity of layered materials could be much smaller than the porosity needed in other materials such as silicon and silicon carbide, which showed that layered materials are more sensitive to the nanopatterned structures than silicon and silicon carbide. This approach was applied to fabricate thermal insulation and heat guiding.

Finally, in Chapter 6, MoS<sub>2</sub>- and WS<sub>2</sub>-nanosheets-based humidity sensors were fabricated to study the humidity response of the layered materials. We found that

transition-metal salts including  $\text{CuCl}_2$  and  $\text{AgNO}_3$  can easily modify the surface of  $\text{MoS}_2$  and  $\text{WS}_2$  nanosheets, which can be further extended as a technique to modify the thermal conductivity of layered materials. The electrical conductance was adjusted by controlling the amount of metal salts for possible commercial applications. We demonstrated the reversal in the humidity response of TMD nanosheets-based devices. The inversion was explained in the context of the change from a "hydrogen bond network" to "charge acceptors" in the sensors driven by the change in the film morphology. The new mechanism was verified by a lumped circuit-based model. This work revealed the humidity effects on the properties of layered materials and proved that morphology and metal decoration are crucial for the fabrication of high-performance sensors. The work gives a new perspective on the aging and performance reversal of nanosheet-based devices in complex working environments.

In this thesis, we show the importance of thermal conductivity measurement of materials, and our data can be used to compare data measured by different techniques to guide the related simulation work. Many opportunities may arise from the results of this thesis. The thermal properties of the layered materials studied, exhibited a huge change when their thickness decreased to a few nanometers and the capability of fabricating a large area of suspended crystalline film may encourage the investigation of heat transport in other layered materials, especially monolayers and a few-layers structures where the phonon scattering mechanisms are quite different from bulk structures. Furthermore, fabrication of large-area (radius  $> 10 \mu\text{m}$ ) of the suspended bilayer heterostructure or twisted bilayer membranes using layered materials would allow us to explore thermal transport at the materials' interface and the misfit angle-dependent thermal conductivity. Our experimental data showed that layered materials are more sensitive to nanopatterning than thin films and membranes of silicon and silicon carbide. these investigations could pave the way to establish a consistent theory of thermal transport in nanopatterned layered structures using EMD and other simulation methods.

In addition, layered materials patterned by nanofabrication methods could be used to explore thermal transport-related applications, in areas such as heat guiding, thermal insulation, and thermoelectricity. For example, the large anisotropic thermal

conductivity of layered materials and the ability to reduce thermal conductivity by nanopatterning with small porosity without impacting electrical conductivity, opens the possibility of using some high Seebeck coefficient layered materials to fabricate high-performance thermoelectric devices. Finally, transition metal salts show the ability to modify the surface of layered materials through stable chemical bonds, which could be further investigated to understand better how metal layers effect on the phonon propagation in layered materials.



# Bibliography

- (1) Hay, B. A Brief History of the Thermal Properties Metrology. 38.
- (2) Narasimhan, T. N. Thermal Conductivity through the 19th Century. *Physics Today* **2010**, *63* (8), 36–41. <https://doi.org/10.1063/1.3480074>.
- (3) Hansen, J.; Nazarenko, L.; Ruedy, R.; Sato, M.; Willis, J.; Del Genio, A.; Koch, D.; Lacis, A.; Lo, K.; Menon, S.; Novakov, T.; Perlwitz, J.; Russell, G.; Schmidt, G. A.; Tausnev, N. Earth's Energy Imbalance: Confirmation and Implications. *Science* **2005**, *308* (5727), 1431–1435. <https://doi.org/10.1126/science.1110252>.
- (4) Shalf, J. The Future of Computing beyond Moore's Law. *Phil. Trans. R. Soc. A.* **2020**, *378* (2166), 20190061. <https://doi.org/10.1098/rsta.2019.0061>.
- (5) Song, C.; Noh, G.; Kim, T. S.; Kang, M.; Song, H.; Ham, A.; Jo, M.; Cho, S.; Chai, H.-J.; Cho, S. R.; Cho, K.; Park, J.; Song, S.; Song, I.; Bang, S.; Kwak, J. Y.; Kang, K. Growth and Interlayer Engineering of 2D Layered Semiconductors for Future Electronics. *ACS Nano* **2020**, *14* (12), 16266–16300. <https://doi.org/10.1021/acsnano.0c06607>.
- (6) Yalon, E.; McClellan, C. J.; Smithe, K. K. H.; Muñoz Rojo, M.; Xu, R. L.; Suryavanshi, S. V.; Gabourie, A. J.; Neumann, C. M.; Xiong, F.; Farimani, A. B.; Pop, E. Energy Dissipation in Monolayer MoS<sub>2</sub> Electronics. *Nano Lett.* **2017**, *17* (6), 3429–3433. <https://doi.org/10.1021/acs.nanolett.7b00252>.
- (7) Gu, X.; Li, B.; Yang, R. Layer Thickness-Dependent Phonon Properties and Thermal Conductivity of MoS<sub>2</sub>. *Journal of Applied Physics* **2016**, *119* (8), 085106. <https://doi.org/10.1063/1.4942827>.
- (8) Sood, A.; Xiong, F.; Chen, S.; Cheaito, R.; Lian, F.; Asheghi, M.; Cui, Y.; Donadio, D.; Goodson, K. E.; Pop, E. Quasi-Ballistic Thermal Transport Across MoS<sub>2</sub> Thin Films. *Nano Lett.* **2019**, *19* (4), 2434–2442. <https://doi.org/10.1021/acs.nanolett.8b05174>.
- (9) Zhao, L.-D.; Chang, C.; Tan, G.; Kanatzidis, M. G. SnSe: A Remarkable New Thermoelectric Material. *Energy Environ. Sci.* **2016**, *9* (10), 3044–3060. <https://doi.org/10.1039/C6EE01755J>.
- (10) Zhang, Z.; Xie, Y.; Ouyang, Y.; Chen, Y. A Systematic Investigation of Thermal Conductivities of Transition Metal Dichalcogenides. *International Journal of Heat and Mass Transfer* **2017**, *108*, 417–422. <https://doi.org/10.1016/j.ijheatmasstransfer.2016.12.041>.
- (11) Yin, Y.; Baskaran, K.; Tiwari, A. A Review of Strategies for Developing Promising Thermoelectric Materials by Controlling Thermal Conduction. *Phys. Status Solidi A* **2019**, *216* (14), 1800904. <https://doi.org/10.1002/pssa.201800904>.
- (12) Kim, S. E.; Cahill, D. G. Pushing Low Thermal Conductivity to the Limit. *Science* **2021**, *373* (6558), 963.

- (13) Borup, K. A.; de Boor, J.; Wang, H.; Drymiotis, F.; Gascoin, F.; Shi, X.; Chen, L.; Fedorov, M. I.; Müller, E.; Iversen, B. B.; Snyder, G. J. Measuring Thermoelectric Transport Properties of Materials. *Energy Environ. Sci.* **2015**, *8* (2), 423–435. <https://doi.org/10.1039/C4EE01320D>.
- (14) Greppmair, A.; Galfe, N.; Amend, K.; Stutzmann, M.; Brandt, M. S. Thermal Characterization of Thin Films via Dynamic Infrared Thermography. *Review of Scientific Instruments* **2019**, *90* (4), 044903. <https://doi.org/10.1063/1.5067400>.
- (15) Wang, H.; Chu, W.; Chen, G. A Brief Review on Measuring Methods of Thermal Conductivity of Organic and Hybrid Thermoelectric Materials. *Adv. Electron. Mater.* **2019**, *5* (11), 1900167. <https://doi.org/10.1002/aelm.201900167>.
- (16) Hänninen, T. Implementing the 3-Omega Technique for Thermal Conductivity Measurements. 37.
- (17) Wang, H.; Sen, M. Analysis of the 3-Omega Method for Thermal Conductivity Measurement. *International Journal of Heat and Mass Transfer* **2009**, *52* (7–8), 2102–2109. <https://doi.org/10.1016/j.ijheatmasstransfer.2008.10.020>.
- (18) Sandell, S.; Chávez-Ángel, E.; El Sachat, A.; He, J.; Sotomayor Torres, C. M.; Maire, J. Thermoreflectance Techniques and Raman Thermometry for Thermal Property Characterization of Nanostructures. *Journal of Applied Physics* **2020**, *128* (13), 131101. <https://doi.org/10.1063/5.0020239>.
- (19) Graczykowski, B.; El Sachat, A.; Reparaz, J. S.; Sledzinska, M.; Wagner, M. R.; Chavez-Angel, E.; Wu, Y.; Volz, S.; Wu, Y.; Alzina, F.; Sotomayor Torres, C. M. Thermal Conductivity and Air-Mediated Losses in Periodic Porous Silicon Membranes at High Temperatures. *Nat Commun* **2017**, *8* (1), 415. <https://doi.org/10.1038/s41467-017-00115-4>.
- (20) Reparaz, J. S.; Chavez-Angel, E.; Wagner, M. R.; Graczykowski, B.; Gomis-Bresco, J.; Alzina, F.; Torres, C. M. S. A Novel High Resolution Contactless Technique for Thermal Field Mapping and Thermal Conductivity Determination: Two-Laser Raman Thermometry. *Review of Scientific Instruments* **2014**, *85* (3), 034901. <https://doi.org/10.1063/1.4867166>.
- (21) Xiao, P.; Chavez-Angel, E.; Chaitoglou, S.; Sledzinska, M.; Dimoulas, A.; Sotomayor Torres, C. M.; El Sachat, A. Anisotropic Thermal Conductivity of Crystalline Layered SnSe<sub>2</sub>. *Nano Lett.* **2021**, *21* (21), 9172–9179. <https://doi.org/10.1021/acs.nanolett.1c03018>.
- (22) Shi, L.; Li, D.; Yu, C.; Jang, W.; Kim, D.; Yao, Z.; Kim, P.; Majumdar, A. Measuring Thermal and Thermoelectric Properties of One-Dimensional Nanostructures Using a Microfabricated Device. *Journal of Heat Transfer* **2003**, *125* (5), 881–888. <https://doi.org/10.1115/1.1597619>.
- (23) Volklein, F. THERMAL CONDUCTIVITY AND DIFFUSIVITY OF A THIN FILM SiO<sub>2</sub>-Si<sub>3</sub>N<sub>4</sub> SANDWICH SYSTEM. 7.
- (24) Gotti, R.; Lamperti, M.; Gatti, D.; Marangoni, M. Laser-Based Primary Thermometry: A Review. *Journal of Physical and Chemical Reference Data* **2021**, *50* (3), 031501. <https://doi.org/10.1063/5.0055297>.
- (25) Raman, C. V.; S., F. R. A New Radiation. *Indian J. Phys* **1928**, *2*, 387–398.

- (26) Novoselov, K. S. Electric Field Effect in Atomically Thin Carbon Films. *Science* **2004**, *306* (5696), 666–669. <https://doi.org/10.1126/science.1102896>.
- (27) Neto, A. H. C. The Electronic Properties of Graphene. *Rev. Mod. Phys.* **2009**, *81* (1), 54.
- (28) Meyer, J. C.; Geim, A. K.; Katsnelson, M. I.; Novoselov, K. S.; Booth, T. J.; Roth, S. The Structure of Suspended Graphene Sheets. *Nature* **2007**, *446* (7131), 60–63. <https://doi.org/10.1038/nature05545>.
- (29) Hart, T. R.; Aggarwal, R. L.; Lax, B. Temperature Dependence of Raman Scattering in Silicon. *Phys. Rev. B* **1970**, *1* (2), 638–642. <https://doi.org/10.1103/PhysRevB.1.638>.
- (30) Menéndez, J.; Cardona, M. Temperature Dependence of the First-Order Raman Scattering by Phonons in Si, Ge, and  $\alpha$ -Sn: Anharmonic Effects. *Phys. Rev. B* **1984**, *29* (4), 2051–2059. <https://doi.org/10.1103/PhysRevB.29.2051>.
- (31) Ángel, E. C. Confined Acoustic Phonons in Si Nanomembranes: Impact on Thermal Properties. *Universitat Autònoma de Barcelona* **2014**, 240.
- (32) Graczykowski, B.; El Sachat, A.; Reparaz, J. S.; Sledzinska, M.; Wagner, M. R.; Chavez-Angel, E.; Wu, Y.; Volz, S.; Wu, Y.; Alzina, F.; Sotomayor Torres, C. M. Thermal Conductivity and Air-Mediated Losses in Periodic Porous Silicon Membranes at High Temperatures. *Nat Commun* **2017**, *8* (1), 415. <https://doi.org/10.1038/s41467-017-00115-4>.
- (33) Sledzinska, M.; Graczykowski, B.; Placidi, M.; Reig, D. S.; Sachat, A. E.; Reparaz, J. S.; Alzina, F.; Mortazavi, B.; Quey, R.; Colombo, L.; Roche, S.; Torres, C. M. S. Thermal Conductivity of MoS<sub>2</sub> polycrystalline Nanomembranes. *2D Mater.* **2016**, *3* (3), 035016. <https://doi.org/10.1088/2053-1583/3/3/035016>.
- (34) Li, G.; Ding, G.; Gao, G. Thermoelectric Properties of SnSe<sub>2</sub> Monolayer. *J. Phys.: Condens. Matter* **2017**, *29* (1), 015001. <https://doi.org/10.1088/0953-8984/29/1/015001>.
- (35) Sun, B.-Z.; Ma, Z.; He, C.; Wu, K. Anisotropic Thermoelectric Properties of Layered Compounds in SnX<sub>2</sub> (X = S, Se): A Promising Thermoelectric Material. *Phys. Chem. Chem. Phys.* **2015**, *17* (44), 29844–29853. <https://doi.org/10.1039/C5CP03700J>.
- (36) Xu, P.; Fu, T.; Xin, J.; Liu, Y.; Ying, P.; Zhao, X.; Pan, H.; Zhu, T. Anisotropic Thermoelectric Properties of Layered Compound SnSe<sub>2</sub>. *Science Bulletin* **2017**, *62* (24), 1663–1668. <https://doi.org/10.1016/j.scib.2017.11.015>.
- (37) Wang, H.; Gao, Y.; Liu, G. Anisotropic Phonon Transport and Lattice Thermal Conductivities in Tin Dichalcogenides SnS<sub>2</sub> and SnSe<sub>2</sub>. *RSC Adv.* **2017**, *7* (14), 8098–8105. <https://doi.org/10.1039/C6RA27761F>.
- (38) Li, M. O.; Esseni, D.; Nahas, J. J.; Jena, D.; Xing, H. G. Two-Dimensional Heterojunction Interlayer Tunneling Field Effect Transistors (Thin-TFETs). *IEEE J. Electron Devices Soc.* **2015**, *3* (3), 200–207. <https://doi.org/10.1109/JEDS.2015.2390643>.
- (39) Roy, T.; Tosun, M.; Hettick, M.; Ahn, G. H.; Hu, C.; Javey, A. 2D-2D Tunneling Field-Effect Transistors Using WSe<sub>2</sub>/SnSe<sub>2</sub> Heterostructures. *Appl. Phys. Lett.* **2016**, *108* (8), 083111. <https://doi.org/10.1063/1.4942647>.

- (40) Su, Y.; Ebrish, M. A.; Olson, E. J.; Koester, S. J. SnSe<sub>2</sub> Field-Effect Transistors with High Drive Current. *Appl. Phys. Lett.* **2013**, *103* (26), 263104. <https://doi.org/10.1063/1.4857495>.
- (41) Chung, K.-M.; Wamwangi, D.; Woda, M.; Wuttig, M.; Bensch, W. Investigation of SnSe, SnSe<sub>2</sub>, and Sn<sub>2</sub>Se<sub>3</sub> Alloys for Phase Change Memory Applications. *Journal of Applied Physics* **2008**, *103* (8), 083523. <https://doi.org/10.1063/1.2894903>.
- (42) Rai, R. K.; Islam, S.; Roy, A.; Agrawal, G.; Singh, A. K.; Ghosh, A.; N., R. Morphology Controlled Synthesis of Low Bandgap SnSe<sub>2</sub> with High Photodetectivity. *Nanoscale* **2019**, *11* (3), 870–877. <https://doi.org/10.1039/C8NR08138G>.
- (43) Ding, Y.; Xiao, B.; Tang, G.; Hong, J. Transport Properties and High Thermopower of SnSe<sub>2</sub>: A Full Ab-Initio Investigation. *J. Phys. Chem. C* **2017**, *121* (1), 225–236. <https://doi.org/10.1021/acs.jpcc.6b11467>.
- (44) Huang, Y.; Chen, X.; Zhou, D.; Liu, H.; Wang, C.; Du, J.; Ning, L.; Wang, S. Stabilities, Electronic and Optical Properties of SnSe<sub>2(1-x)</sub>S<sub>2x</sub> Alloys: A First-Principles Study. *J. Phys. Chem. C* **2016**, *120* (10), 5839–5847. <https://doi.org/10.1021/acs.jpcc.6b00794>.
- (45) Saritha, K.; Suryanarayana Reddy, A.; Ramakrishna Reddy, K. T. Investigation on Optical Properties of SnSe<sub>2</sub> Thin Films Synthesized by Two – Stage Process. *Materials Today: Proceedings* **2017**, *4* (14), 12512–12517. <https://doi.org/10.1016/j.matpr.2017.10.053>.
- (46) Martínez-Escobar, D.; Ramachandran, M.; Sánchez-Juárez, A.; Narro Rios, J. S. Optical and Electrical Properties of SnSe<sub>2</sub> and SnSe Thin Films Prepared by Spray Pyrolysis. *Thin Solid Films* **2013**, *535*, 390–393. <https://doi.org/10.1016/j.tsf.2012.12.081>.
- (47) Evans, B. L.; Hazelwood, R. A. Optical and Electrical Properties of SnSe<sub>2</sub>. *J. Phys. D: Appl. Phys.* **1969**, *2* (11), 1507–1516. <https://doi.org/10.1088/0022-3727/2/11/304>.
- (48) Bertrand, Y.; Leveque, G.; Raisin, C.; Levy, F. Optical Properties of SnSe<sub>2</sub> and SnS<sub>2</sub>. *J. Phys. C: Solid State Phys.* **1979**, *12* (14), 2907–2916. <https://doi.org/10.1088/0022-3719/12/14/025>.
- (49) Zou, B.; Zhou, Y.; Zhang, X.; Zhang, M.; Liu, K.; Gong, M.; Sun, H. Thickness-Dependent Ultralow In-Plane Thermal Conductivity of Chemical Vapor-Deposited SnSe<sub>2</sub> Nanofilms: Implications for Thermoelectrics. *ACS Appl. Nano Mater.* **2020**, *3* (10), 10543–10550. <https://doi.org/10.1021/acsnm.0c02550>.
- (50) Liu, X.; Li, Z.; Min, L.; Peng, Y.; Xiong, X.; Lu, Y.; Ao, J.-P.; Fang, J.; He, W.; Li, K.; Wu, J.; Mao, W.; Younis, U.; Divakar Botcha, V. Effect of Stress Layer on Thermal Properties of SnSe<sub>2</sub> Few Layers. *Journal of Alloys and Compounds* **2019**, *783*, 226–231. <https://doi.org/10.1016/j.jallcom.2018.12.317>.
- (51) Minnich, A. J. Determining Phonon Mean Free Paths from Observations of Quasiballistic Thermal Transport. *Phys. Rev. Lett.* **2012**, *109* (20), 205901. <https://doi.org/10.1103/PhysRevLett.109.205901>.
- (52) Zhang, H.; Chen, X.; Jho, Y.-D.; Minnich, A. J. Temperature-Dependent Mean Free Path Spectra of Thermal Phonons Along the *c*-Axis of Graphite. *Nano Lett.* **2016**, *16* (3), 1643–1649. <https://doi.org/10.1021/acs.nanolett.5b04499>.

- (53) Sanchez-Martinez, M.-Á.; Alzina, F.; Oyarzo, J.; Sotomayor Torres, C.; Chavez-Angel, E. Impact of the Regularization Parameter in the Mean Free Path Reconstruction Method: Nanoscale Heat Transport and Beyond. *Nanomaterials* **2019**, *9* (3), 414. <https://doi.org/10.3390/nano9030414>.
- (54) Chung, D. D. L.; Takizawa, Y. Performance of Isotropic and Anisotropic Heat Spreaders. *Journal of Elec Materi* **2012**, *41* (9), 2580–2587. <https://doi.org/10.1007/s11664-012-2177-4>.
- (55) Yamaguchi, S.; Tsunekawa, I.; Komatsu, N.; Gao, W.; Shiga, T.; Kodama, T.; Kono, J.; Shiomi, J. One-Directional Thermal Transport in Densely Aligned Single-Wall Carbon Nanotube Films. *Appl. Phys. Lett.* **2019**, *115* (22), 223104. <https://doi.org/10.1063/1.5127209>.
- (56) Ferrari, A. C.; Bonaccorso, F.; Fal'ko, V.; Novoselov, K. S.; Roche, S.; Bøggild, P.; Borini, S.; Koppens, F. H. L.; Palermo, V.; Pugno, N.; Garrido, J. A.; Sordan, R.; Bianco, A.; Ballerini, L.; Prato, M.; Lidorikis, E.; Kivioja, J.; Marinelli, C.; Ryhänen, T.; Morpurgo, A.; Coleman, J. N.; Nicolosi, V.; Colombo, L.; Fert, A.; Garcia-Hernandez, M.; Bachtold, A.; Schneider, G. F.; Guinea, F.; Dekker, C.; Barbone, M.; Sun, Z.; Galiotis, C.; Grigorenko, A. N.; Konstantatos, G.; Kis, A.; Katsnelson, M.; Vandersypen, L.; Loiseau, A.; Morandi, V.; Neumaier, D.; Treossi, E.; Pellegrini, V.; Polini, M.; Tredicucci, A.; Williams, G. M.; Hee Hong, B.; Ahn, J.-H.; Min Kim, J.; Zirath, H.; van Wees, B. J.; van der Zant, H.; Occhipinti, L.; Di Matteo, A.; Kinloch, I. A.; Seyller, T.; Quesnel, E.; Feng, X.; Teo, K.; Rupesinghe, N.; Hakonen, P.; Neil, S. R. T.; Tannock, Q.; Löfwander, T.; Kinaret, J. Science and Technology Roadmap for Graphene, Related Two-Dimensional Crystals, and Hybrid Systems. *Nanoscale* **2015**, *7* (11), 4598–4810. <https://doi.org/10.1039/C4NR01600A>.
- (57) Jariwala, D.; Sangwan, V. K.; Wu, C.-C.; Prabhumirashi, P. L.; Geier, M. L.; Marks, T. J.; Lauhon, L. J.; Hersam, M. C. Gate-Tunable Carbon Nanotube–MoS<sub>2</sub> Heterojunction p-n Diode. *Proc. Natl. Acad. Sci. U.S.A.* **2013**, *110* (45), 18076–18080. <https://doi.org/10.1073/pnas.1317226110>.
- (58) Massicotte, M.; Schmidt, P.; Vialla, F.; Schädler, K. G.; Reserbat-Plantey, A.; Watanabe, K.; Taniguchi, T.; Tielrooij, K. J.; Koppens, F. H. L. Picosecond Photoresponse in van Der Waals Heterostructures. *Nature Nanotech* **2016**, *11* (1), 42–46. <https://doi.org/10.1038/nnano.2015.227>.
- (59) Chhowalla, M.; Jena, D.; Zhang, H. Two-Dimensional Semiconductors for Transistors. *Nat Rev Mater* **2016**, *1* (11), 16052. <https://doi.org/10.1038/natrevmats.2016.52>.
- (60) Zhao, Y.; Qiao, J.; Yu, Z.; Yu, P.; Xu, K.; Lau, S. P.; Zhou, W.; Liu, Z.; Wang, X.; Ji, W.; Chai, Y. High-Electron-Mobility and Air-Stable 2D Layered PtSe<sub>2</sub> FETs. *Adv. Mater.* **2017**, *29* (5), 1604230. <https://doi.org/10.1002/adma.201604230>.
- (61) Deng, Y.; Luo, Z.; Conrad, N. J.; Liu, H.; Gong, Y.; Najmaei, S.; Ajayan, P. M.; Lou, J.; Xu, X.; Ye, P. D. Black Phosphorus–Monolayer MoS<sub>2</sub> van Der Waals Heterojunction p–n Diode. *ACS Nano* **2014**, *8* (8), 8292–8299. <https://doi.org/10.1021/nn5027388>.
- (62) Yu, X.; Yu, P.; Wu, D.; Singh, B.; Zeng, Q.; Lin, H.; Zhou, W.; Lin, J.; Suenaga, K.; Liu, Z.; Wang, Q. J. Atomically Thin Noble Metal Dichalcogenide: A Broadband Mid-Infrared Semiconductor. *Nat Commun* **2018**, *9* (1), 1545. <https://doi.org/10.1038/s41467-018-03935-0>.

- (63) Liu, Y.; Zhang, S.; He, J.; Wang, Z. M.; Liu, Z. Recent Progress in the Fabrication, Properties, and Devices of Heterostructures Based on 2D Materials. *Nano-Micro Lett.* **2019**, *11* (1), 13. <https://doi.org/10.1007/s40820-019-0245-5>.
- (64) Li, D.; Gong, Y.; Chen, Y.; Lin, J.; Khan, Q.; Zhang, Y.; Li, Y.; Zhang, H.; Xie, H. Recent Progress of Two-Dimensional Thermoelectric Materials. *Nano-Micro Lett.* **2020**, *12* (1), 36. <https://doi.org/10.1007/s40820-020-0374-x>.
- (65) Gong, Y.; Lin, Z.; Chen, Y.-X.; Khan, Q.; Wang, C.; Zhang, B.; Nie, G.; Xie, N.; Li, D. Two-Dimensional Platinum Diselenide: Synthesis, Emerging Applications, and Future Challenges. *Nano-Micro Lett.* **2020**, *12* (1), 174. <https://doi.org/10.1007/s40820-020-00515-0>.
- (66) Bonell, F.; Marty, A.; Vergnaud, C.; Consonni, V.; Okuno, H.; Ouerghi, A.; Boukari, H.; Jamet, M. High Carrier Mobility in Single-Crystal PtSe<sub>2</sub> Grown by Molecular Beam Epitaxy on ZnO(0001). *2D Mater.* **2022**, *9* (1), 015015. <https://doi.org/10.1088/2053-1583/ac37aa>.
- (67) Yim, C.; Passi, V.; Lemme, M. C.; Duesberg, G. S.; Ó Coileáin, C.; Pallecchi, E.; Fadil, D.; McEvoy, N. Electrical Devices from Top-down Structured Platinum Diselenide Films. *npj 2D Mater Appl* **2018**, *2* (1), 5. <https://doi.org/10.1038/s41699-018-0051-9>.
- (68) Zhang, W.; Qin, J.; Huang, Z.; Zhang, W. The Mechanism of Layer Number and Strain Dependent Bandgap of 2D Crystal PtSe<sub>2</sub>. *Journal of Applied Physics* **2017**, *122* (20), 205701. <https://doi.org/10.1063/1.5000419>.
- (69) Wang, Y.; Li, L.; Yao, W.; Song, S.; Sun, J. T.; Pan, J.; Ren, X.; Li, C.; Okunishi, E.; Wang, Y.-Q.; Wang, E.; Shao, Y.; Zhang, Y. Y.; Yang, H.; Schwier, E. F.; Iwasawa, H.; Shimada, K.; Taniguchi, M.; Cheng, Z.; Zhou, S.; Du, S.; Pennycook, S. J.; Pantelides, S. T.; Gao, H.-J. Monolayer PtSe<sub>2</sub>, a New Semiconducting Transition-Metal-Dichalcogenide, Epitaxially Grown by Direct Selenization of Pt. *Nano Lett.* **2015**, *15* (6), 4013–4018. <https://doi.org/10.1021/acs.nanolett.5b00964>.
- (70) Moon, H.; Bang, J.; Hong, S.; Kim, G.; Roh, J. W.; Kim, J.; Lee, W. Strong Thermopower Enhancement and Tunable Power Factor *via* Semimetal to Semiconductor Transition in a Transition-Metal Dichalcogenide. *ACS Nano* **2019**, *13* (11), 13317–13324. <https://doi.org/10.1021/acsnano.9b06523>.
- (71) Guo, S.-D. Biaxial Strain Tuned Thermoelectric Properties in Monolayer PtSe<sub>2</sub>. *J. Mater. Chem. C* **2016**, *4* (39), 9366–9374. <https://doi.org/10.1039/C6TC03074B>.
- (72) Yin, S.; Zhang, W.; Tan, C.; Chen, L.; Chen, J.; Li, G.; Zhang, H.; Zhang, Y.; Wang, W.; Li, L. Thermal Conductivity of Few-Layer PtS<sub>2</sub> and PtSe<sub>2</sub> Obtained from Optothermal Raman Spectroscopy. *J. Phys. Chem. C* **2021**, *125* (29), 16129–16135. <https://doi.org/10.1021/acs.jpcc.1c02522>.
- (73) Chen, X.; Zhang, S.; Wang, L.; Huang, Y.-F.; Liu, H.; Huang, J.; Dong, N.; Liu, W.; Kislyakov, I. M.; Nunzi, J. M.; Zhang, L.; Wang, J. Direct Observation of Interlayer Coherent Acoustic Phonon Dynamics in Bilayer and Few-Layer PtSe<sub>2</sub>. *Photon. Res.* **2019**, *7* (12), 1416. <https://doi.org/10.1364/PRJ.7.001416>.

- (74) Schmidt, A. J.; Cheaito, R.; Chiesa, M. A Frequency-Domain Thermoreflectance Method for the Characterization of Thermal Properties. *Review of Scientific Instruments* **2009**, *80* (9), 094901. <https://doi.org/10.1063/1.3212673>.
- (75) Sandell, S.; Maire, J.; Chávez-Ángel, E.; Sotomayor Torres, C. M.; Kristiansen, H.; Zhang, Z.; He, J. Enhancement of Thermal Boundary Conductance of Metal–Polymer System. *Nanomaterials* **2020**, *10* (4), 670. <https://doi.org/10.3390/nano10040670>.
- (76) Rai, A.; Sangwan, V. K.; Gish, J. T.; Hersam, M. C.; Cahill, D. G. Anisotropic Thermal Conductivity of Layered Indium Selenide. *Appl. Phys. Lett.* **2021**, *118* (7), 073101. <https://doi.org/10.1063/5.0042091>.
- (77) Jang, H.; Wood, J. D.; Ryder, C. R.; Hersam, M. C.; Cahill, D. G. Anisotropic Thermal Conductivity of Exfoliated Black Phosphorus. *Adv. Mater.* **2015**, *27* (48), 8017–8022. <https://doi.org/10.1002/adma.201503466>.
- (78) Serrano, J.; Kremer, R. K.; Cardona, M.; Siegle, G.; Romero, A. H.; Lauck, R. Heat Capacity of ZnO: Isotope Effects. *Phys. Rev. B* **2006**, *73* (9), 094303. <https://doi.org/10.1103/PhysRevB.73.094303>.
- (79) Schmidt, A. J.; Chen, X.; Chen, G. Pulse Accumulation, Radial Heat Conduction, and Anisotropic Thermal Conductivity in Pump-Probe Transient Thermoreflectance. *Review of Scientific Instruments* **2008**, *79* (11), 114902. <https://doi.org/10.1063/1.3006335>.
- (80) Cui, Y.; Li, M.; Hu, Y. Emerging Interface Materials for Electronics Thermal Management: Experiments, Modeling, and New Opportunities. *J. Mater. Chem. C* **2020**, *8* (31), 10568–10586. <https://doi.org/10.1039/C9TC05415D>.
- (81) Fu, Y.; Hansson, J.; Liu, Y.; Chen, S.; Zehri, A.; Samani, M. K.; Wang, N.; Ni, Y.; Zhang, Y.; Zhang, Z.-B.; Wang, Q.; Li, M.; Lu, H.; Sledzinska, M.; Torres, C. M. S.; Volz, S.; Balandin, A. A.; Xu, X.; Liu, J. Graphene Related Materials for Thermal Management. *2D Mater.* **2019**, *7* (1), 012001. <https://doi.org/10.1088/2053-1583/ab48d9>.
- (82) Lohrasbi, S.; Hammer, R.; Essl, W.; Reiss, G.; Defregger, S.; Sanz, W. A Comprehensive Review on the Core Thermal Management Improvement Concepts in Power Electronics. *IEEE Access* **2020**, *8*, 166880–166906. <https://doi.org/10.1109/ACCESS.2020.3021946>.
- (83) Song, H.; Liu, J.; Liu, B.; Wu, J.; Cheng, H.-M.; Kang, F. Two-Dimensional Materials for Thermal Management Applications. *Joule* **2018**. <https://doi.org/10.1016/j.joule.2018.01.006>.
- (84) Licht, A.; Pfister, N.; DeMeo, D.; Chivers, J.; Vandervelde, T. E. A Review of Advances in Thermophotovoltaics for Power Generation and Waste Heat Harvesting. *MRS Advances* **2019**, *4* (41–42), 2271–2282. <https://doi.org/10.1557/adv.2019.342>.
- (85) Balandin, A. A.; Ghosh, S.; Bao, W.; Calizo, I.; Teweldebrhan, D.; Miao, F.; Lau, C. N. Superior Thermal Conductivity of Single-Layer Graphene. *Nano Lett.* **2008**, *8* (3), 902–907. <https://doi.org/10.1021/nl0731872>.
- (86) El Sachat, A.; Könenmann, F.; Menges, F.; Del Corro, E.; Garrido, J. A.; Sotomayor Torres, C. M.; Alzina, F.; Gotsmann, B. Crossover from Ballistic to Diffusive Thermal

Transport in Suspended Graphene Membranes. *2D Mater.* **2019**, *6* (2), 025034. <https://doi.org/10.1088/2053-1583/ab097d>.

(87) Jo, I.; Pettes, M. T.; Kim, J.; Watanabe, K.; Taniguchi, T.; Yao, Z.; Shi, L. Thermal Conductivity and Phonon Transport in Suspended Few-Layer Hexagonal Boron Nitride. *Nano Lett.* **2013**, *13* (2), 550–554. <https://doi.org/10.1021/nl304060g>.

(88) Cai, Q.; Scullion, D.; Gan, W.; Falin, A.; Zhang, S.; Watanabe, K.; Taniguchi, T.; Chen, Y.; Santos, E. J. G.; Li, L. H. High Thermal Conductivity of High-Quality Monolayer Boron Nitride and Its Thermal Expansion. *Sci. Adv.* **2019**, *5* (6), eaav0129. <https://doi.org/10.1126/sciadv.aav0129>.

(89) Yuan, P.; Wang, R.; Wang, T.; Wang, X.; Xie, Y. Nonmonotonic Thickness-Dependence of in-Plane Thermal Conductivity of Few-Layered MoS<sub>2</sub>: 2.4 to 37.8 Nm. *Phys. Chem. Chem. Phys.* **2018**, *20* (40), 25752–25761. <https://doi.org/10.1039/C8CP02858C>.

(90) Yarali, M.; Wu, X.; Gupta, T.; Ghoshal, D.; Xie, L.; Zhu, Z.; Brahmi, H.; Bao, J.; Chen, S.; Luo, T.; Koratkar, N.; Mavrokefalos, A. Effects of Defects on the Temperature-Dependent Thermal Conductivity of Suspended Monolayer Molybdenum Disulfide Grown by Chemical Vapor Deposition. *Adv. Funct. Mater.* **2017**, *27* (46), 1704357. <https://doi.org/10.1002/adfm.201704357>.

(91) Aiyiti, A.; Hu, S.; Wang, C.; Xi, Q.; Cheng, Z.; Xia, M.; Ma, Y.; Wu, J.; Guo, J.; Wang, Q.; Zhou, J.; Chen, J.; Xu, X.; Li, B. Thermal Conductivity of Suspended Few-Layer MoS<sub>2</sub>. *Nanoscale* **2018**, *10* (6), 2727–2734. <https://doi.org/10.1039/C7NR07522G>.

(92) Bae, J. J.; Jeong, H. Y.; Han, G. H.; Kim, J.; Kim, H.; Kim, M. S.; Moon, B. H.; Lim, S. C.; Lee, Y. H. Thickness-Dependent in-Plane Thermal Conductivity of Suspended MoS<sub>2</sub> Grown by Chemical Vapor Deposition. *Nanoscale* **2017**, *9* (7), 2541–2547. <https://doi.org/10.1039/C6NR09484H>.

(93) Gu, X.; Li, B.; Yang, R. Layer Thickness-Dependent Phonon Properties and Thermal Conductivity of MoS<sub>2</sub>. *Journal of Applied Physics* **2016**, *119* (8), 085106. <https://doi.org/10.1063/1.4942827>.

(94) Zhao, Y.; Cai, Y.; Zhang, L.; Li, B.; Zhang, G.; Thong, J. T. L. Thermal Transport in 2D Semiconductors—Considerations for Device Applications. *Advanced Functional Materials* **2020**, *30* (8), 1903929. <https://doi.org/10.1002/adfm.201903929>.

(95) Wang, H.; Hu, S.; Takahashi, K.; Zhang, X.; Takamatsu, H.; Chen, J. Experimental Study of Thermal Rectification in Suspended Monolayer Graphene. *Nat Commun* **2017**, *8* (1), 15843. <https://doi.org/10.1038/ncomms15843>.

(96) Kurşun, B.; Sivrioğlu, M. Heat Transfer Enhancement Using U-Shaped Flow Routing Plates in Cooling Printed Circuit Boards. *J. Braz. Soc. Mech. Sci. Eng.* **2018**, *40* (1), 13. <https://doi.org/10.1007/s40430-017-0937-z>.

(97) Song, J.; Lu, L.; Li, B.; Zhang, B.; Hu, R.; Zhou, X.; Cheng, Q. Thermal Routing via Near-Field Radiative Heat Transfer. *International Journal of Heat and Mass Transfer* **2020**, *150*, 119346. <https://doi.org/10.1016/j.ijheatmasstransfer.2020.119346>.



- (98) Late, D. J.; Huang, Y.-K.; Liu, B.; Acharya, J.; Shirodkar, S. N.; Luo, J.; Yan, A.; Charles, D.; Waghmare, U. V.; Dravid, V. P.; Rao, C. N. R. Sensing Behavior of Atomically Thin-Layered MoS<sub>2</sub> Transistors. *ACS Nano* **2013**, *7* (6), 4879–4891. <https://doi.org/10.1021/nn400026u>.
- (99) Sledzinska, M.; Quey, R.; Mortazavi, B.; Graczykowski, B.; Placidi, M.; Reig, D. S.; Navarro-Urrios, D.; Alzina, F.; Colombo, L.; Roche, S.; Torres, C. M. S. *Record Low Thermal Conductivity of Polycrystalline MoS<sub>2</sub> Films: Tuning the Thermal Conductivity by Grain Orientation*. <https://pubs.acs.org/doi/abs/10.1021/acsami.7b08811> (accessed 2019-05-08). <https://doi.org/10.1021/acsami.7b08811>.
- (100) Lu, M.-H.; Feng, L.; Chen, Y.-F. Phononic Crystals and Acoustic Metamaterials. *Materials Today* **2009**, *12* (12), 34–42. [https://doi.org/10.1016/S1369-7021\(09\)70315-3](https://doi.org/10.1016/S1369-7021(09)70315-3).
- (101) Sledzinska, M.; Graczykowski, B.; Maire, J.; Chavez-Angel, E.; Sotomayor-Torres, C. M.; Alzina, F. 2D Phononic Crystals: Progress and Prospects in Hypersound and Thermal Transport Engineering. *Adv. Funct. Mater.* **2020**, *30* (8), 1904434. <https://doi.org/10.1002/adfm.201904434>.
- (102) Kasprzak, M.; Sledzinska, M.; Zaleski, K.; Iatsunskyi, I.; Alzina, F.; Volz, S.; Sotomayor Torres, C. M.; Graczykowski, B. High-Temperature Silicon Thermal Diode and Switch. *Nano Energy* **2020**, *78*, 105261. <https://doi.org/10.1016/j.nanoen.2020.105261>.
- (103) Sledzinska, M.; Graczykowski, B.; Alzina, F.; Melia, U.; Termentzidis, K.; Lacroix, D.; Sotomayor Torres, C. M. Thermal Conductivity in Disordered Porous Nanomembranes. *Nanotechnology* **2019**, *30* (26), 265401. <https://doi.org/10.1088/1361-6528/ab0ecd>.
- (104) Cai, Y.; Lan, J.; Zhang, G.; Zhang, Y.-W. Lattice Vibrational Modes and Phonon Thermal Conductivity of Monolayer MoS<sub>2</sub>. *Phys. Rev. B* **2014**, *89* (3), 035438. <https://doi.org/10.1103/PhysRevB.89.035438>.
- (105) Zulfiqar, M.; Zhao, Y.; Li, G.; Li, Z.; Ni, J. Intrinsic Thermal Conductivities of Monolayer Transition Metal Dichalcogenides MX<sub>2</sub> (M = Mo, W; X = S, Se, Te). *Sci Rep* **2019**, *9* (1), 4571. <https://doi.org/10.1038/s41598-019-40882-2>.
- (106) Xiao, P.; Kim, J.-H.; Seo, S. Simple Fabrication of Highly Sensitive Photodetectors Using MoS<sub>2</sub> Nanoparticles and Ag Nanowires. *Science of Advanced Materials* **2017**, *9* (9), 1626–1630.
- (107) Radisavljevic, B.; Radenovic, A.; Brivio, J.; Giacometti, V.; Kis, A. Single-Layer MoS<sub>2</sub> Transistors. *Nature Nanotech* **2011**, *6* (3), 147–150. <https://doi.org/10.1038/nnano.2010.279>.
- (108) Lim, J.; Wang, H.-T.; Tang, J.; Andrews, S. C.; So, H.; Lee, J.; Lee, D. H.; Russell, T. P.; Yang, P. Simultaneous Thermoelectric Property Measurement and Incoherent Phonon Transport in Holey Silicon. *ACS Nano* **2016**, *10* (1), 124–132. <https://doi.org/10.1021/acsnano.5b05385>.
- (109) Gupta, A.; Arunachalam, V.; Vasudevan, S. Liquid-Phase Exfoliation of MoS<sub>2</sub> Nanosheets: The Critical Role of Trace Water. *J. Phys. Chem. Lett.* **2016**, *7* (23), 4884–4890. <https://doi.org/10.1021/acs.jpcllett.6b02405>.

- (110) Xiao, P.; Chavez-Angel, E.; Chaitoglou, S.; Sledzinska, M.; Dimoulas, A.; Sotomayor Torres, C. M.; El Sachat, A. Anisotropic Thermal Conductivity of Crystalline Layered SnSe<sub>2</sub>. *Nano Lett.* **2021**, *21* (21), 9172–9179. <https://doi.org/10.1021/acs.nanolett.1c03018>.
- (111) Arrighi, A.; Corro, E. D.; Urrios, D. N.; Costache, M. V.; Sierra, J. F. F.; Watanabe, K.; Taniguchi, T.; Garrido, J. A.; Valenzuela, S. O.; Torres, C. M. S.; Sledzinska, M. Heat Dissipation in Few-Layer MoS<sub>2</sub> and MoS<sub>2</sub>/HBN Heterostructure. *2D Mater.* **2021**. <https://doi.org/10.1088/2053-1583/ac2e51>.
- (112) Reparaz, J. S.; Chavez-Angel, E.; Wagner, M. R.; Graczykowski, B.; Gomis-Bresco, J.; Alzina, F.; Sotomayor Torres, C. M. A Novel Contactless Technique for Thermal Field Mapping and Thermal Conductivity Determination: Two-Laser Raman Thermometry. *Review of Scientific Instruments* **2014**, *85* (3), 034901. <https://doi.org/10.1063/1.4867166>.
- (113) Yuan, P.; Wang, R.; Wang, T.; Wang, X.; Xie, Y. Nonmonotonic Thickness-Dependence of in-Plane Thermal Conductivity of Few-Layered MoS<sub>2</sub>: 2.4 to 37.8 Nm. *Phys. Chem. Chem. Phys.* **2018**, *20* (40), 25752–25761. <https://doi.org/10.1039/C8CP02858C>.
- (114) Termentzidis, K. *Nanostructured Semiconductors Amorphization and Thermal Properties*; 2017.
- (115) Plimpton, S. Fast Parallel Algorithms for Short- Range Molecular Dynamics. *Journal of Computational Physics* **1995**, *117* (1), 44. <https://doi.org/10.1006/jcph.1995.1039>.
- (116) Chen, Z.; Lu, C. Humidity Sensors: A Review of Materials and Mechanisms. *Sens Lett* **2005**, *3* (4), 274–295. <https://doi.org/10.1166/sl.2005.045>.
- (117) Smith, A. D.; Elgammal, K.; Niklaus, F.; Delin, A.; Fischer, A. C.; Vaziri, S.; Forsberg, F.; Rålander, M.; Hugosson, H.; Bergqvist, L.; Schröder, S.; Kataria, S.; Östling, M.; Lemme, M. C. Resistive Graphene Humidity Sensors with Rapid and Direct Electrical Readout. *Nanoscale* **2015**, *7* (45), 19099–19109. <https://doi.org/10.1039/C5NR06038A>.
- (118) Late, D. J. Liquid Exfoliation of Black Phosphorus Nanosheets and Its Application as Humidity Sensor. *Microporous and Mesoporous Materials* **2016**, *225*, 494–503. <https://doi.org/10.1016/j.micromeso.2016.01.031>.
- (119) Zhao, J.; Li, N.; Yu, H.; Wei, Z.; Liao, M.; Chen, P.; Wang, S.; Shi, D.; Sun, Q.; Zhang, G. Highly Sensitive MoS<sub>2</sub> Humidity Sensors Array for Noncontact Sensation. *Adv. Mater.* **2017**, *29* (34), 1702076. <https://doi.org/10.1002/adma.201702076>.
- (120) Guo, H.; Lan, C.; Zhou, Z.; Sun, P.; Wei, D.; Li, C. Transparent, Flexible, and Stretchable WS<sub>2</sub> Based Humidity Sensors for Electronic Skin. *Nanoscale* **2017**, *9* (19), 6246–6253. <https://doi.org/10.1039/C7NR01016H>.
- (121) He, P.; Brent, J. R.; Ding, H.; Yang, J.; Lewis, D. J.; O'Brien, P.; Derby, B. Fully Printed High Performance Humidity Sensors Based on Two-Dimensional Materials. *Nanoscale* **2018**, *10* (12), 5599–5606. <https://doi.org/10.1039/C7NR08115D>.
- (122) Zhang, S.-L.; Choi, H.-H.; Yue, H.-Y.; Yang, W.-C. Controlled Exfoliation of Molybdenum Disulfide for Developing Thin Film Humidity Sensor. *Current Applied Physics* **2014**, *14* (3), 264–268. <https://doi.org/10.1016/j.cap.2013.11.031>.

- (123) Duan, Z.; Jiang, Y.; Yan, M.; Wang, S.; Yuan, Z.; Zhao, Q.; Sun, P.; Xie, G.; Du, X.; Tai, H. Facile, Flexible, Cost-Saving, and Environment-Friendly Paper-Based Humidity Sensor for Multifunctional Applications. *ACS Appl. Mater. Interfaces* **2019**, *11*, 21840–21849.
- (124) Guo, J.; Wen, R.; Liu, Y.; Zhang, K.; Kou, J.; Zhai, J.; Wang, Z. L. Piezotronic Effect Enhanced Flexible Humidity Sensing of Monolayer MoS<sub>2</sub>. *ACS Applied Materials & Interfaces* **2018**, *10* (9), 8110–8116. <https://doi.org/10.1021/acsami.7b17529>.
- (125) Awais, M.; Khan, M. U.; Hassan, A.; Bae, J.; Chattha, T. E. Printable Highly Stable and Superfast Humidity Sensor Based on Two Dimensional Molybdenum Diselenide. *Sci Rep* **2020**, *10* (1), 5509. <https://doi.org/10.1038/s41598-020-62397-x>.
- (126) Li, N.; Chen, X.-D.; Chen, X.-P.; Ding, X.; Zhao, X. Fast-Response MoS<sub>2</sub>-Based Humidity Sensor Braced by SiO<sub>2</sub> Microsphere Layers. *IEEE Electron Device Lett.* **2018**, *39* (1), 115–118. <https://doi.org/10.1109/LED.2017.2778187>.
- (127) Yadav, S.; Chaudhary, P.; Uttam, K. N.; Varma, A.; Vashistha, M.; Yadav, B. C. Facile Synthesis of Molybdenum Disulfide (MoS<sub>2</sub>) Quantum Dots and Its Application in Humidity Sensing. *Nanotechnology* **2019**, *30* (29), 295501. <https://doi.org/10.1088/1361-6528/ab1569>.
- (128) Ren, J.; Guo, B.; Feng, Y.; Yu, K. Few-Layer MoS<sub>2</sub> Dendrites as a Highly Active Humidity Sensor. *Physica E: Low-dimensional Systems and Nanostructures* **2020**, *116*, 113782. <https://doi.org/10.1016/j.physe.2019.113782>.
- (129) Mondal, S.; Kim, S. J.; Choi, C.-G. Honeycomb-like MoS<sub>2</sub> Nanotube Array-Based Wearable Sensors for Noninvasive Detection of Human Skin Moisture. *ACS Appl. Mater. Interfaces* **2020**, *12* (14), 17029–17038. <https://doi.org/10.1021/acsami.9b22915>.
- (130) Agmon, N. The Grotthuss Mechanism. *Chemical Physics Letters* **1995**, *244* (5–6), 456–462. [https://doi.org/10.1016/0009-2614\(95\)00905-J](https://doi.org/10.1016/0009-2614(95)00905-J).
- (131) Geissler, P. L. Autoionization in Liquid Water. *Science* **2001**, *291* (5511), 2121–2124. <https://doi.org/10.1126/science.1056991>.
- (132) Barsan, N.; Weimar, U. Conduction Model of Metal Oxide Gas Sensors. *J. Electroceramics* **2001**, *7*, 143–167.
- (133) Kim, W.; Javey, A.; Vermesh, O.; Wang, Q.; Li, Y.; Dai, H. Hysteresis Caused by Water Molecules in Carbon Nanotube Field-Effect Transistors. *Nano Lett.* **2003**, *3* (2), 193–198. <https://doi.org/10.1021/nl0259232>.
- (134) Fournier, J. A.; Carpenter, W. B.; Lewis, N. H. C.; Tokmakoff, A. Broadband 2D IR Spectroscopy Reveals Dominant Asymmetric H<sub>5</sub>O<sub>2</sub><sup>+</sup> Proton Hydration Structures in Acid Solutions. *Nature Chem* **2018**, *10* (9), 932–937. <https://doi.org/10.1038/s41557-018-0091-y>.
- (135) Zundel, G. Hydrogen Bonds with Large Proton Polarizability and Proton Transfer Processes in Electrochemistry and Biology. In *Advances in Chemical Physics*; Prigogine, I., Rice, S. A., Eds.; John Wiley & Sons, Inc.: Hoboken, NJ, USA, 2007; pp 1–217. <https://doi.org/10.1002/9780470141700.ch1>.
- (136) Shkrob, I. A.; Schlueter, J. A. Can a Single Molecule Trap the Electron? *Chemical Physics Letters* **2006**, *431* (4–6), 364–369. <https://doi.org/10.1016/j.cplett.2006.09.106>.

- (137) Mozumder, A. Conjecture on Electron Trapping in Liquid Water. *International Journal of Radiation Applications and Instrumentation. Part C. Radiation Physics and Chemistry* **1988**, 32 (2), 287–291. [https://doi.org/10.1016/1359-0197\(88\)90200-7](https://doi.org/10.1016/1359-0197(88)90200-7).
- (138) Burman, D.; Santra, S.; Pramanik, P.; Guha, P. K. Pt Decorated MoS<sub>2</sub> Nanoflakes for Ultrasensitive Resistive Humidity Sensor. *Nanotechnology* **2018**, 29 (11), 115504. <https://doi.org/10.1088/1361-6528/aaa79d>.
- (139) Wang, S.; Li, H.; Zhang, J.; Guo, S.; Xu, W.; Grossman, J. C.; Warner, J. H. Epitaxial Templating of Two-Dimensional Metal Chloride Nanocrystals on Monolayer Molybdenum Disulfide. *ACS Nano* **2017**, 11 (6), 6404–6415. <https://doi.org/10.1021/acsnano.7b02838>.
- (140) Smith, A. D.; Elgammal, K.; Niklaus, F.; Delin, A.; Fischer, A. C.; Vaziri, S.; Forsberg, F.; Råsander, M.; Hugosson, H.; Bergqvist, L.; Schröder, S.; Kataria, S.; Östling, M.; Lemme, M. C. Resistive Graphene Humidity Sensors with Rapid and Direct Electrical Readout. *Nanoscale* **2015**, 7 (45), 19099–19109. <https://doi.org/10.1039/C5NR06038A>.
- (141) Borini, S.; White, R.; Wei, D.; Astley, M.; Haque, S.; Spigone, E.; Harris, N.; Kivioja, J.; Ryhänen, T. Ultrafast Graphene Oxide Humidity Sensors. *ACS Nano* **2013**, 7 (12), 11166–11173. <https://doi.org/10.1021/nn404889b>.
- (142) Li, N.; Chen, X.-D.; Chen, X.-P.; Ding, X.; Zhao, X. Fast-Response MoS<sub>2</sub>-Based Humidity Sensor Braced by SiO<sub>2</sub> Microsphere Layers. *IEEE Electron Device Lett.* **2018**, 39 (1), 115–118. <https://doi.org/10.1109/LED.2017.2778187>.
- (143) Jha, R. K.; Guha, P. K. Liquid Exfoliated Pristine WS<sub>2</sub> Nanosheets for Ultrasensitive and Highly Stable Chemiresistive Humidity Sensors. *Nanotechnology* **2016**, 27 (47), 475503. <https://doi.org/10.1088/0957-4484/27/47/475503>.
- (144) Sun, L.; Wang, B.; Wang, Y. A Novel Silicon Carbide Nanosheet for High-Performance Humidity Sensor. *Adv. Mater. Interfaces* **2018**, 5 (6), 1701300. <https://doi.org/10.1002/admi.201701300>.
- (145) Park, S. Y.; Kim, Y. H.; Lee, S. Y.; Sohn, W.; Lee, J. E.; Kim, D. H.; Shim, Y.-S.; Kwon, K. C.; Choi, K. S.; Yoo, H. J.; Suh, J. M.; Ko, M.; Lee, J.-H.; Lee, M. J.; Kim, S. Y.; Lee, M. H.; Jang, H. W. Highly Selective and Sensitive Chemoresistive Humidity Sensors Based on RGO/MoS<sub>2</sub> van Der Waals Composites. *J. Mater. Chem. A* **2018**, 6 (12), 5016–5024. <https://doi.org/10.1039/C7TA11375G>.
- (146) Wells, R. A.; Johnson, H.; Lhermitte, C. R.; Kinge, S.; Sivula, K. Roll-to-Roll Deposition of Semiconducting 2D Nanoflake Films of Transition Metal Dichalcogenides for Optoelectronic Applications. *ACS Appl. Nano Mater.* **2019**, acsanm.9b01774. <https://doi.org/10.1021/acsnm.9b01774>.
- (147) Fan, X.; Xu, P.; Zhou, D.; Sun, Y.; Li, Y. C.; Nguyen, M. A. T.; Terrones, M.; Mallouk, T. E. Fast and Efficient Preparation of Exfoliated 2H MoS<sub>2</sub> Nanosheets by Sonication-Assisted Lithium Intercalation and Infrared Laser-Induced 1T to 2H Phase Reversion. *Nano Lett.* **2015**, 15 (9), 5956–5960. <https://doi.org/10.1021/acs.nanolett.5b02091>.
- (148) Fan, R.; Huh, S.; Yan, R.; Arnold, J.; Yang, P. Gated Proton Transport in Aligned Mesoporous Silica Films. *Nature Mater* **2008**, 7 (4), 303–307. <https://doi.org/10.1038/nmat2127>.

- (149) Zhang, S.-L.; Jung, H.; Huh, J.-S.; Yu, J.-B.; Yang, W.-C. Efficient Exfoliation of MoS<sub>2</sub> with Volatile Solvents and Their Application for Humidity Sensor. *J Nanosci Nanotechnol* **2014**, *14* (11), 8518–8522. <https://doi.org/10.1166/jnn.2014.9984>.
- (150) Guo, S.; Arab, A.; Krylyuk, S.; Davydov, A. V.; Zaghloul, M. E. Fabrication and Characterization of Humidity Sensors Based on CVD Grown MoS<sub>2</sub> Thin Film. In *2017 IEEE 17th International Conference on Nanotechnology (IEEE-NANO)*; IEEE: Pittsburgh, PA, USA, 2017; pp 164–167. <https://doi.org/10.1109/NANO.2017.8117408>.
- (151) Yue, Q.; Shao, Z.; Chang, S.; Li, J. Adsorption of Gas Molecules on Monolayer MoS<sub>2</sub> and Effect of Applied Electric Field. *Nanoscale Res Lett* **2013**, *8* (1), 425. <https://doi.org/10.1186/1556-276X-8-425>.

# List of Publications

1. **P. Xiao**, E. Chavez-Angel, S. Chaitoglou, M. Sledzinska, A. Dimoulas, C. M. Sotomayor Torres, A. El Sachat. Anisotropic Thermal Conductivity of Crystalline Layered SnSe<sub>2</sub>, *Nano Letters*, 21, 21, 9172-9179 (2021).
2. **P. Xiao**, D. Mencarelli, E. Chavez-Angel, C. H. Joseph, A. Cataldo, L. Pierantoni, C. M. Sotomayor Torres, M. Sledzinska. Reversing the Humidity Response of MoS<sub>2</sub>- and WS<sub>2</sub>-Based Sensors Using Transition-Metal Salts, *ACS Applied Materials & Interfaces*, 13, 19, 23201-23209 (2021).
3. **P. Xiao**, A. El Sachat, E. Chávez-Angel, G. Nikoulis, J. Kioseoglou, K. Termentzidis, C. M. Sotomayor Torres, M. Sledzinska. Thermal insulation and heat guiding using nanopatterned MoS<sub>2</sub>, *arXiv preprint arXiv:2204.04999* (2022).
4. **P. Xiao**, J.H. Kim, S.M. Seo. Simple Fabrication of Photodetectors Based on MoS<sub>2</sub> Nanoflakes and Ag Nanoparticles. *Sensors*, 22, 4695 (2022).
5. **P. Xiao**, J.H. Kim, S. Seo, Flexible and Stretchable Liquid Metal Electrodes Working at Sub-Zero Temperature and Their Applications, *Surface and Interface Engineering for Organic Device Applications*, 14 (15), 4313 (2021).
6. **P. Xiao**, HJ Gwak, S Seo, Fabrication of a flexible photodetector based on a liquid eutectic gallium indium, *Materials*, 13 (22), 5210 (2021).
7. A. El Sachat, **P. Xiao**, D. Donadio, F. Bonell, M. Sledzinska, A. Marty, C. Vergnaud, H. Boukari, M. Jamet, G. Arregui, Z.K. Chen, F. Alzina, C.M. Sotomayor Torres, E. Chavez-Angel, Effect of crystallinity and thickness on thermal transport in layered PtSe<sub>2</sub>, *npj 2D Materials and Applications*, 6, 32, 1-9 (2022).
8. D. Navarro-Urrios, E. S.Kang, **P. Xiao**, M.F. Colombano, G. Arregui, B. Graczykowski, N. E Capuj, M. Sledzinska, C.M. Sotomayor-Torres, G. Fytas, Optomechanical crystals for spatial sensing of submicron sized particles, *Scientific reports*, 11 (1), 1-7 (2021).
9. M. Sledzinska, G. Jumbert, M. Placidi, A. Arrighi, **P. Xiao**, Francesc Alzina, Clivia M Sotomayor Torres, Fracturing of Polycrystalline MoS<sub>2</sub> Nanofilms, *ACS Applied Electronic Materials*, 2 (4), 1169-1175 (2020).
10. R.C Ng, A. El Sachat, F. Cespedes, M. Poblet, G. Madiot, J. Jaramillo-Fernandez, **P. Xiao**, O. Florez, M. Sledzinska, C. M. Sotomayor-Torres, E. Chavez-Angel,

Excitation and detection of acoustic phonons in nanoscale systems, arXiv preprint arXiv:2203.15476, (2022).

- Selected oral talks in Conferences and Workshops

1. **P. Xiao**, A. El Sachat, E. Chávez Angel, G. Nikoulis, J. Kioseoglou, K. Termentzidis, C. M. Sotomayor Torres, and M. Sledzinska. Thermal conductivity control in layered MoS<sub>2</sub> by phononic engineering. Nanoscale and Microscale Heat Transfer VII, 29<sup>th</sup> May – 2<sup>nd</sup> June 2022 (**oral talk**).

2. **P. Xiao**, A. El Sachat, E. Chávez Angel, G. Nikoulis, J. Kioseoglou, K. Termentzidis, C. M. Sotomayor Torres, and M. Sledzinska. Reduction of thermal conductivity of layered MoS<sub>2</sub> using phononic crystals. Spanish network in Nanolithography (NANOLITO), 26<sup>th</sup> – 27<sup>th</sup> January 2022 (**oral talk**).

3. **P. Xiao**, E. Chavez-Angel, S. Chaitoglou, M. Sledzinska, A. Dimoulas, C. M. Sotomayor Torres, A. El Sachat. Measurement of cross-plane and in-plane thermal conductivity of free-standing SnSe<sub>2</sub>, E-MRS 2021 Fall Meeting. 20<sup>th</sup> - 23<sup>rd</sup> September 2021 (**oral talk**).

4. **P. Xiao**, C. Hardly Joseph, E. Chavez-Angel, A. Cataldo, D. Mencarelli, L. Pierantoni, C. M. Sotomayor Torres, M. Sledzinska. Reversing of humidity response of MoS<sub>2</sub>- and WS<sub>2</sub>-based sensors with metal coatings, Graphene and 2DM (GO2021). 20<sup>th</sup> -21<sup>st</sup> April 2021 (**oral talk**).